Energy and Charge Transfer during Electron Beam Melting

Paul R. Carriere

Doctor of Philosophy

Department of Mining and Materials Engineering

McGill University

Montreal,Quebec

2018-04-15

A thesis submitted to McGill University in partial fulfillment
of the requirements of a degree of
Doctor of Philosophy

Dedications

This thesis is dedicated to my parents, Rene and Madeleine Carriere. Your commitment to your family and each other is an inspiration to everyone you know. Thank you for decades of support, encouragement and happiness.

This dissertation is also dedicated to Astou Sene. Since the first day we met, your light and laughter has transformed my world. I am thankful that your abundance of life has spilled over into mine.

Acknowledgements

There are countless people who have directly and indirectly supported this work throughout the years. At McGill University, I would like to first thank Jan Krygier for his support in standing up the McGill electron beam system on many levels. In times of adversity, your positive attitude and generous nature was a much needed diversion. I would also like to thank Dr. Sriraman Rajagopalan for helping me navigate the daunting world of Materials Engineering. Your commitment to the craft is a model to novices and experts alike. Basel Alchikh-sulaiman deserves recognition for his support and perseverance. I hope our discussions of technology and industry were as helpful for you as they were for me. I'd like to thank Mr. Csaba Szalacsi from the McGill machine shops for his valuable advice regarding what is and isn't possible, as well as his trust in lending me the machinist tools and not the student ones. I'd like to also thank Prof Raynald Gauvin and Dr Hendrix Demers for their thoughtful discussions on electron microscopy and Prof Mathieu Brochu for his time discussing additive manufacturing. Honorable mention to Jim Bobyn for helping with the many adminstrative hurdles. I'd also like to thank Sam Rudinski, Jerome LeBouef, Jason Milligan, Abhi Ghosh, Chris Marion and Neslihan Alpay Sari for bringing levity and fun to department. Finally, I would like to thank Barbara Hanley, the MinMat 'PhD mom', for ensuring we don't forget to tie our shoes before running out the door.

Outside of McGill, I would like to thank the entire PAVAC team for their helpful support and discussions in running the electron beam system, including Dmitri Sandler, Jason Gao, and Shah Khosraviani with a special thanks to Ralf Edinger. Without your technical and professional advice, this project would not have been possible.

I'd like to thank Prof Hani Henein from the University of Alberta about his insight into the dimensionality of solidification and Prof Todd Palmer from Penn State University for his advice on electron beam welding. I'd also like to thank Prof Steve Cockcroft, Prof Daan Maijer and Prof Chad Sinclair from UBC for their advice on various components of this project. I'd also like to thank Vivian Cheung from UBC for helping to coordinate the

EBW experiments in Richmond. An extra special thanks to Dr Fredrique Larouche from AP&C for materially supporting this research.

Finally, I would like to thank my supervisor, Prof Stephen Yue. Your support over a long and sometimes overwhelming journey was needed, and your attitude towards research, collaboration and life provided lessons that I will never forget. Understanding how to bridge science to technology will always be a challenge, and you provided wisdom that few could share. You are a true Starman amongst your peers.

Abstract

Discovered nearly 150 years ago, electron beams contribute to nearly every discipline of science and technology. Recently, this mature field has found new purpose in the domain of Additive Manufacturing, resulting in significant industrial and academic interests. In nearly all cases, the process is examined through the lens of a single commercial supplier with limited access to fundamental process parameters. The objective of this thesis is to examine the fundamental science and technology underpinning electron beam powder bed fusion, beginning with thermionic emission and ending with single layers of consolidated powder.

Between these points, the generation and control of an electron beam is explained, highlighting the specific opportunities and challenges compared to laser-based processes. Slotted Faraday Cup measurements experimentally demonstrate many of the issues associated with steering and focusing a beam of negatively charged particles. Using a novel calorimetric measurement technique, the fraction of absorbed energy is directly measured and compared to Monte-Carlo simulations over a range of process conditions. Next, the combined effects of beam and geometric parameters are examined with respect to dissimilar electron beam welding of titanium to niobium. The differences in material properties magnify how small variations to the process inputs induce large variations in melt pool stability via convective and evaporative heat transfer. These concepts of energy absorption and melt pool stability are extended in the final chapter, which directly measures the absorbed current during pulsed electron beam melting of solid and powder titanium. Our results show, that above the melting temperature, energy and charge transfer are coupled, which we attribute to the ionization of the Ti vapor. To the best of our knowledge, these measurements are the first of their kind, and suggest a new domain of investigation for electron beam powder bed fusion.

Aberégé

Découvert a près de 150 ans, les faisceaux d'électrons ont contribué à presque toutes les disciplines de la science et technologie. Récemment, ce domaine mature a trouvé un nouvel objectif dans le domaine de la fabrication additive, résultant en des intérêts industriels et académiques significatifs. Dans presque tous les cas, le processus est examiné à travers la lentille d'un seul fournisseur commercial avec un accès restreint aux paramètres de processus fondamentaux. L'objectif de cette thèse est d'examiner la science et la technologie fondamentale qui sous-tendent la fusion du lit de poudre du faisceau d'électrons, en commençant par l'émission thermionique et en terminant par des couches uniques de poudre consolidée.

Entre ces points, la génération et le contrôle d'un faisceau d'électrons est expliqué, mettant en évidence les opportunits et les défis spécifiques par rapport au processus basé sur le laser. Les mesures de la Coupe Faraday à fentes démontrent expérimentalement plusieurs des problèmes associés à la direction et à la focalisation d'un faisceau de particules chargées négativement. En utilisant une nouvelle technique de mesure calorimétrique, la fraction d'énergie absorbée est directement mesurée et comparée aux simulations de Monte-Carlo sur une gamme de conditions de processus. Ensuite, les effets combinés du faisceau et des paramètres géométriques sont examinés par rapport au soudage dissemblable par faisceau d'électrons du titane au niobium. Les différences dans les propriétés des matériaux amplifient la manière dont les petites variations des intrants induisent de grandes variations dans la stabilité de la masse fondue par transfert de chaleur par convection et évaporation. Ces concepts d'absorption d'énergie et de stabilité de la masse fondue sont développés dans le dernier chapitre, qui mesure directement le courant absorbé lors de la fusion par faisceau d'électrons pulsé de titane solide et pulvérulent. Nos résultats montrent qu'au-dessus de la température de fusion, l'énergie et le transfert de charge sont couplés, ce que nous attribuons l'ionisation de la vapeur de Ti. Au meilleur de nos connaissances, ces mesures sont les premières du genre et suggèrent un nouveau domaine d'investigation pour la fusion de lit de poudre par faisceau d'électrons.

Preface

Published over 35 years ago, *Electron Beam Technology* by Schiller remains to this day the most comprehensive reference on thermal processing using high-power electron beams. Yet despite a surge of interests in electron-beam powder bed fusion, this seminal textbook has been largely overlooked by the AM community. A possible explanation could be that nearly all research is currently conducted using equipment provided by a single original equipment manufacturer, Arcam AB. In this case, the subtle details of generating a stable electron beam are encapsulated in proprietary hardware and algorithms, restricting direct access to specific process parameters such as accelerating voltage and beam speed.

In comparison, the laser powder bed fusion community has a variety of vendors as well as a deeper pool of laser scientists to draw from. The mechanisms involved during laser/powder interactions have been examined in far greater detail than in the electron beam space, and it could be argued that this has resulted is greater industrial acceptance. In many cases, an electron beam is conceptualized as being identical to a laser, except that it works in a vacuum and has a bigger spot size. Yet, as meticulously detailed by Schiller, the science of high power electron beam optics is the science of charge transfer, implying that unlike a laser, beam/matter interactions must consider both energy and charge transfer within the powder bed.

In a manner of speaking, this dissertation 'peels back the onion' on electron beam powder bed fusion by demonstrating how electron beam welding is transformed into electron beam additive manufacturing. In essence, this research is based on the detailed analysis of electron beam technology provided 35 years ago and leverages the significant advances in powder metallurgy, digital controls, instrumentation and signal processing to further the art.

Contribution of Author

In terms of technical contributions, it should be noted that the author was the first and, until a year ago, only student to work in the McGill electron beam processing lab as the sole equipment operator. The mechanical fixturing, thermocouple instrumentation, signal processing, optics calibrations and gCode compiler presented in this dissertation were built by the author. The acquisition and curve fitting routines associated with Faraday Cup measurements of Ch. 3 were constructed by the author, while the physical Faraday Cup was provided by PAVAC. Similarly, the single layer powder height measurements of Ch. 3 were conducted in collaboration with Basel Alchikh-Sulaiman. The electron beam welds of Ch. 5 were conducted at PAVAC Industries by PAVAC staff, with on-site supervision of the author. Otherwise, all other electron beam processes; mechanical, electrical and software designs; as well as process analyses were conducted at McGill by the author.

Original Contributions to Knowledge

In terms of scientific contributions, the transient calorimetric measurements of pulsed electron beam absorption of Ch. 4 are the first of their kind in the literature. By demonstrating experimental agreement between measurement and Monte Carlo simulation, this work opens the possibility for further development tailored towards three dimensional absorption calculations. The work of Ch. 4 resulted in a publication in the journal *Vacuum*.

In the dissimilar Nb-Ti welds of Ch. 5, the composite heat transfer analysis and deflection pattern frequency analysis represents a novel scientific contribution. Comparing welds at different working distances and accelerating voltage is a unique approach to understanding the effects of beam power density. This work was presented as a poster at the 2015 Superconducting RF conference at Whistler, British Columbia, Canada and supported the development of a commercial Welding Procedure Specification.

The gCode compiler architecture of Ch. 3 and preliminary powder melting results were presented as a talk at the 2016 International Conference on High-Power Electron Beam Technology in Reno, Nevada. A similar talk was given at the 2016 Materials Science and Technology Conference in Salt Lake City, Utah. The scientific contribution of this effort is demonstrating the various inter-dependencies associated with creating a variable voltage electron beam process.

The single powder layer fixturing and heating algorithms described in Ch. 3 were adapted from the single layer work of many authors and appropriately referenced. The distinct scientific contribution is the in-situ sintering and optical profilometry, which enables direct surface topology measurements of single powder layers. While many authors quote packing density by averaging multiple layers, our approach directly measures the powder/substrate interface dynamics. With additional work, this novel powder spreading technique will be detailed in a forthcoming journal article.

To the best of our knowledge, the data presented concerning charge absorption of powder Ti in Ch. 6 are the first of their kind and offer a unique method to correlate charge and energy transfer during electron beam melting. Also, to the best of our knowledge, these experiments represent the first room-temperature electron beam melting of powder, leading us to define the term ‘contact-sintering’. These findings were presented as a talk at the 2017 Materials Science and Technology Conference in Pittsburgh, Pennsylvania, and will be published in a forthcoming article.

Table of Contents

List of Tables

List of Figures

CHAPTER 1
Introduction

One of the first known industrial application of electron beams can be traced to 1907, when Marcello Pirani realized that the heat generated at the anode of a cathode-ray tube could be used to melt refractory metal powders.[1] One hundred and ten years later, state-of-the-art electron beam systems manufacture jet engine components directly from powder by selectively welding thousands of stacked 2D layers in a process broadly referred to as Additive Manufacturing (AM).[2] Despite the explosive interests in electron beam AM techniques, few references give consideration to the underlying science of electron beam/matter interactions, which is by definition the transfer of charge and energy.

Beginning from the primary process parameters surrounding electron beam optics, and transient heat transfer, this dissertation will examine the Electron Beam Powder Bed Fusion (EB-PBF) process as an evolved version of Electron Beam Welding (EBW), highlighting some of the key advantages and challenges surrounding this exciting field. As specific examples, the interplay between cathode material, spot size and working distance will be discussed in the literature review Ch 2. Chapter 3 will detail equipment and software developed by the author related to melting a 2D pattern onto a hot workpiece. In Ch. 4, precision thermocouple measurements and Monte Carlo simulations be used to examine how the incident beam energy is absorbed by a metal. In Ch. 5, the relationships between toolpaths, material properties and heat transfer will be demonstrated with dissimilar electron beam welding experiments. In Ch 6, the importance of sinter state and incident energy will demonstrate how charge and energy transport during electron beam melting is coupled. Combined, these individual topics will demonstrate the challenges and opportunities in creating superior AM parts using electron beam technology by deconvolving a complex, multi-step process, with an analysis that begins at the cathode and ends at a single layer of consolidated powder.

1.1 Electron Beam Welding Evolves

The birth of EBW can be traced to 1948, when Dr. Karl Steigerwald observed that modifications to his electron microscope resulted in melting and evaporation of his samples.[1] Immediately recognizing the industrial significance, Steigerwald shifted his research from microscopy to electron beam machining and welding. Ten years later, Dr. Steigerwald observed the depth-to-width ratio of his welds increased dramatically above a specific power threshold, an observation which birthed the keyhole welding technique.[3]

Since that time, high power EBW has been applied towards the fabrication nuclear fuel elements, fifth generation fighter jets, superconducting particle accelerators and offshore wind turbines.[1, 3, 4, 5, 6, 7] Despite the high costs; the ability to minimize oxidation, generate high powers with variable power density, operate at large stand-off distances, and automate the process has made EBW the go-to joining technology for high-value products and exotic materials.

Although EBW technology has reached a mature technology level, there has been growing interest in electron beam-based AM technology, specifically with the introduction of the the Arcam Electron Beam Melting(EBM™) process. At its core, the process is based on previously stated advantages of EBW, as well as the seamless integration of modern digital control systems, state-of-the-art electron beam optics and powder metallurgy.

Unlike the overwhelming majority of electron-beam powder melting literature, the work presented in this dissertation was not performed using commercial Arcam EBM™ equipment. Instead, this research was conducted with a digitally controlled electron beam welding system installed at McGill. With this open-architecture, new opportunities for instrumentation and beam control were explored. The approach was motivated by the desire to further understand and characterize the beam/matter interactions by manipulating beam parameters outside of conventional Arcam technology envelop, including accelerating voltage and pulsed beam operation.

Overall, the objective of this dissertation is to examine and demonstrate how EBW evolved into the EB-PBF process, highlighting the similarities and differences associated with melting powders and solids. This approach is motivated by the commonly held belief that metal AM is the digital extension of multi-pass welding.[8] A significant distinction between welding and powder bed fusion is associated electrostatic charging of the loose powder. This phenomenon is currently not well understood, as it requires an extensive understanding of electron beam optics, powder metallurgy, heat transfer and as will be shown, plasma physics. Thus, this dissertation introduces each one of these items separately, and examines charge transfer and powder smoke as the final topic.

1.1.1 Additive Manufacturing Market Drivers

The adoption of any new manufacturing technology depends on its ability to reduce lead times, lower costs and/or improve performance. The aerospace industry is acutely sensitive to these issues, as passenger safety, supply chain logistics, mean-time-between overhauls and cost per available seat mile dictate whether operators maintain their ageing fleet or invest in modern equipment.

As a specific example, Boeing recently made the first delivery of it's 737-8 jetliner, otherwise known as the MAX 8.[9] Despite a design which can be traced back to the 60's, Boeing holds an order book of over 3,700 aircraft, a feat largely due to a 14% reduction in specific fuel consumption. While aerodynamic improvements contributed towards this improvement, the single largest factor in improved fuel burn is the increased pressure ratio and higher operating temperatures of the CFM Leap 1B turbofan engines.[9] In other words, the reduced operating costs made possible by advanced materials and manufacturing has forced operators to re-evaluate the costs of maintaining their legacy fleet against procuring new, efficient airliners.

Considering the importance of this technology-push in selling more aircraft, it should come as no surprise that Boeing has recently described the future of Additive Manufacturing (AM) as less of a nicety and more of a necessity.[8] Broadly speaking, AM offers a path which could simultaneously optimize both materials and manufacturing of specific components.

The recently unveiled General Electric Advanced TurboProp(ATP) engine is a clear demonstration of this effect.[10] Approximately 35% of the components in the ATP will be fabricated using AM, reducing 855 conventional manufactured components to 12 AM components.[10, 11] AM technology enabled the use of new materials and design elements

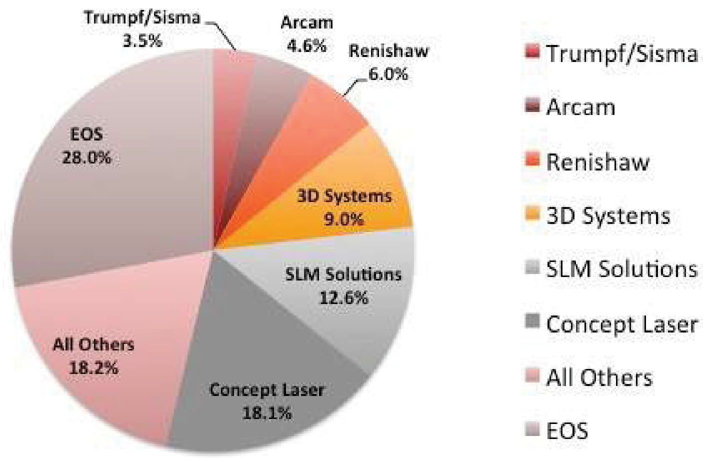

Figure 1–1: Metal additive manufacturing equipment makers by market share-2016[13]

that minimize power losses associated with assembly joints. Compared to the equivalent Pratt & Whitney Canada PT-6, the ATP will have the highest power-to-weight ratio in its class, and 33% longer time between overhaul and 20% lower fuel burn.[12] The use of AM technology has also significantly compressed the development cycle, as the program is expected to be completed approximately one year ahead of schedule.[12]

With the ability to simultaneously reduce lead times, lower costs and improve performance, Additive Manufacturing (AM) has already made an impact in the aerospace sector. Similarly, some commentators believe that the versatility of AM will also democratize manufacturing and to enable a new generation of entrepreneurs.[8] In 2016, the market for metal additive manufacturing systems and materials was worth $950M, but for reasons stated above, is projected to grow to $6.6B by 2026.[13]

In terms of metal AM original equipment suppliers, the 2016 market breakdown is shown in Fig. 1–1, demonstrating the key companies and technologies.

In light of recent acquisitions and the announcement of new companies, the breakdown of Fig.1–1 has most likely evolved. Nevertheless, it should be noted that laser-based systems dominate the market place, with EOS far and above the largest original equipment manufacturer. In comparison, the only EB-PBF equipment manufacturer, Arcam AB, has a market share of roughly 5%, and a global installed machine base of just over 150 machines.[14]

Despite this small segment, the EB-PBF process should be considered as complementary and not competitive to Laser Powder Bed Fusion (L-PBF).[15] Although an exhaustive list comparing the advantages of the two technologies is disputed, the most obvious advantages of laser based systems are:

- Better surface finish and resolution
- Lower initial investment costs
- More material options
- Greater customer adoption and understanding

In comparison, the advantages of EB-PBF include:

- Lower cost and safer feedstock powder
- Higher process productivity
- Reduced support structures and post-processing
- A vacuum build environment

In one case study, it was found that the per-unit cost of a post-processed grade 5 titanium bracket manufactured by EB-PBF was approximately 70% less than the equivalent part made using L-PBF.[16] A large fraction of this cost differential was related to the 350% reduction of EB-PBF support structures, as well as the ability to nest 5 parts per build, as opposed to 2 parts per build in the L-PBF case. In another study, it was found that the ability to nest and stack two 2-part layers in an Arcam Q20 system resulted in a per-unit costs of \$244, compared to a per unit costs of \$551 from a single layer of 8 parts in an EOS M 290 machine.[17]

One of the most optimized EB-PBF processes is the manufacture of acetabular cups used in orthopedic hip implants. The ability to stack parts during EB-PBF as well as the higher beam power leads to deposition rates as high as 200 g h^{-1}.[18] As such, over 50,000 orthopedic implants have been printed using EB-PBF technology, and it is estimated that 1 out of 30 hip surgeries involves components that come from an Arcam system.[19] In another example of part stacking, over 600 individual Ti parts were printed during a single build, with the results shown in Fig. 1–2.

As a final use-case, Avio Aero recently announced serial production of EB-PBF γ-TiAl blades for the low-pressure turbine of the GE9X aircraft engine. As of August 2017,

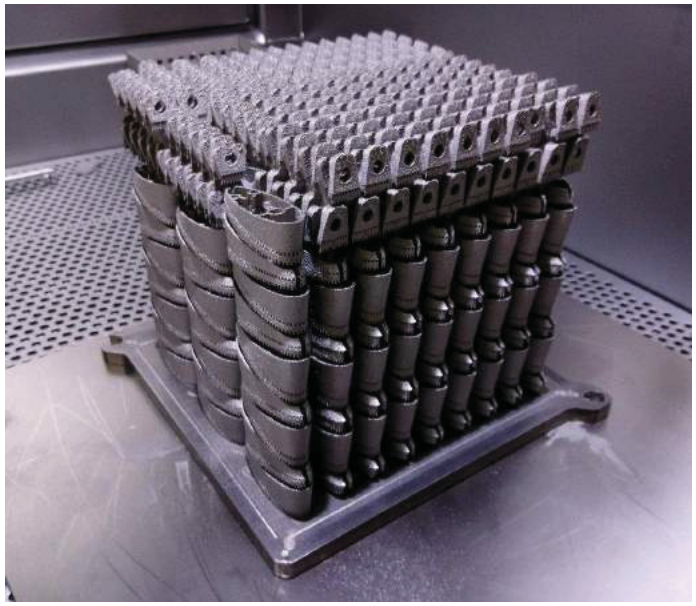

Figure 1–2: Example of nested and stacked build using EB-PBF. Parts were built from Ti64 powder using Arcam hardware. Image provided with permission, courtesy of Metron Advanced Engineering

there are 21 Arcam machines installed at the Cameri plant, each capable of producing 6 blades over the course of a 3 day build campaign.[20] The enabling feature in this application is the ability to build the parts in a 1100^{o}C vacuum environment, thus reducing the possibility of thermal expansion-induced cracking.[21]

As these examples demonstrate, EB-PBF has application-specific advantages over the more popular L-PBF process. Interestingly, the debate of laser versus electron beam has a long history in the welding community, with supporters on either side claiming superiority.[22, 1, 23] Both technologies are still being used to weld today, and if history is any indicator, a similar pattern will be repeated for Powder Bed Fusion (PBF)-based AM processes.

1.2 Overview of Arcam EBM and Process Challenges

Before discussing the specific process parameters associated with PBF, it is worth briefly examining the current commercial EB-PBF workflow to frame the context of this dissertation. First, the CAD design of the part to be fabricated is brought into a separate software package where it is optimally oriented with respect to the z build direction. This step must consider how to efficiently pack parts within the build volume as well as the

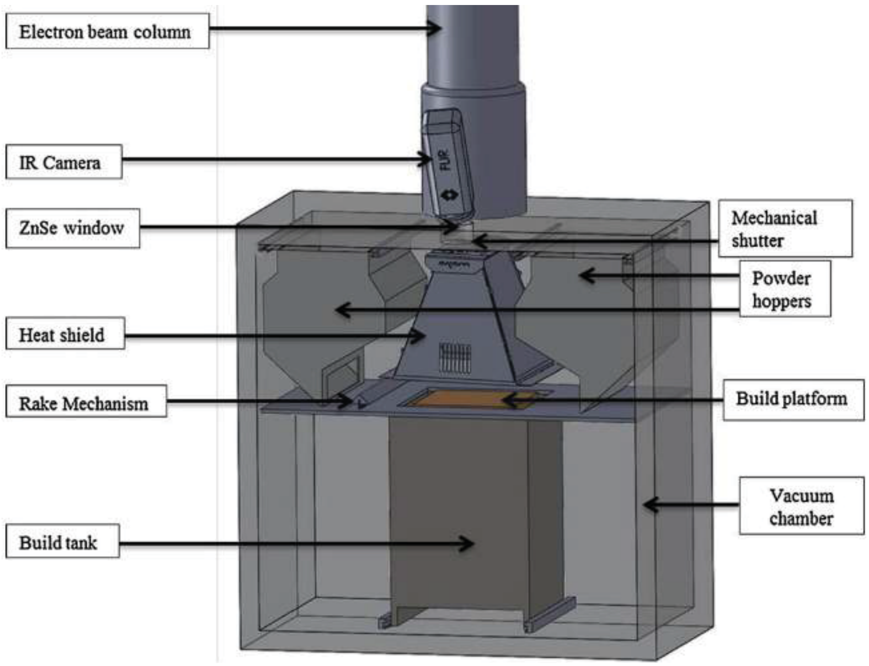

Figure 1–3: CAD model of Arcam A2 System[24]

orientation of critical surfaces, features, tolerances and stresses. Additional structures are often added within the build volume that provide structural support to overhanging surfaces, normalize the heat transfer throughout build volume, and/or act as witness coupons which capture the overall the build quality. This process is generally referred to as Design for Additive Manufacturing (DfAM) and represents a key component in achieving good the dimensional and property tolerances.

The hardware required to bring the digital model into the physical world is shown in Fig.1–3. First, the powder hoppers are loaded with the appropriate feedstock, and the stainless steel build platform is aligned with respect to the powder rake. The chamber is sealed and the system pumped down to a vacuum pressure of 10^{-5}-10^{-6}mbar.

Once a satisfactory vacuum pressure is reached, the chamber is pre-heated by rapidly scanning the high-power beam over the build plate. This heating step is important for numerous reasons. For one, heating accelerates the outgassing of water vapor adsorbed on the chamber walls. EB-PBF is a 'hot' process, in that the temperature of the build volume is much greater than ambient (600-1100^{o}C). In order to efficiently sustain this hot volume without active water cooling, the build volume is thermally isolated. This is achieved using a vacuum environment, a weak thermal link between the build platform and build tank, and adding heat shields above the build surface, all of which are detailed in Fig. 1–3. The sum of these convective, conductive and radiative isolation mechanisms results in a very long temperature decay time constant. Thus, the pre-heating step stabilizes the thermal gradient between the build platform and the ambient atmosphere over an extended period, which in turn, stabilizes the initial powder temperature. In the simplest sense, beam parameters which accurately melt warm powder could overheat hot powder, or inadequately melt colder powder, therefore proper thermal stabilization is a key consideration for achieving high quality builds.

Once the chamber has been pre-heated, the DfAM-processed file is loaded into the machine software, which slices the 3D model into 2D layers of thickness z_B, which is equivalent to depth the build table lowers during each areal melt operation. The powder is raked onto the build surface, and a series of electron beam heating processes are performed:[25]

1. Preheating: Heat full build surface to lightly sinter and outgas powder
2. Contour melting: Melt outer contour of 2D part slices
3. Hatch melting: Melt inner contour of 2D part slices
4. Postheating: Heat full build surface to maintain chamber heat balance

This process repeats until the 3D build is completed. The details each one of these steps will be defined in more detail in the literature review of Ch 2.

Because of the long time constant, the chamber requires an extended cooling period before it is exposed to atmosphere. Once the chamber is opened, the build tank is removed and placed within a special grit-blasting machine which removes loosely adhered particles. According to the requirements of the part, subsequent post-processing and inspection steps might be performed.

One of the most complicated systems associated with this process is the build compiler, as it is responsible for generating the machine commands associated with heating, sintering and melting the powder with the electron beam. This system must also consider the beam history and conduction environment, such that heat does not build up in certain locations, causing the process to become unstable. The build compiler must also generate these commands within the hardware and timing limitations of each sub-system. A simple solution would be to operate the process with a low power beam and long delays, ensuring that the absorbed heat has adequate time to diffuse over a large volume. Unfortunately, this is not an economical solution, since it significantly extends an already long build process. Thus, the build compiler must generate these commands in such a way that maximize productivity.

Using a combination of user-specified parameters and proprietary algorithms called 'build themes', the Arcam build compiler manages this complexity by directly controlling only 3 machine parameters: focus coil current, deflection coil current and bias electrode voltage. These inputs are then transformed into the beam radius, σ; beam speed, v; and beam current, I_b. The transformation of these machine outputs, as well as a custom built process compiler, will be outlined in Ch. 3.

In comparison to L-PBF, EB-PBF is distinct in that it must 1) maintain a hot, stable build environment 2) synchronize the complex focusing characteristics of a high power electron beam 3) manage the electrostatic charging of powder. Despite the inability to build completed parts, all three of these topics are directly addressed in this dissertation.

1.2.1 Dimensionless PBF Process Analysis

Without proprietary algorithms to control the beam scanning strategy, an equation was derived in the early stages of this research to guide comparisons between different beam and materials parameters. This equation is based on a dimensionless parameter that captures the first order effects associated with both L-PBF and EB-PBF, and serves as a guide when discussing the various components of this research. The dimensionless melt parameter, γ_m, is based on distinct four elements:

- The incident beam, whether electron or laser beam
- The fraction of incident energy absorbed by the workpiece
- The geometric definition of layer being melted
- The enthalpy increase needed to melt the metal

Except for of the second item, each of these parameters can be described independently of the others, enabling laser and electron beam processes with different materials to be compared.

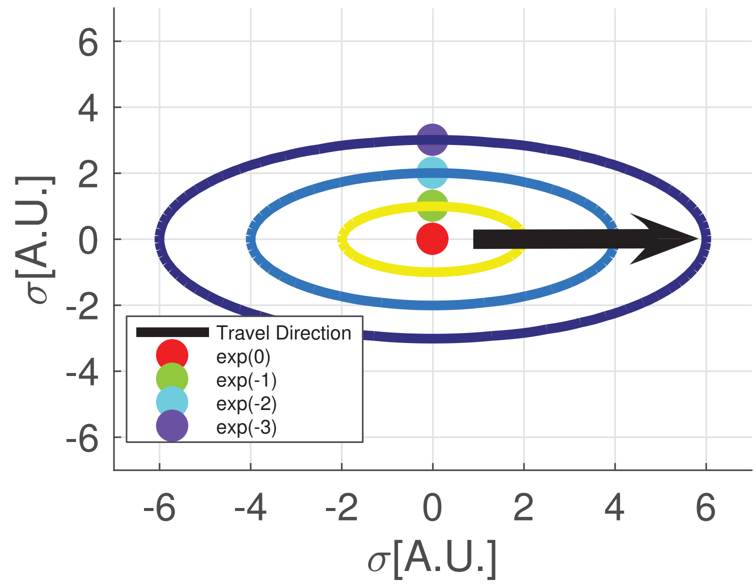

Figure 1–4: Normalized power density distribution of an elliptical beam at $t = 0$ with $\sigma_x = 2\sigma_y$. The exponential decay distances of Eq.1.1 are shown in the contour plots.

Beginning with the beam, the power density of a stigmatic, focussed electron beam of incident power $P = V_{acc}I_b$ can be approximated by an elliptical, Gaussian distribution. If the beam crosses the origin along the $+x$ axis with speed v[mm s^{-1}], the time dependent local power density, p[W mm^{-2}] is:

$$\begin{aligned} p(x,y,t) &= \frac{V_{acc}I_b}{2\pi\sigma_x\sigma_y} exp\left(-\left[\frac{(x-vt)^2}{2\sigma_x^2} + \frac{y^2}{2\sigma_y^2}\right]\right) \\ &= p_0\ exp\left(-\left[\frac{(x-vt)^2}{2\sigma_x^2} + \frac{y^2}{2\sigma_y^2}\right]\right) \end{aligned} \tag{1.1}$$

where V_{acc}[kV] is the accelerating voltage, I_b[mA] is the incident beam current and σ_i[mm] beam distribution parameter along the x and y directions, respectively. The beam Peak Power Density (PPD), defined by the symbol p_0 in Eq. 1.1, is one of the most important parameters affecting any beam based process and will be repeatedly referenced throughout this dissertation. Of particular note is the quadratic relationship between PPD and beam distribution, σ. A contour plot of the elliptical beam, normalized according to σ_y, is shown in Fig. 1–4.

One important feature to recognize is that the amplitude of $p(x, y, t)$ is strictly defined by p_0. Also, the coordinate system of this beam is defined according to σ, which represents a more natural unit of length in the build plane than meters or inches.

As the beam spot of Fig. 1–4 travels along the work plane, the incident energy along the transverse(y) direction can be calculated by the time integration of Eq. 1.1:

$$
\begin{aligned}
q_0(y) &= \int_{-\infty}^{\infty} p(0, y, t) dt \\
&= \frac{V_{acc} I_b}{\sqrt{2\pi}\sigma_y v} exp\left(\frac{-y^2}{2\sigma_y^2}\right) \\
&= q_0 \ exp\left(\frac{-y^2}{2\sigma_y^2}\right)
\end{aligned}
\tag{1.2}
$$

where q_0[J mm^{-2}] is the maximum incident energy per unit area, which will be referred to as the peak incident fluence. By inspection, if the beam is translated along the y-axis, the transverse beam distribution becomes σ_x. For the elliptical distribution of Fig. 1–4, this change in direction reduces the peak fluence by a factor of 2, despite maintaining identical beam power. Similarly, if a stationary beam is pulsed on the workpiece for time τ, Eq.1.1-1.2 gives the incidence fluence as:

$$
\begin{aligned}
q_0(x, y) &= \int_{-\infty}^{\infty} p(x, y, t) dt \\
&= \tau \ \frac{V_{acc} I_b}{2\pi\sigma_x\sigma_y} * exp\left(-\left[\frac{x^2}{2\sigma_x^2} + \frac{y^2}{2\sigma_y^2}\right]\right) \\
&= q_0 \ exp\left(-\left[\frac{x^2}{2\sigma_x^2} + \frac{y^2}{2\sigma_y^2}\right]\right)
\end{aligned}
\tag{1.3}
$$

where q_0 is also defined as the peak incident fluence. These equations demonstrate the interplay between power, spot size and interaction time. These definitions also highlight the importance of precisely defining the beam distribution parameter, σ.

The physics surrounding Eq.1.1-1.3 will be addressed in the literature review of Ch. 2, including issues concerning beam brightness, working distance, alignment and travel speed. Direct measurements of σ using the slotted Faraday Cup technique will also be presented in Ch. 3.

To determine the energy absorbed by the workpiece, the dimensionless, workpiece-dependent absorption coefficient η $[A.U.]$ is multiplied by the incident energy, with the condition that $\eta < 1$. In this case, the *absorbed* peak fluence can be written as ηq_0. High resolution measurements of η during solid melting will be presented in Ch 4.

As a beam of charged particles, the complementary incident charge per unit area deposited by the beam can be written as $j_0 = q_0/V_{acc}[\mathrm{C\ mm^{-2}}]$, while the charge absorbed by the workpiece can be written as $\eta_e j_0$. Unlike the energy absorption coefficient, the charge absorption coefficient can be greater than one, provided the high energy incident beam stimulates low energy charge transfer mechanisms. These concepts will be explored in the pulsed powder measurements of Ch. 6.

Next, we define a thin, porous layer with thickness t_l and packing density Φ, where a fully dense layer implies Φ=1, and a powder layer with 40% porosity equates to $\Phi = 0.6$. Using a conservation of mass argument along with state-of-the-art optical profilometry, the packing density of a single powder layer is directly estimated in Ch. 3.

Furthermore, to assign this layer definition to a specific material, we define the volumetric enthalpy of the material referenced to 25^{o}C as $\rho(H_T - H_{25C})$ $[\mathrm{J\ mm^{-3}}]$, where $\rho[\mathrm{g\ mm^{-3}}]$ is the material density and $H_T[\mathrm{J\ g^{-1}}]$ is the enthalpy at temperature T. If the initial material temperature is T_0, the volumetric enthalpy of melting becomes $\rho(H_l - H_{T_0})$, where H_l is the enthalpy in the liquidus state. Unlike the $c_p(T_m - T_0)$ definition, this formulation includes the latent heat of transformation and in Sec. 3.3, thermocouple measurements of the $\beta \rightarrow \alpha$ latent heat during cooling of Ti are demonstrated.

Combining the layer geometry and volumetric enthalpy of melting, we define $\delta h_m[J\ mm^{-2}]$ as surface enthalpy of the melting:

$$\delta h_m = t_l \Phi \rho (H_l - H_{T_0}) \tag{1.4}$$

To demonstrate the physical meaning of Eq. 1.4, consider the following layer combinations of thickness(t_l), packing density(Φ) and initial temperatures(T_0)

1. Ti with t_l= 120μm, Φ= 0.5, T_0= 25^{o}C
2. Ti with t_l= 200μm, Φ= 0.42, T_0= 700^{o}C
3. Inconel 718 with t_l=50μm, Φ=1, T_0= 25^{o}C

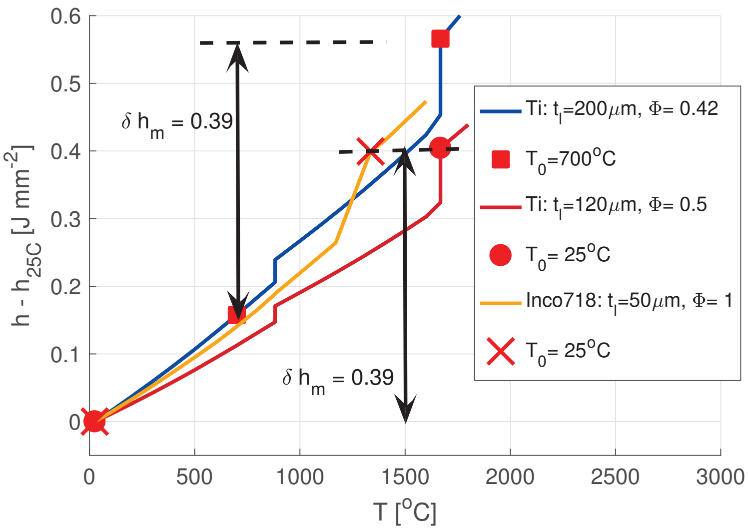

Figure 1–5: Surface enthalpy of melting, δh_m, for different layer definitions of thickness(t_l), holding temperature(T_0) and packing density(Φ). Thermophysical material parameters taken from *Mills*.[26]

The surface enthalpy of melting for these different layer definitions are equal, with δh_m= 0.39 J mm^{-2}. Graphically, the definition of δh_m is shown in Fig.1–5, with temperature along the x-axis and surface enthalpy along y-axis.

Figure 1–5 shows that δh_m is determined by the difference along the y-axis between T_0 and T_l, and is independent of material, geometry or initial temperature. This last feature is important, as PBF processes can have widely different initial temperatures, especially if the heat of interacting melt tracks is taken into consideration.

Having defined the beam, absorption, layer geometry and melting enthalpy, we define the dimensionless melt parameter γ_m for a travelling beam as the ratio of absorbed peak fluence (Eq.1.2) over the surface enthalpy of the melting (Eq.1.4).

$$\gamma_m = \eta \frac{q_0}{\delta h_{surf}} = \eta \frac{V_{acc} I_b}{\sqrt{2\pi} \sigma_y v} * \frac{1}{t_l \Phi \rho (H_l - H_{T_0})} \tag{1.5}$$

For pulsed beam operation, we can define the equivalent dimensionless melt paramter as:

$$\gamma_m = \eta \frac{q_0}{\delta h_{surf}} = \eta \frac{V_{acc} I_b \tau}{2\pi \sigma_x \sigma_y} * \frac{1}{t_l \Phi \rho (H_l - H_{T_0})} \tag{1.6}$$

In both cases, the threshold for adiabatic melting at the center of the beam is defined by the condition that $\gamma_m > 1$. In other words, γ_m a represents the minimum threshold for melting *any* material with *any* beam. In terms of PBF, $\gamma_m \approx 5 - 15$ to compensate for convective and conductive heat loss, as well as re-melting multiple subsurface layers. In Ch. 5, the γ_m parameter is used to interpret the differences in melting Nb and Ti during the dissimilar-material EBW.

Having defined a generalized condition for melting, and how each component integrates into this dissertation, it worth describing how γ_m relates to the commonly referenced volumetric energy density, E_d.

In order to generate overlapping melt tracks within each 2D plane, the hatch spacing between melt tracks, h_s, should be some fraction of the beam radius, $kh_s = \sigma$, where $1 < k < 3$.[27, 28] If the hatch spacing equals the beam Full Width Half Maximum (FWHM) along the transverse direction, then k= 2.35 according to the beam definition of Eq. 1.1. Similarly, if the process analysis concerns powder layers which have reached steady state thickness, then Φt_l=z_B, where z_B is the build table displacement. Also, if the powder size distribution across the build table is uniform, the beam absorptivity η will also be constant. And finally, if the process includes scanning strategies and geometries which minimize the thermal interactions between melt tracks, the initial starting temperature, T_0, will be constant.

If all these conditions are met, Eq. 1.5 reduces to:

$$\gamma_m = \frac{\eta}{\sqrt{2\pi}\Phi\rho(H_l - H_{T_0})} * \frac{V_{acc}I_b}{k\sigma * \Phi t_l * v} = \psi * \frac{P}{h_s * z_B * v} \tag{1.7}$$

where the $\psi[mm^3\ J^{-1}]$ prefactor includes all the assumptions stated above. In this case, we see that the generalized γ_m parameter encompasses the volumetric energy density, and explicitly defines the underlying assumptions. The validity of these assumptions likely explain the recent spate of articles boldly entitled *"Is the energy density a reliable parameter for materials synthesis by selective laser melting?"* and *"On the limitations of Volumetric Energy Density as a design parameter for Selective Laser Melting"*.[29, 30]

In conclusion, γ_m represents an expanded definition of the volumetric energy density equation, enabling dimensionless comparisons between different operating modes, pulsed and traveling; beams, via σ and η; materials, via η, ρ, $H_l - H_{T_0}$ and Φ; and processes, via v, t_l and T_0.

With that said, Eq.1.5 and 1.6 will serve as a guide throughout the course of this dissertation and will help explain the sub-systems associated with the single powder layer experiments of Ch. 6.

1.3 Document Conventions

Where possible, the symbol conventions used in this document are chosen to match the comprehensive 2017 AM review article entitled: *Additive manufacturing of metallic components–process, structure and properties* by DebRoy *et al.*[31]

A fundamental component of this research is based on parametric process mapping using the notation $[X_1\text{: } X_d\text{:}X_2]$. For example, when mapping out the effect of beam current, the definition I_b= [1:2:12]mA represents a vector of values from 1mA to 12mA in 2mA increments, i.e. $<$1, 3, 6, 9, 12$>$mA. Also, the `Courier` font will be used throughout this dissertation to distinguish specific software-based process algorithms, such as `preheat` or `pulsePat`.

Because this investigation concerns melting both powder and solid material, the term ‘workpiece’ refers to an object being processed by the electron beam. And finally, since this research was not conducted using commercial Arcam equipment, the process of sintering and melting powder with an electron beam will be referred to as EB-PBF, in accordance with ASTM F42 terminology.[32]

CHAPTER 2
Review: Electron Beam Optics and Generalized Thermal Processing

Electron beam systems are designed to focus an image of the electron beam current density onto the workpiece surface. This is done by applying a voltage potential between the anode and cathode which accelerates the emitted electrons. In a sense, the electrons act as a medium whereby power is transferred from the electrical supply to localized positions on the workpiece with power densities between 0.1-100 kW mm^{-2}.[23, 1] The process of generating and controlling an electron beam is referred to as electron beam optics and form a critical component of any thermal electron beam processing technique. As an example of the importance of electron beam optics, the electromagnetic lenses are one of the only subsystems built in-house during the fabrication of Arcam's EB-PBF hardware. [33]

In this chapter, the physics surrounding the generation and control of these high power beams will be discussed. The relationship between different optical parameters and their limitations will introduced throughout the chapter, with a focus on high-brightness beams used for EBW and EB-PBF. The chapter starts with a physics-based review of the electron beam column, followed by a summary review of a specific electron beam column. The following section reviews the thin lens equation and how it defines to the power density on the workplane surface. Next, a brief review of transient heat transfer is given, and how beam specific properties dictate the resulting heat transfer between the beam and workpiece. The chapter concludes with an example-based review of how these beam-specific properties affect different elements of thermal electron beam processing. This approach demonstrates that although relatively new, EB-PBF represents an evolution of over 70 years of high-brightness electron beam theory and application.

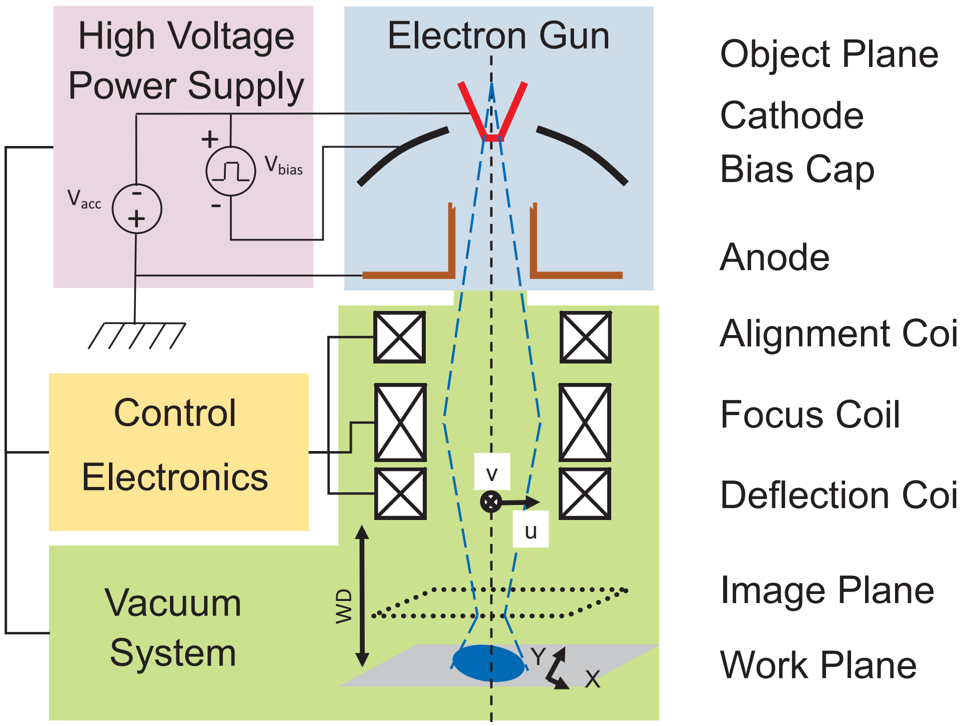

Figure 2–1: Schematic of electron beam system with sub-components. The cathode, bias cap and anode are shown in red, black and orange, respectively. The components forming the electron beam gun are shown in the blue bounding box, while the electron beam column and processing chamber are highlight with a green bounding box, demonstrating decoupled vacuum chambers

2.1 Summary of Electron Beam Column

The critical components of an electron beam system are shown schematically in Fig. 2–1, which are segmented into four sub-systems: the high voltage power supply, the control electronics, the vacuum system and the electron beam column.

Within this system, the trajectory, power and spot size of the electron beam is governed by Newton's Second Law and the Lorentz force:

$$\frac{d(m\mathbf{v})}{dt} = e\mathbf{E} + e\mathbf{v} \times \mathbf{B} \tag{2.1}$$

where m is the electron rest mass, e is the electron charge, $\mathbf{E}$ is the electric field, $\mathbf{B}$ is the magnetic field and $\mathbf{v}$ is the relativistic-corrected particle velocity.

Within the gun, a thermionic electron beam is generated by heating a cathode to a sufficiently high temperature, causing the cathode surface to emit free electrons. By applying a high voltage between the cathode and anode, V_{acc}, a electric field is generated between the electrodes according to $\mathbf{E} = -\nabla V$, where V is the local electrostatic potential. In the absence of a magnetic field, Eq. 2.1 demonstrates that this field will accelerate the free electrons away from the cathode. A third electrode, referred to as the bias electrode, regulates the rate which electrons are emitted by perturbing the $\mathbf{E}$ field near the cathode surface. This perturbation is defined according to the fixed cathode/bias geometry and the variable bias voltage, V_{bias}. The cathode, bias and anode electrode assembly is referred to as the electron gun, while the electrical waveforms associated with the bias and accelerating voltage are provided by the high voltage power supplies.

After passing through the center bore of the anode, the electrons enter the electric-field free region, and are steered through a sequence of electrically-controlled $\mathbf{B}$ fields which manipulate their trajectory according to Eq. 2.1. If the gun column contains a vacuum constriction, it is possible to decouple the gun and chamber pressure, enabling the introduction of process gas, a feature highlighted by the bounding boxes of Fig.2–1.[34, 35] If the process chamber pressure is high, electron scattering will affect the beam optics via charge compensation and beam refraction.[36, 37] The electromagnetic lenses, high voltage power supply and vacuum systems are all regulated via the control electronics, enabling process synchronization.

The $\mathbf{E}$ and $\mathbf{B}$ fields affect electrons similar to how refractive media affect photons, thus much of the same terminology is used between light and electron beam optics. In electron optics, the particle velocity v is analogous to the refractive index n in light optics.[38] In light optics, lens are constructed from materials with a fixed n, requiring mechanical motion to focus and deflect the beam. In electron optics, Eq. 2.1 implies that a continuously variable $\mathbf{B}$ results in continuously variable lens properties, with no moving parts. This attribute is extremely valuable for processes that require fast, two dimensional beam scanning, such as EB-PBF, multi-beam EBW and electron beam surface technologies.[39, 40, 18] The major disadvantages of electron optics compared to light optics is the repelling force associated with space-charge effects, the inability to build electron lens with negative focal lengths and the large aberrations associated with magnetic coil windings.[36, 37]

Within the context of conventional geometric optics, the distance between the exit of the electron beam column and the workpiece is referred to as the working distance, or WD. The settings of electron gun define the beam crossover point within the gun, and thus the intrinsic power density of the beam. By setting the appropriate focal length within the focus lens, the gun crossover can be imaged onto the workpiece surface. For the geometry of Fig. 2–1, we see that the workplane is beneath the gun crossover plane, implying that the beam is in the over-focussed condition.

When the image of the gun crossover matches the working plane, the beam is said to be at sharp focus. Near this sharp focus condition, the local current density of the electron beam can be approximated by an elliptical, Gaussian current distribution:

$$\begin{aligned} j(x,y) &= \frac{I_b}{2\pi\sigma_u\sigma_v} exp\left(-\left[\frac{(x-x_o)^2}{2\sigma_u^2}+\frac{(y-y_o)^2}{2\sigma_v^2}\right]\right) \\ &= j_o\ exp\left(-\left[\frac{(x-x_o)^2}{2\sigma_u^2}+\frac{(y-y_o)^2}{2\sigma_v^2}\right]\right) \end{aligned} \tag{2.2}$$

where $j[\text{ A mm}^{-2}]$ is the current density, $[x_0,y_0]$ is the beam center and j_o is chosen such that $\int j(x,y)dA = I_b$, assuming no loss of beam current due to apertures or scattering. For the sake of simplicity, the coordinate axes of the electron beam distribution and deflection coils, $[u,v]$, and workplane, $[x,y]$, will be taken as coincident, although this is seldom the case in practice.

To first order, all the electrons generated at the cathode are accelerated to the same potential V_{acc}. Therefore Eq. 2.2 implies that the localized power density of the electron beam can be described by:

$$\begin{aligned} p(x,y) &= V_{acc} * j(x,y) \\ &= \frac{V_{acc}I_b}{2\pi\sigma_x\sigma_y} exp\left(-\left[\frac{(x-x_o)^2}{2\sigma_x^2}+\frac{(y-y_o)^2}{2\sigma_y^2}\right]\right) \\ &= p_0\ exp\left(-\left[\frac{(x-x_o)^2}{2\sigma_x^2}+\frac{(y-y_o)^2}{2\sigma_y^2}\right]\right) \end{aligned} \tag{2.3}$$

where p $[Wmm^{-2}]$ is the power density, and p_o represents the PPD of the beam such that $\int p(x,y)dA = V_{acc}I_b$. Since a thermionic electron beam is composed of particles accelerated to the same kinetic energy, electron optics are best described according to the current density, j [A mm^{-2}].[38]

In the literature, there is some ambiguity regarding the beam distribution parameter, σ, and how that relates to beam spot size. The assumed Gaussian electron distribution lacks a strong physical foundation and there is no universally-accepted beam radius definition. Similarly, accurate measurements of the beam power density is a challenging task.[41, 42] To address this issue, the beam diameter will be defined according to its Full Width Half Maximum (FWHM), which is strictly a geometric parameter, independent any specific analytical form. As the name implies, the FWHM represents the distance separating two points which have 1/2 the maximum power density. The asymmetry of Eq. 2.3 implies that the FWHM is direction-dependent, and can be mathematically defined as:

$$FWHM_i = 2\sqrt{2ln(2)}\sigma_i \approx 2.355\sigma_i \tag{2.4}$$

where σ_i represents the effective beam distribution parameter along any line defined according to $y = mx$, which equals $(1/\sigma_x^2 + m^2/\sigma_y^2)^{-0.5}$. For the elliptical beam of Eq. 2.3, the FWHM along the y axis is $2.355\sigma_y$ while the FWHM along the x axis is $2.355\sigma_x$. By inspection of Eq. 2.3, the $1/e$ or $1/e^2$ beam diameter can be defined by $2\sqrt{2}\sigma_i$ and $4\sigma_i$, respectively. It bears repeating that the definition in Eq. 2.3 is a phenomenological idealization, whereas the FWHM is a measurable, physical quantity which also describes non-Gaussian, defocussed beams.[42, 43, 44, 45]

The preceding discussion introduced the primary beam parameters related to electron beam processing, namely: beam current, I_b; accelerating voltage, V_{acc} and FWHM, which combine to define the net beam power and PPD. Due to the nature of charged particle physics, these parameters are not independent. Specifically, the coupled function of the electron gun in terms of shaping beam trajectory and regulating beam power implies that the electron beam should be optimized with respect to the economics and requirements of the specific application. A variety of electron beam applications, and their corresponding beam properties, are listed in Table 2–1.

When refining reactive metals, e$^-$beams require a high net power to increase process productivity, with less importance placed on the beam size or PPD. Conversely, electron

Process	Power [W]	PPD [W m^{-2}]	V$_{acc}$ [kV]	FWHM [cm]
Refining	10^5-10^7	10^3-10^4	20-50	0.01-0.05
Evaporation	10^3-10^6	10^3-10^4	10-40	0.002-0.03
Welding	10^2-10^5	10^5-10^7	15-180	10^{-4}-10^{-2}
Machining and EB-PBF	10-10^3	10^5-10^9	20-150	10^{-6}-10^{-4}
Microscopy	10^{-11}-10^{-5}	10^8-10^{13}	5-100	10^{-10}-10^{-8}

Table 2–1: Electron beam applications and corresponding beam parameters[38].

microscopy requires the finest possible beam spot with negligible power. Close inspection of Table 2–1 demonstrates that for welding and EB-PBF, some compromise between these extremes must be made in order to balance the conflicting requirements of process productivity and resolution. In the following section, some of the phenomena which dictate these compromises will be discussed. For greater details, the interested reader is referred to the numerous textbooks on the subject, including Schiller's *Electron Beam Technology*, Sedlacek's *Electron physics of vacuum and gaseous devices*, the American Welding Society's *Recommended practices for electron beam welding and allied processes*, *Electron beam welding* by Schultz and *Plasma, Electron and Laser Beam Technology* by Arata.[6, 36, 38, 1, 46]

2.2 Electron Gun

A typical triode electron gun used for thermal processing contains three basic components: the anode, the cathode and the bias electrode. The cathode is the electron source and in the case of the system installed at McGill, is made of thin, tungsten ribbon. Because of the negative electric potential of the cathode with respect to the grounded anode, negatively charged electrons emitted from the cathode see a potential gradient, and accelerate towards the anode. A bias voltage, V_{bias}, which is more negative with respect to the cathode, is applied to the bias electrode in order to regulate and shape the electron flow. These components are shown in greater detail in Fig. 2–2.

In a sense, the physics of an electron gun can be visualized as an elastic membrane stretched over three flat contours of differing heights.[38] The shape of these contours are related to electrode geometry, and the height is proportional to the applied potential. Thus, the kinetic energy and trajectory can be understood by visualizing the electrons

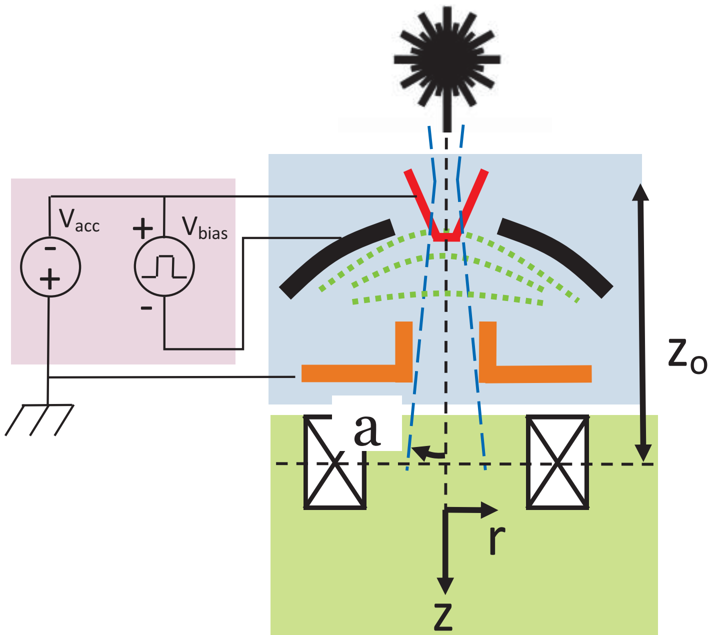

Figure 2–2: Schematic of PAVAC LASERTRON electrostatic lens, which utilizes a laser incident on the backside of the cathode to heat to electron emission temperatures. The cathode is shown in red, the anode shown in orange, the bias electrode in black. The effective electron beam trajectory with aperture a is shown by the dashed blue lines, while the dashed green lines represent the potential contours between electrodes. The distance of the virtual electron crossover with respect to the focus coils, is shown the arrow marked z_o

rolling down the gradient of maximum descent, an analogy born from the relationship between electrostatics and potential energy.

Although a detailed treatment of electromagnetism is not the objective of this dissertation, it is worth highlighting two important attributes relating to electron beam optics. First, an electric field represents the potential gradient generated between electrodes at different voltages, $\mathbf{E} = -\nabla V$. From Eq. 2.1, this relationship implies that the accelerating force applied to the electrons is a function the potential applied between electrodes. Second, at the metallic electrode surface, Gauss's law states that electric field lines must be parallel to the surface normal. Therefore, by careful design of electrode geometries and applied potentials, the resulting potential contours within the gun will dictate the initial trajectories of the electrons.

An electron gun serves two purposes, first, it extracts a controlled rate of free electrons from the cathode, i.e. the beam current I_b. The electron gun also defines the trajectories of the electrons as they exit the gun, thus acting as the first lens in the electron beam column.[47, 38]

2.2.1 Cathode

To generate free electrons, a cathode must be heated to provide the electrons with sufficient kinetic energy to overcome the work function barrier of the material and escape into the vacuum. Since the cathode temperature will significantly impact the beam characteristics and cathode lifetime, the physics surrounding electron emission will be discussed.

If electrons are emitted without the application of an external field, the image charge formed upon leaving the surface will create a dipole electric field which prevents their escape.[38] If a strong electric field is applied near the cathode surface, the potential barrier is overcome and the Richardson-Dusham equation defines the emission current density of the cathode:[36, 48, 49]

$$j_{eT} = AT^2 * exp(-e\phi/kT) \tag{2.5}$$

where j_{eT}[A m^{-2}] is the emission current density, A[A m^{-2}K^{-2}] is the Richardson constant, T[K] is the temperature, e[C] is the electron charge, k[J K^{-2}] is the Boltzmann

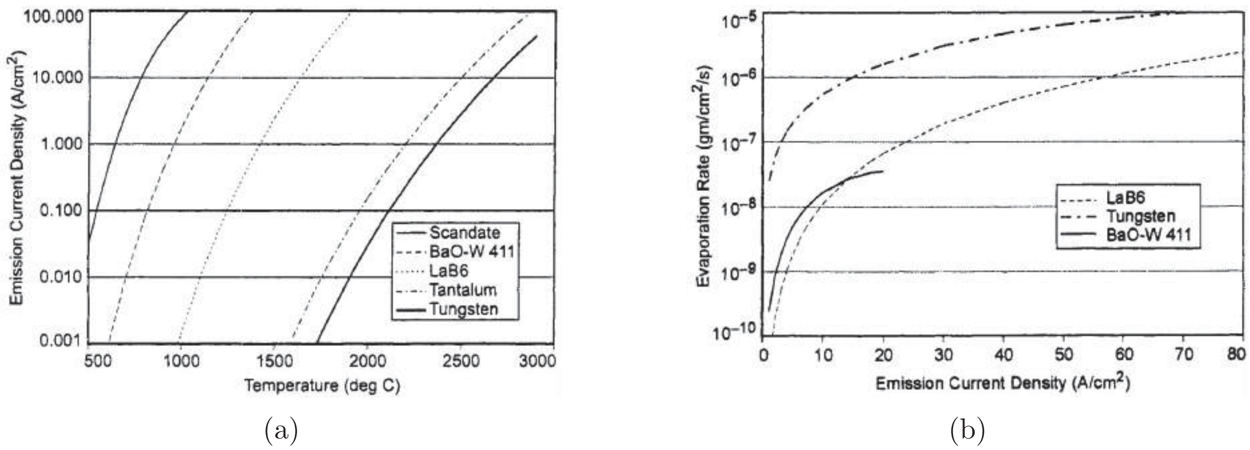

Figure 2–3: Electron emission and evaporation rate of various cathode materials[49] Left: temperature versus emission current density $j_{cathode}$ of various cathode materials. Right: emission current density versus evaporation rate of various cathode materials.

constant and ϕ[eV] is the effective, Schottky-effect corrected work function of the material. The Richardson constant, A, has a theoretical value of $\approx$120*10^4 but experiments show that it varies according to material, surface roughness, crystal orientation, adsorbed atoms and sputter deposited material.[48, 49, 38] It is common to observe cathodes made of the same material, with the same dimensions give different current density, or that the same cathode will have varying current density over the course of operation.

Equation 2.5 is often referred to as the saturation or temperature-limited current density, because it defines the maximum permissible current density at a given temperature. The nominal emission characteristics of some common cathode materials are shown in Fig. 2–3a, with useful emission current densities beginning at approximately 0.1 A mm^{-2}. From this figure, we see that tungsten begins emitting electrons at approximately 2700^{o}K, while lathanum hexaboride, or LaB6, begins emitting electons at approximately 1600^{o}K.[37] This difference in emission temperatures is attributable to the mean work function of tungsten and LaB6, which is 4.52eV and 2.69eV, respectively.[48] For microscopy applications, properly aligned <100> LaB6 single crystal cathodes are generally operated at 1800^{o}K, generating a current density of 4 A mm^{-2}.[37]

The upper limit on cathode operating temperature is set according to the desired cathode lifetime, which depends on the chemical stability of the material as well as its

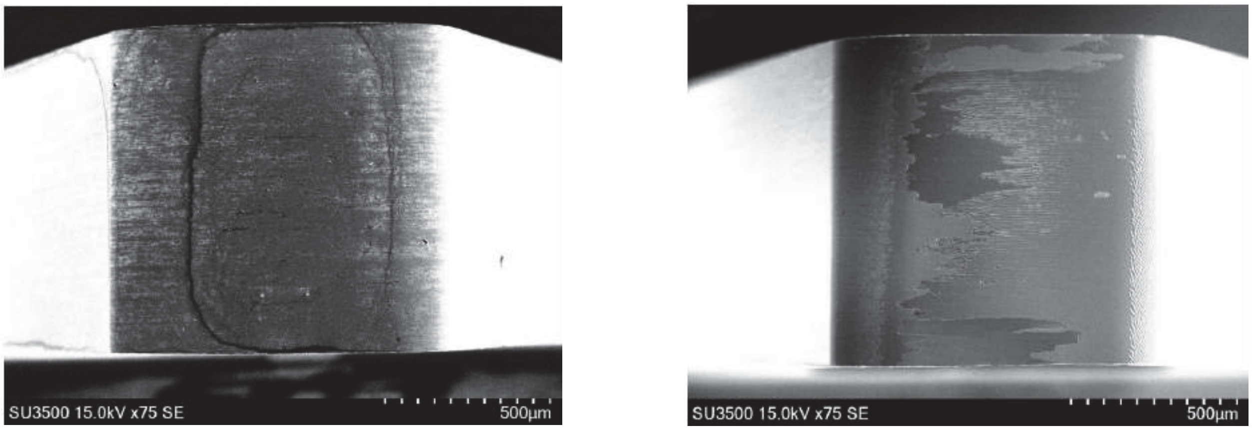

(a) (b)

Figure 2–4: The surface of a cathode Left: before Right: after use, demonstrating the effect of cathode evaporation and ion etching

evaporation rate. The evaporation rate versus current density of common cathode materials is shown in Fig. 2–3b, again demonstrating an exponential temperature dependence. In most cases, the evaporation rate restricts the upper limit for the current density, which implies that for a fixed accelerating voltage, the only means with which to increase the beam power is to increase cathode emission area.

Cathode lifetime is also impacted by ion-induced sputtering. The ions can come from metal vapor generated during processing or poor vacuum conditions. The positively charged ions will be accelerated towards the cathode surface and the kinetic energy of these ions will erode and polish the cathode surface. Cathode erosion is an important consideration in electron beam optics, since it can impact the emission characteristics of the cathode, and cause variations in the beam characteristics.[23, 50] An example of a virgin and ion-etched tungsten cathode used at McGill is shown in Fig.2–4a and Fig 2–4b, respectively.

For Electron Beam Welding (EBW) applications, tungsten is the favored cathode material because of its reliability, stability and relative costs and are found in the Arcam S and A-series EB-PBF system. Tungsten cathodes are operated at approximately 2700^{o}K, generating an j_{eT} of 0.1-1 A mm^{-2}. Compared to more exotic cathode materials, tungsten is robust to contamination, requiring an operating pressure of 10^{-5} mbarr.[36] Neverthless, water vapor appreciably reduces W cathode lifetime, since contact between water and

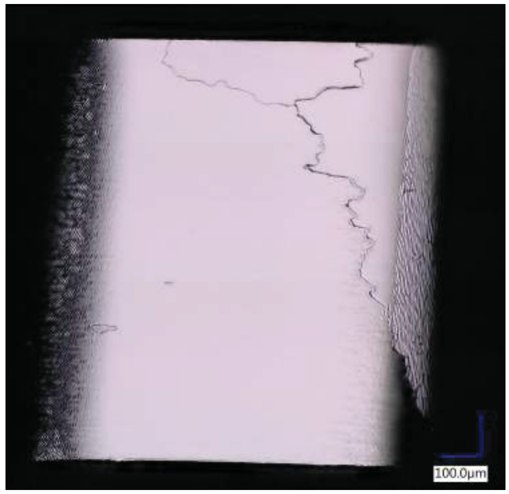

Figure 2–5: Surface structure of conditioned cathode after approximately 40 hours of use at McGill using optimized cathode heating routines. The grain boundaries of the cathode are clearly delineated due to ion etching. Also, on right hand-side of cathode, ion-etching appears to be grain-dependent

the hot W surface forms free hydrogen and tungsten oxide, whose evaporation rate is much faster than pure W.[38] By paying careful attention to the gun cleanliness, vacuum pressure and heating schedules, it is possible to generate conditioned cathodes with a uniform surface finish, as shown in Fig. 2–5.

Lanthanum hexaboride(LaB6) cathodes are regularly used in high power microwave devices and electron microscopes, and have recently been deployed in the latest Arcam Q-series EB-PBF systems. From Fig.2–3a, LaB6 cathodes are capable of generating higher current densities than tungsten at lower temperatures and lower evaporation rates. As will be discussed in a subsequent section, this higher current density increases the beam brightness, which results in a reduced beam FWHM.

For comparable j_{eT}, the evaporation rate plot of Fig. 2–3b shows that LaB6 cathodes have a reduced evaporation rate compare to tungsten, resulting in cathode lifetimes as high as 800 hours.[18] Despite the theoretical advantages of smaller FWHM and longer lifetimes, LaB6 cathodes pose significant technological challenges compared to W. Specifically, LaB6 cathodes are chemically reactive when hot and can be contaminated by a poor vacuum environment, which might include backstreaming pump oil or metal, oxygen and water vapor. These vapors impact the cathode via different mechanisms, and special attention must be given to organic vapors associated with so-called 'wet' vacuum systems.[36] The reactivity of LaB6 requires a sophisticated vacuum system in order to reach 10^{-6}mbar vacuum pressures, which in turn increase the capital costs of LaB6 systems.[18]

LaB6 cathodes are fabricated via a powder metallurgy route, and machined into their final shape.[49] When hot, the La atoms become mobile within the B lattice, and preferentially evaporate from the cathode. Therefore, La must be supplied by diffusion from the bulk to the surface in order to maintain the correct stoichiometry. The need to mechanically support the cathode, provide electrical contact for resistive heating and inhibit diffusion of contaminating species from the contact points requires significant engineering of the cathode structure. Thus, LaB6 cathodes are more expensive than their tungsten counterparts, increasing the per unit costs of LaB6 cathodes, while the per hour costs is roughly the same.[51]

2.2.2 Current regulation

In the previous section, the current emitted by the cathode surface was derived under the assumption of a strong electric field near the cathode surface. In other words, every electron emitted from the cathode falls down the potential gradient. This mode of operation is referred to as the temperature-limited regime, since the temperature of the cathode dictates the beam current.[36] Although temperature-limited operation is economical for high power processes such as refining and evaporation, it does not provide the power density stability and response rates necessary for welding and EB-PBF applications.[52, 36]

By introducing a bias electrode with additional voltage controls, it is possible to rapidly modulate the local electric field near the cathode surface. This configurable gradient dictates the number of electrons extracted from the cathode, providing a rapid and accurate means for power regulation. This mode of current regulation is referred to as operating in the space-charge limited regime.[36] One advantage of space-charge operation is that the beam current is not strongly dependent on the stability of the cathode temperature, enabling much faster power regulation rates.

Figure 2–2 shows that voltage applied to the bias electrode is the sum of the accelerating voltage and the bias voltage power supply. In the system installed at McGill, the bias voltage can be either more negative or positive then the accelerating voltage. Also, the machine definition of bias voltage in the McGill system does not reflect the true voltage potential of the electrode. In order to maintain consistency with the equipment and the gCode compiler, the term associated with the machine interface, $[+bias]$, will be used. At the maximum $[+bias]$ value of 980V, the potential between the cathode and the bias voltage is 0V, implying that the true bias electrode voltage, V_{bias} is:

$$V_{bias} = V_{acc} + ([+bias] - 980) \tag{2.6}$$

Considering that the maximum value $[+bias]$ is 980V, Eq. 2.6 implies that the voltage applied to the bias electrode during current emission will always be more negative than the accelerating voltage.

The relationships between accelerating voltage, bias voltage and cathode temperature with regards to beam current are demonstrated by peaking curve measurements conducted at McGill, shown in Fig. 2–6. These measurements were conducted by defocusing the electron beam, fixing $[+bias]$ value, incrementing the laser power and recording the beam current displayed on the graphical user interface. Because of the high powers involved, a large, thermally anchored copper block was used as the beam target.

As shown in Fig. 2–2, the McGill electron beam gun utilizes a laser incident on the backside of the cathode to raise the temperature of the tungsten ribbon cathode. From Fig. 2–6, we see that a measurable beam current is emitted at a laser powers of approximately 30W, which implies that the laser is providing sufficient power to raise the mean cathode temperature to the order of 2700°C. Comparing the peaking curves of Fig. 2–6a to Fig. 2–6b, we see that at 30W of laser power, neither the accelerating voltage nor $[+bias]$ affect the emission current, confirming the gun is operating in the temperature-limited regime.

Focusing on Fig. 2–6a, we observe that this behaviour changes as the laser power is increased. For laser powers above 50W, the beam current is independent of the laser power for $[+bias]$= 650-750V, implying that the beam is operating in the space-charge

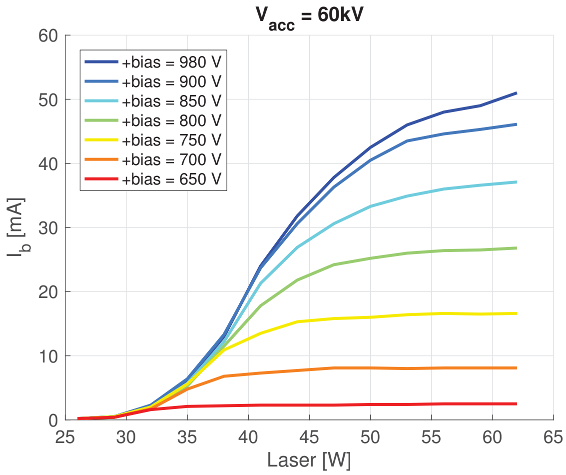

(a)

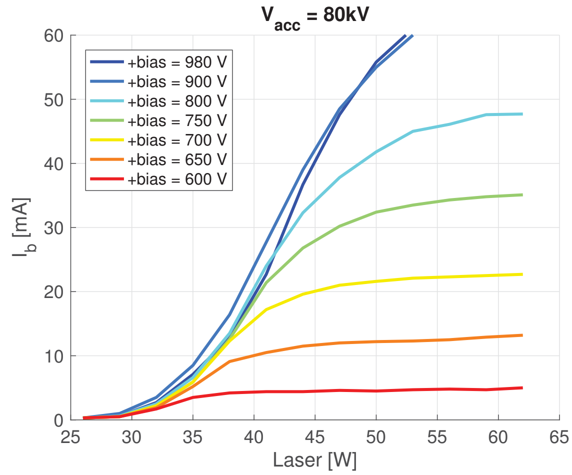

(b)

Figure 2–6: Peaking Curve measurements at 60kV and 80kV using 1.5mm cathode stick-out and 25.4mm anode stand-off distance

limited regime. For $[+bias]$ values above 750V, the beam current is a function of both laser power and bias voltage, implying a mixed space-charge and temperature-limited response.

By comparing Fig. 2–6a to Fig. 2–6b, one observes that in the space-charge limited regime, the higher accelerating voltage results in greater I_b at for any given $[+bias]$. This is explained by recognizing that since the geometry of the gun is unchanged, the electric field at cathode surface increases with voltage, according to Eq. 2.6.

The results of Fig. 2–6 demonstrate that the beam current, I_b is not a simple, independent machine output, but a function of the laser power, bias voltage and accelerating voltage. In order to maintain the requested beam current, the control electronics regulate the bias voltage. Conversely, the emission current of the cathode depend on the material, temperature, surface state and emission area. A subtle but important implication of this regulation scheme is that if the emission characteristics of the cathode change, the control electronics will automatically adjust the bias voltage. Although this will maintain the requested beam power, it will be shown that the focussing characteristics of the beam can change.[23]

2.2.3 Beam Brightness

Besides regulating the beam current, the electrodes also perform a focussing action, and changes to the electric fields generated within the gun also affect the focal spot parameters.[53, 36] This is related to the second function of the electron gun: shaping the initial trajectory of the electrons along the optical axis, z.

Although electron beam processing is generally concerned with the beam FWHM, the optical quality of an electron beam is more accurately described according to a parameter called brightness, B $[A\ mm^{-2}\ sr^{-1}]$:

$$B = \frac{j_0}{\Omega} \tag{2.7}$$

where j_0[A mm^{-2}] is the previously defined current density and $\Omega[sr]$ is the beam solid angle. The solid angle is a measure of how a three dimensional object projects onto the two dimensional perspective of the observer, and is directly related to depth-of-field. An everyday example of solid angles is the sun and the moon, which have the comparable solid angles, despite their differences in distance and size.

For a radially-symmetric paraxial electron beam, Eq. 2.7 can be written to give the effective beam brightness:

$$B = \frac{I_b}{\pi\sigma^2}\frac{1}{\pi a^2} \tag{2.8}$$

where I_b[mA] is the beam current, σ[mm] is the beam distribution parameter, and a[rads] is the beam semi-angle with respect to the optical axis, otherwise known as the aperture, which is shown in Fig. 2–2. For guns operating above 10kV, the beam aperture is in the range of $a \approx 10^{-3}$ rads.

A high brightness electron beam will have a combination of high current density and/or parallel electron trajectories. Although physically impossible, a beam of infinite brightness implies either an infinitely small beam spot or perfectly parallel trajectories. If it were possible to create an aberration-free lens, it follows that a perfectly collimated electron beam could be focused to a infinitely small spot, demonstrating the interplay between solid angle and spot size via the brightness parameter.

Viewed another way, for two beams of equivalent current and accelerating voltage, the high brightness beam will have the smaller FWHM at a specific working distance, or an equivalent FWHM at a longer working distance. High brightness beams are desirable for EBW applications because of the ability to weld large, complex components at working distances up to 1.5 meters.[54] In terms of EB-PBF, this extended of working distance translates into an increased build area. In the case of an Arcam A2 system, the WD between the build surface and the chamber roof is roughly 330mm.[24]

In an electron microscope, beam currents are on the order μA or smaller. These small currents permit the use of beam-blocking apertures within the optical column which reduce the solid angle and increase the beam brightness. The use of a-limiting apertures is challenging in a high-power EBW and EB-PBF applications because of the need to absorb large amounts of power. In the absence of apertures and electron acceleration, brightness is a conserved quantity after the anode, and can only be reduced by lens aberations.[37, 48] Because of this restriction, it is important to engineer the electron gun such that the beam brightness is maximized at the exit of the anode.

For an axially-symmetric electron beam, the on-axis(r=0) solid angle of the beam can be approximated in terms of the tangential and axial electron energies. [55] The average tangential energy is defined according to the thermal distribution of the electrons before leaving the cathode. This value is simply kT, where k[eV ^{o}K^{-1}] is Boltzmann constant and T[^{o}K] is the cathode temperature and kT is 0.1-0.25eV cathodes operating between 1000-3000^{o}K. For high accelerating fields, the axial energy of the electrons is defined by the kinetic energy of the electrons, eV_{acc}. It follows that the average solid angle is the π times the ratio of the tangential and normal velocities:

$$\Omega = \pi \frac{kT}{eV_{acc}} \tag{2.9}$$

Using this simplified definition, Eq.2.9 can be substituted into Eq.2.7 to give:

$$B = j_0 \frac{eV_{acc}}{\pi kT} \tag{2.10}$$

which demonstrates that maximum permissible brightness can be improved by increasing the current density of the cathode, j_0 or increasing the accelerating voltage, V_{acc}.

Returning to the current density plots of Fig. 2–3, Eq. 2.10 explains the motivation of using LaB6 cathodes. Compared to W, LaB6 has both a higher current density, and

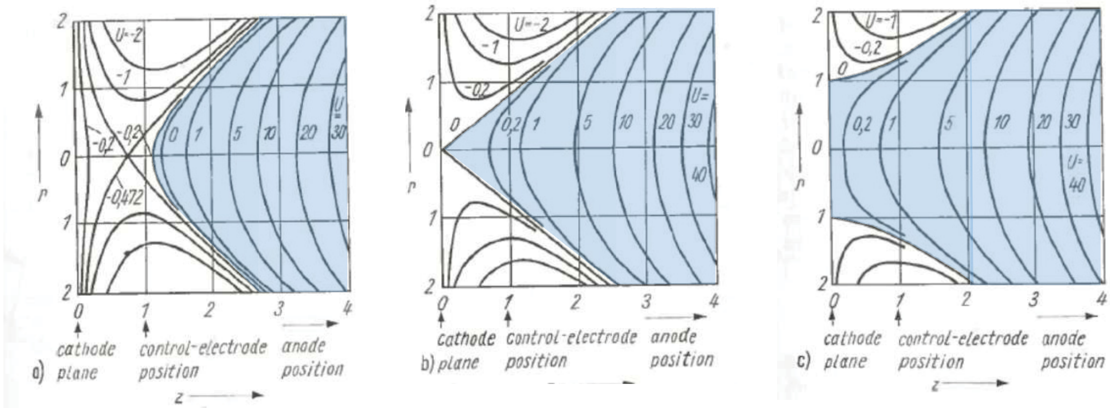

Figure 2–7: Current regulation via bias electrode, $I_b = A * j_{eT}$ using a electrostatic potential field in-front of the plane cathode, with area of positive electron potential gradient shown in blue. [36]. (a) Negative potential in front of cathode and beam current pinched off due to high negative bias voltage $A = 0$ (b) Negative potential in front of cathode except at cathode center, implying on-set of current emission, medium negative bias voltage $A \approx 0$ (c) positive potential in front of cathode over extended area, low negative bias voltage, $A > 0$

lower emission temperature, resulting in a higher beam brightness and smaller FWHM. In the case of Arcam EB-PBF systems, the LaB6 guns have a FWHM$<$ 150μm while the W-based guns have a FWHM$<$300μm, although the details regarding WD and chamber pressure were not provided. [18, 24]

In terms of power regulation, the bias electrode modulates the area which sees the accelerating gradient. This concept is graphically demonstrated in the images of Fig. 2–7, which shows that by modulating the local electric field near the cathode surface, the beam current can be regulated according to $I_b = A * j_{eT}$.

The focussing action of the bias electrode can now be understood by examining the the potential contours of Fig. 2–7. The rightmost panel implies that electrons emitted from different portions of the cathode will follow different trajectories because of the electric field curvature. The implication is that the effective solid angle of the beam, and thus its brightness, is a function of beam current.

It should be noted that the derivation of Eq. 2.10 concerned the electric field distribution of the center panel of Fig. 2–7, i.e. the on-axis field with no curvature. Since brightness is a function of electron trajectory defined by the local electric field, changes to the **E** field to regulate current will also affect beam brightness. Thus, for conventional triode guns, the beam brightness can only be optimized for range of bias voltage settings.[53] As the beam current is varied from this optimal range, B decreases significantly. In the case of Arcam W and LaB6 cathodes, the beam FWHM grows very rapidly for currents above 40 and 55mA, respectively.[18]

At this point, it should be clear that FWHM is only one component of the beam quality. A better definition is brightness, which combined with the working distance, will give both the FWHM and the aperture angle, which then defines the depth of field.

These concepts are summarized in Fig. 2–8, which graphically demonstrate the parameters associated with electron gun brightness.

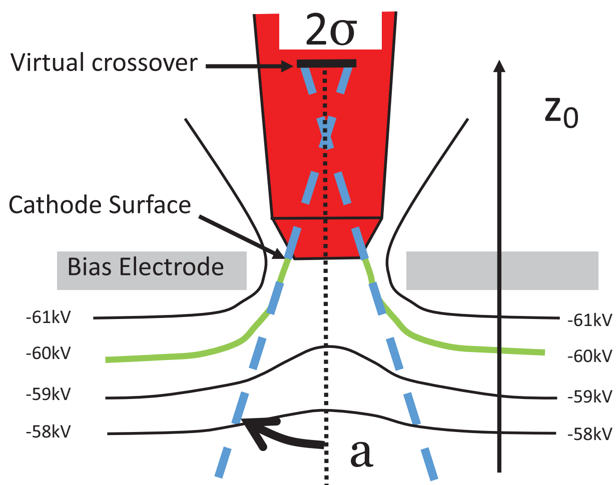

Figure 2–8: Electron beam brightness: virtual electron crossover, beam aperture and equipotential lines, adapted from[53] The diameter of the virtual crossover is 2σ, while the effective beam semi-angle is shown in blue. The cathode equipotential of -60kV is shown in green, demonstrating its influence of beam aperture

One feature to note is that according to the ray-tracing diagram, the perceived 'source' of electrons, appears behind the electron-emitting cathode. This is a general feature of high current electron beams, as space-charge effects cause significant beam dispersion at the cross-over. Thus high current guns are often designed to have laminar beam trajectories. Similarly, the -60kV potential contour of Fig. 2–8 demonstrate the sides of the cathode are emitting electrons, causing growth of the beam semi-angle and loss of brightness. This demonstrates that the requested beam current forces the gun to operate outside its optimal brightness. Another implication is that electrostatic fields associated with regulating the beam current will also shift the axial position of the virtual crossover, and important consideration which will be discussed regarding current-dependent sharp focus.

In electron microscopy, the problem of coupled beam current and brightness is solved with the use of current-limiting apertures. Specifically, since the current-limiting aperture can optimize the beam semi-angle, designers can freely optimize the emitted current density of the gun to achieve peak brightness. For high-power EB-PBF applications, electron microscope maker JEOL is proposing a 4-electrode gun, whereby the voltage of the fourth electrode introduces another degree of freedom with which to extend the range of optimal beam brightness.[53] In another article, JEOL claims that a pulsed electron beam increases the beam brightness, although the physics surrounding this effect are not clear.[56]

2.2.4 Electrostatic Lens: Space-charge

The preceding section concerned how the electric field generated within the gun affect the power and trajectory of the beam. This discussion ignored the important charged nature of electron beams, which create a self-field which interacts with other electrons. Space-charge effects are greatest when the charge density is high and the electron velocity is low, i.e. directly in front of the cathode. Specifically, the energy of the emitted electrons has a Maxwell-Boltzmann-type distribution, which implies a greater number of slow electrons than fast electrons. Electrons emission creates a cloud a few nanometers in front of the cathode which repels the slowest electrons. [38]

In comparison to the maximum possible current density defined in the Richardson-Dusham Eq. 2.5, space charge effects limit the maximum current density extracted from the cathode. The simplest analytical expression can be obtained from an infinite parrallel plate accelerator, whereby the emitted electrons have zero initial velocity. In this limit, the resulting current density is given by the Child-Langmuir law[22]:

$$j_{s-c} = \frac{4\epsilon_0}{9}\sqrt{\frac{2e}{m_e}}\frac{V_{acc}^{3/2}}{d^2} = 2.3 * 10^{-10}\frac{V_{acc}^{3/2}}{d^2} \tag{2.11}$$

where j_{s-c}[A cm^{-2}] is the space charge limited current density, ϵ[F m^{-1}] is permittivity of free-space, e[C] the electron charge, m_e[g] is the electron mass, and d[cm] is the distance between plates. Equation 2.11 shows that space-charge limited beam current is proportional to $V_{acc}^{3/2}$, a relationship which is retained for more complex electrode geometries. This enables the definition of a new parameter called the beam perveance:

$$I_b = \int_A j_{s-c} dA = PV^{3/2} \tag{2.12}$$

where P[A/V$^{3/2}$] is only dependent on the geometry electrodes, which then define the maximum current density within the gun. Thus, P gives an indication of how space charge will affect the beam.[48, 38, 36] The perveance of low current beams used for electron microscopy is 10^{-10} - 10^{-9}[A V$^{-1.5}$], while the high power beams used for thermal processing are 10^{-9} - 10^{-6}[A V$^{-1.5}$.[57, 36]. Thus, in high power applications like thermal electron beam processing, the repulsive nature of electrons will in fact impact the beam optics.

As the beam travels to the workpiece, space-charge effects will also cause the beam semi-angle to increase, reducing the beam brightness.[48, 38]. For instance, a 60kV/10mA beam will have a perveance of roughly 10^{-9}. Assuming a beam radius of r_0= 0.5mm, the beam diameter will double after a distance of $\approx 500 r_0$= 250mm, assuming the beam diameter is kept constant along the optical axis.

Because of the beam aperture a, the beam radius is not constant along the path, and increases and decreases as it passes from the gun, to the focus coil and finally onto the workpiece, thus mitigating the net effect of beam growth. In later sections, pervaence will be used to explain the compression of the depth of field for high current beams.

To precisely calculate and minimize the perveance, advanced simulation software is needed, including CST particle studio, OmniTrak, Beam Optics Analyser, SLAC-EGUN, OperaFEA or Charged Particle Optics Software. [58, 48]. These software suites are generally used in the design of radio and radar systems, but have been applied in the design of guns used for EB-PBF.[48] Generally, the software solves the electrostatics fields for a given gun geometry and voltage. Electron trajectories through the field are then

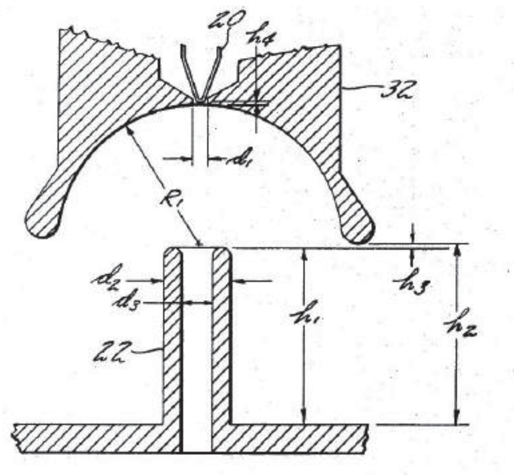

Figure 2–9: Rogowski-type electron gun configuration for operation between 90-150kV, with cathode(20), bias electrode (32) and anode(22).[47] In this design, the anode pin height was $h1$= 33.0mm, with an outer and inner diameter of $d2$= 15.0mm and $d3$= 7.0mm, respectively. The radius of the bias electrode surface was $R1$= 30.0mm, with a bias electrode to anode gap of $h3$=7.92mm

calculated, indicating how space-charge affects the electric fields. The electric field is then recalculated, and the process is repeated until some convergence criteria is met. [48]

2.2.5 Summary: Rogowski Gun Geometry

The McGill electron beam gun is based on a variation of the Rogowski design, shown schematically in Fig. 2–9. The defining element of this design is the protruding anode pin, which acts as an aperture, resulting in a small beam divergence angle and large brightness. This design is in contrast to the Steigerwald-type gun, which has a flat anode plate.[47]

Figure 2–9 concerns a 1974 patent for a gun design which could be operated between 90-150kV. In this embodiment, the cathode form was changed from a hairpin to a ribbon cathode and this patent outlines the geometric modifications needed to get good weld penetration at a working distance of 300mm. First, the cathode emission surface was shifted from $h4$=+0.1mm to $h4$=-0.64mm from the bias electrode plane. The cathode aperture was enlarged from $d1$= 2.54mm to 4.72mm, and the anode height was reduced from $h1$= 40.0mm to 33.0mm. This example is the first demonstration that the weld quality is strongly related to the beam quality, while the latter can be modified by changes to the gun geometry. It is assumed that these modifications were based on informed guesses, highlighting the usefulness of modern simulation software.

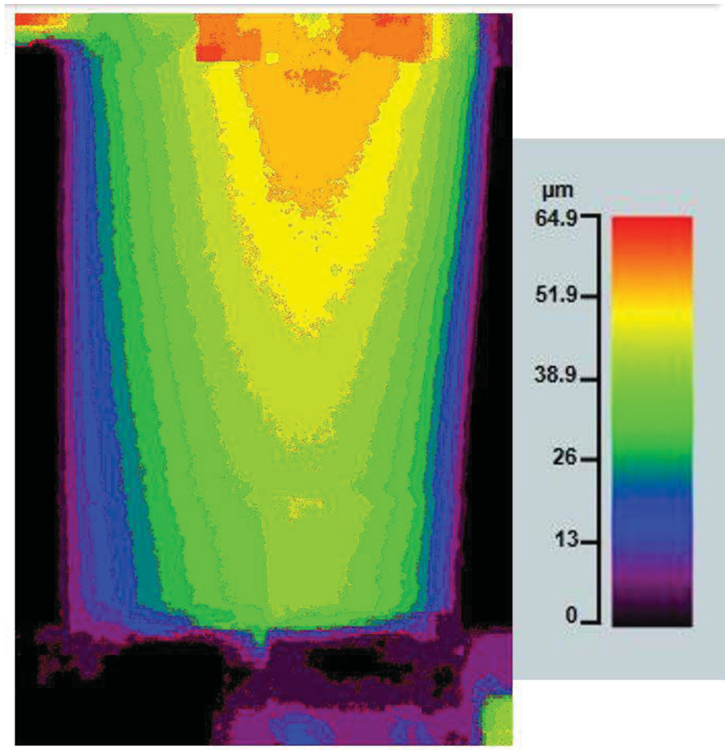

Figure 2–10: Height contours of cathode, after installation into cathode holder. This measurements shows a roughly 0.75mm^2 emission area, an aspect ratio of roughly 0.74 and a height variation of roughly $46\mu m$

Another example demonstrating gun geometry concerns cathode ion erosion. A 2D height profile of as-installed McGill cathode is shown in Fig.2–10, which shows that manufacturing tolerances in the cathode, cathode holder and installation fixture result in a emission surface which is rounded and biased to the right hand side.

When installing new cathodes, care is taken to maintain a nearly identical cathode position with respect to the alignment jig. This was done by inspecting the cathode position with respect to the alignment jig using a top-down microscope in order to minimize the effects of parallax.

Some cathodes were purposely used in beyond their lifetime in order to observe the effects of ion erosion and evaporation. Images of these 4 heavily damaged cathodes were taken after removal from the gun, but while still installed in the cathode holder. Their macro wear profiles are overlaid in Fig. 2–10. To overlay the images, the clocking of the

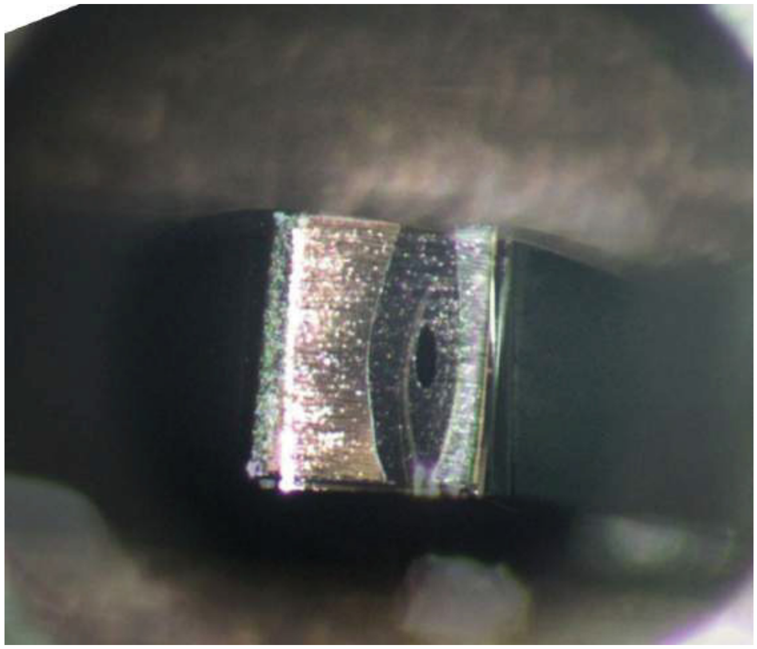

Figure 2–11: Overlay of 4 separate cathode wear profiles

cathode alignment jig was maintained and the outer diameter of the alignment bore was used to align the images.

From Fig.2–11, we see that good reproducibility in the cathode position was maintained. Interestingly, it can also be observed that that the erosion profile for each cathode begins and grows with the same orientation.

Comparing Fig. 2–10 and Fig. 2–11 shows that the peak cathode position roughly matches the erosion initiation point. This can be understood considering that as the negative bias voltage is reduced, the first region to emit electrons will be highest region of the cathode, as shown in Fig. 2–7. Since these cathodes were operated at low beam currents in a poor vacuum, the high points of the cathode receive the majority of the ion bombardment, and thus, the enhanced erosion.

2.3 Beam Optics

The following section details the trajectory shaping mechanisms of magnetic lens, as well as a short discussion on spurious beam shaping mechanisms.

Once emitted from the anode, the electron beam enters a series of magnetic fields which steer, shape and focus the power source onto the work piece. For electron beam processes operating at energies less than 100keV, the non-relativistic definition of particle velocity can be used with only minor errors.[38] Under this simplification, the motion of the electrons in the electric-field free region can be defined as Eq. 2.1 :

$$m\frac{d\mathbf{v}}{dt} = e\mathbf{v} \times \mathbf{B} \tag{2.13}$$

Equation 2.13 demonstrates that the force applied to a beam of electrons is always normal to the velocity, $\mathbf{v}$. Unlike the electric field, a magnetic field can only change the direction of the electrons, not their energy. Another feature of Eq.2.13 is that the force applied to the electrons is a function their position within $\mathbf{B}$ field, as well as their trajectory and speed, $\mathbf{v}$. Specifically, the non-relativistically corrected electron speed can be defined by [36]:

$$v = \sqrt{\frac{2eV_{acc}}{m_e}} = 5.93 * 10^5 \sqrt{V_{acc}} \tag{2.14}$$

Eq. 2.13 and 2.14 implies that the strength of the magnetic lens is a function of the beam energy/accelerating voltage, an important consideration which will be revisited during the examination of a variable accelerating voltage process compiler.

2.3.1 Magnetic Deflection

When a charged particle enters a homogenous magnetic field normal to its velocity, it will follow a circular trajectory according to the corresponding Larmor radius. Thus, when electron beam exists such a a field, it's trajectory is changed according to:[36]

$$sin(\theta) = 2.97 * 10^5 \frac{l * B}{\sqrt{V_{acc}}} \tag{2.15}$$

where l[m] is the length of the field and B[T] is the magnetic field strength, as shown in the schematic of Fig. 2–12. By winding current-carrying wires, magnetic induction is used to generate the variable strength B field according to Ampere's Law, which can be defined in the simplest approximation as:

$$B = \mu_0 \frac{NI_a}{S} \tag{2.16}$$

where μ_0 is the permeability of free space, N is the number of coil windings, I_a is the current waveform created by the signal amplifier and S is the pole piece spacing. Assuming

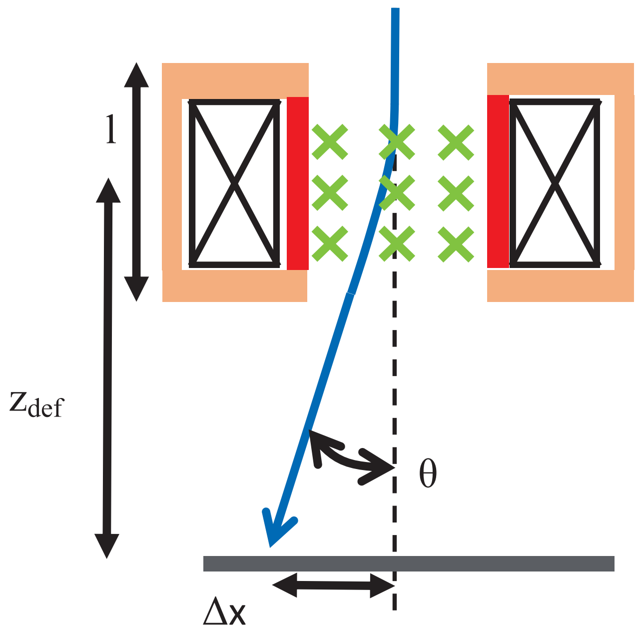

Figure 2–12: Magnetic deflection schematic, with beam shown in blue and magnetic field into page. The deflection coil window is shown in red, while the magnetic yoke is shown in orange

$l << z_{def}$, we can see from Fig. 2–12 that the displacement of the beam spot is given by:

$$\Delta x = z_{def} * tan(\theta) \tag{2.17}$$

If we further assume for small θ, $sin(\theta) \approx tan(\theta) \approx \theta$, Eq. 2.15-2.17 can be combined and differentiated to the give the beam velocity:

$$v = \frac{dx}{dt} = 2.97 * 10^5 \mu_0 \frac{N * l * z_{def}}{\sqrt{V_{acc}} S} * \frac{dB}{dI_a} \frac{dI_a}{dt} \tag{2.18}$$

Equation 2.18 demonstrates that by generating a time-variable magnetic field along the beam path, one is able to control one of the fundamental EB-PBF process parameters: beam speed and position. To deflect the beam in $[x, y]$ coordinate system of the workplane, crossed dipole magnet are used, which are schematically shown in Fig. 2–13.

At large deflection angles, ($\geq 15^o$) the approximations used to derive Eq.2.18 no longer applies and the constant deflection angle rate generated by the dipole will result in variable beam speeds on the workplane. During EB-PBF, this effect will be most

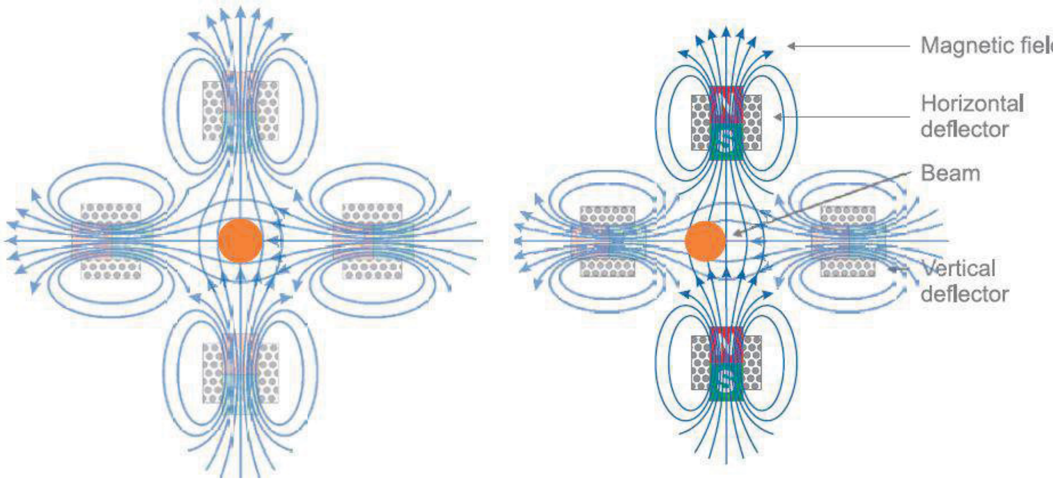

Figure 2–13: Crossed dipole deflection coils. In the left image, the beam spot (orange) is not deflected. By energizing the vertical dipole magnets, a vertical B field is generated which deflects the beam to the left. Image provided with permission, courtesy of pro-beam[52]

pronounced at the periphery of the build. For similar geometric reasons, the beam path length of the beam at wide deflection angles will be extended. This implies the need for fast, dynamic focussing, otherwise the beam will be defocussed at the periphery of the workplane.[36] Finally, the angular projection of a circular beam will result in an elliptical spot at the workplane periphery, which can be managed using fast-response quadrapole magnets. The issues associated with wide-angle deflection can be addressed with a combination of hardware and software, as well as careful considerations of the tolerances of beam size, position and speed.

According to Eq.2.15-2.17, modifying the static beam spot position is relatively straightforward using conventional magnetic materials and electronics. Generating fast, precise and synchronized magnetic fields necessary for EB-PBF, multi-spot EBW or electron beam surface treatment requires special considerations.[36, 59, 60, 61] At high deflection frequencies, eddy currents induced in the inner bore of the magnets can shield the magnetic field from the beam path, implying that the dB/dI_a term in Eq.2.18 has a frequency-dependent response. This implies that the window between the beam axis and the magnet, shown in red in Fig. 2–13, must meet special design considerations. Using thin metal walls with low electrical resistance can help reduce this problem, while ceramic windows between the beam axis and magnet windings work best.[62, 36, 22]

While generating high resolution, low-power signals is relatively straightforward, selecting the appropriate power amplifier for the deflection coils also requires careful design, captured by the dI_a/dt term of Eq. 2.18. Specifically, the maximium velocity and acceleration of the beam will be dictated by the amplifier frequency response and coil inductance.[62] Using high frequency, phase compensated signals can reduce the loss of toolpath fidelity in the amplifier and inductor.

Finally, because of the close proximity of the magnetic lenses in the beam column, the magnetic circuits, shown as the orange section of Fig. 2–13, should be designed to minimize the mutual inductance between coils. Considerations regarding the frequency-dependent losses of the magnetic materials, and the associated magnetic resistance of the circuit, should be accounted for.[61]

Although these issues apply to all magnetic electron lens, they are especially acute for deflection systems used during EB-PBF because of the tight requirements on beam position, speed and acceleration.

2.3.2 Focus Coil

After exiting the anode, the electron beam will have a diverging trajectory. Focus coils, which are based on a magnetically-confined solenoid, are used to converge the distributed current density onto the workpiece surface. An image of a magnetic focusing lens, as well as a description of the axial and tangential magnetic fields, is given in Fig. 2–14.

Electron focusing is the result of the coupled interaction of the charged particles with the rotationally symmetric $\mathbf{B}(r, z)$ field. When an electron enters the magnetic field parallel to the optical axis, it will interact with the fringing B_r field of the lens, as shown in Fig. 2–14. Due to symmetry, the strength of this B_r field is zero along the axis($r = 0$) and increases with increasing radius.

According to the right hand rule, the vector product - $e(v \times B_r)$ produces a azimuthal force into the paper, F_θ, resulting in azimuthal acceleration and azimuthal velocity, v_θ. This rotational velocity interacts with the axial component of the field (B_z), producing a

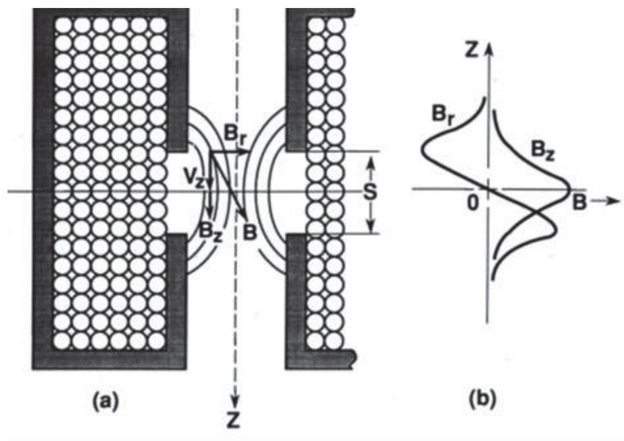

Figure 2–14: Magnetic focus lens: Left: geometry of focus coil with magnetic circuit with bore diameter D and gap width s. Right: Magnetic fields parallel to beam axis, with $r \neq 0$. [37]

radial force $F_r = -e(v_\theta \times B_z)$, which causes the electron trajectory to spiral toward the z-axis.

With increasing radial position comes increasing B_r field strengths and greater radial acceleration towards the axis. This explains the focussing action of the lenses, since a beam of parallel electrons entering the lens will converge to a point one focal length, f[m] away from the lens. The focal length of the magnetic circuit shown in Fig.2–14 is given by:

$$f = K(s, D)\frac{V_r}{(N * w_b)^2} \tag{2.19}$$

where K is an geometrical constant related to the gap width s and bore diameter D of the lens, N is the number of magnetic winding, w_b is the lens current, and V_r is the relativistically-corrected accelerating voltage, $V_r = V_{acc}(1 + 0.98 * 10^{-6} * V_{acc})$.[36]

The focussing characteristics of a magnetic lens is hampered by spherical and chromatic aberrations. Spherical aberrations are related to the idealization of the focussing B_r field described above, and cannot be eliminated, only reduced. The effects of spherical aberration result in a diameter of least confusion,$d_{\ddot{o}}$ which is proportional to:

$$d_{\ddot{o}} \propto \left(\frac{z_i}{f}\right)^4 \alpha^3 \tag{2.20}$$

where z_i is the image plane distance and f is the focal length of the magnetic focussing lens. Equation 2.20 demonstrates that the effects of spherical aberration are related to the distance to the workpiece, the design of the lens and the gun, and should be optimized for a given geometry/application. Chromatic aberrations are explained by examining Eq. 2.19 and recognizing that fluctuations in the beam energy or lens current will result fluctuations in the focal length. Modern power supplies are often based on switch mode, insulated-gate bipolar transistor technology with low voltage ripple, a critical requirement for reducing chromatic aberations.[54]

Finally, astigmatism is caused by asymmetry along the beam axis within the focus coil. Using a low-speed deflection coil after the anode, known as an alignment coil, one can steer the beam axis onto the magnetic axis of the coil, as shown in the column arrangement of Fig. 2–1. Asymmetry in the **B** field of the lens can be mitigated by appropriate manufacturing methods, and further compensated using quadrapole correctors. As a general rule, magnetic-lens induced aberrations decrease with decreasing beam semi-angle, but small a will also imply small current/power density at the workplane, requiring a compromise between power and spot size.[53, 36]

2.3.3 Quadrapole Lens

Quadrapole lens, also known as stigmators, are used to transform the cross-sectional beam shape. A quadrapole lens, shown in Fig. 2–15, has a similar form to a crossed dipole lens, with the major difference being a rotation of the coil windings. A quadrapole lens is not radially symmetric, and generates a magnetic field strength proportional to the distance from the $r = 0$ axis. A magnetic quadrapole can be understood as two, mutually perpendicular lens, one which focusses the beam while the other defocusses, which enables elliptically shaped beams to focused into a circular shape. Alternatively, it is possible to transform a circular cross section into an elliptical one, a feature which can be useful for correcting the previously discussed wide deflection angle aberrations.[36]

Besides correcting aberrations, the ability to generate elliptical beams with a quadrapole lens has some interesting metallurgical applications. Scanning elliptical beams with aspect ratios as high as 20:1 was used improve the throughput of electron beam surface treatement.[22] Workers at Lawerence Livermore National Labs have recently

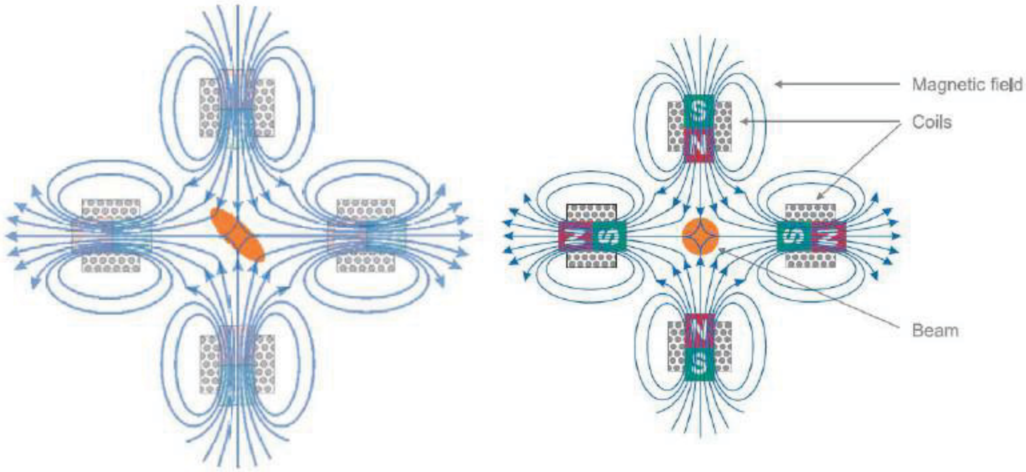

Figure 2–15: Electron Beam Stigmators: Left, astigmatism beam. Right: corrected using a magnetic quadrapole lens (right).Image provided with permission, courtesy of probeam[52]

demonstrated a degree of microstructural control during L-PBF of 316 stainless steel using elliptically shaped laser spots.[63]. Finally, Arcam has recently proposed using elliptically shaped electron beams to reduce the evaporation rate of during EB-PBF at high beam powers.[64] In all three cases, the elliptical beams generated using stigmators offer the opportunity to enlarge or compress the longitudinal FWHM of the beam. Thus, elliptical beams offer the ability to decouple net power and power density, without inducing a reduction in peak power density associated with defocussed beam.

2.3.4 Spurious Focussing

As will be discussed further in Ch. 4 high energy electrons interact with matter via a series of elastic and inelastic scattering events. The cross section of these scattering effects is inversely related to the to medium density, implying that even under high vacuum, electrons can interact with the sparse vapor within the chamber. The degree of scattering increases with decreasing accelerating voltage, increasing path length and increasing molecular weight of the scattering medium.[36]

A single elastic scattering event is characterizaed by a large deflection angle, whereby the beam electron significantly departs from its initial trajectory. Thus, elastic scattering causes an increase in effective beam diameter, without significant loss of beam energy.

Phenomenologically, gas defocussing can be modelled at the workpiece as the sum of two Gaussian distributed current densities, $j_1 + kj_2$. The j_1 distribution is associated with the scattering-free beam diameter, while j_2 captures the gas-induced beam defocussing with an extended beam FWHM. Although power loss to elastic scattering is low, the $k < 1$ factor accounts for energy losses during transit.[36]

When the electron beam inelastically scatters a vapor molecule, the interaction can result in excitation, dissociation or ionization of the vapor. In the case of an ionization process, the resulting reaction is:

$$e^-_{eV_{acc}} + A_2 \rightarrow e^-_{eV_{acc}} + A_2^+ + e^-_{kT} \tag{2.21}$$

where $e^-_{eV_{acc}}$ is the high-energy beam electron, A_2 is the neutral vapor particle, A_2^+ is the positively charged gas ion and e^-_{kT} is a low-energy Secondary Electron(SE).[65, 36] Similar to elastic scattering, the ionization rate depends on the beam current, gas pressure and ionization cross-section.[38]

While the incident electron trajectory is relatively unaffected by the elastic scattering event, the newly created, low-energy charged species can affect the space-charge surrounding the beam, and thus indirectly affect its focussing characteristics. This can be seen by examining the electric field generated outside the perimeter of an idealized beam of charged particles of radius r_0:

$$E_r = \frac{e}{2\pi\epsilon_0}(N(e^-_{eV_{acc}}) + N(e^-_{kT}) - N(A_2^+))\frac{1}{r} \qquad r > r_0 \tag{2.22}$$

where $N(e^-_{eV_{acc}})$ is the number high-energy beam electrons per unit length, I_b/ev_z. $N(e^-_{kT})$ and $N(A_2^+)$ are the number of low energy Secondary Electrons (SE) and positively charged ions, respectively. By introducing the ratio $\phi = (N(A_2^+) - N(e^-_{kT}))/N(e-_{eV_{acc}})$, Eq. 2.22 can be re-written as:

$$E_r = -\frac{dV}{dr} = \frac{I_b}{2\pi\epsilon_0 v_z}(1-\phi)\frac{1}{r} \qquad r > r_0 \tag{2.23}$$

which can be integrated from r_0 to the chamber wall. Assuming the distance from the beam to the wall is $\gg r_0$, Eq.2.23 can be integrated from r_0 to ∞, giving the radial electric potential:

$$V_r = -\frac{I_b}{2\pi\epsilon_0 v_z}(1-\phi)ln(r/r_0) \qquad r > r_0 \tag{2.24}$$

At low pressure ($p < 10^{-7}$mbar); the degree of ionization will be small ($\phi \ll 1$), resulting in a negative potential well centered on the beam. This negative potential will attract positive ions and repel the low energy SE, thus increasing ϕ and reducing V_r. The steady state potential depends on the ionization rate and recombination rate of the positive ions. In this case, the positive ions neutralize some of the defocussing associated with high pervaence beam discussed in Sec. 2.2.4, and is referred to as electrostatic self-focussing.[36, 66]

If the ionization rate is further increased, the intrinsic space-charge of the beam can be overcompensated. This can occur if $\phi > 1$, which results in a positive potential well centered at the beam. In this case, the positive ions will be pushed to the chamber wall while the SE will be drawn to the beam axis. The electric field will stabilize when the beam-induced ionization rate matches the recombination rate of ions and secondary electrons.

This simple model only applies to some of the phenomena observed during electron beam refining applications, which have higher beam currents and lower accelerating voltage/v_z than those is associated with EBW and EB-PBF. This model also does not account for the axial charge density gradients, which can create potential gradients along the length of the beam axis.[36]

Nevertheless, the variables introduced offer some qualitative picture of the intense evaporation and ionization process during keyhole electron beam welding.[1] Specifically, the high rates of inelastic scattering within the vapor capillary will create positive ions and SE. Combined with large amounts of elastic scattering, a distance-dependent beam defocussing is expected within the keyhole and surrounding vapor plume. The electric and magnetic fields generated within the keyhole act like a complex refractive medium, and are qualitatively similar to plasma refraction and absorption observed during keyhole laser welding.[67]

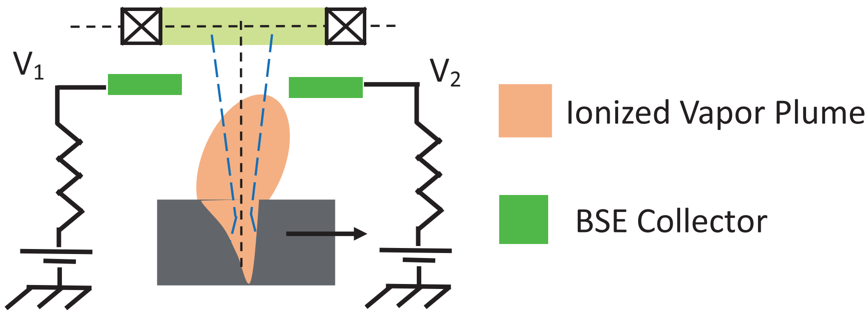

Figure 2–16: Backscatter electron detector configuration for focus regulation during keyhole EBW. Regulation mechanism is based on differential signal between detector signals $V1$ and $V2$ which is related to asymetry in vapor plume (orange) and keyhole shape. Adapted from[36, 66, 68].

Since the electric force felt by the electrons is inversely proportional to the beam velocity (Eq. 2.23 and Eq. 2.14), high energy electrons will be less susceptible to vapor-induced defocussing. This can partially explain why the depth-to-width ratio of keyhole welds is proportional to the accelerating voltage.[36] In other words, for constant power and FWHM, the higher energy beam can penetrate deeper into the keyhole plasma, resulting in a deeper welds. Similarly, the spurious focussing effects association with electron scattering partially explains the observation that stable, pore-free keyholes welds are observed when the beam is under focussed by approximately 0.3-0.75 penetration depths beneath the surface.[36, 1]

Although the beam/plasma interactions during keyhole EBW are complex and not fully understood, sampling the current scattered out of the keyhole using Back-Scattered Electrons (BSE) detectors and using the signal to regulate the focus current has been succefully used to stabilize keyhole welding.[36, 66, 68]. A schematic outlining one manifestation of this technique is shown in Fig. 2–16.

The principle of Fig. 2–16 is that the asymmetry of the keyhole results in a asymmetric, weakly ionized plasma plume, which is detected by the BSE detectors ahead of and behind the beam axis. By examining the difference between signals $V1$ and $V2$, information regarding the shape and penetration of the electron beam is generated.[36, 66, 68] With this differential signal, a feedback loop is formed with the focus coil. With careful calibration, it is possible to regulate weld penetration within 2% over the entire weld seam.[36]

This feedback loop has also been used to regulate the focal length of the magnetic lens during variable working distance EBW.[69, 70] Antennas tuned to the characteristic the plasma spectrum have also been proposed as a potential feedback sensor, but additional information regarding this technique could not be found.[36]

2.3.5 Spurious Deflection

The spurious deflection of an electron beam can arise from numerous factors.[71, 72, 1] Residual magnetism, ie, remanence, in the workpiece or the supporting fixtures can cause significant alignment issues. A common example is welding steel after it has been held in a magnetic chuck.[1] Thus, if welding magnetic materials, the residual magnetic field above the workpiece surface should be kept below 15μT.[1] If the electron beam passes near a conductive, grounded surface, eddy-currents will induce beam aberrations. Thus, all elements surrounding the beam path should be kept as radially symmetric as possible. If there are ungrounded or non-conductive elements in the chamber, these components will retain stray charge, resulting in an electric field capable of deflecting the beam. This issue is simply addressed by proper grounding of all chamber components, and/or warpping the materials in grounded, clean aluminum foil.[1] When welding dissimilar metals, a Seebeck coefficient difference of a few millivolts can produce thermoelectric currents on the order of several hundred amperes. This issue is especially problematic when welding dissimilar steels with high permeability and low electrical resistance. [73]

During the EB-PBF process, these considerations are especially acute because tight dimensional tolerances of the 3D part implies a tight control of the residual magnetic fields. The equipment location should have a small and constant magnetic field of less than 100 nT, similar to the requirements of a high resolution SEM. Moving large metal objects near the equipment can induce changes in the static magnetic field, necessitating a recalibration of the beam optics.

2.4 Beam Imaging & Sharp Focus

After emerging from the anode, the diverging electron beam is focussed onto a localized position on the workpiece surface. In electron optics, this is done using a stationary, variable focal-length magnetic lens. Electron beam imaging can be best understood by examining the ray-tracing diagram shown in Fig.2–17a.

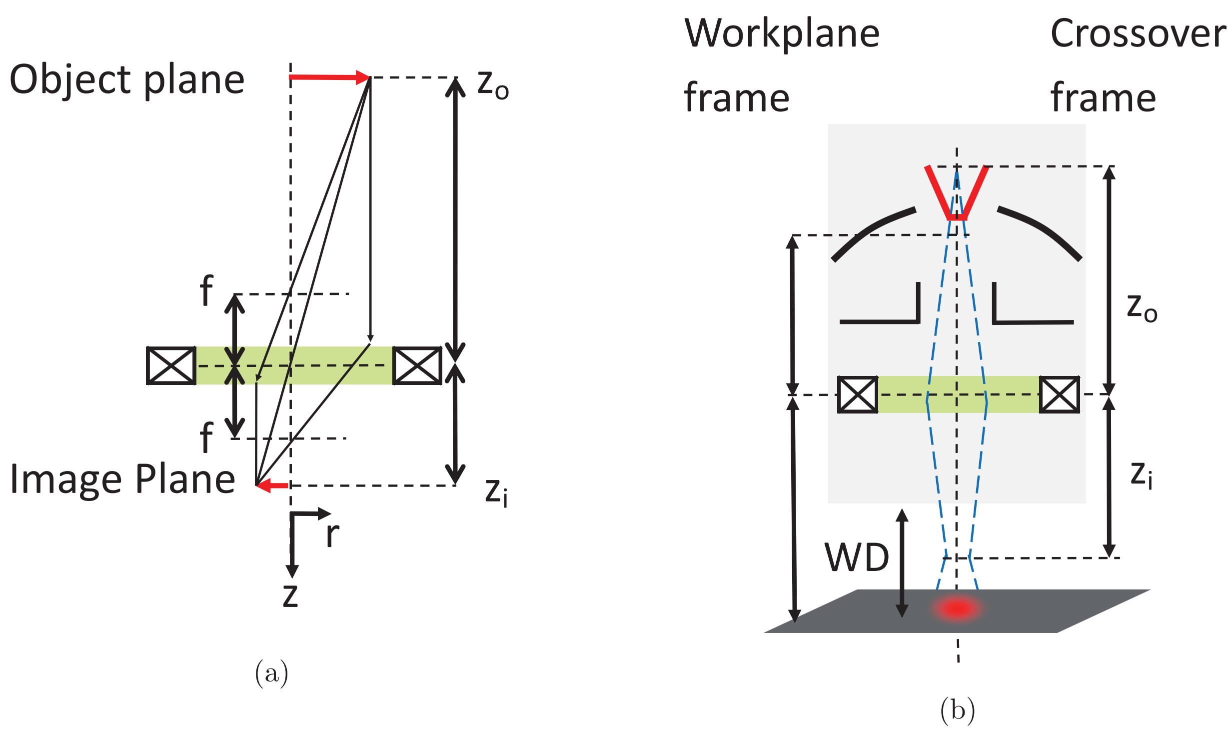

Figure 2–17: Geometric electron beam optics. Left: geometry of thin-lens imaging system, defining object, image and focal plane. Right: Electron beam column, demonstrating electron crossover, and workplane frame for over-focussed condition

Assuming a thin, weak lens, whereby the image and object plane are outside the magnetic field of the lens, the paraxial thin-lens equation states that:

$$\frac{1}{f} = \frac{1}{z_o} + \frac{1}{z_i} \tag{2.25}$$

where f is the focal length of the lens, z_o is the distance between the lens center and object and z_i is lens-image distance. The image magnification is given by:

$$M = \frac{z_i}{z_o} \tag{2.26}$$

where Fig.2–17a demonstrates a demagnified image ($M < 1$). The implication of a demagnified image is that the FWHM at the workplane is smaller than the FWHM in the gun.

Although the thin-lens equation is conceptually straight-forward, it is illustrative to explain the action of beam focussing with respect to the fixed workplane surface, as shown in Fig. 2–17b. From this perspective, the image plane is the fixed surface of the workpiece, and changes to the focal length of the lens move the position along the beam axis which is focussed onto the workpiece. Thus, a sharp-focus beam requires a focal length which matches the lens object plane with the minimum beam diameter created in the gun. This minimum diameter, referred to as the beam crossover, can be either real or virtual, as shown in Fig. 2–8. As discussed in Sec. 2.2, the position of this crossover point is a function of the bias setting, which implies that the current within the focus coil must be modified according to the requested beam current in order to maintain sharp-focus.

Returning to Fig. 2–17b, a defocussed beam implies that the lens is imaging the beam current distribution, i.e. the object, before or after the gun crossover. If the gun crossover is imaged above the workplane, the beam is said to be over-focussed. Viewed from the workplane perspective, this implies that the lens object is after the gun crossover, which is the condition shown in Fig. 2–17b. Similarly, if the gun crossover is imaged below the workplane, the beam is under-focussed, implying the lens object is behind of the crossover.

Setting the focal length such that the gun crossover is imaged onto the workplane results in a Gaussian-distributed current density. Conversely, if the focal length is set to image the cathode emission surface, which occurs after the crossover, a uniform, tophat

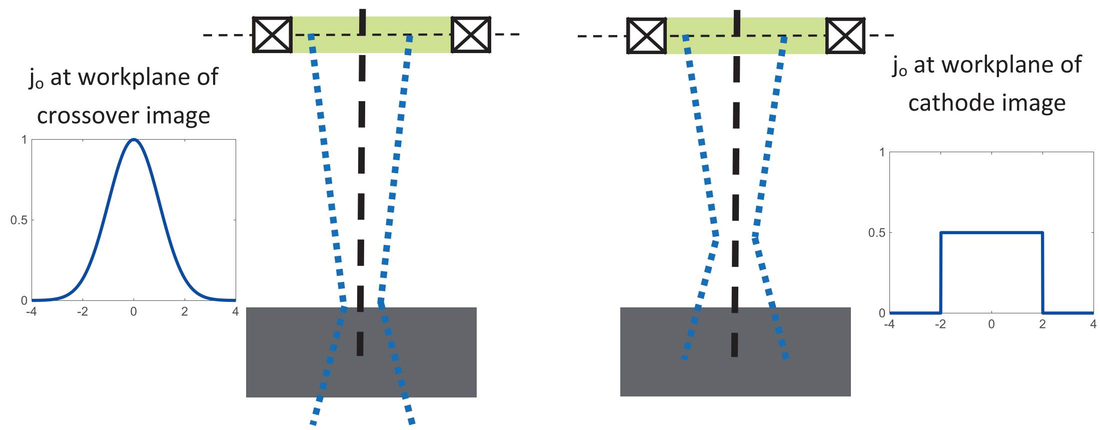

Figure 2–18: Normalized workplane current density for $I_b = 2\pi$. Left: Virtual crossover imaged onto workpiece surface, with Gaussian distribution parameter σ=1. Right: Cathode emission surface imaged onto workpiece surface, Gaussian distribution parameter r=2 . [6]

power density will result. These two imaging conditions are shown in Fig. 2–18, along with their corresponding current density at the workplane.

A tophat current density can reduce the temperature gradients within the center of the beam spot, resulting in reduced convection. This mode has been used for single crystal turbine blade repair, laser directed energy deposition, electron beam lithography, electron beam surface polishing and hardening.[74, 39, 36, 75]

Equation 2.26 implies that the de-magnification of the gun cross-over depends on the distance between the focus lens and workplane. In other words, the FWHM of a sharp-focus beam increases with WD, highlighting one of the geometric challenges associated both laser and electron beam powder-bed fusion. Specifically, the ability to build large components requires an extended distance between the deflection lenses and the build surface. In the case of the Arcam A2 system, the working distance is 330mm while the build surface is 200 x 200 mm. This results in a path length difference of approximately 30 mm between the center and the corner of the build surface. Similarly, a deflection angle of 23^o is required to reach the corners of the build chamber, resulting in an elongation of the FWHM by roughly $1/\cos(23^o)$=1.09. In one case, it was shown that the combined effects of path length and wide-angle aberrations increased the FWHM of the beam by

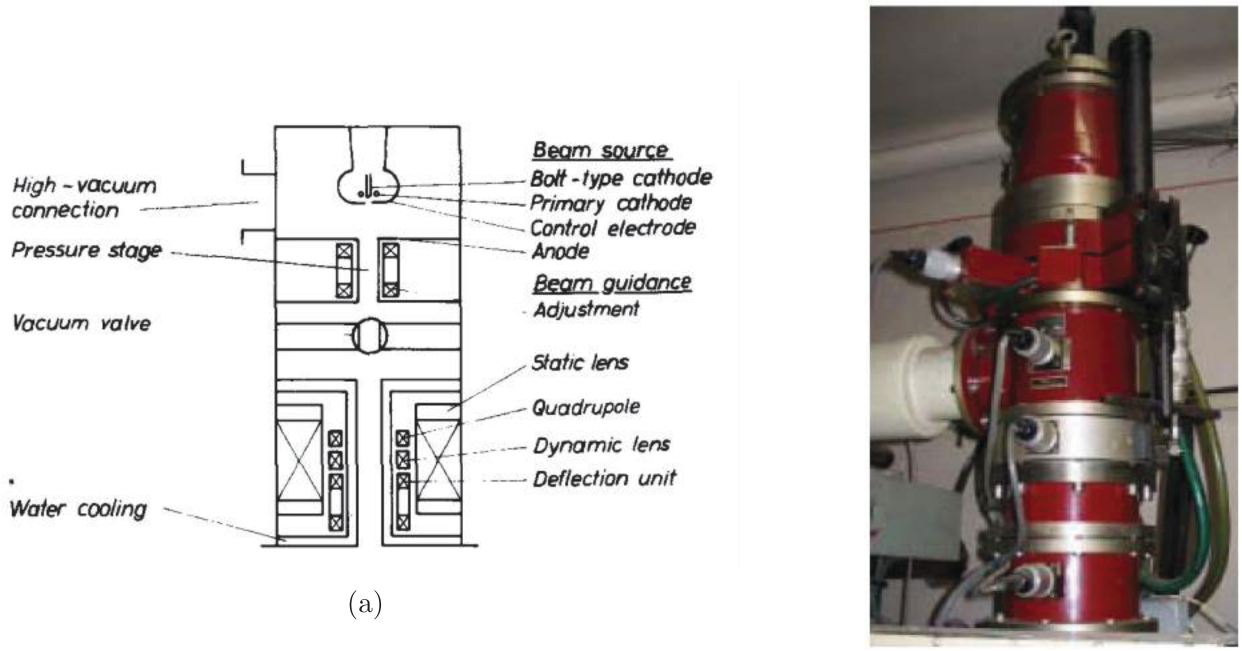

(a)

(b)

Figure 2–19: Electron gun used for high-speed surface remelting, the von Ardenne CTW60, which has a 60kV/5kW operating power.[76, 59] Left: Schematic diagram of the electron beam column. Right: Image of installed system

roughly 50% in the corners compared to the center, highlighting the importance proper part placement within the build volume.[18]

2.4.1 Example: Electron beam surface processing

To summarize the previous sections, a system designed for electron beam surface hardening will be presented, while some of the system applications will be discussed in Sec. 2.6.2. The process requirements for e-beam hardening are similar to those of EB-PBF, namely, precise local energy input over a large working area and high process productivity. The electron beam column, schematically shown in Fig. 2–19 is a 60kV/5kW system developed by the von Ardenne Institute in the 1980s.[22, 59]

The gun is a triode-type, thermionic gun which utilizes a indirectly-heated, bolt-type tungsten cathode. The anode forms part of an integrated, water-cooled pressure stage. The narrow bore constricts the gas flow between the working and gun chamber, enabling the vacuum pressures within the gun and process chamber to be decoupled. Generally, it is preferred to maintain a lower gun pressure in order to extend cathode life and stabilize the cathode emission. Integrating the constriction into the anode has the advantage that, at this point in optical path, the beam diameter is still small. Placing the constriction further down the optical axis would require either a larger bore, extensive thermal management or multi-stage focussing elements. The pressure decoupling stage includes a set of low-speed deflection coils, known as alignment coils, which statically align the beam axis with the focus lens axis, reducing astigmatism-related aberrations.

Following the vacuum valve is a set of nested focus, stigmator, and deflection lenses. The deflection coils are capable of scan frequencies as high as 100kHz with a range of $\pm 12^o$.[22] One interesting feature of this design is the use static and dynamic focussing lenses. The static lens provides the large magnetic field needed to roughly focus the beam crossover onto the workplane. Because of the wide-angle deflection area, a second set of low inductance focus coils provides the small and rapid focal length adjustments needed to scan the focussed beam over the large processing area. These adjustments are also synchronized with the stigmator, which compensates for wide-angle, projection-based aberrations.

The nested set of coils also includes a water-cooled, heat absorbing jacket. Although the details of this component are not given, one can assume that this feature acts like an aperture, intercepting the large angle electron trajectories and increasing beam brightness. As previously discussed, monitoring the temperature of the cooling water is critical in order to eliminate the risk of beam-induced melt-through.[76]

2.5 Beam Optics and Heat Transfer

While the previous section concerned the relations between beam brightness, power, power density, FWHM and beam deflection, this section reviews how these parameters affect the quantity and distribution of heat within the point of interaction. While the transport of heat out of the liquid pool determines the solidification microstructure and residual stress, this section focuses on how beam parameters affect the deposition of heat into the solid and/or liquid.

In the simplest case, a material rapidly heated below its melting point and the peak temperature is almost exclusively determined by the incident energy distribution. The precise meaning of 'rapid' can be understood by examining the characteristic thermal diffusion length:

$$L_{th} = 2\sqrt{\alpha\tau} \tag{2.27}$$

where α is the thermal diffusivity and τ is the interaction period and L_{th} is the characteristic dimension over which heat has diffused during time τ.[77] As a conservative estimate, assume a beam FWHM= 1mm and a scanning speed of 1000 mm s^{-1}. The corresponding interaction time is τ= FWHM/v= 1mS which for titanium ($\alpha \approx 8$ mm^2 s^{-1}) gives L_{th}= 0.2mm. This simple argument shows that in absence of convection, the absorbed heat remains concentrated around the beam spot, while the condition FWHM >> L_{th} implies adiabatic heating. During electron beam sintering and surface hardening, the travel speeds are on the order of 10 000 mm s^{-1}, implying that the heating process is adiabatic. [78, 22, 79]

The previous argument detailed how the heat would be distributed during time τ, with no reference to the amount of heat absorbed. A derivation of the incident energy begins with the sharp focus power density, Eq. 2.3. If the beam travels relative to the workpiece along the x axis with velocity v, crossing the origin at $t = 0$, the time-dependent power density within the fixed reference frame becomes:

$$p(x, y, t) = p_0 * exp\left(-\left[\frac{(x - vt)^2}{2\sigma_x^2} + \frac{(y)^2}{2\sigma_y^2}\right]\right) \tag{2.28}$$

The incident energy per unit area along transverse y axis can be calculated by integrating Eq. 2.28 at $x = 0$, such that:

$$\begin{aligned} q(y) &= \int_{-\infty}^{\infty} p(0, y, t)dt \\ &= \frac{V_{acc}I_b}{\sqrt{2\pi}v\sigma_y} exp\left(\frac{-y^2}{2\sigma_y^2}\right) \\ &= q_0 \ exp\left(\frac{-y^2}{2\sigma_y^2}\right) \end{aligned} \tag{2.29}$$

where $q(y)$ has units of [J mm^{-2}] and q_0 represents peak incident energy density, which occurs along the longitudinal axis of the beam, $y = 0$. A similar calculation can be made for a stationary beam pulsed for time τ. For simplicity, assume that the beam spot is symmetric, i.e. $\sigma_x = \sigma_y = \sigma$. In this case, the beam distribution can be described in polar coordinates, $r = \sqrt{x^2 + y^2}$, resulting in a local energy fluence is given by:

$$\begin{aligned} q(r) &= \int_0^\tau p(r,t)dt \\ &= \tau \frac{V_{acc} I_b}{2\pi\sigma^2} exp\left(\frac{-r^2}{2\sigma^2}\right) \\ &= q_0 * exp\left(\frac{-r^2}{2\sigma^2}\right) \end{aligned} \tag{2.30}$$

where q_0 is the incident energy density at the end of the pulse, which has units of [J mm^{-2}]. In pulsed laser processing, q_0 is commonly referred to as the peak fluence, a term which will be henceforth adopted for travelling beams.

By equating the peak fluence of the travelling and pulsed beams, we can calculate the equivalent dwell time of the travelling beams according to according to:

$$\tau = \sqrt{2\pi}\frac{\sigma}{v} = 1.06\frac{FWHM}{v} \approx \frac{FWHM}{v} \tag{2.31}$$

which justifies the previous approximation used for determining the adiabatic heating threshold.

In both cases, q_0 represents the incident peak fluence, which is distinct from the absorbed energy. But compared to lasers, electron beams are relatively insensitive to surface finish and material state.[1, 23, 36] For thermal processing, electron beam energy absorption is only dependent on the effective atomic number of the material and the incident angle. In nearly all cases, the absorbed energy is defined as ηq_0, where η is a model-dependent absorption coefficient which may or may not be calibrated against caliometric measurements.[80, 81] The physical mechanisms for electron beam absorption will be further discussed in Ch. 4.

If the absorbed fluence is sufficiently high to cause melting, convection will impact the distribution of mass, momentum and heat within the beam interaction zone. The importance of conduction and convection within the melt can be assessed according to the Peclet number, which compares the relative magnitudes of heat transported by convection and conduction within the liquid:[82, 31, 83]

$$Pe = \frac{U_l L}{\alpha} \tag{2.32}$$

where U_l is the liquid velocity, α is the thermal diffusivity and L is the characteristic length of the liquid. For a typical case of electron beam melting of titanium, the liquid velocities are on the order of 100 mm s^{-1}, with a characteristic length on the order of the beam FWHM, L= 1mm. Using the thermal diffusivity of pure Ti($\alpha \approx$ 8 mm^2 s^{-1}) gives a Pe=12, which implies that convective heat transport within the liquid is at least a order of magnitude greater than conduction.[84, 80, 26] Precise calculation of Eq.2.32 requires advanced simulations, but as a general rule, Pe increases with increasing Peak Power Density (PPD).[83]

Convection within the melt pool is driven by combination of forces, including buoyancy, thermocapillary, vapor recoil and electromagnetic.[84, 80] For the PPD used in EBW and EB-PBF, the thermocapillary and vapor recoil forces have the greatest effect on the size and shape of the weld pool, the weld macro and microstructures, as well as the weldability of the material. [84, 80]

Thermocapillary convection, otherwise known as Marangoni convection, is a response to the surface tension gradient along the liquid surface. Although surface tension gradients can arise because of compositional gradients, for most electron-beam process, it is the temperature gradients within the liquid which drives Marangoni flow. Titanium alloys free of tramp impurities such as sulfur have a surface tension temperature coefficient of $d\gamma/dT$= -0.26*10^{-3} N m^{-1} K^{-1}.[26, 84] The negative coefficient implies that hot liquid at the center of the beam will be pulled to the cooler outer edge of the liquid pool, resulting in a wide and shallow melt. Assuming the formation of a boundary layer, the fluid velocities along the surface, U_l, can be estimated according to:[85, 82]

$$U_l^{3/2} = \frac{d\gamma}{dT}\frac{dT}{dr}\frac{W^{1/2}}{0.664\rho^{1/2}\mu^{1/2}} \tag{2.33}$$

where dT/dr is the temperature gradient, W is the melt pool width and μ is the melt pool viscosity. For Titanium with a dT/dr 10^5 K m^{-1}, W= 10^{-3}m, μ= 0.005 N s m^{-1} and ρ=

4500 kg m^{-3}, the estimated fluid velocity is 0.4 m s^{-1}, which agrees with similar approximations for pulsed laser welding of stainless steel and keyhole welding of Ti64.[82, 84, 86] Compared to the roughly 10^{-3}m liquid pool dimensions, these fluid velocities demonstrate a very high degree of recirculating flow and thus heat transport. An important implication of Eq. 2.33 is fluid flow velocity decreases with temperature gradient, which has significant implications for the reduced gradients associated with the high holding temperatures used in EB-PBF.[18]

When the vapor pressure of the constituent alloy elements becomes comparable to the pressure within the vacuum chamber, vapor will be emitted from the surface. Reliable calculation of the vapor pressure requires complex numerical models involving heat, mass, and momentum balances in both the gas and liquid of the weld pool.[87, 80] Escaping vapor can evaporatively cool the weld pool, while conservation of momentum requires that the vapor flux creates an opposing pressure on the liquid surface. This vapor recoil pressure can have a dramatic effect on the melt pool shape.[80, 85, 87] Since the vapor pressure has an exponential temperature dependence, the recoil pressure will be proportional to the peak fluence and power density of the beam. This can be seen from the recoil-pressure melt depressions modelling results of Klassen *et al*, shown in Fig. 2–20.

Experimentally, bead-on-plate welds of Ti64 were performed using a modified Arcam S12 EBM system. The experiments used identical beam powers of 300W (60kV/5mA), and FWHM= 235μm. The difference between the left and the right columns of Fig. 2–20 is the travel speed, which was 2000 and 600 mm s^{-1}, respectively. From these values, the beam PPD can be calculated as 4.7 kW mm^{-2}, with peak fluences of 0.6 J mm^{-2} on the left and 2.0 J mm^{-2} on the right. In both cases, a shallow, hemispherical fusion zone was observed both numerically and experimentally.

The simulations were performed using 2D, free-surface Lattice Boltzmann technique, where the beam is travelling into the plane of the page. These simulations accounted for convective mass and heat transport, latent heat and the vapor recoil pressure. The Marangoni convection, multi-component vaporization and ionization effects were not considered. Detailed relationships regarding vapor transport across the Knudsen layer were solved to determine the corresponding vapor recoil pressure.[87]

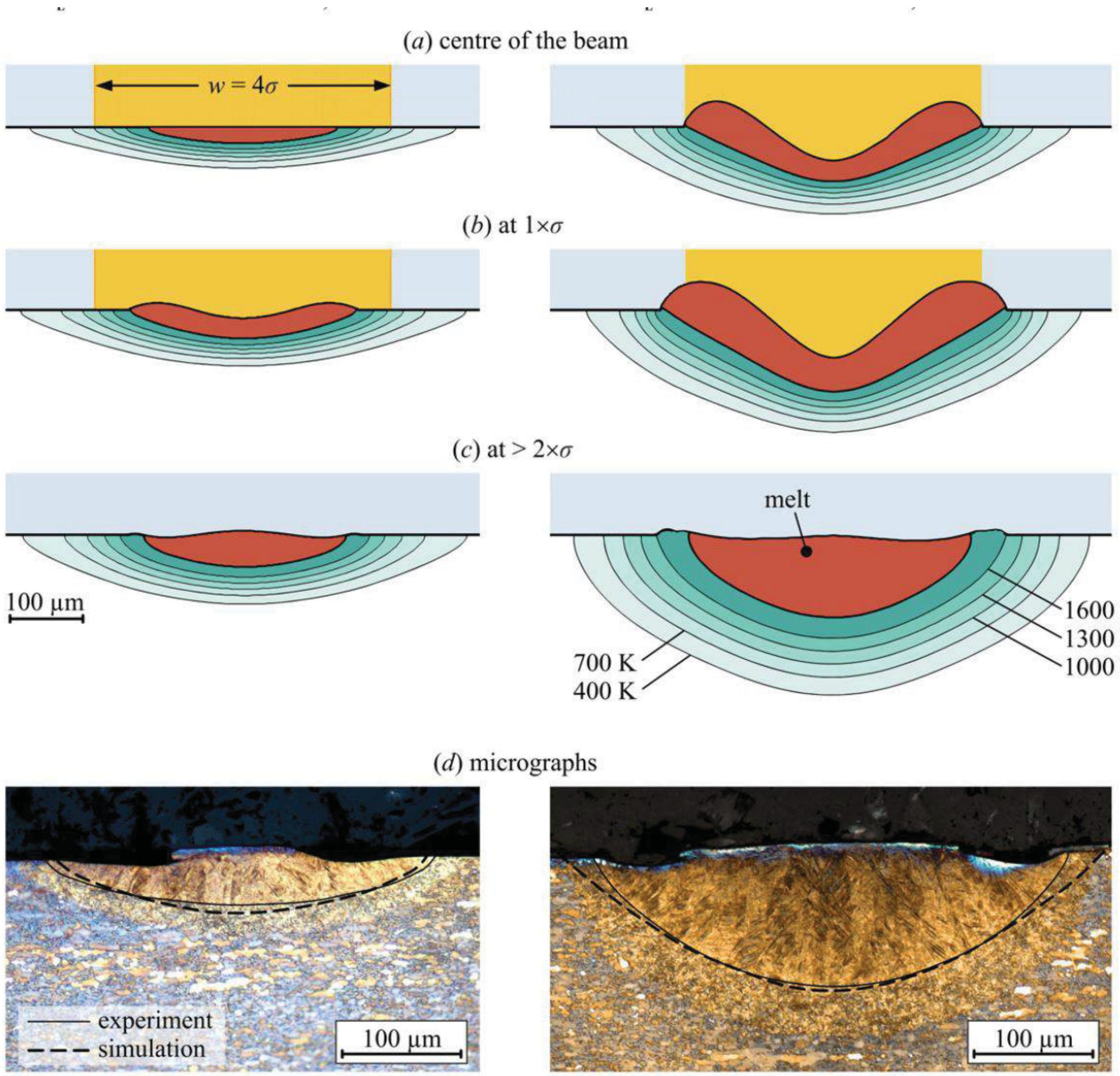

Figure 2–20: Lattice Boltzmann simulation of vapor depression formed during electron beam melting of solid Ti64 with experimental comparison to continuous single tracks in a modified Arcam S12. The solid material is melted with a beam power of 300W (60kV/5mA) and a FWHM=235μm, which results in a PPD of 4.7 kW mm^{-2}. Left: vapor depression and experimental results for a v= 2000 m s^{-1}, q_0= 0.6 J mm^{-1}. Right: Vapor depression formed with v= 600 mm s^{-1}, q_0= 2.0 J mm^{-1}

The topmost row shows the liquid depression after the beam has travelled halfway into the plane of the paper. The slower beam on the right hand side has resulted in an appreciable vapor depression after an incidence fluence of 1 J mm^{-2}. Despite the identical PPD, the simulation results in the left panel demonstrate no vapor depression after a fluence of 0.3 J mm^{-2}. The simulation results in the second row show the melt pool geometry after the beam has travelled an additional $100\mu m$ into the page, showing that the vapor depression of both the slow and fast beams has increased. The final row shows the simulations results after the beam has travelled an additional $200\mu m$ into the page, which marks the end of energy deposition and beginning of solidification. Excellent agreement between simulation and experiment is observed.

Numerically, it was determined that when the surface temperature exceeds approximately 2950 K, the vapor pressure (5E-4 mbar) approaches the build chamber pressure(2E-3mbar He). At this temperature, the recoil of the expanding vapor along longitudinal axis becomes large enough to accelerate the melt towards the outside the pool, initiating a vapor depression. The maximum temperature, pressure and liquid flow velocities simulated in the left panels of Fig. 2–20 were 3150K, 1.1 m s^{-1} and 2E-3mbar, respectively. The corresponding values in the high fluence panel on the right were 3250K, 1.3 m s^{-1} and 4E-3mbar.

These simulations demonstrate an important physical restriction on the beam melting of any alloy, in that evaporation sets a soft ceiling for the maximum achievable surface temperature. In other words, once evaporation has been initiated, evaporation will transform the absorbed beam energy into metallic vapor at the surface. But as Fig. 2–20 shows, increased evaporation creates a deeper melt pool depression. Combined with the movement of liquid away from the beam center due to the Marangoni convection, the thickness of the liquid boundary between the high power beam and the cooler solid shrinks, resulting in a tremendous temperature gradient at the base of the vapor depression. Another feature is that the vapor depression walls will absorb a fraction of the incidence beam energy, reflecting the remaining power into the bottom of the depression and further increasing the evaporation rate.[72, 84] The ratio of reflected and absorbed energy will

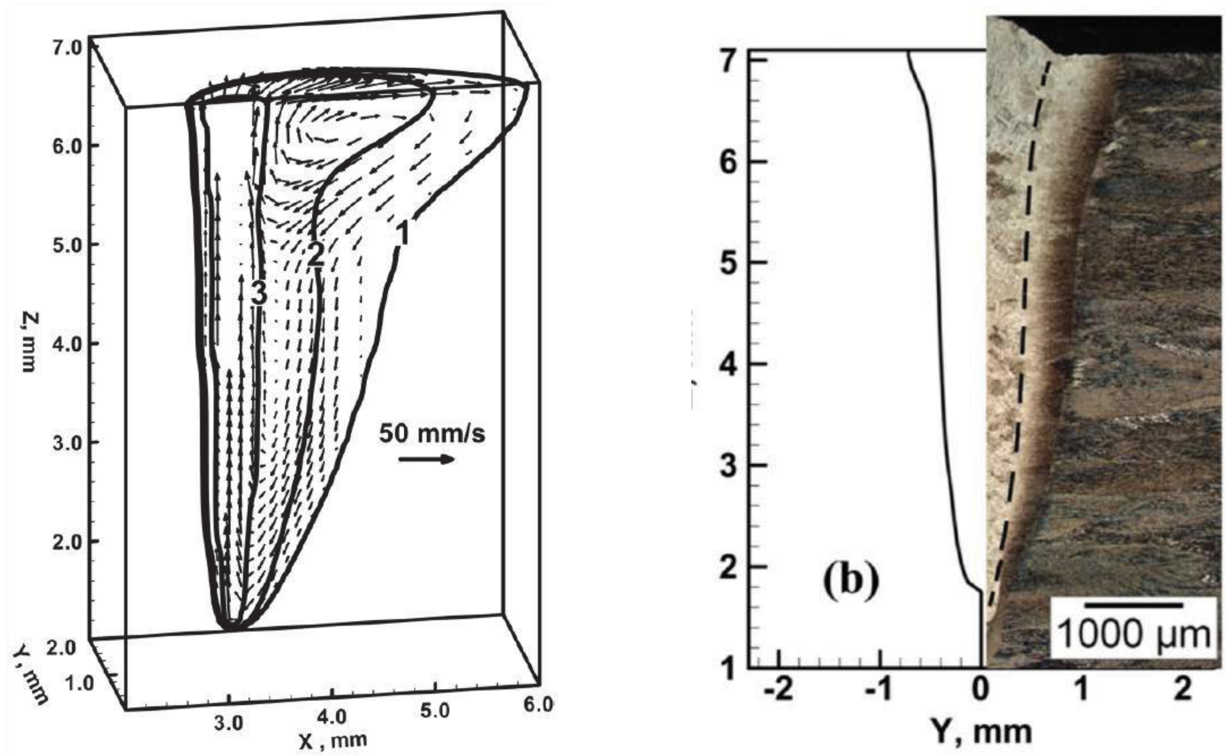

(a) (b)

Figure 2–21: Keyhole EBW of Ti64: fluid flow simulations compared to experimental results.[84] Beam parameters: 1100W (110kV/10mA), FWHM= 0.30mm, and v=16.9 mm s^{-1} resulting in an incident PPD= 10.3 kW mm^{-2} and q_0= 79 J mm^{-2} Left: Simulation of fluid velocity field during keyhole EBW of Ti64. The contours (1), (2) and (3) represent temperature 1873K = solidus temperature, 2000K and 2500K, respectively. Right: Transverse fusion zone cross-section compared to experimentally determined fusion zone boundary, shown by the dotted lines

increase with increasing angle between surface normal and the beam axis.[36] The combination of Marangoni convection, vapor recoil and wall reflections form the basis of keyhole welding, which is shown schematically in Fig. 2–21.

In the experimental/numerical study of Fig. 2–21, keyhole welds were performed on Ti64 using welding speeds nearly 100 times slower than the results presented in Fig. 2–20 (17 vs 2000 mm s^{-1}). The beam PPD was approximately doubled at 10.3 kW mm^{-2}, largely due to the higher accelerating voltage (110kV vs 60kV). The increased V_{acc} and smaller v results in a significantly higher peak fluence of 79 J mm^{-2} and the formation of a 5 mm deep vapor capillary, otherwise known as a keyhole.

The keyhole geometry was simulated by considering the energy balance at the liquid-vapor interface, whereby the recoil pressure exerted by the evaporating surface was balanced by the opposing capillary ($\gamma/r(z)$) and hydrostatic pressure head ($\rho g z$) forces closing the cavity.[84] Compared to the results of Fig. 2–20, these simulations accounted for Marangoni convection along the liquid surface but have assumed conditions which restrict the liquid/vapor interface within the keyhole, i.e. no a free surface. The simulations iterated the energy balance along the keyhole depth until convergence, then mapped the keyhole geometry onto a coarser mesh to numerically solve the 3D mass, momentum, and energy balance equations within the weld pool.

It was numerically determined that the minimum wall temperature of 2632 K was near the top surface of the keyhole while the maximum T=3034 K was at the keyhole base. The temperature gradient along the keyhole can be understood since higher vapor pressures are needed to counteract the increasing hydrostatic forces and capillary forces along the keyhole. This 400K temperature gradient induced Marangoni convection from the keyhole bottom to the surface and outwards, significantly enhancing heat transfer within the keyhole and weld pool. In both simulations, enhanced evaporation due to the more volatile aluminium was ignored, despite being a well-known effect in EB-PBF and electron beam cold hearth remelting.[88, 65, 89, 31]

2.5.1 Review of Analytical Heat transfer Models

Although illustrative, the previous examples are computationally complex and require some degree of empirical confirmation and model adjustment. A practical way to develop intuition regarding the complex heat transfer during electron beam heating is to use of simpler models which provide a first order approximation of the relevant beam and material parameters.[31]

Arguably the most important approximation is the assumed distribution of the heat source, as this can be used as a fudge factor for effects like Marangoni convection and keyhole formation. In the following section, three heat source distributions will be described, along with their relation to the specific beam parameters. While these models are generally used to understand how heat is transferred out of the Fusion Zone (FZ), i.e. solidification, they will illustrate process parameters that are relevant for heating, conduction-mode and keyhole-mode welding. When possible, normalized process parameters will be introduced that indicate the relative magnitudes of different beam and material parameters. These models are not meant to precisely predict the weld zone shape, but offer functional relationships between both process and material parameters. In other words, these models can be used to assess how changes in material or process influence the weld geometry.[90]

Point Source-Hemisphere FZ. The first widely accepted transient heat transfer model for welding was published in 1941 and is referred to as the Rosenthal model, which is based on the following assumptions: [91]

- Steady-state heat flow in moving coordinate system of the beam $[x, y, z]$
- Point-like heat source with infinite temperature at the origin
- Temperature-independent thermophysical material properties
- No convection within the melt region
- No evaporative or radiative heat loss
- Workpiece is either thin(2D) or semi-infinite

As will be shown, the appropriateness of the point-like heat source is one of the weakest assumptions of the model, and is only applicable when certain relationships between the source, material and process are met.

Christensen normalized the Rosenthal model into material and machine-independent dimensionless parameters, demonstrating good experimental agreement over several orders of magnitude when using tungsten inert gas(TIG), metal inert gas(MIG) and submerged arc welding (SAW) on steel, Al, Cu and Sn, providing a fundamental basis to compare processes.[92] In this formulation, the spatial coordinates are normalized according to the Peclet number, where the characteristics length becomes one half the coordinate axis value, and the fluid velocity is replaced by the beam travel speed, v:

$$[x^*, y^*, z^*] = \frac{v[x, y, z]}{2\alpha} \tag{2.34}$$

where $[x^*, y^*, z^*]$ is the normalized coordinate dimension. As per convention, x^* is the longitudinal travel direction, y^* is transverse to the beam motion, and z^* is along the thickness of the part. All three dimensions are with respect to the moving, Lagrangian coordinate system of the beam. To visualize this moving reference frame, consider the analogous problem of smoke emitted from a smoke stack in a steady wind, where the density of smoke downwind represents the temperature.[93]

Equation 2.34 defines the isotherms according to the dwell time of the source (via, v) over the rate at which it is diffused away, α. The implication is that materials with low thermal diffusivity like Ti ($\alpha \approx 8$ mm s^{-1}) will have much more closely spaced isotherms compared to materials with high diffusivity, like copper ($\alpha \approx 116$ mm s^{-1}). Similar comparisons apply between the powder and solid materials, as the powder will have a significantly smaller thermal diffusivity, resulting in greater heat concentration. This will be seen in the heat transfer analysis of the dissimilar Nb-Ti welds of Ch. 5.

Next, Christensen defined the dimensionless temperature T^* according to:

$$T^* = \frac{T - T_0}{T_m - T_0} \tag{2.35}$$

where T_0 is the initial temperature, and T_m is the melting temperature, resulting in a FZ boundary defined at $T^* = 1$. Because of the omission of convection, temperatures above the melting point cannot be accurately predicted. Christensen also defined a dimensionless operating parameter, n, which relates the material and heat source according to:

$$\begin{aligned} n &= \eta \frac{I_b V_{acc} * v}{4\pi\alpha^2 c_p \rho (T_m - T_0)} \\ &= \eta \frac{I_b V_{acc} * v}{4\pi\alpha^2 \rho (H_m - H_0)} \end{aligned} \tag{2.36}$$

where η is the absorption coefficient, I_b is the electron beam current, V_{acc} is the electron beam accelerating, c_p is the specific heat capacity and ρ is the density. The relation between the enthalpy rise, beam power, travel speed and thermal conductivity are captured within the operating parameter n. The second expression in Eq. 2.36 includes the enthalpy substitution, $c_p(T_m - T_0) = (H_m - H_0)$ [J g^{-1}], which allows the effects of latent heat to be included in the corresponding temperature isotherms.[94] The corrresponding volumetric enthalpy of melting is $\rho * (H_m - H_0)$ [J mm^{-3}] where the density ρ is taken at the reference temperature T_0 according to conservation of mass.[94]

As an example, the volumetric enthalpy of melting for Ti calculated from the $c_p\rho(1668C - 25C)$ expression using room temperature thermophysical parameters is 3.9 J mm^{-3}.[26] The corresponding volumetric enthalpy rise, $\rho(H_{1668C} - H_{25C})$, is 4.540E-3*(1484-0)= 6.7 J mm^{-3} which includes the latent heat of the α/β transformation and the melting. In the case of EB-PBF with a holding temperature of 700C, the $c_p\rho(T_m - T_0)$ expression yields a volumetric enthalpy of melting 3.1 J mm^{-3}, using material parameters at 700C. The corresponding $\rho(H_{1668C} - H_{700C})$ expression is 4.44E-3*(1484-484)= 4.4 J mm^{-3}. Although these transformations do not seem to significantly affect slower arc-welding processes, it is expected that the roughly 30% difference in volumetric enthalpy will be important for fast heating processes such as EB-PBF.[94]

Regardless of the n form, after an initial transient heating distance, the steady state isotherms in the moving coordinate system can be expressed in dimensionless form according to:[92, 94]

$$T^* = \frac{n}{R^*} exp(-(R^* - x^*)) \tag{2.37}$$

where R^* is the radial distance from the point source ($R = \sqrt{x^2 + y^2 + z^2}$) normalized according to the Peclet transformation of Eq. 2.34. A key feature of Eq. 2.37 is that at the origin, the model temperature is infinite because of the $1/R^*$ asymptote. Also, the isotherms in the $y - z$ plane will always been circular.

During arc-welding experiments, it was demonstrated that the predicted FZ was greater than expected for small $n(<0.001)$ and smaller than expected for large $n(>100)$. These limits are to be expected, since convection will play a increasingly larger role for slow travel speeds (small n), thus expanding the FZ. Conversely, at fast travel speeds (large n), the Rosenthal model will erroneously predict melting because of the infinite temperature associated with a point source.

Because of the additive nature of heat, a superposition of multiple point sources can be used to approximate more complex heat distributions, but care must be taken to properly account and distribute of each individual source to maintain the net power and boundary conditions, respectively.[94]

Distributed Source-Shallow FZ. One shortcoming of the Rosenthal model is the assumed point-source, which causes the isotherms in the transverse $y - z$ plane to always be circular, resulting in a constant FZ depth-to-width ratio of 0.5. [90] Similarly, the Rosenthal model will always erroneously predict some degree of melting.

Using a Gaussian-distributed heat source, Cline and Anthony derived the quasi steady state temperature distribution of a travelling laser, which can be adapted to the electron beam as:[93]

$$\begin{aligned} T^*(\dot{x},\dot{y},\dot{z}) &= \eta \frac{I_b V_{acc}}{\sqrt{2\pi^3}\sigma\alpha\rho(H_m - H_0)} \int_0^\infty \frac{d\mu}{(1+\mu^2)} exp\left(-\frac{(\dot{x}+\sigma^*\mu^2)^2+\dot{Y}^2}{2(1+\mu^2)} - \frac{\dot{z}^2}{2\mu^2}\right) \\ &= \eta \frac{v * q_0}{\pi\alpha\rho(H_m - H_0)} \int_0^\infty \frac{d\mu}{(1+\mu^2)} exp\left(-\frac{(\dot{x}+\sigma^*\mu^2)^2+\dot{Y}^2}{2(1+\mu^2)} - \frac{\dot{z}^2}{2\mu^2}\right) \end{aligned} \tag{2.38}$$

where the constant of integration μ represents the time transformation according to $\mu^2{=}2\alpha t'/\sigma^2$ and T^* represents the dimensionless temperature. Similar to the Christensen normalization, σ^* is the Peclet normalized beam distribution parameter: [90]

$$\sigma^* = \frac{v\sigma}{2\alpha} \tag{2.39}$$

while the coordinate axes are normalized against the beam distribution parameter:

$$[\dot{x},\dot{y},\dot{z}] = \frac{[x,y,z]}{\sigma} \tag{2.40}$$

Functionally, Eq. 2.38 demonstrates that the temperature distribution will be intimately linked to the beam distribution parameter, σ. This feature is further highlighted by the integration constant, μ, which is the thermal diffusion length divided by the beam radius. The resulting isotherm will depend on the numerical solution of the $\int d\mu$ integral, while the magnitude of the isotherms will be largely determined by the magnitude of the prefactor, which is proportional to the ratio of the peak fluence and volumetric enthalpy.

Numerical solutions of Eq. 2.38 along the $[\dot{x},0,0]$ axis are provided in Fig.2–22a for a range of σ^* values. Assuming a 0.5mm FWHM beam incident on Ti with, the corresponding velocities range between 0 and 2048 mm s^{-1}.

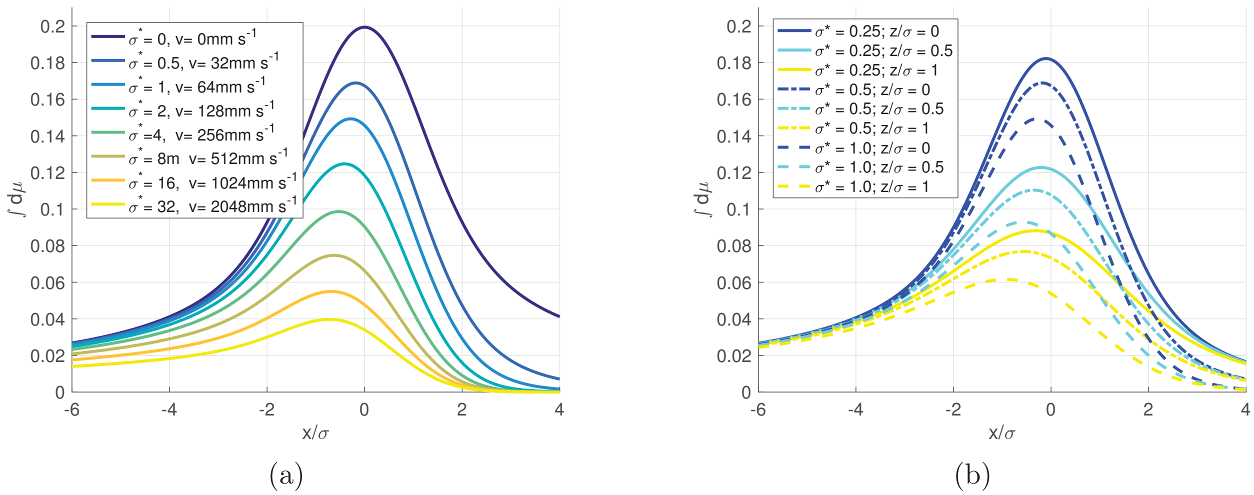

Figure 2–22: Solutions to the distributed heat source integral along centerline. Right: Integral solutions of Eq.2.38 of along top centerline for different values of σ^*. Speeds calculated for solid Ti and a FWHM≈=0.5mm. Left: Integral solutions of Eq.2.38 for different combinations of σ^* and $\dot{z}$

From this result, we see that as σ^* increases, the integral maximum decreases, corresponding to a decrease in peak temperature. This result supports the introductory discussion of adiabatic heating, since high σ^* values imply that the temperature contours are largely determined by the source distribution, and not the conduction of heat, as in the Rosenthal equation.

Integral solutions of Eq.2.38 along $[\dot{x}, 0, 0]$, $[\dot{x}, 0, -0.5]$, $[\dot{x}, 0, -1]$ for different σ^* values are given in Fig. 2–22b. These results show a similar trend in that the integral maximum decreases with depth, implying a corresponding decrease in temperature.

As a final demonstration, three dimensional isosurfaces of $\int d\mu$ for $\sigma^* = 0.1, 1$ are shown in Fig.2–23.

From these figures, we observe that the size of the isosurface decreases with increasing σ^*, as expected. But unlike the Rosenthal model, the figures demonstrate isosurfaces with variable aspect-ratios, which, depending on the prefactor of Eq.2.38, will determine the resulting FZ dimensions.

Assuming the integral component of Eq. 2.38 has an order of magnitude estimate of 0.1, Eq. 2.38 can be rearranged to give the following relationship between the beam

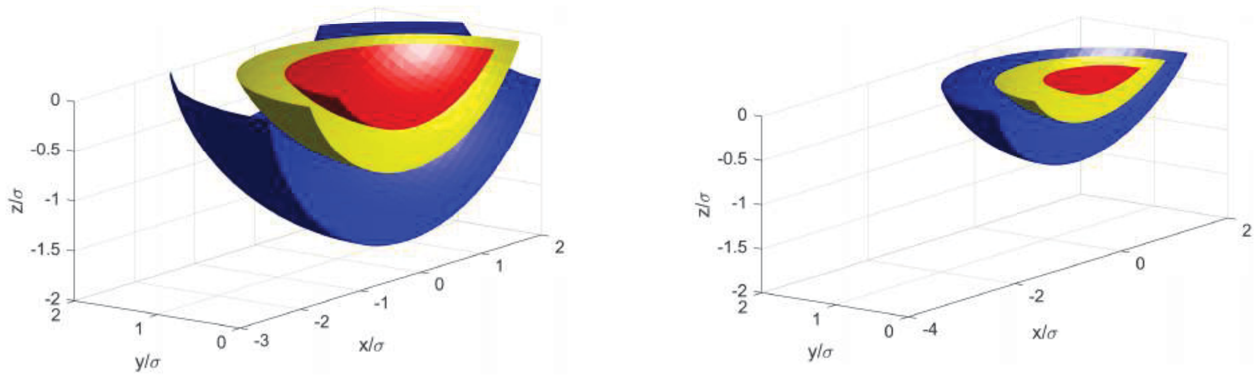

(a) (b)

Figure 2–23: Isosurfaces of distributed heat source integral in 3D with $\int d\mu$= 0.13(red), 0.1(yellow) 0.07(blue). Left: $\sigma^* = 0.1$, Right: $\sigma^* = 1$

distribution and the Ti melting threshold(T^*= 1):

$$\begin{aligned}\frac{I_b V_{acc}}{\sigma} &= 10\alpha\sqrt{2\pi^3}\rho(H_{1668C} - H_{25C}) \\ &\approx 10 * 8 * 7.8 * 5 \approx 3000\ W\ mm^{-1}\end{aligned} \tag{2.41}$$

where the ΔH estimate was previously provided. Roughly, Eq.2.41 implies that a 1kW beam requires roughly a $\sigma \approx 0.3$mm or a FWHM$\approx$ 0.8mm to induce melting, values which are in agreement with the parameters used in this work.

By examining arc-welding processes with FWHM= 3.7-10mm and v$\approx$ 10 mm s^{-1}, Eagar experimentally demonstrated that the Rosenthal equation accurately captures the FZ dimensions when $\sigma^* \approx 0$, explaining the agreement between the Rosenthal equation and slow, low power density welding processes. The converse implication is that fast processes ($\sigma^* > 0.1$) require a distributed source for accurate estimates. In terms of melting titanium with a focussed electron beam, ‘fast’ corresponds to speeds greater than 10 mm s $^{-1}$.

By analyzing the depth of fusion of focussed 100kV bead-on-plate welds of Al and stainless steel alloys, Elmer empirically observed the following relationship:[95]

$$z_{FZ} = C\frac{q_0}{\rho(H_m - H_0)} \tag{2.42}$$

where C is a dimensionless empirical constant based on the material and process. This functional form agrees with Eq.2.41, if one considers that the beam FWHM is large compared to the depth of penetration, in which case, heat transfer is essentially only along the z axis, and the melting depth becomes proportional to ratio of beam fluence and enthalpy of melting. This equation has a similar form to the γ_m parameter introduced in the previous chapter, whereby the depth of melt penetration is replaced by the powder layer depth t_l.

Unlike the Rosenthal solution, which only depends on beam power, these derivations demonstrate the importance of FWHM with respect to the parameter, $\sigma*$ and the coordinate axes $[\dot{x}, \dot{y}, \dot{z}]$. The corresponding implication is that the electron beam brightness, WD and aberrations, which define the FWHM, becomes increasingly important during high productivity processes.

As a final note, the Cline and Anthony model is only appropriate for estimating the fusion zone dimensions. To estimate the solidification microstructure associated with high σ^* process, the related Goldak double ellipsoid model is recommended.[96] This numerical model is based on a leading and trailing edge Gaussian heat distribution, where the length of the trailing edge Gaussian distribtion factor σ is roughly a factor of 4 longer than the leading edge. The longer trailing edge distribution effectively captures the effect of Marangoni convection transporting heat towards rear of the weld pool.[97]

Line heat source-Keyhole FZ. Keyhole Electron Beam Welding (EBW) is defined by the formation of a deep vapor capillary formed within the workpiece, as previously shown in the schematic of Fig. 2–21. The distinguishing feature of keyhole welding is the vapor cavity, which allows the incident energy to be distributed within the material.[36] Because of this internal heat distribution, the beam is capable of generating high-aspect ratio welds.

If the beam penetrates completely through the workpiece, the uniform, through-thickness temperature distribution can be estimated using the 2D Rosenthal solution:[94]

$$T^* = \eta \frac{V_{acc} I_b}{2\pi \alpha d \rho (H_m - H_0)} * exp(-x^*) K_o(r^*) \tag{2.43}$$

where d is the material thickness, K_o is the zero-order Bessel function of the first kind, r is the in-plane radial distance from the source($r = \sqrt{x^2 + y^2}$) and x^* and r^* are the Peclet normalizations of $x_i^* = vx_i/2\alpha$.

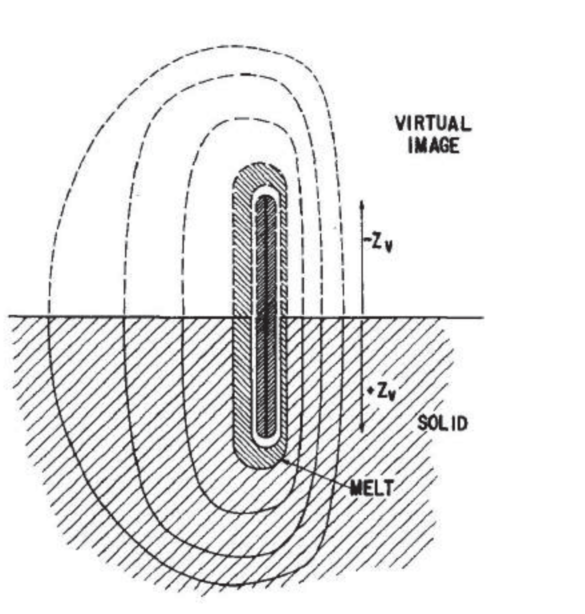

Figure 2–24: Heat source model during partial penetration keyhole welding, with temperature countours[93]

If the keyhole does not fully penetrate through the material, the use of a finite-length line source must be used, as shown in Fig. 2–24.

The depth and distribution of the source defined in Fig. 2–24 is empirically determined for each process.[81] The virtual heat source outside of the workpiece ensures that the adiabatic boundary condition $dT/dz = 0$ is maintained at the workpiece surface.[94]

Unlike rapid heating conditions associated with distributed sources, keyhole welds are generally performed at much slower speeds $v \approx 10$ mm^{-1}. Despite this slower speed, Geidt empirically determined the penetration depth z_{FZ}[m], over a range of process parameters and materials: [98]

$$z_{FZ} = \frac{3}{10} \frac{V_{acc} I_b}{\kappa (T_m - T_0)} \left(\frac{\alpha}{v * FWHM} \right)^{0.625} \tag{2.44}$$

Despite the different heat source definition, Eq. 2.44 demonstrates that the beam FWHM has a role in determining the depth of keyhole penetration. This apparent contradiction will be address in the following section.

2.5.2 Source Model Summary

By analyzing over 50 weld trials for different combinations of beams and materials, Elmer *et al* identified that the beam p_0 and the process q_0 defined the appropriateness of

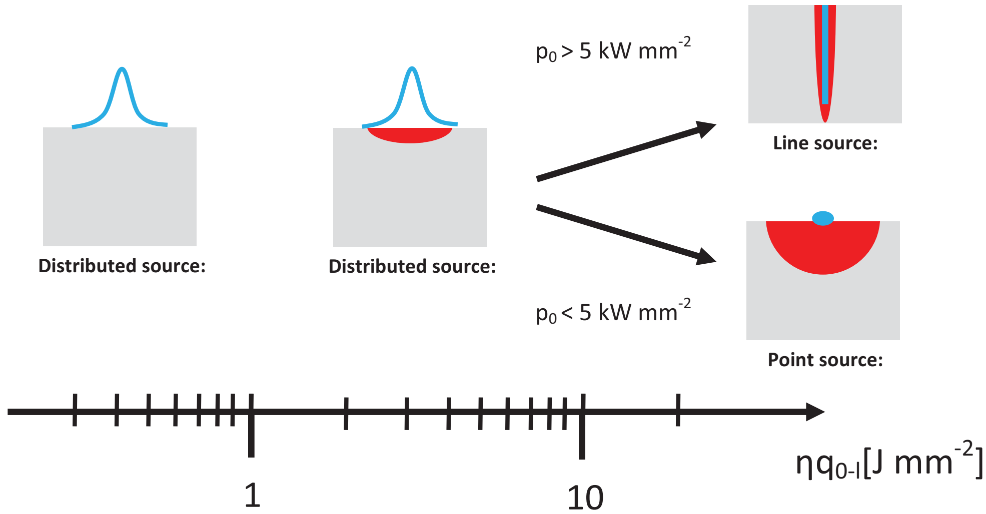

Figure 2–25: Heat source modes and corresponding FZ zone shapes as a function of centerline energy fluence, q_0 and peak power density, p_0. The values presented are order of magnitude estimates, and the precise values depend on beam, material and interaction parameters

a particular heat source model.[99] For the materials investigated, it was determined that no melting is observed for $q_0 < 1$ [J mm^{-2}]. For $1 < q_0 < 10$, the FZ geometry matched the distributed heat source model. For $q_0 > 10$, the heating mode was dependent on the p_0, with $p_0 <$ 5kW mm^{-2} associated with a point-like source and hemispherical fusion zones. For $p_0 >$ 5kW mm^{-2} the FZ shape suggested the formation of a keyhole, which could be modelled according the distributed line source. This explains why keyhole welding was not observed before the invention of high p_0 electron beams by Dr Steigerwald. This spectrum of heating source models is graphically summarized in Fig. 2–25:

This section demonstrates how the beam parameters of power($V_{acc}I_b$); beam distribution (σ) and travel speed, v, affect the heat transfer within the melt pool. From Fig.2–25, we saw how these parameters lead to different heat transfer modes within the solid or liquid. In the case of laser and electron beam PBF, high beam powers are desirable for high productivity, while a small σ is desirable for geometric resolution. As shown in Fig. 2–25, and demonstrated in the p_0= 4.7 kW mm^{-2} modelling of Fig. 2–20, the resulting high p_0 can induce rapid vaporization of the liquid and formation of a keyhole. In order to mitigate the possibility of keyhole-induced defects, the beam speed v must be modified such that ηq_0 results in a shallow, distributed melt pool which extends 2-3 layers beneath powder.

This interpretation does not appear to be unique to electron beam processing either. For comparison, in an EOSINT M280 Laser Powder Bed Fusion (L-PBF) system, the FWHM is approximately $60\mu m$, with the maximum power is 400W. During the melting of Inconel 718 powder, a PPD of 72 kW mm^{-2} was used, but keyhole formation is suppressed using v= 960mm s^{-1}, resulting in a peak fluence of q_0= 4.6 J mm^{-2}.[97] In another example, a custom built L-PBF system had a FWHM= $30\mu m$ and P=42W, resulting in a p_0= 39 kW mm^{-2}, yet the process parameters that gave good quality builds in Ti64 required a q_0= 6.4 J mm^{-2}.[100]

2.6 Effects of Beam Optics

In the following section, the effect of various beam components will be examined for both EBW and EB-PBF, using examples taken from the literature.

2.6.1 Focus Coils

The ability to dynamically change the focal position can strongly influence the properties of the liquid melt via σ and the corresponding p_0 and q_0 parameters. When combined with the variable beam power, dynamic electron beam focussing offers the ability to control both the shape of weld bead, as well as the depth of the fusion zone. This section will first begin by looking at the effects of beam focus on electron beam welding, before examining the effects on EB-PBF.

As previously discussed, the properties of the electron beam are defined by the FWHM and the angle of convergence. During conduction-mode welding, the convergence angle does not play a significant role compared to the FWHM.

During keyhole EBW, the peak fluence, Peak Power Density (PPD) and beam convergence angle will significantly impact the depth of penetration, with small angles producing a deep and narrow fusion zone and large convergence angles producing more concave-shaped keyholes.[101] The convergence angle is a first order function of the accelerating voltage and working distance, and affects how the beam interacts with the leading edge of the keyhole. This interaction, and the resulting vapor pressure forces,

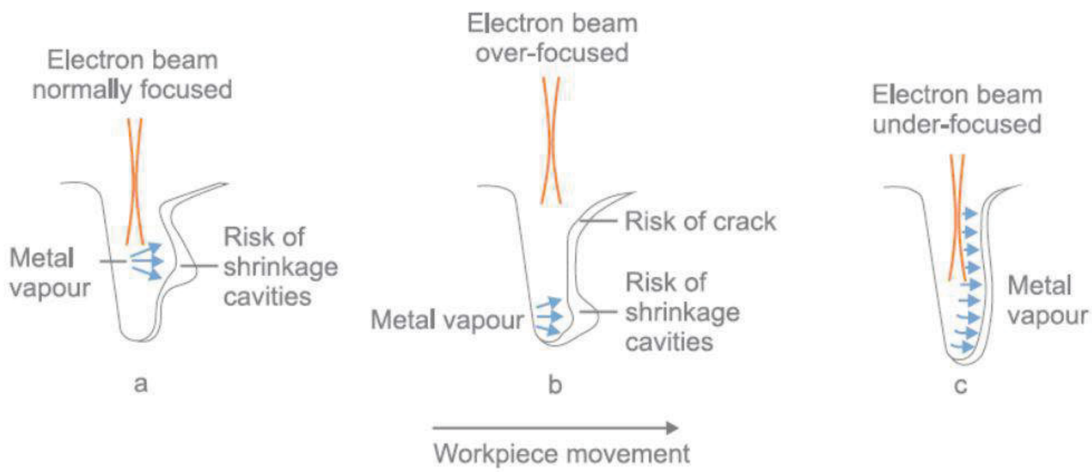

Figure 2–26: The effect of crossover position during keyhole EBW.[52] In this image, 'normally focussed' refers to the previously discussed sharp-focus condition. Image provided with permission, courtesy of pro-beam

have been shown to play a dramatic effect on the convective melt flows, and thus weld penetration depth.[102, 101]

Because of the complex interactions during keyhole-mode welding, the position of the beam cross-over with respect to the workpiece will also affect the quality of the weld, with the effects of sharp, over and under-focussed electron beams shown in Fig. 2–26.

The prevailing theory surrounding focus position and keyhole defects is that localized vaporization of the leading edge of the keyhole creates a dynamic pressure on the trailing edge of the keyhole liquid. This dynamic pressure can induce keyhole oscillations, which leads to variations in penetration depth along the weld, commonly referred to as root spiking.[36, 1] If the molten metal along the trailing edge collapses into keyhole base, this can lead to periodic porosity along the weld.[103, 102] Finite element models have shown that an under focussed beam uniformly heats the leading edge of the keyhole, thus stabilizing the local vapor recoil gradients and the keyhole.[101]

The focus setting sensitivity to keyhole defects is significantly reduced if full penetration welds can be performed.[52, 103] If not possible, careful experimentation of travel speed, focus setting, acceleration voltage and working distance are needed to generate a stable, defect-free keyhole welds.[1]

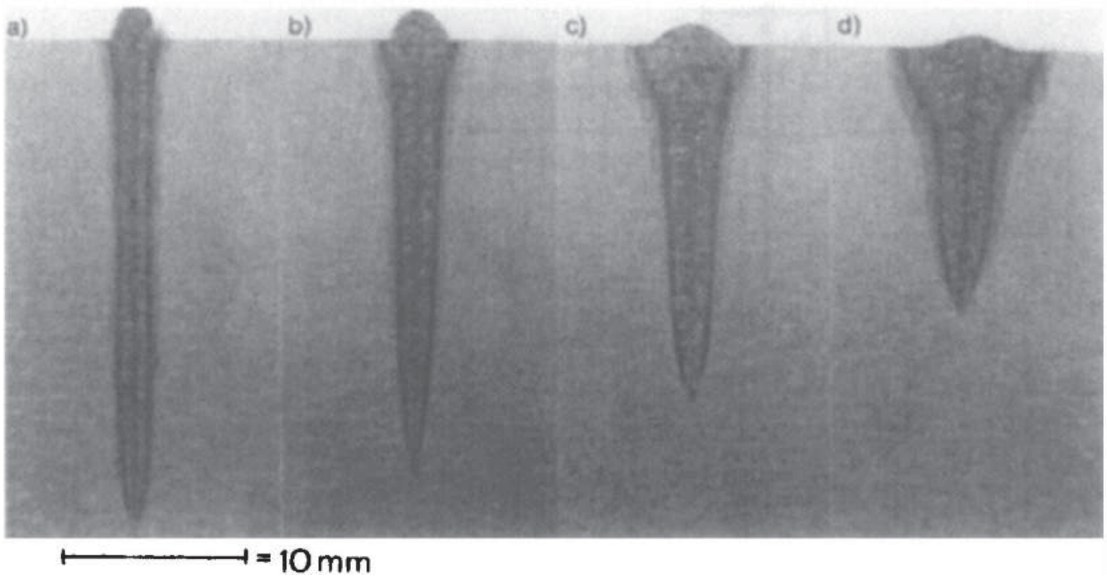

Figure 2–27: Effect of accelerating voltage and image plane distance during keyhole EBW.[1] Image plane distance, z_i, is defined as distance between workpiece surface and focus coil center, as shown in Fig.2–17. All welds were conducted with 5kW of incident power. Welds a) and b) were conducted at z_i= 350mm, with V_{acc}= 150kV and 60kV, respectively. Welds c) and d) were conducted at z_i= 1200mm, with V_{acc}= 150kV and 60kV. Material unknown and travel speed unknown.

Another feature related to beam focus and convergence angle is the shape of the keyhole. Although collimated keyhole welds give a narrow FZ and Heat Affected Zone (HAZ), the partially ionized plasma at the surface of the workpiece, combined with the Marangoni convection within the keyhole, gives a characteristic 'nail-head' FZ shape.[104] The curvature under the nailhead, combined with the thermal contraction stress during solidification, promotes microfissures in materials prone to hot-cracking.[104] To a certain degree, the curvature under the nail head can be controlled by modifying the optics in order to control how the beam interacts with the partially-ionized plasma and keyhole leading edge.[23, 101] This effect is demonstrated by the 5kW welds of Fig. 2–27, which show optimized FZ profiles for different combinations of V_{acc} and work distance.

Another example of using the beam focus to control the weldment quality is during rotating, circumferential welds. If a fixed focus value is used, the beginning of the weld will have a hump of re-solidified material, while the weld end will have a material crater. This response is a function of the Marangoni-convection, and more fully discussed in

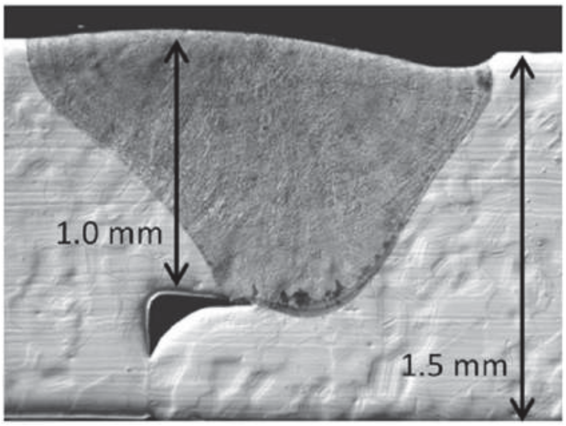

(a)

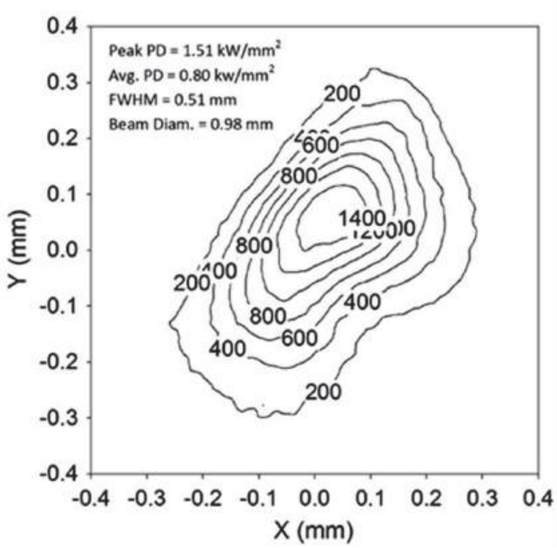

(b)

Figure 2–28: Conduction mode EBW of Nitronic 40 in overfocussed condition, using Hamilton Standard 605 electron beam welder with ribbon cathode. Left: WZ cross section Right: power density map of 605W (110kV/5.5mA) in overfocussed condition (+29-32mA from sharp focus)[105]. The welds were performed at v=25.4 mm s^{-1} with a FWHM=0.51mm, resulting in an incident centerline energy of q_0= 44.8 J mm^{-2}

Sec. 2.6.2. To solve this issue, the focus coil current is linearly ramped from very defocussed to optimum setting at the beginning of the weld, and the reverse is applied during the weld end. This creates a variable q_0 along the weld, and minimizes these transient defects.[1]

In another example, workers at Lawrence Livermore National Labs investigated conduction-mode EBW of Nitronic 40 stainless steel.[105] An interesting feature of this work was the precise characterization of the beam power density using the Enhanced Modified Faraday Cup, with a power density map shown in Fig. 2–28.

These 605W (110kV/5.5mA) welds were performed in the over focussed condition (+29-32mA from sharp focus), which resulted in an asymmetric power density distribution, shown in Fig.2–28b, which has a maximum value of 1.5 kW mm^{-2} and q_0= 44.8 J mm^{-2}. Although the orientation of the beam and weld axes were not specified, it is interesting to note the asymmetric profile of the weld crown, which shows an undercut of $\approx 50\mu m$. Although this asymmetry could be a result of step-joint configuration, it is expected that the power density of Fig.2–28b results in asymmetric Marangoni convection.

As a final note, this alloy has a nominal composition of Fe-21 wt%Cr - 6 wt% Ni - 9 wt% Mn, whereby the nominal Mn content is 4 times greater, and the N content is 3 times greater than 304 stainless steel. Greater amounts of high vapor pressure of Mn and the volatile N results in a material which keyholes easily, therefore, these experiments used Nitronic 40 with a reduced nitrogen level to improve weld stability.[106]

In the Arcam EB-PBF process, the process parameters are restricted in order to minimize the likelihood of keyhole formation.[99, 107] Specifically, the beam power and travel speed are coupled such that the process operates in the distributed source regime, $q_0 < 10$ J mm^{-2}. The Arcam control algorithms do not permit users to select the absolute value of the focus coil current, instead, the user selects a Focus Offset (FO), which references a look-up table based on previous calibrations.[108, 109] Within this scheme, a positive focus offset(FO) implies the over-focussed condition while a negative FO implies under-focussed condition.[108, 110]

Similar to how a sharp-focussed beam does not yield optimum weld quality during keyhole EBW, using a FO= 0mA does not imply an optimized EB-PBF part. A nice demonstration of this effect was recently made by Beraud *et al.* while optimizing the fabrication of vertical struts using an Arcam A1 system.[110] To calibrate the machine, a series of thin, vertical walls were printed with fixed travel speeds and beam currents, and variable FO between [-3:3:30]mA. The effective thickness of each wall was measured with the results plotted in Fig.2–29a. *Authors note: In the above example, [-3:3:30]mA represents a vector of values from -3mA to 30mA in 3mA increments, ie <-3, 0, 3,...,24, 27, 30>mA*

From these results, a FO =+7mA resulted in the minimum wall thickness and inverse heat transfer modelling was used to estimate the beam diameter to be $450\mu m$. The model parameters were then used to develop an optimal scanning strategy for building the vertical struts, resulting in substantially increased the strut size accuracy.[110] This empirical approach must be conducted for each combination of powder, layer thickness, beam current and travel speed. Also, it is not clear how this approach will be affected by cathode drift and cathode-to-cathode variations, features which are known to affect the weld quality during EBW.[23, 111]

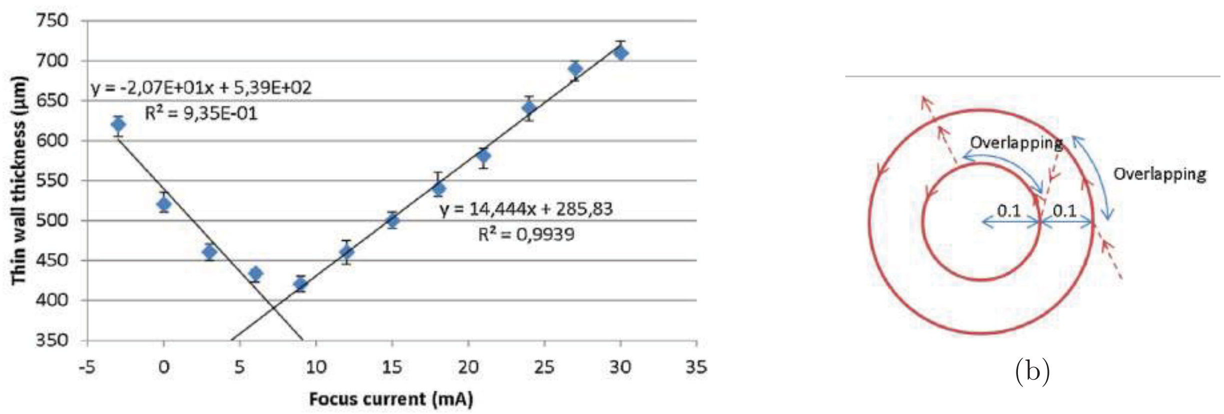

(a)

(b)

Figure 2–29: Optimization of focus setting and deflection pattern for the generation of vertical struts using EB-PBF.[110] Beam parameters were fixed at v = 1400 mm/s, V_{acc}=60kV and I_b=5mA, giving peak fluence of q_0 ≈=1.1 J mm^{-2}, with a build table translation Δz = 50μm/layer. Left: The effect of focus offset on the printing of thin Ti64 walls. Right: Concentric, circular deflection pattern used to build vertical struts with optimized focus settings (r_{inner}= 0.272mm and r_{outer}= 0.372 mm)

In another example, Gong *et al* built 10mm cubes using an Arcam S400 system with nominal build parameters, varying the FO [+4:4:24]mA and examining the part porosity using the Archimedes method.[107] From Fig. 2–30a, porosity increased significantly for focus offsets greater than 16mA. Surface roughness in the xy plane was observed to increase significantly at higher FO, which is likely a combination of melt pool discontinuities, lack of melt pool overlap and powder spreading instability resulting from the larger σ and the smaller q_0.[107]

Tammas-Williams *et al* conducted a detailed study of generalized defects during EB-PBF using an Arcam S12 system and X-ray Computed Tomography.[112] They found that focus offset had a very substantial effect on the volume fraction of pores and determined that FO between 6 and 12mA was optimal for the machine input parameters of I_b= 5.7mA, hatch spacing h=0.2mm and v_{begin}= 324mm/s. Safdar *et al* found some correlation between $x - z$ surface roughness and FO using an Arcam S12, but it is not clear whether the q_0 was adjusted to compensate for the enlarged FHWM.[113]

A recent 2017 publication from Oak Ridge National Labs showed the relationship between beam diameter and defect formation when printing Ti64 using an Arcam A2x

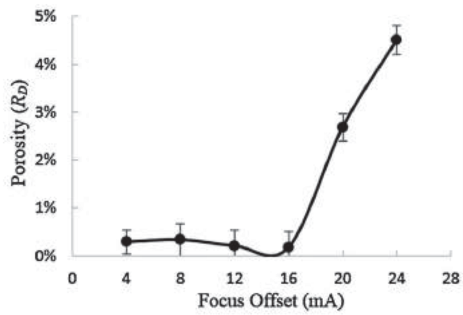

(a)

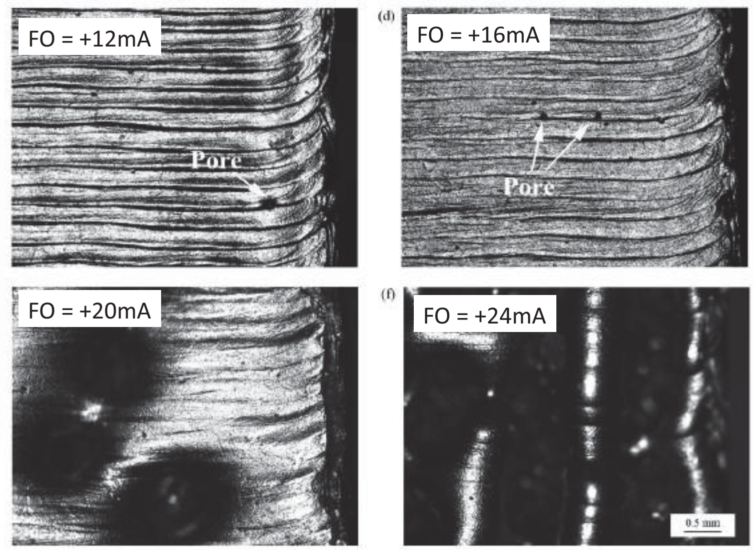

(b)

Figure 2–30: Porosity as a function of focus offset for Ti64 on Arcam S400 with $\Delta z = 50\mu$m/layer[107]. Left: Porosity of cubes as a function of focus offset. Right: Surface roughness as a function of focus offset

system with 50μm layers and a 0.2mm hatch spacing.[45] The work focussed on so-called 'chimney pores', which initiate along the sides of the part and grow upwards along the build direction over hundreds of layers. Using focus offset/FWHM tables provided by Arcam, the authors unequivocally demonstrated that chimney pores nucleate and propagate for a FWHM$>$ 400μm and are eliminated for FWHM$<$300μm, corresponding to peak fluence of q_0= 0.38 and 0.51 J mm^{-2}, respectively.

In a recent paper from Carnegie Mellon demonstrated the ability to control the local microstructure of Ti64 cubes built with an Arcam S12 by modifying the speed function and the focus offset in a controlled manner. Specifically, high SF/low FO was used in areas of refined microstructure, while low SF/high FO offset was used in areas of coarse microstructure.[114] Using a travel speed of v= 49 mm s^{-1} and a 360W beam (60kV/6mA), Al Bermani varied the FO from [-50:10:50]mA during beam on plate welds of Ti64, showing that the maximum depth of penetration occurred at FO=10mA.[108]

Although FO refers to the nominal offset of the focus coil current, it should be noted that the relationship between focus offset and beam current is non linear. As was previously discussed, the perveance of the beam increases with beam current, implying that high current beams will suffer from more space-charge effects. As will be shown, this results in a reduced depth-of-field for high current beam, with the implication that a suitable FO range for low beam currents will be compressed compared to higher beam currents.

Alignment Coil

One of the most important prerequisites for accurate EBW is a properly-aligned electron beam. Generally speaking, a properly aligned beam refers to having the axis of the beam align with the magnetic axis of the focus coil.[52] If not properly aligned, a change in the focus setting will shift the center of beam spot. This aberration can be understood since a misaligned beam will not enter a radially symmetric focussing field, resulting in focal lengths which vary over the beam cross-section.[37]

A misaligned beam causes issues during EBW joint alignment since often, a focussed low-power beam is used to determine the beam position relative to the joint using a boroscope.[1, 36] With this mechanical alignment in place, the part is fused by increasing the beam current and focus setting. If misaligned, the high current beam may miss the fraying surfaces, and it is easy to see why beam alignment becomes increasingly important for high power, high aspect-ratio keyhole welds. This effect will be demonstrated experimentally with dissimilar EBW of Nb-Ti joints.

In the EB-PBF process, spherical aberrations will cause errors in the part dimensions, as well as defects within the part. In the Arcam systems, an auto-calibration routine based on a 2D array of Faraday Cups, as well as in-situ recalibration, is performed.[115]

In both cases, automatic beam alignment is based on a target with well defined geometric dimensions. A sensor capable of detecting a signal associated with the reflected back-scattered electrons, or associated X-rays is also needed. By modifying the beam alignment and focus setting, the detected signal can be used to determine whether the beam is more or less aligned with respect to the expected signal output.[52, 115]

2.6.2 Deflection-based Processing of Solids

The ability to magnetically deflect an electron beam represents a useful capability during EBW and a necessary component of EB-PBF. Having described the principle and challenges of magnetic deflection in Sec. 2.3.1, and the heat transfer implications via q_0,

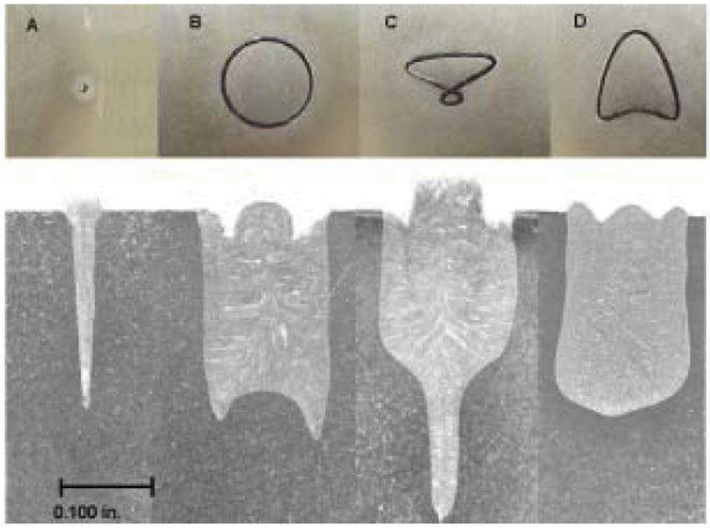

Figure 2–31: Deflection pattern and resulting fusion zone shape during electron beam welding.[116] Image provide courtesy of PTR-Precision Technologies, Inc. Enfield, CT

this section will examine the capabilities enabled by electron beam deflection. The section begins with a discussion about beam deflection during conventional EBW, followed by an introduction to the multi-beam EBW process. Some examples of electron beam surface modification using areal scanning patterns will also be introduced. This section concludes with a review of beam deflection during EB-PBF, and the associated challenges and opportunities.

Conventional EBW:. In most EBW systems, the workpiece is translated relative to the fixed electron beam column such that the fraying surfaces are coincident with the optical axis of the beam.[1] Using the deflection coils, a deflection pattern can be repeatedly scanned over the workpiece as it moves under the column. The purpose of the deflection patterns is to modify the effective power density of the beam and the resulting liquid convection currents. This capability makes it possible to join materials normally unsuitable for welding.[23] The concept of beam-deflection applied to conventional EBW is demonstrated in Fig.2–31, which show the fusion zone shape as a function of deflection pattern.

Panel A of Fig. 2–31 shows the characteristic high aspect ratio keyhole weld formed with a static beam. In panel B, the circular deflection pattern shown in the top row dramatically changes the FZ shape. Unlike the Gaussian distributed power density of the static beam, which has the peak power density at $y = 0$, the pattern in panel B results in an effective power density defined by the shape of the deflection pattern. Specifically, the circular deflection pattern increases the FZ area, and also results in protrusions at the bottom of the FZ. The fact that the depth of these protrusions are not equal can be understood considering that the beam is moving with or against the longitudinal axis at the edges of the circle pattern. Assuming the workpiece was moving into the plane of the paper, the pattern is assumed to move in a counter-clockwise direction, since the keyhole moves from the hot trailing edge of the fusion zone towards the right, resulting in a deeper penetration compared to the colder leading edge pattern on the left.

The FZ associated with deflection pattern in panel C represents a hybrid between panels A and B. Specifically, the smaller segment of the figure 8 deflection pattern concentrates the power density near the $y = 0$ axis, resulting in a deep keyhole. The larger segment of the figure 8 pattern results in a greater power density distribution and a wider FZ. Finally, the scallop shape of pattern D does not concentrate as much energy on the outer edges of the pattern as does Panel B, resulting in reduced undercut and no FZ protrusion.

Periodic beam deflection is a useful method to control the EBW process, as it opens many new processing capabilities. A larger liquid pool allows gas porosity to rise and escape from the weld pool and also relaxes the joint fit-up requirements.[1] Generally, the longitudinal component of the deflection pattern increases the FZ depth, while the transverse component increases the FZ width. Transverse deflection stabilizes through-thickness welds, thus opening the welding process window. Similarly, circular patterns increase the keyhole diameter, suppressing the likelihood of root spiking and keyhole porosity. Parabolic oscillation similar to panel D in Fig. 2–31 minimizes undercutting along the weld crown. Finally, deflection frequencies less than 25 Hz are capable of moving the keyhole within the liquid metal, while deflection frequencies greater than 25 Hz expand the keyhole diameter. These frequencies are process-specific, but demonstrate how deflection affects the convective heat transfer and evaporation within the FZ. [1]

Beam deflection is also useful for controlling the microstructure of the weld zone. Beam oscillation is believed to have reduced segregation of Inconel 718 welds by promoting fragmentation of the solidifying dendrites, which then act as inoculants within the local melt pool.[117] Similarly, it was found that the churning action induced by 2mm/600Hz circular beam oscillation during EBW of Ti64 improved the mechanical properties of the weldment, due to the enhanced melt pool convection and homogenized heat extraction.[118]

Multi-Beam EBW:. The previous examples demonstrated conventional, low frequency deflection applied to EBW (f_{def} < 1kHz). Deflection systems capable of magnetically coupling to the beam at frequencies as high as 100kHz has enabled many new electron beam processing technologies. The first such industrial system was detailed in Sec. 2.4.1, and was used for surface processing of transformation-hardening steels and annealing silicon wafers using areal scanning patterns.[22, 119, 76, 60]

Using advanced digital waveform generators, it is possible to multiplex the beam between multiple, concurrent operations. This capability is related to the fact that the time constants associated with heat conduction are generally much longer than the time constant associated with the amplifier/coil system.[62] The beam is therefore capable of jumping between multiple locations without significant conduction losses during the 'beam off' cycle. In one of the simplest applications, fast deflection can be used to perform radial welds of gear assemblies using multiple weld pools, as shown in Fig. 2–32. The motivation for multi-pool welding is that it generates a more symmetric heat input, which reduces the asymmetric weld shrinkage and thus the overall gearbox noise levels.[52, 120]

In the example shown in Fig. 2–32b, the fraying surfaces of the radial weld are defined by:

$$[x(s), y(s)] = r[cos(2\pi s), sin(2\pi s)] \tag{2.45}$$

where r[mm] is the radius of the weld, and s is the parameteric variable which defines the contour of the weld, and has a value between [0...1]. Using conventional, single pool welding, the deflection waveforms needed to fuse the components is:

$$[x(t), y(t)] = V(r)[cos(2\pi f_{def} t), sin(2\pi f_{def} t)] \tag{2.46}$$

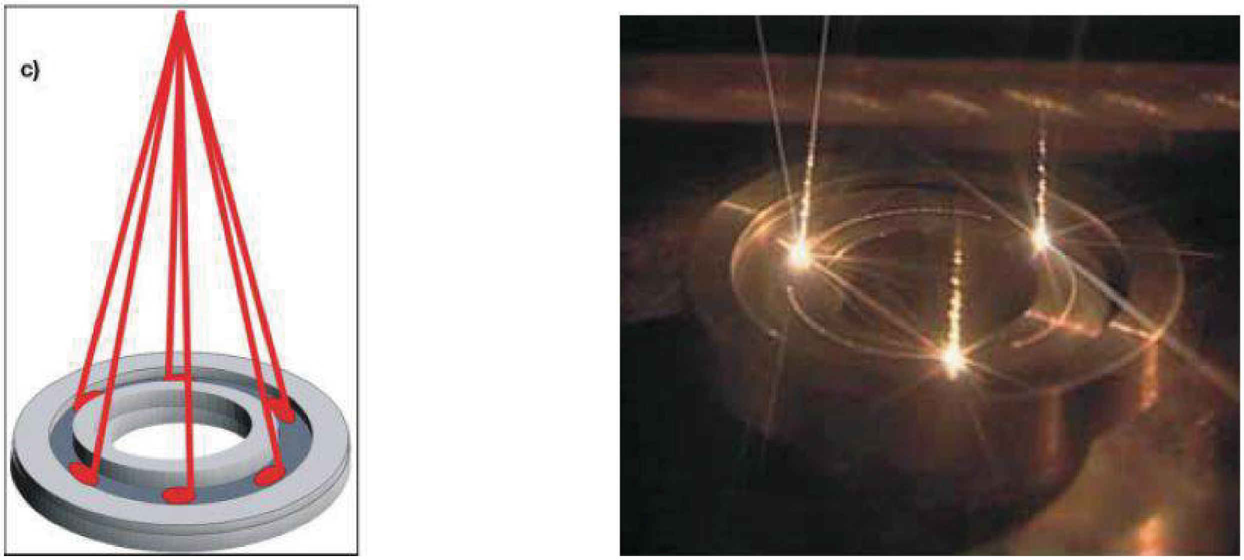

(a) (b)

Figure 2–32: Multi-beam welding of gear assemblies: Left: Schematic showing 6 concurrent melt pools. Right: Image shown multi-pool welding of gear assembly using 3 concurrent weld pools. Image provided with permission, courtesy of pro-beam [121]

where f_{def} is the deflection frequency and $V(r)$ is the voltage amplitude needed to match the weld radius for a given deflection coils, accelerating voltage and WD. In this case, we see that s has been substituted by $f_{def}t$. By inspection, the corresponding travel speed of this weld is $v = 2\pi r f_{def}$.

If the beam is equally multiplexed between 3 weld pools, the deflection waveforms are modified by a phase term $\phi(t)$ such that:

$$[x(t), y(t)] = V(r)[cos(2\pi f_{def}t + \phi(t)), sin(2\pi f_{def}t + \phi(t))] \tag{2.47}$$

where $\phi(t)$[rads] is the 3-step staircase waveform which oscillates the phase between 0, $\pi/3$ and $2\pi/3$, as shown in Fig. 2–33a. The corresponding phase-modulated $x(t)$ waveform is shown in Fig. 2–33b.

Although it appears that Fig. 2–33b represents 3 distinct sinusoids, the waveform is in fact a single waveform jumping between different phase values. While the speed of each individual weld pool is maintained at $v = 2\pi r f_{def}$, the deflection pattern is truncated to avoid overlapping welds. To maintain the fluence of each individual weld pool, the

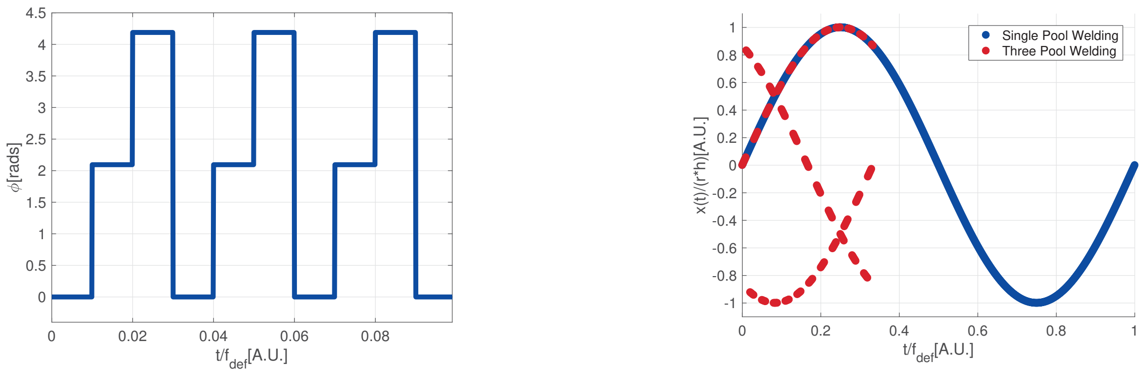

(a)

(b)

Figure 2–33: Multi-pool welding using deflection waveform modulation. Left: $\phi(t)$ phase signal used to multiplex between 3 concurrent waveforms. Right: $x(t)$ waveforms for single pool and multipool welding

net beam power must be increased by a factor of 3, with a corresponding increase in productivity.

This simple example demonstrates a key concept of multi-beam processing: the 'off' period of the beam must be smaller than the characteristic time scales of heat transport, $L^2/4\alpha$.

In another example, fast beam deflection combined with mechanical workpiece translation can be used to perform concurrent heat-treatment and welding processes, as shown in Fig. 2–34. In this case, the beam is multiplexed between different locations, where the duty cycles and deflection patterns are modified according to the subprocess requirements. Using a diffuse deflection pattern ahead of the weld pool will preheat the workpiece, and can help alleviate cold cracks. Using a similar pattern behind the weld pool will reduce the thermal gradients during solidification and suppress quenched microstructures like martensite and hot-cracking defects.[23, 40, 52, 120] Multi-keyhole processes have shown some promise in alleviating porosity associated with welded cast-iron and die-cast aluminium structures and also assisted in the welding of dissimilar materials.[122] In all case, the ability to digitally control the time and location of the beam during welding enables unconventional heating and cooling profiles.

Fu *et al* investigated the formation of crack-free welds of a near-α Ti-Al-Sn-Zr alloy using multi-beam EBW. [40, 120] Using computer modelling, they found that the duty

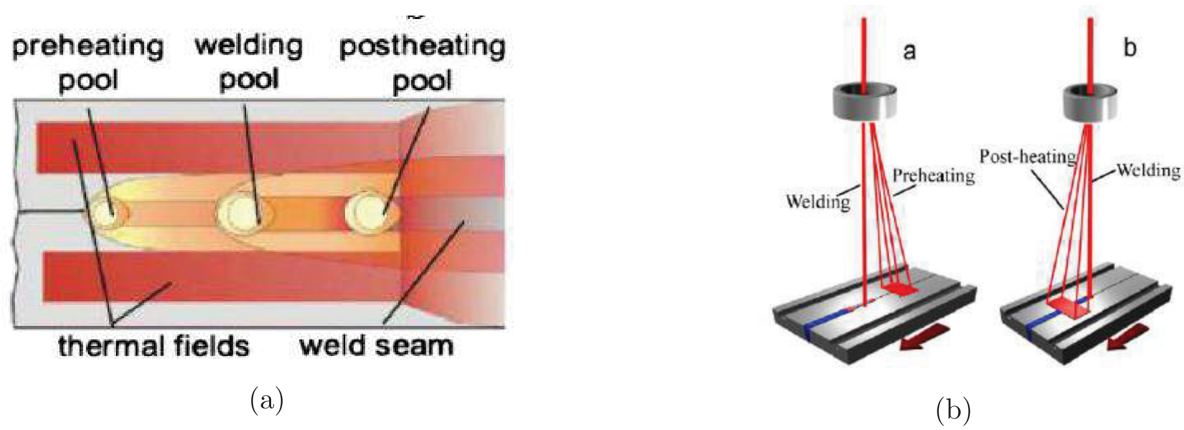

Figure 2–34: Multi beam welding with pre and post heating. Reduced undercut with a post-heat treatment, and time multiplex of beam[40]

cycle between heat treatment(pre/post) and welding was a critical process parameter, with two separate heating processes shown in Fig. 2–34b. The larger net heat input resulted in coarser microstructure compared to conventional EBW, while the post-weld heat treatment resulted in a weld crown which did not have an undercut. A group at Pern University in Russia recently demonstrated multi-keyhole EBW of an Al-Mg alloy.[122] In this study, it was determined that the charge input into each keyhole played an important role in stabilizing the process.

Electron Beam Surface Texturing:. Another interesting application of digitally controlled beam deflection is the Surfi-Sculpt^{TM} process invented by TWI.[123, 124] Shown in Fig. 2–35, the process controllably displaces molten material using a series of beam 'swipes', making high-aspect ratio surface features called 'proggles', up to 2mm in height. It is believed that the surface features are formed by a combination of vapor recoil forces and Marangoni convection along the swipe path. By carefully controlling the beam velocity and repetition rate, a liquid film is formed along the swipe path. According to Eq.2.29, reducing the velocity at the end of the swipe increases the local fluence, resulting in shallow keyhole. This keyhole induces the liquid film to flow *against* the travel direction, effectively digging-out surface features. As previously discussed, wide-angle deflection increases the beam aberrations and results in slightly irregular proggles compared with those produced at the centre.[123]

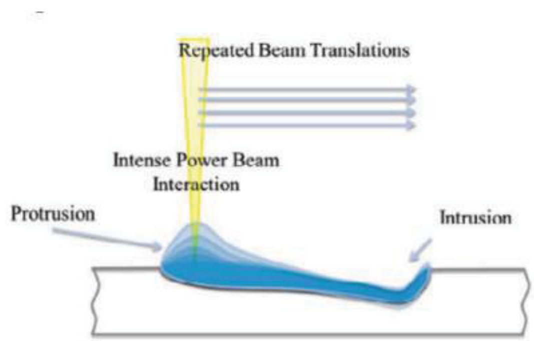

(a)

(b)

Figure 2–35: Surfi-Sculpt Left: Schematic demonstrating the combined vapor recoil and Marangoni fluid flow against the swipe direction. Right: A Surfi-Sculpt protrusion, or 'proggles' grown at an angle to the substrate [123, 124]

The first application of Surfi-Sculpt was to improve the quality of titanium/carbon-fiber joints by combining the advantages of adhesive bonding and mechanically fastened joints. Surfi-Sculpt composite joints have demonstrated an ultimate failure load increase of over 70% compared to similar bonded joints. This is believed to be due to the additional energy required to break the mechanical interlocking between the composite and the proggles. [125, 123]

Areal Scanning and Surface Processing. Fast deflection coils can be used to rapidly heat large surface areas in a process called areal scanning. In the simplest case, a sawtooth waveform is rapidly deflected along the transverse direction, while the workpiece slowly stepped along the longitudinal direction. An example of bi-directional areal scanning is shown in Fig.2–36a, with the corresponding $[x(t), y(t)]$ waveforms shown in Fig. 2–37b.

From Fig.2–37b, we can see that beam speed, and thus the local fluence, is determined by the transverse scanning pattern direction, ie (dy/dt). The spacing between line scans is determined by the longitudinal x waveform. In order to have a roughly uniform fluence over the areal pattern, the longitudinal spacing should be some fraction of the transverse beam FWHM. Compared to deflection-based EBW, areal scanning is defined by a high-aspect ratio deflection patterns, which is longer along the transverse direction.

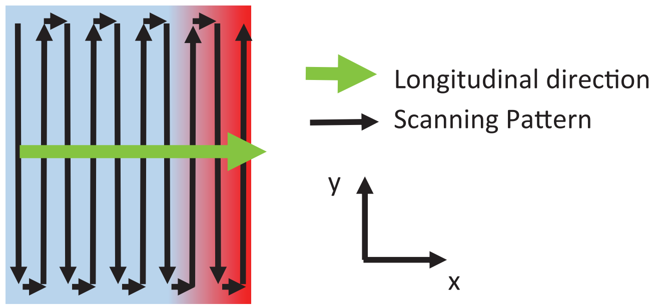

(a)

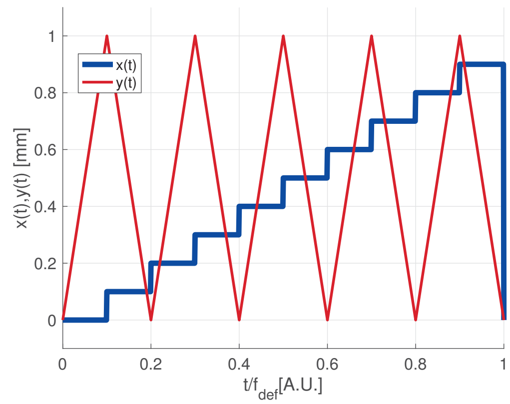

(b)

Figure 2–36: Areal scanning using bi-directional scan patterns. Left: Scan pattern on workpiece Right: $[x(t), y(t)$ waveforms used to generated deflection pattern

As suggested by the color gradient in Fig. 2–36a, areal scanning results in two orthogonal coordinate axes: one which follows the beam ($\pm y$), and another which corresponds to the longitudinal scan direction($+x$).

Areal electron beam scanning can be used to selectively modify surface properties by controlling the heating and cooling rates of the materials. In the case of large net heat inputs and slow transverse motion, the workpiece heating and cooling rates are relatively low, resulting in an annealing process. In one application, work hardened austenitic stainless steel orthopedic implants were locally annealed at the thin membrane sections. After insertion into the patient, the annealed membranes can be hydroformed to the outer mold of the patients bone.[39]

Similar to the multi-pool welding example, areal scanning patterns can be multiplexed between various positions, resulting in the multi-beam areal processing, as shown in the multi-beam surface annealing example of Fig. 2–37.

If the local heating rates are increased, and the part has sufficient thermal mass, the material will self-quench at rates as high as 10^4-10^5 K s^{-1}.[39] This enables the possibility of transformation hardening steels by selecting beam parameters which heat the surface above the austenitizing temperature but below the melting temperature. The result is a hard, martensitic case with minimal changes in surface finish. A similar concept can

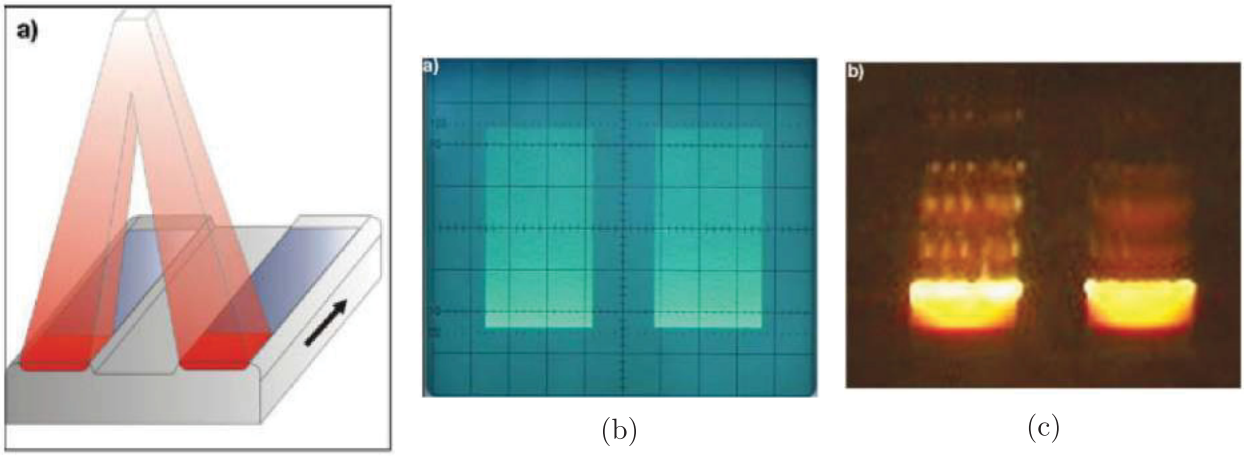

(b) (c)

(a)

Figure 2–37: Surface Annealing of strip steel using fast deflection.[121] Left: Schematic diagram of surface annealing with transverse beam deflection. Center: XY oscilloscope pattern of deflection signal with extended persist. Right: Image of multiplexed deflection pattern for local electron beam annealing

be used to harden components which have been nitrided, with an example of selectively hardened cam shafts shown in Fig. 2–38.

Surface remelting of ion nitrided steel surfaces was demonstrated using a 3kW beam with a beam FWHM= 0.5mm and a longitudinal translation speed of 5-50 mm s^{-1}. [126, 127] The beam was deflected at 10kHz over distance of 14mm, resulting in a nominal transverse beam speed of $v = d * f$= 140 m s^{-1} and a longitudinal fluence of q_0= 4-40J mm^{-2}. The hardness of the base material was 250HV, while the nitrided layer was roughly 615HV. After areal scanning, the surface hardness of the nitrided layer increased to 850HV. This increase was attributed to dispersion of nitrogen, martensite induced by rapid-cooling and grain refinement. After processing, the wear resistance was improved by a factor of 3 compared to the base material.

These examples demonstrate that by selecting the appropriate beam parameters, the resulting thermal response can be used for annealing, hardening, or surface remelting. Application areas include surface processing camshafts, sawblades, valve seats, orthopedic implants and combustion engine cylinder heads.[121, 76, 60, 52]

Electron Beam Powder Cladding:. A precursor to the Arcam EB-PBF technology is electron beam cladding process developed by Morimoto using an in-vacua powder

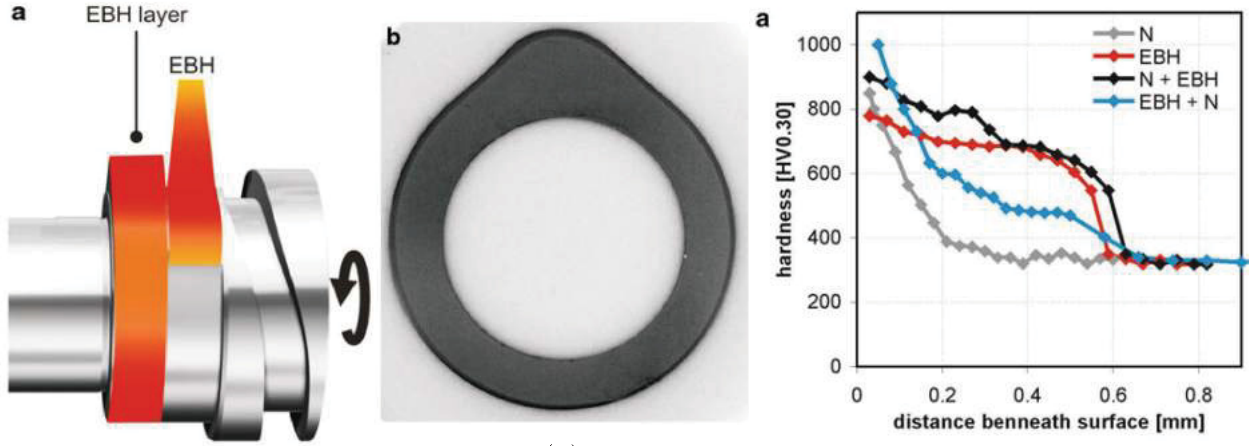

(a) (b) (c)

Figure 2–38: Combined surface nitriding and electron beam surface hardening[39]. Left: Processing geometry of selective hardening. Center: Cross section of hardened cam contour. Right: Surface hardness modification after nitriding(N), electron beam hardening(EBH), N + EBH and EBH + N

dispenser. This process involves the continuous distribution of powder in front of an electron beam which melts and bonds the powder to the substrate, as shown in Fig. 2–39.

Because of the in-vacua deposition and melting, electron beam cladding reduces oxidation and coating porosity.[23] This technique has been used to improve wear and corrosion resistance, with some results showing a tenfold increase in coating hardness compared to the substrate. Layer thicknesses between 50-800μm have been deposited with Ni-based self-fluxing alloy power, Cr_2C_3 and WC-Co powders, with surface hardness as high as 1400HV. [128, 129, 130]

The schematic in Fig. 2–39a merits a quick note because of the similarity to PBF processes. Specifically, a sawtooth waveform is used to deflect the beam transversely to the cladding direction, resulting in a wide bidirectional scan pattern. In some instances, copper blocks were positioned at the pattern turning points, a consideration which will be discussed in later sections. Considering the high transverse speed relative to the longitudinal speed (750 vs 5 mm s^{-1}), we can assume that the 1kW beam is uniformly distributed over the transverse direction. One can calculate nominal fluence to be $q_0 = P/(v * L) = 13$ J mm^{-2}, where L is the transverse scan distance of 15mm.

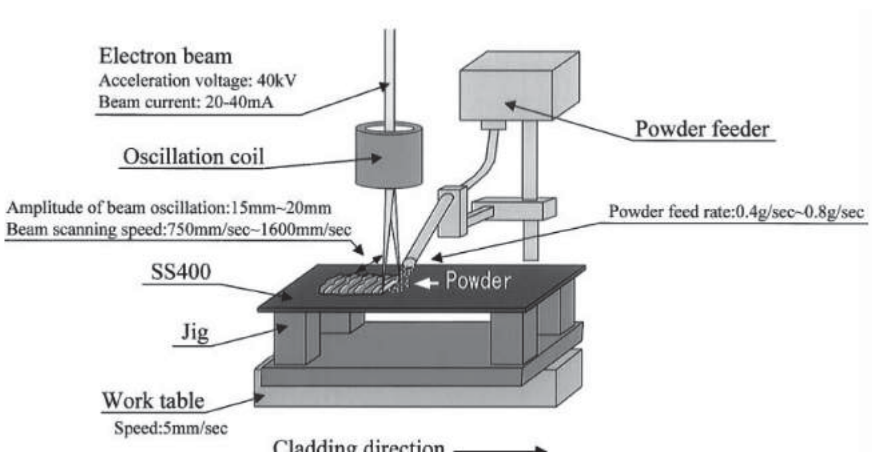

(a)

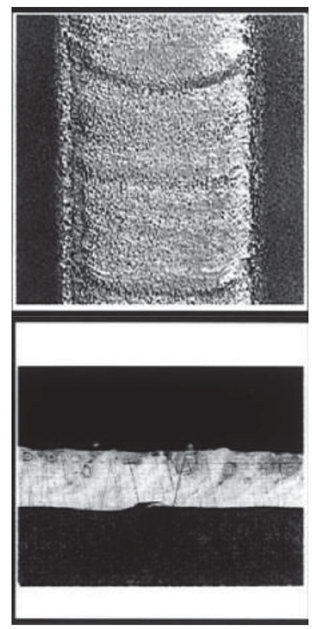

(b)

Figure 2–39: Electron beam powder cladding Left: Schematic of in-vacua powder feeder, electron beam, and worktable capable of powder feed rates of 0.4-0.8[g s^{-1}]. Right: Clad track of Ni-based self-fluxing alloy deposited v= 5 mm^{-1}, P= 1kW, transverse deflection of 15mm with 0.4 g s^{-1} feed rate [128]

Although techniques such as pulsed laser and induction hardening can result in similar surface modifications, the ability to rapidly and selectively heat the component surface with fast-deflection is unique to the electron beam deflection coils. But similar to the EB-PBF process, the net energy input can be sufficiently high to cause the entire part to be heated to high temperatures, thus diminishing the desired fast cooling rates. For thermal surface treatment, careful consideration must be given to the thermal time constant, the process time constants and the thermal mass of the component. Optimized processes require application specific instrumentation and heat sinking/isolation.[121]

2.6.3 Deflection-based Processing of Powders

The preceding sections introduced the concepts of deflection-based welding and areal scanning of solids, which form the basis for the EB-PBF process. In the case of 'fast' processes with high beam PPD, it was shown that the isotherms are largely dictated by the beam dimensions. Thus the peak absorbed fluence, which is proportional to $1/\sigma$, largely determines the threshold between heating and melting. The 'fast' condition, defined by the $\sigma^* > 0.1$, easily extends to powder, which has a reduced effective thermal diffusivity compared to the solid counterpart.[131, 132]

Within the context of adiabatic heating, the dimensionless parameter γ_m is useful for analyzing electron beam powder sintering and melting, and was previously defined as the peak absorbed energy per unit area(ηq_0), divided by the melting enthalpy per unit area(δh_m):

$$\gamma_m = \eta \frac{q_0}{\delta h_m} = \eta \frac{V_{acc} I_b}{\sqrt{2\pi}\sigma_y v} * \frac{1}{\Phi t_l \rho (H_m - H_0)} \tag{2.48}$$

where t_l is the powder layer thickness, Φ is the powder packing density, ρ is the density at temperature T_0, and $H_m - H_0$ is the enthalpy increase from initial temperature T_0 to melting temperature. The advantage of dimensionless parameters like γ_m is that the combined form highlights first-order relationships of specific process parameters, thus simplifying the system analysis of processes such as EB-PBF.[86]

If the powder raking has reached steady state, the build table displacement (z_B) is equal to the effective layer thickness(Φt_l) due to the consolidation effect.[133] For reference, a Ti64 process at 700^{o}C with z_B= 0.05 mm results in δh_m= 0.22 J mm^{-2} , while a matching 1000^{o}C Inconel 718 process gives δh_m= 0.17 J mm^{-2}.

Because of variable heat transport properties and initial temperatures, the γ_m parameter is a useful reference point for distinguishing between powder heating ($\gamma_m < 1$) and powder melting ($\gamma_m > 1$). As will be shown, the EB-PBF melting processes generally requires $\gamma_m \approx 5$ to give a melting depth which results strong interlayer adhesion and reduced inter-track porosity.[107] This can be understood since γ_m=1 implies that only the beam centerline will melt through the powder, resulting in a theoretical track width of 0.

With this parameter in mind, the 2D powder bed process can be subdivided in 3 distinct components:[134]

1. `Preheat`: Powder sintering with $\gamma_m < 1$ and $v \approx$ 10,000 mm s^{-1}
    - `Preheat1`: Sinter entire powder bed
    - `Preheat2`: Additional sintering of powder above 2D slice
2. `Melt`: Powder Melting with $\gamma_m > 1$
    - `Contour`: Single track weld of contour of 2D slice, $v \approx$ 100 mm s^{-1}
    - `Hatch`: Areal scanning of inner body of 2D slice $v \approx$ 1,000 mm s^{-1}
3. `Postheat`: Heating build surface with $\gamma_m << 1$ and $v \approx$ 10,000 mm s^{-1}

The velocities presented above represent order of magnitude estimates taken from literature. For comparison, the maximum 'jump' speed in a ProX200 L-PBF system is 5,000 mm s^{-1}. [135] The above process omitted the optional `Support Melt` step, as this is outside the scope of this dissertation. [136, 137, 134] *Authors note: the* `Courier` *font will be used throughout this dissertation to distinguish specific processes.*

Preheat

`Preheat` raises the temperature of the powder with the purpose of forming a cake of lightly sintered powder, which we refer to as contact sintering. The as-deposited powder is first subjected to `Preheat1`, based on a repeating areal scan pattern which covers the nearly the entire build platform, making the powder 'jump safe'.[138, 78] The `Preheat2` pattern heats the powder within 5mm of the 2D part slice, resulting in powder which is 'melt safe'.[112] The distinction between both patterns is shown in Fig. 2–40.

By contact sintering the powder using a combination of low γ_m, high v and repeated scans, `Preheat` provides two main outcomes. First, the powder cake provides a degree

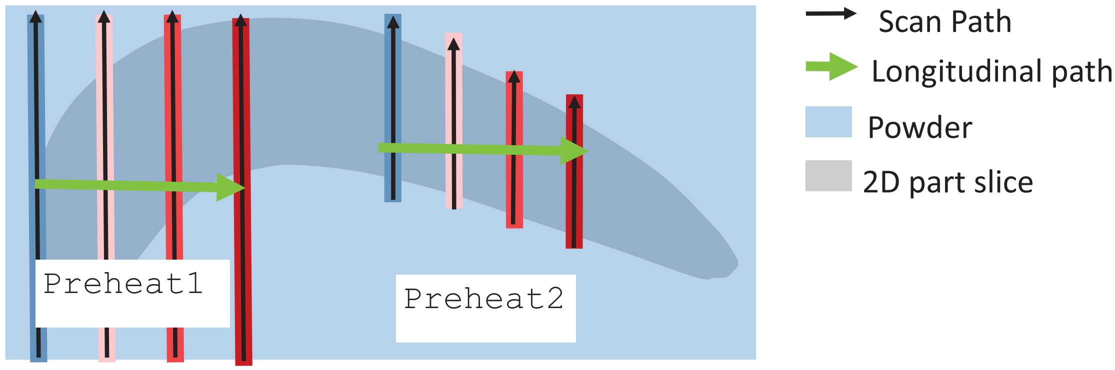

Figure 2–40: Schematic diagram of scan paths used during `Preheat1` and `Preheat2`

mechanical strength within the bed, reducing the need for support structures and enabling so called 'negative' or overhanging surfaces.[131]

Contact sintering the powder also prevents the deleterious phenomenon referred to as powder smoke. As a beam of charged particles, an electron beam locally deposits both energy (q_0) and charge ($j_0 = q_0/V_{acc}$) into the powder. If a large electrical resistance separates the powder from electrical ground, the powder capacitively charges with a corresponding RC time constant. According to Gauss's law, this charge generates an electrostatic field around the particle. If the powder is free flowing and the amount of absorbed charge exceeds a critical threshold, electrostatic repulsion forces between particles can exceed the force of gravity, resulting in powder which literally jumps off the build surface. The prevailing theory is that sintering reduces the powder resistivity, thus reducing the RC time constant. The implication is that once contact sintered, the rate of charge dissipation, $\propto exp(-t/RC)$ exceeds the rate of charge deposition, $\propto I_b$, enabling the powder to be subsequently fused with a high current beam.[137]

From these two examples, we can understand the double meaning of the term contact sintering, in that it refers to powder which has formed point-like neck contacts between powder particles for mechanical support, as well as electrical contact with ground, to suppress powder charging.

The effective RC constant can also be reduced by continually admitting a small flow of He gas into the build chamber to maintain a pressure of roughly 2E-3 mbar.[108] As previously discussed, the ionization process creates thermalized positive He ions by the primary and secondary electrons. Depending on the space charge distribution along the beam and bed, these ions can be drawn towards the negatively charged powder particles, neutralizing both. This ionization process offers an alternate current return path. The ions will also neutralize some of the space charge of the beam, while the effects on beam focusing are unclear.

The beam parameters used during `Preheat` must provide sufficient heat to raise and sustain the powder temperature to achieve a low level of sintering, while also remaining below the critical threshold for powder smoke. By sintering the entire build surface, `Preheat1` prevents the spurious charging of the build surface, which would otherwise introduce electrostatic aberrations into the beam. Also, powder subjected only to `Preheat1` will be recovered after the build completion. Therefore it is important to not over-sinter the powder, as this will limit it's recyclability.[131] According to a recent report, the standard `Preheat1` parameters for Ti64 are a 1.8kW beam (60kV/30mA), FO= 50mA and a v= 14,600 mm s^{-1}, with each section of powder scanned 4 times. Assuming a FWHM equal to the line spacing (1.2mm), this results in an incident peak fluence of q_0= 0.10 J mm^{-2}, a dwell time of τ= 80μs and a peak surface charge density of 1.6 μC mm^{-2}. Estimating γ_m is difficult since the low thermal diffusivity of the powder implies a retention of heat and increasing T_0 with scan number. Also, the absorptivity, η of unmelted powder is currently unknown. Using emissivity corrected IR measurements, Rodriguez *et al* determined that the initial mean temperature of the Ti64 powder after raking was approximately 400^{o}C.[24]. Thus, one can calculate δh_m to be equal to 0.27, 0.22 and 0.14 J mm^{-2} at 400^{o}C, 700^{o}C and 1200^{o}C, respectively. Assuming an η= 1, the corresponding γ_m values are 0.37, 0.45 and 0.70.

Experimentally, Drescher *et al* varied the factory recommended Ti64 parameters for `Preheat2` using an Arcam A1.[78] With a 2.2kW (60kV/38mA) beam and a FO= +62mA, the scanning speed was varied between v=[8.6: 1: 14.6]m s^{-1}. Assuming a FWHM equal to the scan line spacing(1.2mm) these process parameters imply a q_0 between 0.11-0.18 J mm^{-2} and τ= 80-130μs. Assuming η= 1 and T_0= 700^oC, the corresponding γ_m values were between 0.5-0.8, with γ_m=0.8 showing localized powder melting. The compressive strength of the cake increased with q_0 from 4 to 16 MPa. The corresponding surface charge density can be calculated from q_0/V_{acc} to be between 1.6-2.8 μC mm^{-2}. Interestingly, powder smoke was observed for $q_0/V_{acc} = 2.8$ μC mm^{-2}, despite maintaining the factory recommended `Preheat1` parameters.

In a similar study, Smith *et al* maintained the nominal `Preheat1` and `Preheat2` parameters, but linearly increased the scans repetitions during `Preheat2` from [0: 1: 8], which corresponds to a net increase in incident energy.[131] While the packing density of the sintered powder only varied between Φ= 0.49-0.56, the z-axis thermal diffusivity increased by over 200% with increasing scan repetitions. Post-sintering laser-flash analysis showed that the highest powder thermal diffusivity measured of the powder cake was α= 1.1 mm s^{-1}, which was about 1/5 that of solid Ti64. This can be understood since the thermal diffusivity is related to sinter state, and powder sinters with increasing time and temperature, i.e. scan repetitions. Also, for scan repetitions greater than 4, local powder melting was observed at what was assumed to be the beam centerline. This finding is consistent with the concept of γ_m, as the initial powder temperature increases with scan number, resulting in a reduced δh_m.

Algardh *et al* demonstrated the ability to sinter 25-45 μm Ti64 by modifying the standard preheat process parameters as follows: FO was decreased from 35mA to 10mA and beam speed was increased from 14,700 to 22,000 mm s^{-1}. The beam current I_b was ramped from 5-25mA and the number of repetitions was increased to 15. Although no reference was given to the original parameters, these results demonstrate that by decreasing the surface charge density via v and I_b, and extending the `Preheat` time and temperature, powder that is normally unstable with respect to smoke can be fused with the charged electron beam.

Mahale *et al* demonstrated the ability to sinter pure lunar regolith simulant, an oxide with extremely low electrically conductivity, by ball-milling the powder with electrically conductive Al powder. Interestingly, it was observed that smoke-free sintering could be achieved if the accelerating voltage was reduced from 60 to 15kV.[132] In another study, plasma-atomized Ti64 powder exposed to atmosphere at 500^{o}C/4h became unstable due to the excessive powder smoking using standard process parameters.[139] The role of nitrides versus oxides on the smoking behaviour was not investigated.

The above examples demonstrate that the `Preheat` parameters must be carefully tuned to the powder, operating between the boundaries of smoke-free sintering and no localized powder melting (γ_m <1). This requirement is met using low peak fluence and repetitive scanning in order to achieve the required time and temperature for sintering. In order to not over-sinter the powder, considerations of how the incident heat is transported out of the powder is required. Conceptually, these issues are not dissimilar to electron beam hardening, whereby process parameters are required which control the time and temperature of the transformation-hardenable solid, at both the local and bulk levels.

Because of the similarities to `Preheat1`, the `Postheat` processing step will be described. Since the EB-PBF process occurs at hold temperatures above 25^{o}C, heat will be transferred from the hot build surface to the surrounding atmosphere. Although the vacuum build environment suppresses convective heat transfer, heat is conducted from the build plate to atmosphere(Q_c), and radiated from the build surface to the heat shields,(Q_{rad}). Using calibrated IR and thermocouples measurements, Rodriguez calculated the mean radiant temperature of the heat shield enclosure to be 342^{o}C when using standard operating parameters for Ti64. The mean radiant temperature is defined as the equivalent isothermal temperature of a cavity surrounding the 700^{o}C build surface, assuming the cavity is opaque, diffuse, and gray.[24]

In order to sustain a high holding temperature, `Postheat` applies a large areal scan pattern similar to `Preheat`, with the purpose of maintaining the energy balance between heat input ($Q_b = \bar{P}t$) and heat loss ($Q_{rad} + Q_{cond}$). To minimize the temperature fluctuations during melting, a `Postheat` step can be applied at any time within the processing cycle.[134] At the completion of a layer melting process, additional energy is deposited onto the build surface, such that the heat lost over the 2D melting process is compensated by the mean energy input during the process. This concept is shown in the schematic plot of Fig. 2–41

Contour

After completing the `Preheat` process, the `Contour` melting process begins, whereby the electron beam is steered along an offset contour of the 2D slice, as shown in Fig. 2–42.

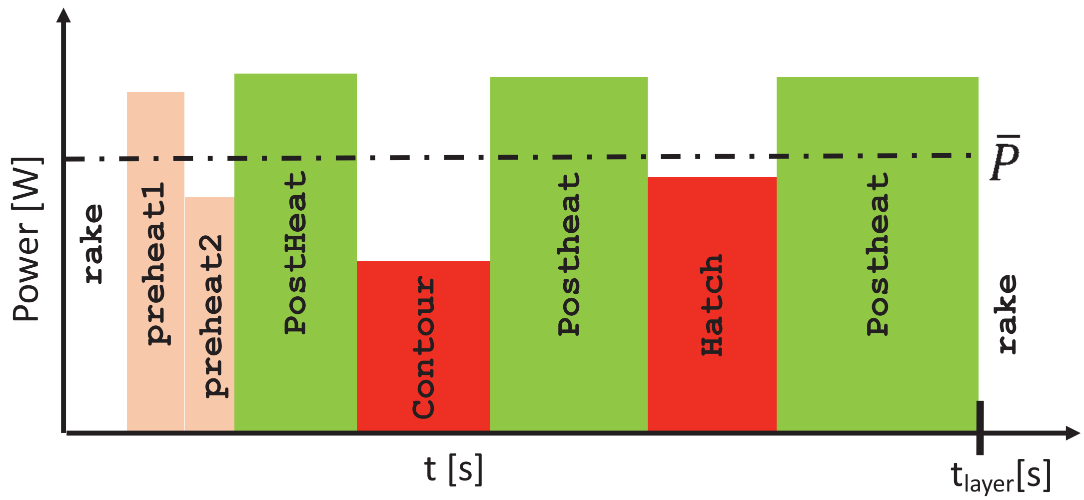

Figure 2–41: Schematic diagram demonstrating `PostHeat` energy balance. Upon completion of the layer melting process, and final `PostHeat` step is added such that $\bar{P}t_{layer}$ balances the corresponding heat loss due to conduction and radiation

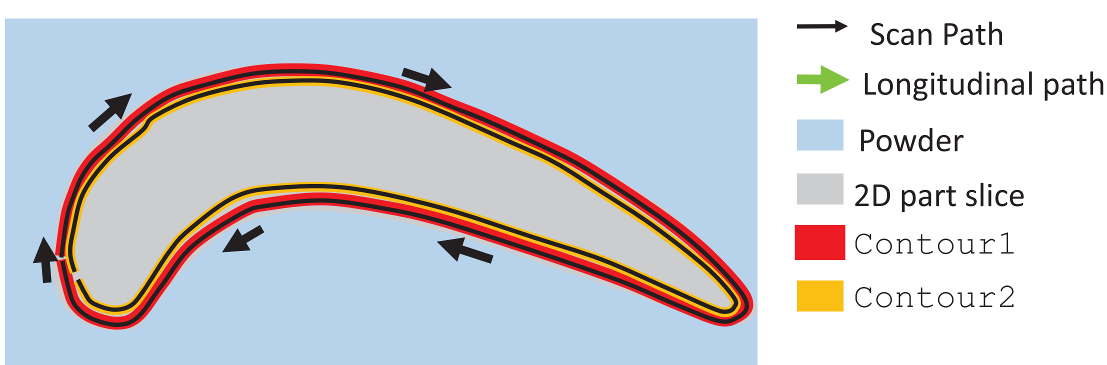

Figure 2–42: Schematic diagram of scan paths used during `Contour Melt`

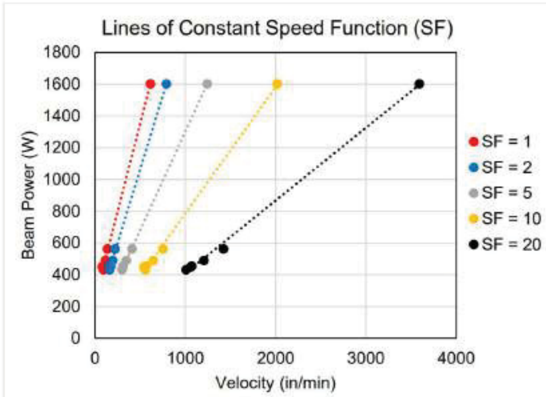

(a)

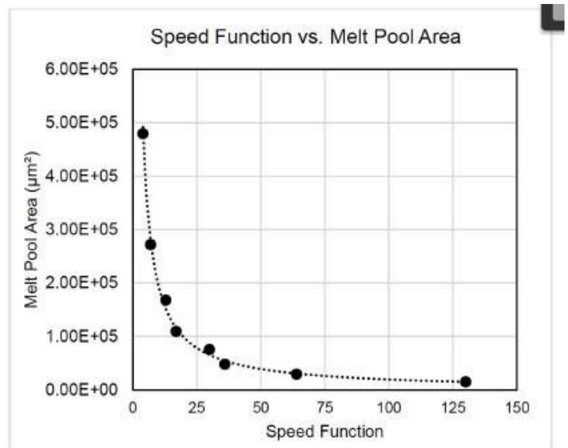

(b)

Figure 2–43: Left: Velocity/Beam power mapping for different speed function settings. Right: Speed function versus melt pool cross sectional area for bead-on-plate single pass welds on Ti64 at 750^{o}C using an Arcam S12 system[114]. Beam current was varied between 6-34 mA and SF between 4-130

The `Contour` process is similar to deflection-based EBW, with the relevant parameters being power, focus setting and translation speed. In the case of the Arcam process, the accelerating voltage is fixed, therefore power is regulated by variations in beam current.

As previously discussed, a high power density beam is desirable for PBF because of the gains in productivity and resolution. Unfortunately, higher power densities can result in keyhole formation if the fluence is not kept below a certain threshold. In the Arcam system, keyholing is prevented by restricting the available current/speed combinations using proprietary algorithms.[107] These algorithms can be modified via a single parameter called the Speed Function (SF), which has a range between -10 to 200. The purpose of the SF is to modulate the beam travel speed based on the requested current, powder layer depth and overall build height.[132, 140, 114] An exemplary plot of the power/speed combinations as a function of SF is shown in Fig. 2–43a.

It is believed that for different power/speed combinations, the SF parameter attempts to maintain a constant melt pool geometry throughout the build process. [132, 114] In 2011, Al Bermani demonstrated that at a fixed beam power of 420W (60kV/7mA) with a FO= 22mA in an Arcam S12, the melt track width of solid Ti64 welds decreased from

0.88mm to 0.55 mm as the SF was varied over [5: 0.5: 11].[108] In 2017, single bead-on-plate welds were performed on solid Ti64 at 750^{o}C in an Arcam S12 system that support this finding.[114] Specifically, the relationship between SF and melt pool cross section area is shown in Fig. 2–43b, showing good agreement over a range of beam currents. In both studies, it was also observed that the melt pool became shallower with increasing SF, a result consistent the concept of Marangoni convection spreading the heat over the surface, instead of allowing the heat to penetrate the material.

In either EB-PBF or L-PBF, performing two offset curvilinear contours melts is recommended. This process creates melt overlap between the contours, as well as overlap between the `Contour` and `Hatch`, mitigating the potential for lack of fusion defects.[112, 141, 134] Compared to single track welds, the overlap between melt tracks changes the wetting and thermal conduction conditions of the melt pool.[107, 97]

Similar to the multi-pool EBW example, Arcam has developed a MultiBeam^{TM} EB-PBF process, whereby the beam is multiplexed between melt pools using the fast deflection capabilities. The motivation for this technology relates to beam utilization. Specifically, an increase the beam power requires a corresponding increase in travel speed to remain below the keyhole threshold. But with increasing speed comes increasing Marangoni convection, making the pool shallow and wide. The implication is that to obtain a uniform, continuous weld bead for a given FWHM, there exists a maximum travel speed. By multiplexing the beam between multiple, slow moving melt pools, MultiBeam^{TM} increases beam utilization without loss of melt quality.[18]

The application of the MultiBeam^{TM} technique is similar to the previous gear welding example, whereby the curvilinear contour is first described by a parametric equation, $[x(s), y(s)]$, where s varies between [0...1]. By applying a staircase waveform to the phase of the parametric contour, $[x(s + \phi), y(s + \phi)]$, and ensuring that the period of the jumps is much shorter than the solidification time($\approx 1mS$)[82], the deflection pattern will jump between multiple, concurrent melt pools. This technique is similar to pulsed welding, and has been used to control the microstructure of Inconel 718 builds.[142]

Figure 2–44: Schematic diagram of scan paths used during `Hatch` melt with longitudinal path along $+x$ direction, and hatch spacing h_s

The accessible process parameters during MultiBeam^{TM} melting are beam current, FO, number of spots, spot time and spot overlap.[143] In one study, Wang *et al* parametrically varied the spot melting parameters and found that the spot parameters(the number of spots, spot time and overlap) had a greater effect on the surface roughness of Ti64 parts compared to FO and I_b. In terms of surface roughness, the optimized process parameters were measured to be 40 spots, 0.4 ms for spot time, 0.6 mm for spot overlap, FO= 3 mA and I_b= 4 mA, resulting in an $Ra = 27\mu$m.

Hatch

After completing the contour melts, the 2D melting process proceeds to the `Hatch` melting step, whereby the beam is scanned in a straight line using end-points defined by the inner section of the 2D slice, generally beginning and ending on previous contour melts. Once a single line has been completed, the beam is stepped one hatch distance, h_s along the longitudinal hatch direction. If bi-directional scanning is used, the beam then moves in the opposite direction, whereas in uni-directional scanning, the beam returns to the opposite end of the path and repeats the scan. The more common bi-directional `Hatch` process is schematically shown in Fig. 2–44.

It is important to note from Fig. 2–44, the longitudinal beam direction is the $\pm y$ axis, whereas the longitudinal hatch direction is along the $+x$ axis. Compared to the contour melting, the scan paths associated with `Hatch` melting are more closely spaced in both

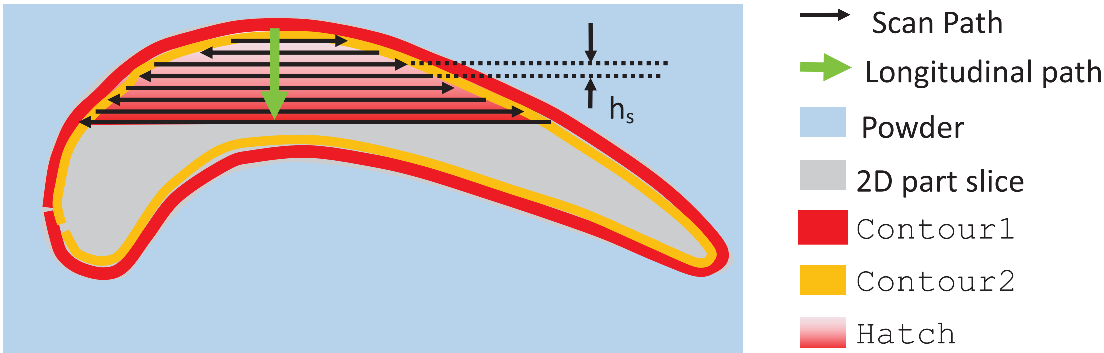

Figure 2–45: Schematic diagram of scan paths used during `Hatch` melt with longitudinal path along $-y$ direction, and hatch spacing h_s

time and space. Depending on the thermal diffusivity, local geometry and preheat temperature, the heat from adjacent hatch lines can interact, raising the local T_0 and reducing δh_m.[136] For bi-directional patterns, this heat interaction will be most pronounced at the turning points and algorithms are employed which increase the beam speed as it exits the turning point.[144] To first order, this algorithm can be understood as reducing q_0 and maintaining a constant γ_m. The process parameters for this effect are controlled via a parameter called the Turning Function.[112]

Another issue surrounding the `Hatch` process is the orientation of the 2D slice relative to the longitudinal hatch direction. As a specific example, consider Fig. 2–45, which shows the same part geometry and a rotated hatch direction.

Rotation of longitudinal hatch directions is common in both electron and laser beam PBF process, as it mitigates the possibility of interlayer defect propagation. [145, 100] But compared to Fig. 2–44, hatching along the $-y$ direction results in more variability in the transverse scan length. This implies that the scan path begins at a high T_0 after exiting the turning point and proceeds into progressively cooler powder. In the Arcam process, algorithms also adjust the beam current and speed (q_0) according to the length of the scan line. [144, 134]

Variable T_0 issues are not as pronounced in laser-based PBF processes, as the holding temperatures are lower, resulting in larger thermal gradients which rapidly draw out the heat from interacting scan lines.[136] Recent modeling work showed that for EB-PBF of Inconel 718 at 1000^{o}C, the effect of interacting lines scans had a significant effect on the resulting part microstructure. In this case, nominal scan velocities of 3,000 mm s^{-1} were used along 2.5mm and 5mm squares with h_s= 0.2mm. It was demonstrated that the resulting liquid solidification velocity was not determined by beam speed, but was more closely related to the longitudinal scan velocity, which was 240 and 120 mm s^1 for the 2.5 and 5mm squares, respectively. These part level effects highlight a key challenge associated with numerical PBF modelling. [136, 97]

The reduced thermal gradients associated with high speed hatching also affect the surface quality of the solidified material, since the reduced longitudinal thermal gradients reduce Marangoni convection.[145]

In a landmark study, Tammas-Williams *et al* demonstrated the effect of `Hatch` parameters on part defects, finding strong correlations between pore distributions, beam scanning strategies, and beam control parameters.[112] One particularly interesting finding was the concentration of pores at the ends of hatch scan paths, suggesting the ability to coalesce and steer porosity with scanning strategy.

In another example, Dehoff *et al* investigated the effects of `Hatch` parameters on the microstructure using both continous and spot melting hatch strategies on Inconel 718. As previously stated, the 1000^{o}C, z_b= 50μm process parameters lead to a δh_m= 0.17 J mm^{-2}. For the proposed beam parameters, γ_m was calculated to be 3.1 over a range of beam currents and travel speeds.[142] In a related study, Cordero *et al* studied the effects of defect generation during EB-PBF of Ti64, with a δh_m= 0.22 J mm^{-2} and a γ_m between 2.5 and 12.2.[45] As a final example, Zah et al conducted a study of EB-PBF of 316L stainless steel using a modified probeam electron beam welding unit.[146] With 316L stainless steel powder with a z_b=100 μm and a preheat temperature of 1080^{o}C, the corresponding $\delta h_m = 0.39$ J mm^{-2}. A 100kV beam was used to conduct a parametric study with I_b=[0.3: 0.3 :1.8]mA and v= [25:25:100] mm s^{-1}, resulting in a range of γ_m= [0.9... 23]. Fully density cubes were built using a $4 < \gamma_m < 10$.

2.7 Summary

This chapter serves as a broad overview of the fundamental science and technology surrounding thermal electron beam processing, which was divided into 3 parts. In the first portion, details surrounding electron beam optics were discussed. The key components of an electron gun were presented, and the dual role of the bias electrode in regulating the beam power and the electron trajectory was demonstrated. The concept of beam brightness was then introduced as a means to characterize the quality of an electron beam. One key feature is that beam brightness is optimized for a range of operating conditions, and will be significantly reduced when operating outside the design window. The effect of various beam parameters such as cathode material, accelerating voltage, space-charge and lens aberrations was discussed with respect brightness. How to focus an electron beam was then presented within the context of the thin-lens equation, and sharp focus was explicitly defined as imaging the virtual gun cross-over onto the workpiece. The idea of demagnification demonstrated one of the challenges associated with maintaining a large working distance and a small spot size, further highlighting the importance of beam brightness. A key message from this portion of the review is that focussing and deflecting an electron beam depends on the beam current, working distance and accelerating voltage, an issue which will re-emerge when examining the custom-built process compiler.

Next, the dominant heat transfer mechanisms were analyzed within the context of Peak Power Density (PPD) and peak fluence. How these process parameters affect Marangoni convection and vapor recoil pressure was examined using published examples of conduction mode and keyhole mode heat transfer modelling. The point-source, distributed source and line source heat models were presented and the applicability of these models was explained within the context of p_0 and q_0. This section demonstrated that although having a high net power and small spot size is desirable for PBF applications, these characteristics can also induce undesirable keyhole formation. Thus, careful selection of the beam speed must be made so that the fluence remains below the threshold for keyhole formation.

In the final section, literature surrounding EB-PBF and EBW was reviewed with respect to specific electron beam process parameters. The role of focus setting was discussed for both keyhole mode welding and EB-PBF. Deflection processing was presented, and examples of how beam deflection can be used to modify the effective p_0 during EBW were presented.

The concept of a multiplexed electron beam was explained with the gear welding example, and additional examples of cladding, Surfi-Sculpt^{TM} and areal surface processing were given. Following these solid material examples, the specific sub-process surrounding Electron Beam Powder Bed Fusion (EB-PBF) was explained with respect to the dimensionless γ_m parameter. Relevant examples of from the literature were provided, outlining the unique challenges of melting powder with a beam of charged particles in a vacuum.

Overall, the purpose of this chapter was to familiarize the reader with the specific details of electron beam technology. Similarly, through a series of published examples, the chapter demonstrated that electron beam additive manufacturing is simply the digital extension of the long established electron beam welding process, with the main distinctions being electrostatic powder charging, and high holding temperatures.

CHAPTER 3
Methods: Electron Beam Instrumentation, Fixturing and Calibration

3.1 Introduction

This chapter reviews four systems developed in support of this dissertation. The first system concerns a Faraday Cup (FC) signal processing workflow, which is used to quantify the incident power density at the workplane. Next, Thermocouple (TC) instrumentation is outlined, including a discussion of welding of dissimilar metal TC junctions and noise suppression. Two variants of workpiece fixturing are then detailed, enabling experiments at variable working distances, incidence angles and holding temperatures. A brief overview of single powder layer deposition and quantification is also presented. In the final section, a custom-built software architecture, capable of generating calibrated machine commands is given. This section also includes an overview of how the software is calibrated for each experimental process. In all cases, examples demonstrating the capabilities of each system are given, highlighting the specific design challenges.

It should be noted that all the components and software were conceived, designed and developed solely by the author. The only exceptions are the Faraday Cup, which was provided by PAVAC Industries, and the single layer powder height measurements, which were conducted with support from Basel Alchikh-Sulaiman.

3.2 Faraday Cup Measurements

Process control during EBW is based on monitoring machine settings such as accelerating voltage(V_{acc}), beam current (I_b), focus coil current (w_b), and vacuum level. Unfortunately, these settings alone cannot determine the p_0 and q_0 of the beam, as no real-time knowledge of the beam distribution parameter, σ, is provided. The beam distribution parameter can be indirectly probed by conducting bead-on plate welds at different focus coil currents (w_b) and examining the resulting fusion zone, but this method is both costly and time-consuming. Arata's AB method, which utilizes an inclined, periodic workpiece, is one such example.[46] Once a set of satisfactory process parameters are identified,

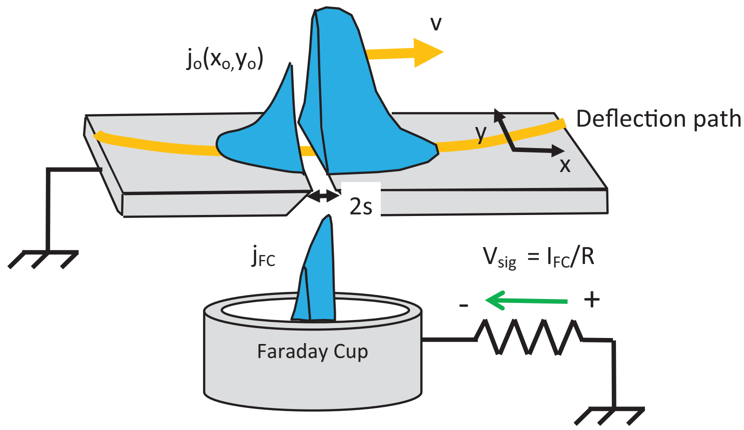

Figure 3–1: Schematic Diagram of Faraday Cup for measuring current density of electron beam

the focus of the electron beam is indirectly controlled by the operator by performing a visual sharp-focus test prior to beginning a weld. This approach is strictly qualitative and depends heavily on operator experience.[23, 111] Even for highly experienced operators, it was determined in one instance that p_0 varied as much as 7% over the course of an 18 month production run, highlighting the need for direct, in-situ, beam characterization techniques.[43]

A Faraday Cup (FC) is the oldest and the simplest device for charge measurement, consisting of a conducting metal cup that collects the incident beam electrons. By grounding the FC with a known resistor, a voltage drop V_{FC}, can be measured and the absorbed beam current can be determined from Ohm's law $I_{FC} = V_{FC}/R$. To characterize the local charge density of the beam, j_0, the top of the Faraday cup is fabricated from a refractory metal with a known gap width, $2s$. By connecting this top plate to ground, only a small slice of the beam distribution is admitted to the FC, as shown in Fig. 3–1.

By translating the beam across the gap such that $j_0(x_0, y_0) = j_0(vt, 0)$, Fig. 3–1 demonstrates that the slotted FC will sample slices of the longitudinal current density profile, σ_x, and cannot distinguish any information about the transverse beam width, σ_y. To solve this problem, one can rotate the axis of the slot with respect to the beam, in order to probe the 2D current density.[43] Another solution is to raster the beam over a small hole.[42] Thus, Faraday Cup measurements non-destructively characterize the current density, and thus power density of the beam, as $p_0 = V_{acc}j_0$. These measurements are useful for transferring welding parameters between machines as well as maintaining quality during a production run.[50, 111] In one example, it was shown that the beam p_0 and FWHM could be controlled to within 2.5% over the course of 90 production welds using pre-weld FC measurements. This value was well within the 5% tolerance band suggested by ASME Boiler and Pressure Vessel code.[111]

Researchers at the Tomsk State University have demonstrated the ability to characterize the beam FWHM by rotating tungsten wires of known diameter into the beam path and measuring the absorbed current. By vertically translating these wires along the optical axis, it was possible to measure the beam convergence angle and brightness.[147] Although rotating wires have less heat absorbing capacity, it is believed that this configuration minimizes the effect of ionization, which can impact the charge measurements.[42]

Arcam has developed an alternative beam characterization method based on the XQAM X-ray sensor. Specifically, the beam is automatically scanned over an array of tungsten crosses positioned over the build surface. By comparing the measured and expected X-ray signal, it is possible to precisely characterize the beam position, speed and focus.[18, 115, 148, 149] Using these values, any measured deviations can be corrected in software.

The slot, wire, pinhole or XQAM beam characterization techniques are based on the precisely dimensioned targets with characteristic lengths which are smaller than the beam FWHM. The signal that is generated from this known geometry can be used to deconvolute the effective beam distribution parameters and thus directly or indirectly calculate the beam distribution parameter, σ. In the following section, the crossed slot technique developed at McGill will be presented.

3.2.1 Signal Acquisition and Processing

The Faraday Cup employed at McGill is based on a 2mm thick tungsten plate, which has been electro-discharge machined with 5 radial slots of width $2s = 0.5mm$. The Faraday Cup installed at a WD=240mm within the McGill electron beam system is shown in Fig. 3–2a, while the W ground plate is shown in Fig.3–2b.

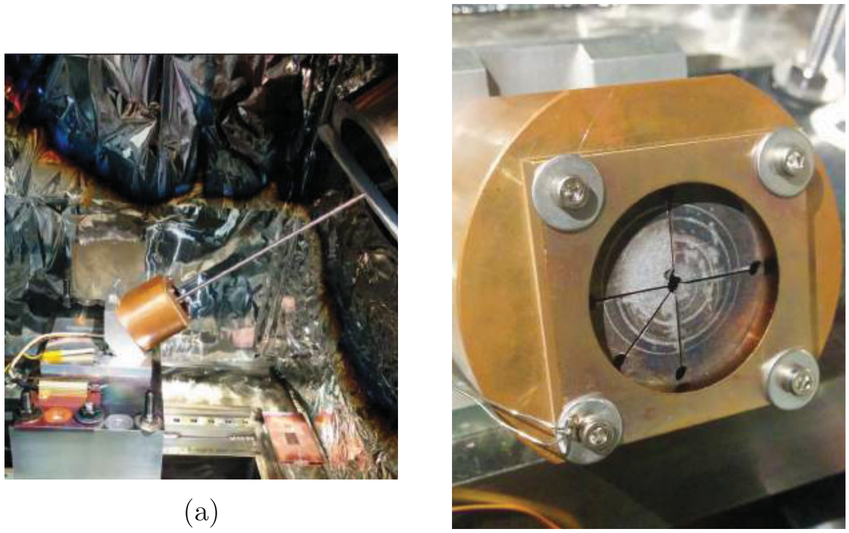

(a)

(b)

Figure 3–2: Faraday Cup installed in McGill electron beam chamber. Left: Faraday Cup installed at WD=240mm, where WD is defined by the distance between the gun muzzle surface and the front face of the W top plate. Right: Front surface of Faraday Cup with W top plate and Cu flange plate, and stainless steel washer instrumented with thermocouple (bottom left) Tungsten plate has a slot width of $2s = 0.5mm$

To bring the voltage signal outside the vacuum chamber for measurement, a 50Ω coaxial cable is fed to a D-Sub vacuum feedthrough and measured using a Rigol DS1102E Digital Oscilloscope using a 100MHz bandwidth, with an extended 1 million point memory capacity. In order to eliminate noise pickup associated with ground loops, the oscilloscope is powered through a TrippLite IS250HG isolation transformer. The output from the u-axis channel of waveform generator is connected to Channel 2 of the oscilloscope, providing a trigger signal to synchronize the Faraday Cup deflection pattern. The signal flow diagram for the Faraday Cup is shown in Fig. 3–3.

To acquire and store the voltage signals, the Virtual Instrument Software Architecture(VISA) is used to establish a communication link between the acquisition laptop and the oscilloscope via a USB cable. A custom-built script providing semi-automated signal labelling was written in LabVIEW, with the virtual instrument interface shown in Fig. 3–4. This virtual instrument stores the resulting oscilloscope traces in a .tdsm file, which is a proprietary file type developed by National Instruments.

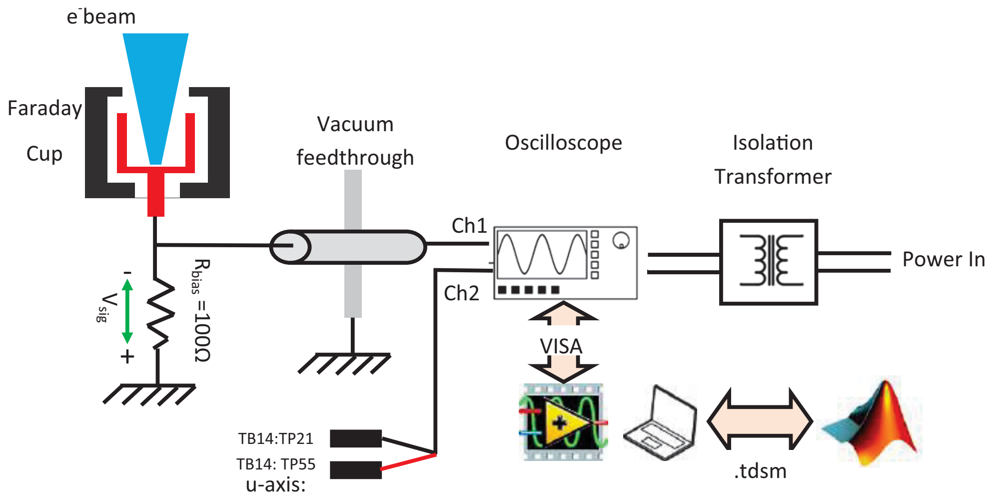

Figure 3–3: Signal Flow diagram for Faraday Cup signal acquisition. Note polarity the Ch2 signal, which is associated with triggering via the u-axis deflection signal.

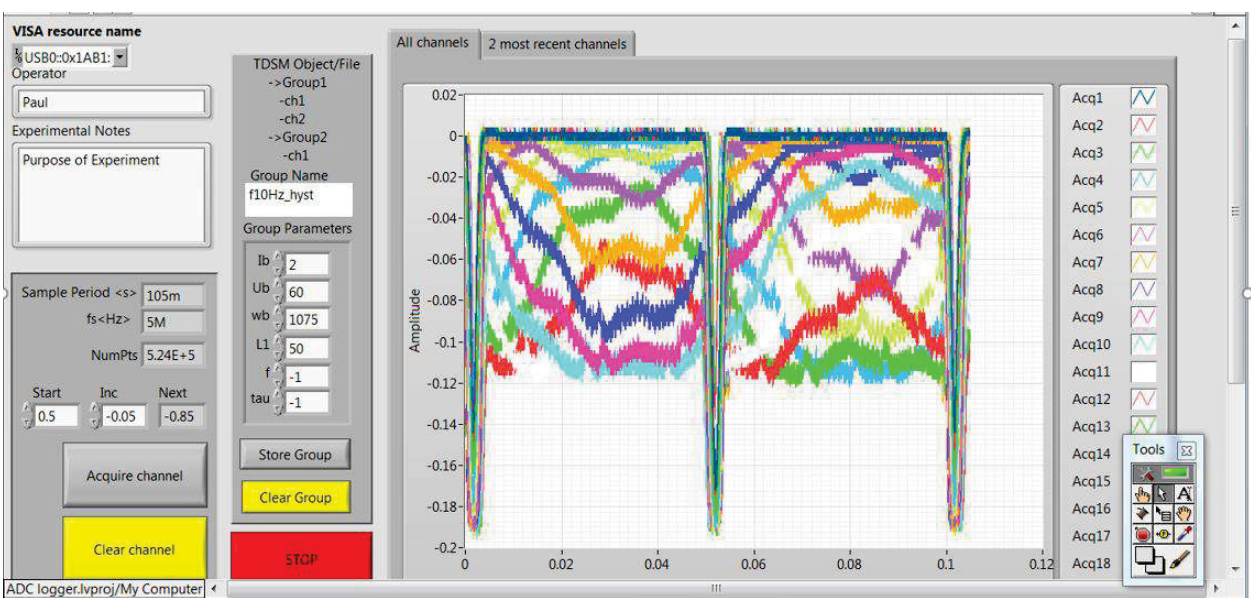

Figure 3–4: LabVIEW virtual instrument graphical user interface for Faraday Cup signal acquisition

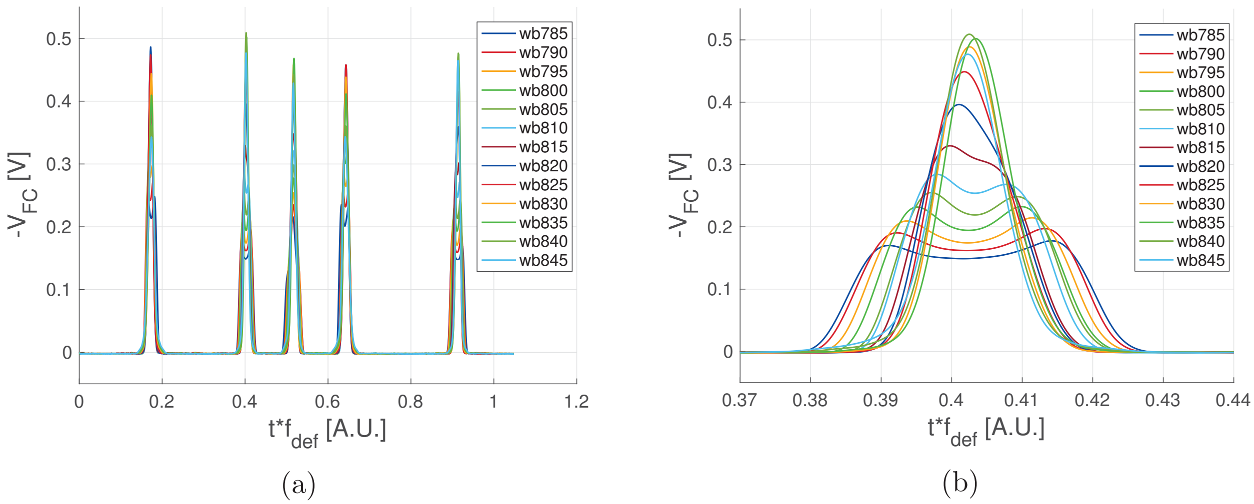

Figure 3–5: Faraday Cup voltage traces at 60kV/8mA and w_b= [785:5:845] using f_{def}=50Hz and r_{def}= 12mm. Left: All signals for range of beam scans. Right: Shifted voltage signals for individual slot width

Returning to Fig. 3–3, the .tdsm files are imported into MATLAB for additional post-processing and data analysis. Fast fourier analysis of the acquired signal show noise peaks at 60Hz, 936Hz, 2.13kHz and 29.99kHz, which are associated with the line, turbopump, deflection coil amplifier and high voltage power supply, respectively. The signals are low-pass filtered using the zero-phase distortion `filtfilt` Matlab function and a 10th order Butterworth filter with a 3dB frequency equal to 10kHz.

A sample of post-processed data is shown in Fig. 3–5, whereby a 60kV/8mA beam was deflected using a circular pattern of the W top plate, and the focus coil current was swept over the range w_b= [785:5:845]mA.

Figure 3–5a demonstrates 5 peaks per acquisition, with 3 close-spaced peaks in the middle. These 3 peaks can be understood by comparing the voltage signal to the W ground plate of Fig. 3–2b, which shows that the slot positions are not equally spaced around the diameter. Figure 3–5b presents the zoomed-in data from one slot, as the beam is incremented in w_b. From this plot, it is clear that the w_b= 785mA is initially in the under-focused condition, as the width of this voltage peak is the widest. The width of the voltage peak decreases with increasing w_b, indicating that the beam is moving from under-focus to sharp focus.

One can use Fig. 3–1 to derive the voltage signal associated with a stationary Gaussian beam over a tungsten slot according to Ohm's Law:

$$\begin{aligned} V_{FC} &= R\int_{-\infty}^{\infty}\int_{-\infty}^{\infty} j(x_o, y_o)dxdy \\ &= \eta_{FC}\frac{I_b R}{2\pi\sigma_x\sigma_y}\int_{-s}^{s} exp\left(-\left[\frac{(x-x_o)^2}{2\sigma_x^2}\right]\right)dx\int_{-\infty}^{\infty} exp\left(-\left[\frac{(y-y_o)^2}{2\sigma_y^2}\right]\right)dy \\ &= \eta_{FC}\frac{I_b R}{\sqrt{2\pi}\sigma_x}\int_{-s}^{s} exp\left(-\left[\frac{(x-x_o)^2}{2\sigma_x^2}\right]\right)dx \end{aligned} \tag{3.1}$$

where η_{FC} is the fraction of charge which is absorbed within the FC and x_o is the position of the beam center. Making the substitution $w = (x - x_0)/\sqrt{2}\sigma_x$, and $dx = \sqrt{2}\sigma_x dw$, Eq. 3.1 becomes:

$$\begin{aligned} V_{FC} &= \eta_{FC}\frac{I_b R}{\sqrt{\pi}}\int_{(-s-x_0)/\sqrt{2}\sigma_x}^{(s-x_0)/\sqrt{2}\sigma_x} exp\left[-w^2\right]dw \\ &= \eta_{FC}\frac{I_b R}{2}\left[erf\left(\frac{s-x_o}{\sqrt{2}\sigma_x}\right) - erf\left(\frac{-s-x_o}{\sqrt{2}\sigma_x}\right)\right] \end{aligned} \tag{3.2}$$

where erf is the error function. If a circular deflection pattern is used, the beam position will be defined according to $x_o = r_{def}sin[2\pi f_{def}(t - t_0)]$, so Eq. 3.2 becomes:

$$V_{FC}(t) = \frac{\eta_{FC} I_b R}{2}\left[erf\left(\frac{s - r_{def}sin[2\pi f_{def}(t-t_0)]}{\sqrt{2}\sigma_x}\right) - erf\left(\frac{-s - r_{def}sin[2\pi f_{def}(t-t_0)]}{\sqrt{2}\sigma_x}\right)\right] \tag{3.3}$$

Equation 3.3 shows that by determining the r_{def} of the circular deflection pattern, it is possible to fit for σ using the voltage signals of Fig. 3–5. As a final note, the sampling frequency must be chosen such that beam travel distance during sample period $1/f_s$ is small, specifically, $\Delta d = v/f_s << \sigma$. For a nominal deflection frequency of 50Hz and r_{def}= 12mm, the travel velocity is $v = 2\pi r_{def} f_{def}$= 3770 mm s^{-1}, which gives a Δd= 74nm for an f_s= 50MHz.

3.2.2 Deflection Coil Calibration

In order to minimize the likelihood of melting the W top plate at high beam powers, a low fluence is required, which implies a fast travel speed, $v = 2\pi r_{def} f_{def}$. For $f_{def} >$ 10Hz, it was observed that r_{def} of the circular deflection pattern decreased with increasing

f_{def}. This observation can be understood as response to the LR circuit of the cross-dipole magnets, as well as the eddy-currents induced in the metallic vacuum chamber walls, effects which were discussed in Sec. 2.3.1.[62] In other words, as the deflection frequency increases, the coupling between the deflection coils and beam decreases. Similarly, when the deflection amplitude of the u and v axis were identical, the pattern had an elliptical shape, implying that each axis has a unique coupling coefficient. *Note: As discussed in the previous section, the deflection axes, [u, v] are not perfectly coincident with the workpiece axis, [x, y]. The deflection coils have been manually rotated to the best possible alignment between the [u, v] axis of the deflection coils and the [x, y] axis of the workpiece.*

These observations imply that for a given deflection axis (u, v), waveform (sin, tri, etc), deflection frequency (f_{def}), signal amplitude (V_{def}) and Working Distance (WD), there is a coefficient $k_i(f)$ [mm V^{-1}] which defines the corresponding deflection radius, such that $r_{def} = V_{def} * k_i$, where i is the u or v axis. Conversely, to determine the voltage needed to achieve a specific deflection radius, $V_{def} = r_{def}/k_i$.

To determine $k_u(f)$ and $k_v(f)$, we can use the signal acquisition system of Fig. 3–3, along with the known dimensions of the Faraday Cup (FC). Specifically, the distance between the outer holes of the FC top plate have been measured to be 32.8mm. Therefore, if the beam focussed and centered on the FC, the deflection amplitude can be incremented to the point where the deflection distance is 32.8mm, giving $k_i(f) = 32.8/(2 * V_{def})$. The factor of 2 is included in the denominator since a waveform amplitude of V_{def} implies a minimum and maximum of $-V_{def}$ and $+V_{def}$, respectively. This measurement concept is shown in Fig. 3–6.

Figure 3–6a demonstrates deflection patterns where the u axis deflection signal =0, and the v axis deflection signal = $V_{def} sin(2\pi f_{def} t)$. In the left image, V_{def} is not sufficiently large to pass the beam through the outer FC holes. In the right image of Fig. 3–6a, the deflection amplitude has been incremented such that the focused beam crosses the edge of the FC holes. To determine the threshold V_{def}, the Faraday cup voltage signal, V_{FC} is monitored, with exemplary measurements shown in Fig. 3–6b. At V_{def}= 4.75V, we see that the beam does not pass through the holes. (Note: The higher voltage peaks are associated with the beam crossing the center slot). At V_{def}= 4.80V, we see

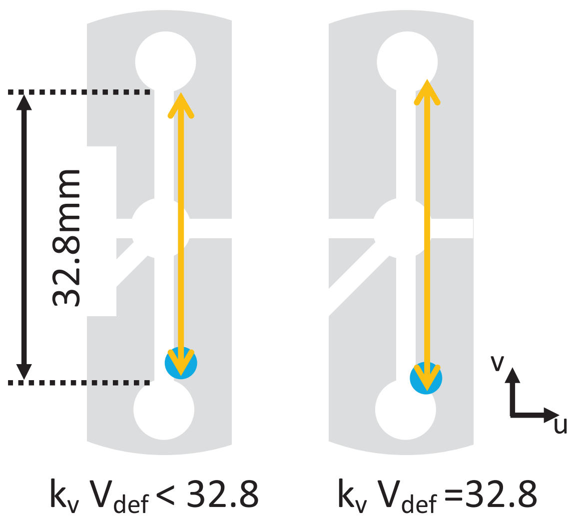

(a)

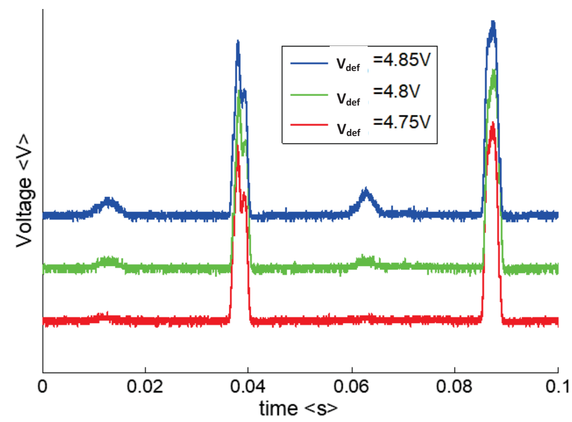

(b)

Figure 3–6: Schematic demonstrating deflection calibration for k_v with f_{def}=2Hz Left: Beam is centered on u axis and the deflection amplitude is increased until the beam path, shown in orange, deflects in the entrance hole of the FC. Right: Voltage signal associated with incrementing V_{def}, which shows the beam passing through both FC holes at V_{def}= 4.80 $\pm$ 0.05V

the emergence of two small voltage peaks at t= 0.1s and t =0.6s, indicating that a small fraction of the beam has been transmitted through the holes, and the deflection amplitude is $2V_{def}$= 32.8mm. The peaks grow further at V_{def}= 4.85V, indicating that a greater portion of the beam passes into the FC, therefore $k_v(2Hz) = 32.8mm/(2 * 4.8V) = 3.41$ mm V^{-1}.

Because this measurement is non-destructive, it can be repeated for different combinations of WD and V_{acc}. Care must be taken to ensure that the beam is properly centered on the FC plate. A non-aligned beam is easily identified since the voltage bumps will not be symmetric. A set of $[k_u, k_v]$ measurements conducted at V_{acc}= 60kV at a WD=240mm is shown in Fig. 3–7.

To maintain the same deflection radius, the data in Fig. 3–7 demonstrates how the deflection amplitude must increase with increasing frequency. For instance, to obtain an r_{def}= 12mm at 5Hz, the deflection amplitudes on the $[u, v]$ axis will be 12 mm*[1/3.12, 1/3.45]V mm^{-1} = [3.84,3.48]V. If the deflection frequency is increased to 50Hz, the deflection amplitudes will be 12 mm*[1/2.56, 1/2.85]V mm^{-1} = [4.68, 4.21]V.

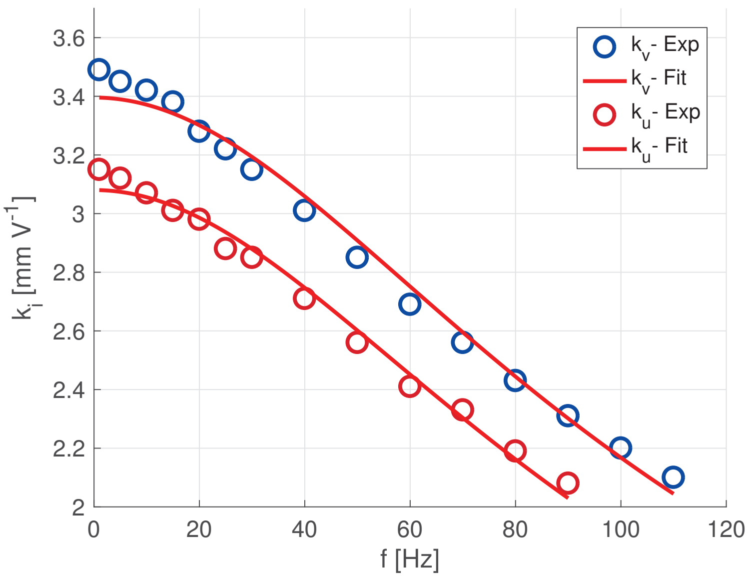

Figure 3–7: Deflection coil transfer function, k_u, k_v at V_{acc}= 60kV, WD= 240mm with LR circuit fit results to Eq.3.4 given in Table 3–1.

axis	k_{DC} [mm V^{-1}]	f_0[Hz]	adj-R^2
u	3.08 ± 0.04	79 ± 3	0.98
v	3.40 ± 0.05	83 ± 3	0.99

Table 3–1: Deflection Coil fit results for WD=240mm at 60kV

Because the bending magnets can be modeled as an inductor in series with a resistor, the data of Fig. 3–7 can be fitted to a circuit model. To first order, the complex circuit impedance is $Z = R + Ls$. Since we are interested in the magnetic coupling between the beam and the inductor, we can model the magnetic bending field as $B(s) = \kappa I(s) = \kappa V(s)/Z = \kappa V(s)/(R + Ls)$, which has a corresponding frequency-amplitude response equal to:

$$k_i(f) = \frac{k_{DC}}{\sqrt{1 + (f/f_0)^2}} \tag{3.4}$$

where k_{DC} [mm V^{-1}] is the small angle, DC deflection coupling, and $f_0 = R/2\pi L$ is the 3dB cut-off frequency. Viewed from another perspective, f_0 is a measure of the magnetic inertia of the deflection coils, with high magnetic inertia associated with a large inductance L and a small f_0. Equation 3.4 is fitted to the data in Fig.3–7, with the fitting results shown in Table 3–1.

Although the fit in Fig.3–7 is not good at small f, this simple model captures the main features of the McGill deflection coils. Specifically, the deflection coils act as a low-pass filter, and dampen the high frequency components of the waveforms. In other words, the 'sharp' features of the staircase or sawtooth waveform will be smoothed out, resulting in extended dwell times at the jump points. This issue will be further discussed when examining the dissimilar Nb-to-Ti electron beam welds. The issues with the model fitting at low deflection frequencies is likely due to eddy current effects, which have a f^2 relationship.

It has been observed that during u-axis deflection, the beam has a small amount of v-axis oscillations. According to the electrical V_{FC} measurements, the period of these oscillations is roughly 2-5 seconds. It is suspected that these oscillations are due to magnetic cross-coupling between the u and v magnetic fields, and could not be remedied. Finally, it has also been observed that using deflection frequencies in excess of $100Hz$ for an extended period of time can blow the 2.2A fuse in the deflection coil current amplifier.

3.2.3 Faraday Cup Curve Fitting

Having calibrated the frequency-dependent deflection signal amplitude to control r_{def}, we fit the Faraday Cup (FC) voltage signal to Eq. 3.3. The extracted fit parameters are $\eta_{FC} I_b R/2$, which is related to the signal amplitude, t_0, the deflection time shift, and σ, which captures the beam distribution. As an example, FC fit results at two separate focus settings are shown in Fig. 3–8.

The signal associated with Fig. 3–8a represents the under-focussed condition at w_b= 785mA. Examining the fit residuals in the lower panel of Fig. 3–8a suggests that the original assumption of a Gaussian-distributed beam is not accurate. Fig. 3–8a represents the same beam focussed using w_b= 840mA. In this case, the residuals demonstrate that the model agreement is much stronger. The corresponding fit results of Fig. 3–8 are shown in Table 3–2.

Non-gaussian, defocussed beams have been documented in EBW literature, and have motivated more sophisticated beam diagnostic tools than those presented here.[106, 43, 150] Despite the fact that a Gaussian distribution does not fully define a defocussed beam, the σ value derived from the curve fit still gives some indication of the beam distribution.

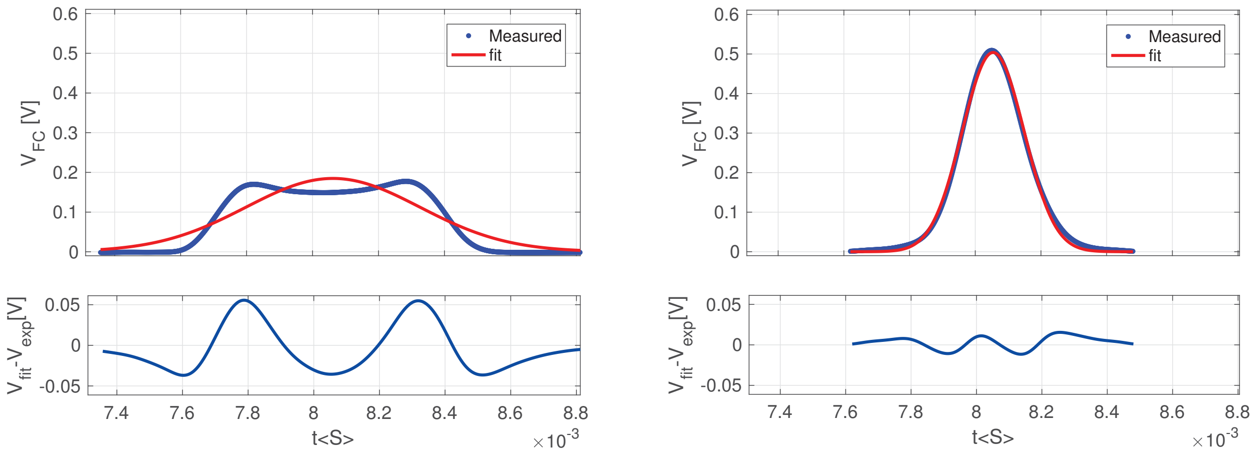

(a) (b)

Figure 3–8: Faraday Cup curve fitting for V_{acc}= 60kV, I_b= 8mA, WD=240mm Left: w_b= 785mA and Right: w_b= 840mA. Results from fits are shown in Table 3–2

w_b[mA]	$\eta_{FC}I_bR/2$ [V]	σ [mm]	t_0 [mS]	adj-R^2
785	0.46	0.99	8.06	0.881
840	0.45	0.32	8.05	0.998

Table 3–2: Fitting results for Faraday Cup signals of Fig. 3–8 with variables defined in Eq. 3.3

Under the caveat that the σ value should be interpreted as the equivalent Gaussian distribution parameter, σ as a function of w_b for each slot is shown in Fig. 3–9.

These results demonstrate that the focus current needed to achieve minimum σ depends on the orientation of the slot. This result can be understood by recognizing that the slotted Faraday Cup (FC) can only determine the longitudinal beam distribution parameter. In other words, the vertical FC slots characterizes the σ_x parameter, while the horizontal slots characterize σ_y. The fact that these minima are not coincident can be attributed to the astigmatism in the McGill beam. In future systems, the incorporation of quadrapole lenses could be used to rectify this aberration, as discussed in Sect. 2.3.

The mean σ between the vertical and horizontal slots is shown by the solid black line in Fig. 3–9, which has a minimum σ= 370μm at w_b= 830mA. With this value, it is possible to calculate the beam PPD according to $p_0 = V_{acc}I_b/2\pi\sigma^2 = 0.6$ kW mm^{-2}, which is much lower than the keyhole threshold of 5 kW mm^{-2}.

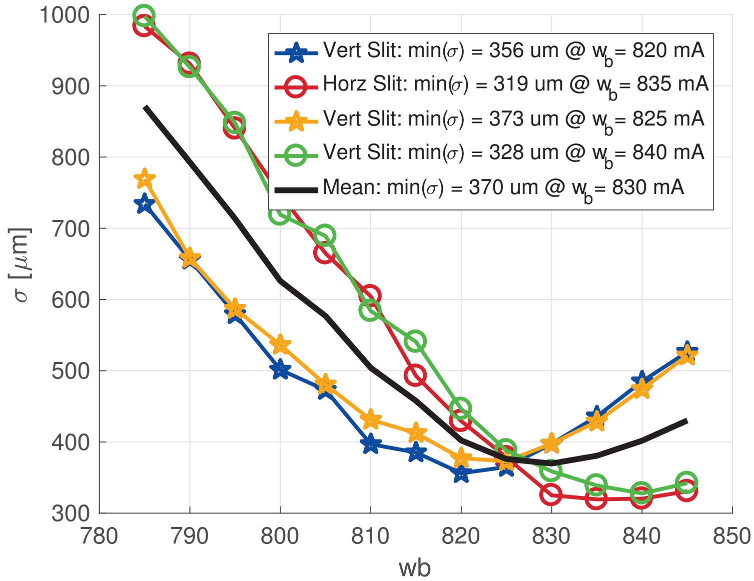

Figure 3–9: Equivalent σ as a function of w_b for 8mA/60kV beam. The vertical and horizontal slots are in reference to the FC cross, shown in Fig. 3–2b

The concept of mean σ has been extended to FC measurements conducted at different beam currents, with the results shown in Fig. 3–10.

These measurements highlight a few issues discussed in the preceding chapter. Firstly, the position of the virtual gun cross-over depends on beam current, which implies that the focal length needed to achieve sharp focus at the workplane is I_b dependent. This concept explains why the w_b needed to achieve minimum σ depends on I_b. Also, we see that the minimum σ increases with I_b, which can be explained according to beam perveance. Specifically, as a greater number of electrons are focussed together, the repulsive fields increase, dispersing the electrons and increasing the beam diameter.

The results of Fig. 3–10 can be further transformed by calculating the equivalent Peak Power Density (PPD), $V_{acc}I_b/2\pi\sigma^2$, as a function of I_b and w_b, with the results shown in Fig. 3–11.

These results further demonstrate key concepts related to electron beam processing with respect to optimizing beam current. First, it is interesting to note that the width of p_0 peak decreases with increasing I_b. In other words, a $\pm$ 10mA FO from optimal at I_b= 2mA does not induce as significant of a change in p_0 as a FO of $\pm$ 10mA at 14mA. As previously discussed, the convective transport within the pool is strongly dependent

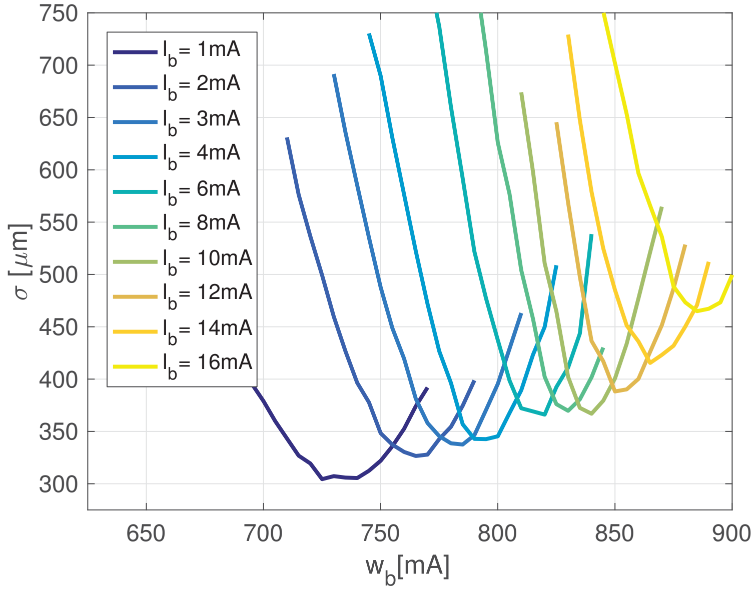

Figure 3–10: Mean σ as a function of focus coil current(w_b) at different beam currents for WD= 240mm and V_{acc}= 60kV

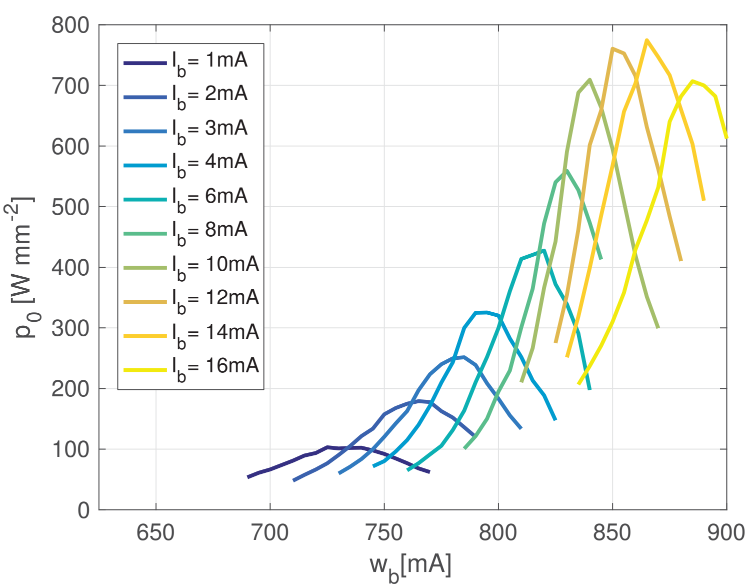

Figure 3–11: Peak power density as a function of beam current and focus setting, derived from Faraday Cup measurements, with WD= 240mm and V_{acc}= 60kV

on p_0, and thus wider $p_0(w_b)$ curves imply stability in the convective heat transfer. This interpretation most likely explains why optimum surface finish during EB-PBF is observed using a low-current beam.

Another feature of Fig. 3–11 is that the maximum p_0 actually *decreases* for $I_b >$ 14mA. Again, this can be explained by the discussion in Ch. 2, which states that the geometry of the gun will only optimize the beam brightness within a certain window. The data of Fig. 3–11 shows that this window at 60kV is $I_b <$ 14mA. It should be stated that the gun was originally designed for operation at 80kV, therefore these measurements are of the gun operating in its non-optimal configuration. Finally, it should be noted that in all cases, tests were performed to ensure that the laser power, and thus the cathode emission temperature, was sufficiently high to be operating in the space-charge limited regime.

This concludes the Faraday Cup beam characterization methodology. Although additional measurements at variable working distances and accelerating voltages were conducted, they will not be presented as it was determined that this method of beam characterization was not compatible with the gCode process compiler. Nevertheless, the results presented here demonstrate many of the issues discussed in the previous section regarding beam optics and beam focussing, and the instrumentation and signal processing workflow is used in subsequent melting experiments

3.3 Thermocouple Measurements

Precision Thermocouple (TC) instrumentation was developed during this research to measure temperature response of the workpiece during electron beam irradiation. This thermal instrumentation is complementary to the current-based Faraday Cup (FC), since the temperature rise associated with electron beam irradiation is proportional to the absorbed energy, $\eta V_{acc} I_b \tau$. These measurements have been used to monitor the sintering behaviour of the metallic powders under different time/temperature schedules, and formed the basis of the transient calorimetry measurements associated with pulsed electron beam heating.

The system has been configured for K-type thermocouples, which are composed of a positive Chromel leg and a negative Alumel leg, with alloy compositions of 10 wt.% Cr -Ni bal. and 2wt.% Mn - 2wt.% Al - 1wt.% Si-Ni bal, respectively. Because of the thermoelectric effect, a dissimilar metal junction formed from these alloys creates a temperature-dependent potential difference of 40 μV per degree Celsius, otherwise known as the Seebeck coefficient. These small voltage signals are susceptible to noise pickup and a significant effort was required to achieve accurate measurements.

The TC signals were acquired using a National Instruments NI-9213 x16 channel thermocouple reader.[151] Three TC channels were routed into the vacuum chamber using a KF40 K-type vacuum feed through. Once in the chamber, each channel was terminated using miniature K-type, ultra-high temperature unglazed ceramic connectors(Omega Engineering SHX-K). This configuration enabled rapid, hot section TC exchanges without introducing dissimilar metal junctions. TC junctions joined to titanium were prone to fracture, therefore a special support plate was fabricated, which minimized the strain on the junction and simplified installation. After the connector, the bare-wire TC's were routed through dual-hole ceramic insulators, which have a peak operating temperature of 1600^{o}C and maintain a close spacing between TC wires.(Omega Engineering DH-1-24-100)

To reduce noise pickup, the TC wire length were kept to a minimum, with a net length of approximately 4'. For applications requiring precise temperature values, the high temperature thermal excursions were kept to a minimum, and the hot section wires were routinely replaced.

3.3.1 Signal Acquisition and Processing

As mentioned, the TC signals were acquired using a National Instruments 9213 thermocouple reader, connected via USB to a battery powered laptop. The TC reader was operated in the high-speed timing mode, which has an input bandwidth of 78Hz, a measurement sensitivity of 0.25^{o}C and an absolute error of less than 5^{o}C over the measurement range.[151]

Initially, it was observed that incident beam influenced the temperature reading of the workpiece, where step changes in the beam power caused unrealistic discontinuities in the temperature reading. These errors are presumably related to ground loops and capacitance associated with the beam current return path. Using a simple experiment described later, it was determined that using a high sampling rate (f_s= 500Hz), grounding the unused channels within the chamber, and disconnecting the NI9213 COM port from

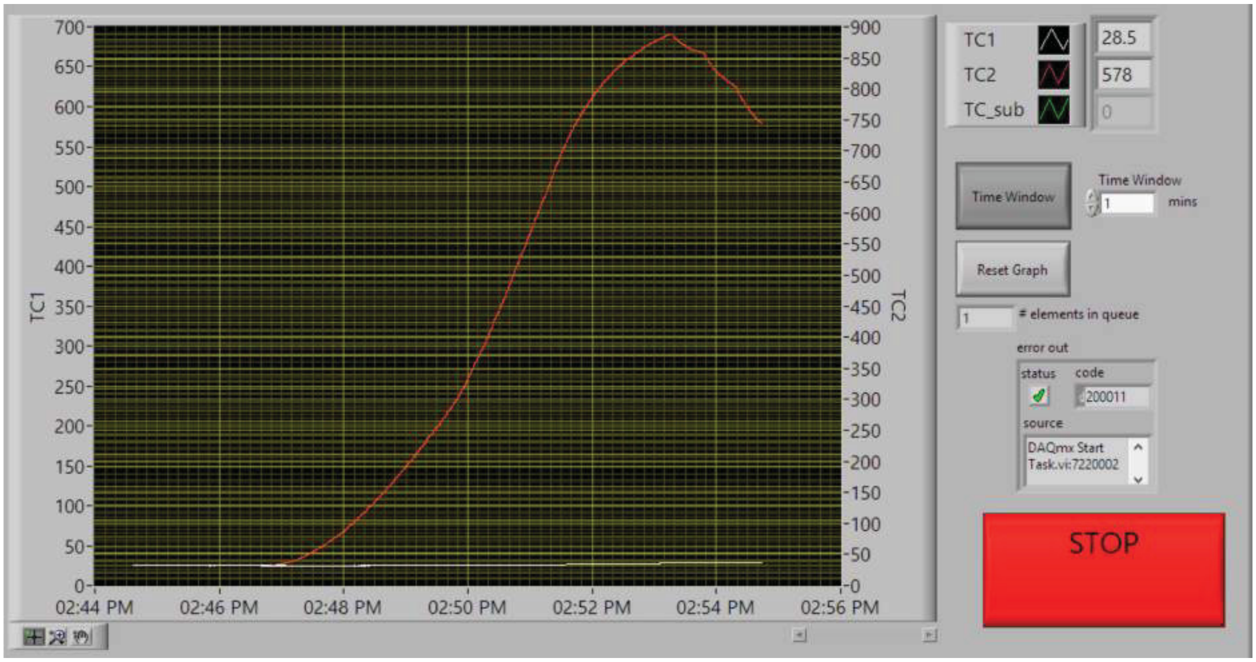

Figure 3–12: LabVIEW virtual instrument graphical user interface for thermocouple signal acquisition

the system ground improved signal fidelity. Also, configuring the LabVIEW TC tasks to use a constant cold-junction compensation temperature of 23^{o}C alleviated some issues. In this configuration, the grounding point was at the TC junctions, and special measures were taken to secure the beam current return path through the workpiece.

The temperature readings were acquired using a custom LabVIEW script, with the graphical user interface shown in Fig. 3–12. Within this LabVIEW script, the temperature readings are stored in a `.tdsm` file, and imported in MATLAB for further analysis.

3.3.2 Thermocouple welding and installation

Accurate temperature measurements require that the TC junction has good thermal contact with the workpiece as well a precise positioning. A joint capable of withstanding high strains implies a strong mechanical joint, good thermal contact and thus accurate temperature readings. A pull test between the TC and the workpiece was conducted after welding each TC joint to ensure sound welds.

A multi-step process was developed to join the TCs to the workpiece, with key features described below with further details documented in a standard operating procedure. First, the desired TC position is scribed onto the backside of the workpiece using a flat

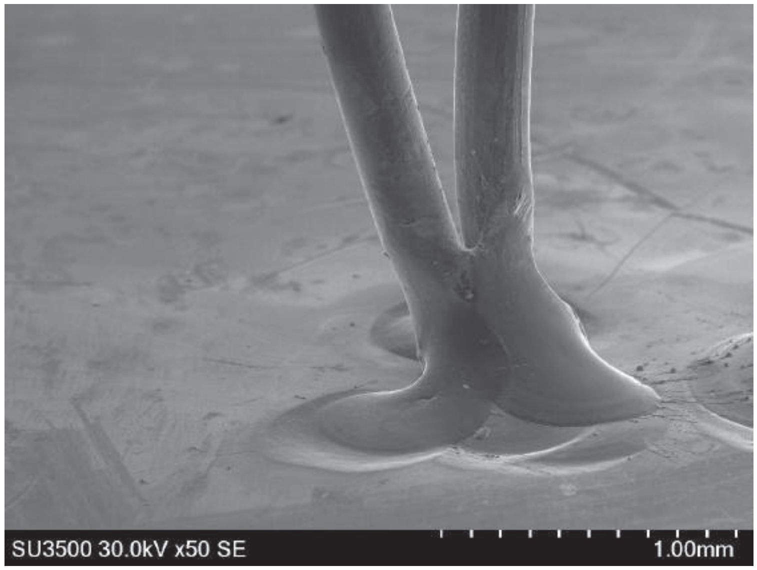

Figure 3–13: AWG 30 thermcouple welded to stainless steel substrate. Note that the junction-to-substrate transition is smooth, and the TC has been welded at four corners of the junction

plate, a machinist block and a height gauge. Next, a flat is ground onto the thermocouple junction using a diamond abrasive wheel and a rotary tool. The flat is then resistively tack welded at the scribed position by holding the wires near the junction with special electrically connected pliers, completing the welding circuit. The tack weld settings are chosen such that the TC can be removed with a light pull. If the TC position is satisfactory, the junction is further fused to the workpiece using a Lampert PUK04 micro-pulse tungsten inert gas welding unit with Ar shielding gas.[152] It was determined that that the state of the tungsten electrode tip had a significant impact on the quality and accuracy of the weld, with worn electrodes giving poor results. Using a freshly ground electrode followed by a single conditioning weld achieved good joint strength and repeatability, with an exemplary joint shown Fig. 3–13.

It was determined that wire lengths of 4-6” between the workpiece and the screw terminals improved handling, simplified routing and reduced junction strain. Also, bending the TC wires outside of the vacuum chamber using a special fixture simplified the installation procedure.

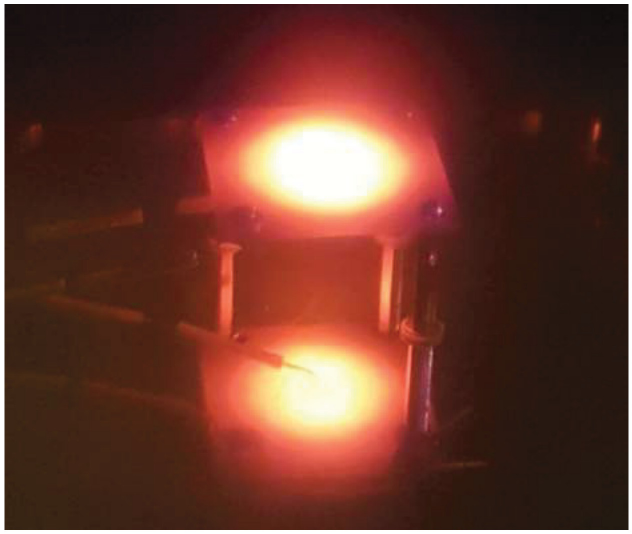

Figure 3–14: Electron beam heating of grade 2 titanium substrate for thermocouple verification using P=210W, with a thermocouple temperature of 918^{o}C. The thermocouple wires can be seen in the reflected image

3.3.3 TC verification: alpha-beta transus of Ti

The procedures and modifications outlined above were derived during benchmark, high temperature thermocouple experiments. In these tests, a defocussed beam was rapidly deflected over a commercially pure Ti plate. The temperature was monitored using a TC joined to the backside of the plate and the beam power was increased such that the TC reading was above the nominal β-transus temperature, $T_{\alpha/\beta}$ = 882^{o}C. Using shade 5 welding eye protection, the deflection pattern was modified to obtain visually uniform heating profile, while maintaining the local fluence/v below the meting threshold. An image of the heated plate within the vacuum chamber can be seen in Fig. 3–14.

Once the temperature reading stabilized at $T > T_{\alpha/\beta}$, the beam power was reduced to P_{off}. At this lower power, the workpiece temperature gradually decreases, passing through this $T_{\alpha/\beta}$ temperature and releasing a transformation enthalpy of $\Delta H_{\alpha/\beta}$= 87 J g^{-1}.[26] As an upper estimate, if one assumes the entire 16.70g plate is above $T_{\alpha/\beta}$, approximately 1.4 kJ will be released during cooling, resulting in an arrest in the cooling curve. The TC response of a 210W beam stepped down to P_{off}= [0, 60 ,120]W is shown in Fig. 3–15a.

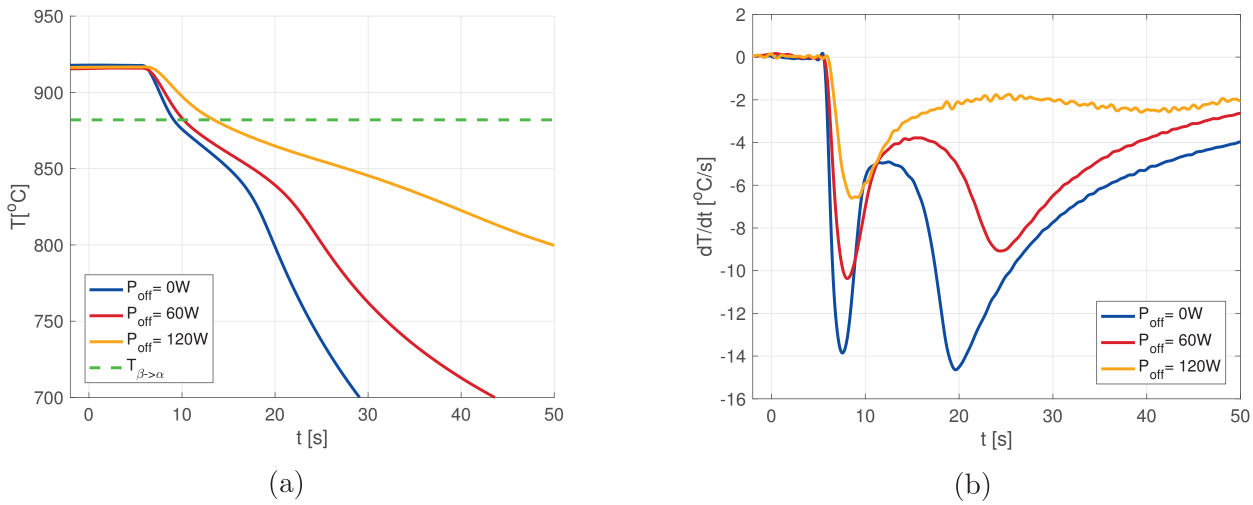

Figure 3–15: Thermocouple response during cooling of cp Ti plate through the β transus temperature. Left: thermocouple signals as the beam power is reduced from 210W to 0, 60 or 120W, with the $T_{\alpha/\beta}$ shown in the dashed line. Right: Time derivative of temperature(dT/dt) as a function of time for different beam powers

As expected, these data demonstrates that the slope of the t/T plot decreases with decreasing P_{off}. Similarly, the dashed line represents the $T_{\alpha/\beta}$ temperature, and one can discern a faint temperature arrest below this temperature.

This thermal arrest is more clearly demonstrated in Fig. 3–15b, which is the time derivative of Fig. 3–15a. From this figure, we see that the highest bulk cooling rate is 15^{o}C s^{-1}. Moreover, this plot demonstrates the effect of the transformation enthalpy on the cooling rate, as the cooling rate decreases then increases with decreasing temperature. The results of Fig. 3–15 are combined into a T versus dT/dt curve, with the results shown in Fig. 3–16.

Compared to the nominal $T_{\alpha/\beta}$ temperature of 882^{o}C, the data in Fig. 3–16 demonstrates that the thermal arrest is spread over a temperature range of 800-900^{o}C. This distributed response is to be expected considering the plate cannot cool uniformly because of the fixturing attachment points. Similarly, the $T_{\alpha/\beta}$ temperature is strongly dependent on trace impurities, which were not quantified for the material used.[153]

Despite these issues, Fig. 3–16 demonstrates that with the grounding and timing modifications outlined above, the incident beam does not influence the thermocouple reading, as the P_{off}= 0W response has a similar form to the P_{off}= 60W condition.

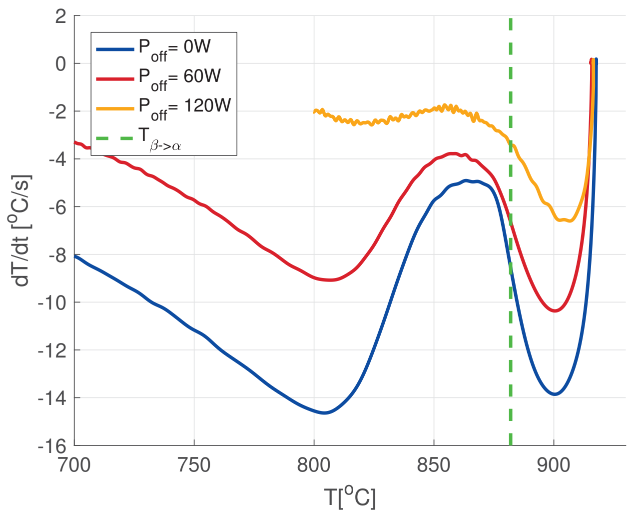

Figure 3–16: Cooling rate as function of temperature for three values of P_{off}

Initially, the TC response was sensitive to the incident electron beam, with discontinuities observed at changes in beam power.

T vs dT/dt measurements were routinely conducted throughout this research to quantify the heating and cooling responses of different process algorithms, proving to be an invaluable analysis tool. These measurements were also critical in quantifying design changes to the custom fixturing, which will be detailed in the following section.

3.4 Fixturing

Significant effort was dedicated to developing purpose-built fixturing for the electron beam experiments conducted at McGill. One of the most significant challenges concerned the inclined angle of the electron beam, which was 55^o from vertical. A CAD model of the system dimensioned with support from the OEM can be seen in Fig. 3–17, and proved useful in testing different design configurations.

Two fixturing modalities were engineered during this work. The first modality utilized a single-axis translation stage, and supported research on electron beam machining, algorithm development and transient calorimetry, with the final result shown in Fig. 3–17. The second design was based on a fixed geometry capable processing single powder layers at high temperatures, as shown in Fig. 3–14.

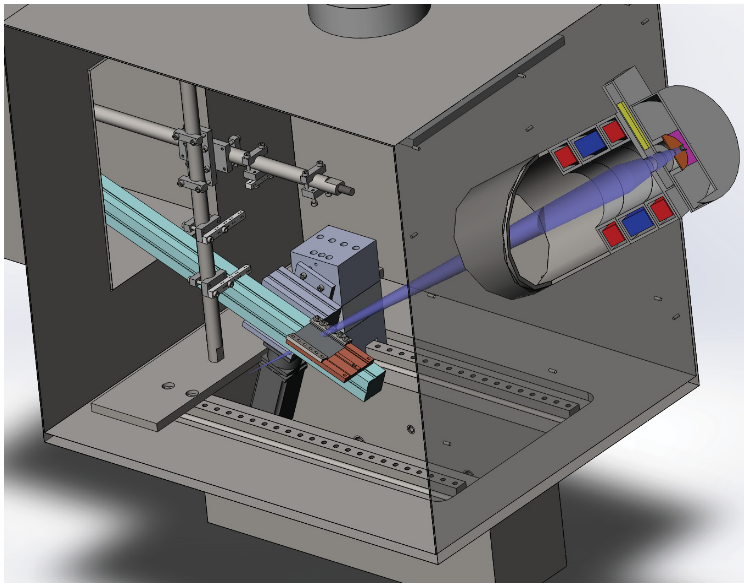

Figure 3–17: Model of electron beam geometry with translation stage fixturing

In both cases, high vacuum design principles, cleaning processes and materials selection were used to fabricate the fixtures.[65, 154] Both fixtures were designed to accommodate low-cost, consumable workpieces. Robust TC instrumentation proved to be challenging, as excessive strain on the hot TC junctions often resulted in detachment. Several iterations were required before a satisfactory, interchangeable TC solution was found. Finally, the fixtures required design features which allowed post-install alignment of the workpiece with the electron beam axis. This included shimming locations, slotted holes and datum edges. In the following section, a brief overview of each fixturing modality will be given.

3.4.1 Translation Stage Fixturing

The translation stage fixturing was originally designed to support research into pulsed electron beam melting and gCode process compiler development. The objective of this work was to use the workpiece as drafting paper for different electron beam 'sketches', enabling rapid process development. After each 'sketch', the processed workpiece was replaced with a virgin workpiece, and the chamber was pumped down. The processed coupon was inspected under the microscope, and the process was modified for the upcoming tests. This rapid development cycle required a fixture which could accommodate low-cost substrates. It was determined that 2"x10'x0.025" 304 stainless steel

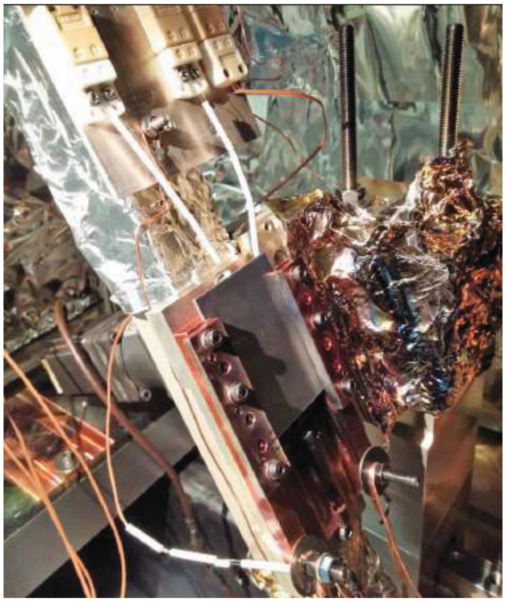

(a)

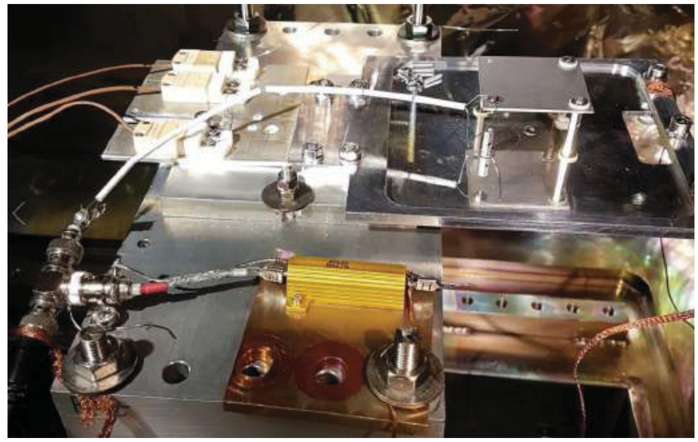

(b)

Figure 3–18: Left: Translation stage fixturing with $\theta = 0^o$ incidence angle. Right: Stationary hot powder fixturing

sheet(3254K327-McMaster Carr) could be sheared into 3" lengths in the McGill machine shop for a finished costs of roughly \$1.00/workpiece.

For most WD used, the deflection radius was roughly 1", therefore the ability to translate the workpiece enabled 2 separate 2"x1.5" 'sketches' on a single workpiece. The low-cost coupons combined with the rapid cycle time resulted in approximately 300 processed workpieces during the course of this work.

The sample fixture and hold down clamps are fabricated from OFHC copper, which rapidly stabilize the temperature field and provide the beam current return path. Another design feature of the translation stage fixture was the ability to vary the incidence angle and working distance. This necessitated the design of a special holding bracket that could be positioned along the chamber mounting rail, and rotated at discrete beam incidence angles of θ = [0, 10, 15, 35, 55, 65]^o, with an error of roughly 2^o. An image of the copper fixture installed on the translation stage in the θ= 0^o and WD=240mm configuration is shown in Fig. 3–18a.

At normal beam incidence ($\theta = 0^o$), the melts patterns can be positioned in the xy workplane using the magnetic deflection coils in combination with the y-axis translation of the stage. For inclined incidence($\theta \neq 0^o$), the beam is magnetically deflected along the x-axis only, while a linear stage provides the y-axis positioning. This approach minimizes changes in working distance, which could be significant at high incidence angle.

After extensive experimentation, it was determined that the translation stage could not sustain extended high temperature processing required to melt single powder layers. This was mainly due to the limited operating temperature of the translation stage and motor. Similarly, there were concerns about metal powder ingress into the motion system, motivating the need for high temperature fixturing.

3.4.2 Hot Powder Fixturing

To successfully melt metallic powder with an electron beam, the powder must first be sintered, which requires fixturing capable of sustaining high temperatures for tens of minutes. To minimize thermal deformation of the workpiece, the fixturing should also thermally isolate the workpiece such that the cooling path is choked at the fixture/workpiece interface. For instance, if the workpiece is tightly held by copper clamps, as in the translation stage fixture, there will be a large fixture/workpiece conduction path drawing heat at the contact points, inducing large thermal gradients and resulting in a thermally deformed workpiece. A weak thermal interface between the workpiece and fixture minimizes these fixture-related gradients. Another requirement to minimize deformation is that the fixturing should not provide any workpiece restraint.

The derived solution is based on supporting the workpiece using 25mm long, 4-40 stainless steel stand-offs above an Al-6061 tray, as shown in Fig. 3–18b. With their extended length and reduced cross section, the stand-offs minimize the conduction path between the hot workpiece and the cool support tray. The thermal isolation is further improved by placing 0.004” thick, high temperature ceramic washers at the workpiece/standoff and standoff/tray interfaces. (McMaster-Carr: 94610A215) To prevent cracking of the ceramic, stainless steel washers are placed between the ceramic and standoff, distributing strain associated with the thermal expansion. To mechanically secure the workpiece and provide an electrical return path, tooth-lock washers are used between the mounting screw and workpiece, which minimize the contact area and accommodate thermal expansion. To electrically isolate the workpiece, the tooth-lock washers are replaced with ceramic washers.

In the implementation shown in Fig. 3–18b, 50x50mm plate with thickness between 0.5-3mm can be used. The plate includes four 3.5mm holes distributed on a 48.0 mm bolt-hole diameter. These holes are larger than the recommended 3.2mm loose fit 4-40 holes, and minimize the possibility of workpiece restraint. Unfortunately, the enlarged holes do not provide positive location of the workpiece, requiring the use of a special alignment fixture.

At high temperatures, thermal radiation dominates the transfer of heat out of the workpiece and the radiative heat loss from both sides of the 50x50mm plate can be estimated from the Stefan-Boltzmann law. Assuming an emissivity of roughly $\epsilon = 0.5$,[26] the net radiative heat transfer from the 900^{o}C/1173^{o}K Ti plate to the cool 25^{o}C/300^{o}K chamber is $\epsilon\sigma_{SB}A(T^4 - T_0^4) = 273$ W. This order of magnitude estimate agrees with the 210W/900^{o}C data taken during the $T_{\alpha/\beta}$ experiments of Fig. 3–16.

To minimize this radiative heat transfer, the Al support tray was polished to a mirror finish. Also, a thin sheet of polished Mo is placed under the workpiece, providing some degree of radiative baffling. The Al mounting tray has a 3mm cavity milled into the surface with a hole at one end, providing a means of powder containment and clean-up. Finally, threaded holes with tooth-lock washers electrically connect the Al tray with the gun muzzle via bare, braided copper wire, grounding the support fixture.

Single layer powder deposition. To melt single layers of powder with the electron beam, five design criteria were identified: (1) the deposition technique must give a repeatable, uniform powder layers of 100-200μm thickness (2) the workpiece must conductively heat the powder by indirect electron beam heating (3) thermocouples joined to the workpiece have minimal material between the powder layer and TC junction (4) the workpiece can be securely grounded (5) the fabrication costs must be low and amenable to hard metals like Ni and Ti alloys.

The initial single layer design was a modification of previous work on single powder layer laser melting.[155, 156, 157] In this design, a cavity of known depth is overfilled with

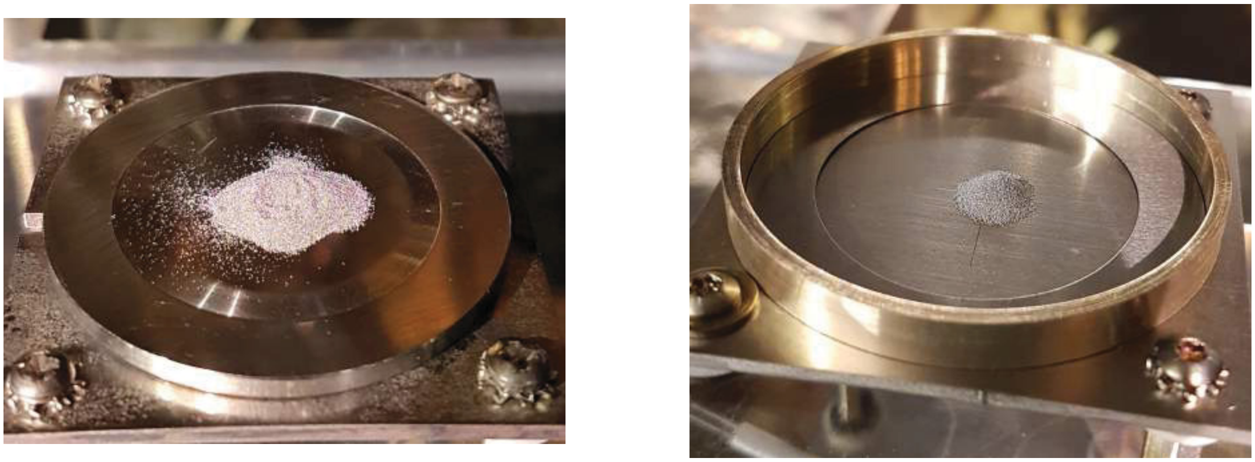

(a)

(b)

Figure 3–19: Methods to deposit single powder layers. Right: Initial powder puck concept using machined cavity. Left: Revised powder press concept with circular shim stock

loose powder. Next, a steel razorblade is swept along the upper rim of the cavity such that powder higher than the cavity height is removed. To conductively heat the powder, the electron beam is rapidly scanned on the outer, powder-free rim of the workpiece. In this way, low-temperature powder heating and beam irradiation is decoupled.

After consultation with a senior McGill machinists, it was decided that turning with a custom-machined 5C collet would give the best geometric tolerances, without the high reoccurring costs associated with plunge electro-discharge machining. To hold the circular workpiece in its fixture, a tungsten plate with a circular inner bore was used, with the final assembly shown in Fig. 3–19a.

Despite holding the step height of the cavity to within $\pm 10\mu m$, all powder cavities had a concave shape, with the best cavity resulting in flatness of approximately $\pm 15\mu$m over the 30mm diameter and the worst cavity having a flatness of $\pm 50\mu$m. This concave shape was attributed to a 0.11^o misalignment between cross slide and spindle of the Bridgeport lathe. After numerous experiments, it was determined that the flatness tolerance could not be improved, prohibiting the formation uniform powder layers.

To address this problem, a revised powder deposition method was developed. In this technique, referred to as the powder press, a 50x50mm sheet is manually ground until the middle region displays a uniform surface finish. Surface profile measurements have shown that this condition represents a flatness of roughly $\pm 5\mu$m. Next, an 'x' is scribed in the center of the plate, and the workpiece is ultrasonically cleaned in hot acetone.

After installation into the fixture, a precisely weighed amount of powder is placed in the center of the workpiece using a polished aluminium funnel block. After carefully removing the funnel, a circular shim stock and retaining ring is placed around the powder mound, as shown in Fig. 3–19b. A surface-ground circular puck with a flatness of $\pm 3\mu m$ is then placed in the bronze retaining ring, sandwiching the powder mound. The puck is then gently rotated, providing a combination of compressive and shear forces to the powder. After pumpdown, the powder is sintered in place by rapidly scanning the electron beam just outside the powder layer.

The advantage of this approach is that the cavity depth is set according to the shim stock thickness, which is available in discrete values ranging from [25:25:375]μm (McMaster-Carr: 98126A039). Another advantage is that, when carefully performed, little-to-no powder is lost during deposition, resulting in a single layer of known mass. When combined with powder layer height measurements, one can also calculate the powder layer packing density, Φ.

As an example, Fig. 3–20a shows 74mg of 45-106μm commercially pure Ti powder deposited with the powder press using a 0.006"/152μm shim. The image was taken using off-axis lighting, which distinguishes the spherical powder particles in dark contrast.

Under high magnification, no large voids were observed over the 266 mm^2 powder area. Using the powder mass and projected area, one can estimate the average solid layer thickness of the powder disk to be $t_{solid} = m_{pow}/(A_{pow}\rho_{solid}) = 60\mu m$.

Using the Zygo NewView 8000 optical profilometer, the height profile of the powder layer along the radial paths at $\theta =$ [-45, 0, 45, 90]^o is shown in Fig. 3–20b. Of particular note is the flatness of the underlying substrate, which in this case is roughly $\pm\ 1\mu m$.

To better interpret the data in Fig. 3–20b, a histogram of the z values is shown in Fig. 3–21. From these data, we see that the mean powder height is $98\mu m$ with a standard deviation of $41\mu m$. Interestingly, the standard deviation value matches the mean radius of this particular powder lot($D_{50}/2$) to within $3\mu m$.

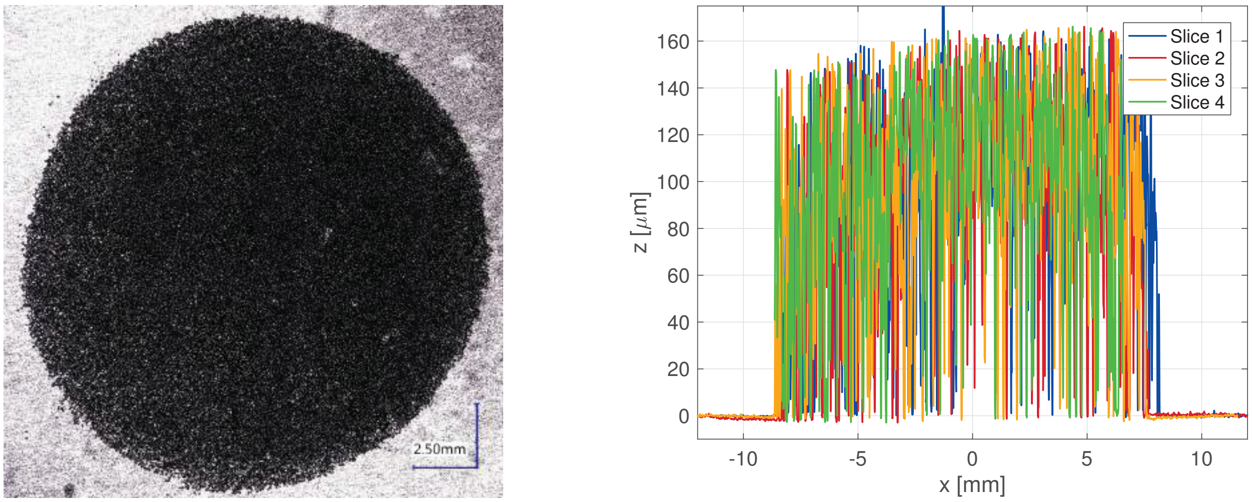

(a) (b)

Figure 3–20: Example of single layer powder deposit using powder press and 45-106μm cp Ti powder. Left: Powder distribution on workpiece using 74mg of powder. The corresponding powder area is A_{pow}= 266 mm^2. Left: Height profiles along powder taken along the θ= -45, 0 45 90^o radial paths

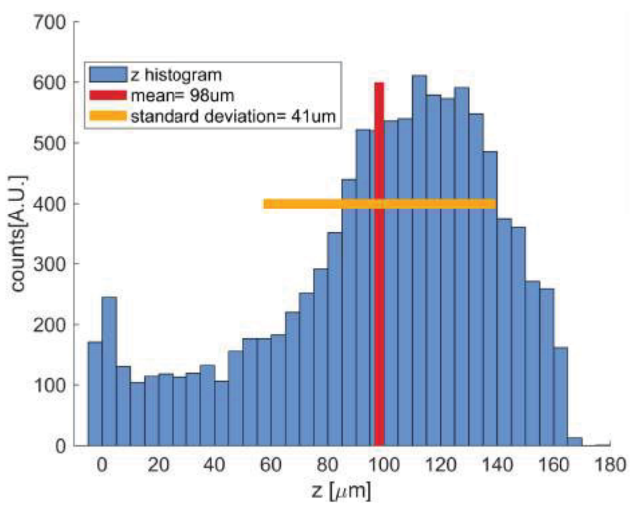

Figure 3–21: Histogram of powder layer height profiles for z height profiles shown in Fig. 3–20b

Assuming the effective powder layer height is the maximum powder height of $160\mu m$, one can calculate the equivalent powder layer density according $\rho_{pow} = m_{pow}/(A_{pow} * z_{pow})$= 1.74 g cm^3, resulting in a packing density of Φ= 38%. Again, this calculation assumes a uniform height over the entire powder layer. For reference, the apparent density of this particular bulk powder is 2.62 g cm^3(Φ= 57%).

Although the single layer analysis requires further development, the presented results are some of the most detailed single layer characterization found in literature. This is due to the fact that all other single layer work concerns laser melting, which does not sinter the powder into position prior to melting. In the laser case, when the experiment is complete, the loose powder cannot be handled for further analysis.

3.4.3 Fixture Installation and Workpiece Alignment

The instrumentation and fixturing of the previous section depends critically on the proper alignment between movable workpiece and fixed axis of the beam. As an example, during single layer melting, the disk of powder is centered on the substrate; meanwhile to preheat the powder, the beam is deflected in a circular pattern around the powder. If the center of deflection pattern and powder disk are not coincident, the beam will contact the powder, resulting in a failed test due to electrostatic powder ejection. Therefore, workpiece/beam alignment is a necessary condition for all powder experiments. In the following section, the procedure for installing and aligning the hot powder fixture will be described, while a similar process applies to aligning the translation stage.

First, a long threaded rod is screwed into an alignment block, which is mounted onto the gun muzzle, as shown in Fig. 3–2a. The threaded rod is coincident with the beam axis and provides coarse alignment as well as determination of the WD. After fixture installation, the origin of the workpiece is scribed with a cross using a height gauge and machinist blocks.

Next, the vacuum chamber is pumped down, and the build compiler subroutine `alignTest` generates gCode tailored for workpiece alignment. Specifically, the subroutine creates a pulse pattern using three different beam current/focus setting combinations, such that pulses are located along either the x or y axis. In Fig. 3–22b, a series of 60kV pulses at I_b= [6,10,14]mA and w_b= [792, 815, 828]mA are shown.

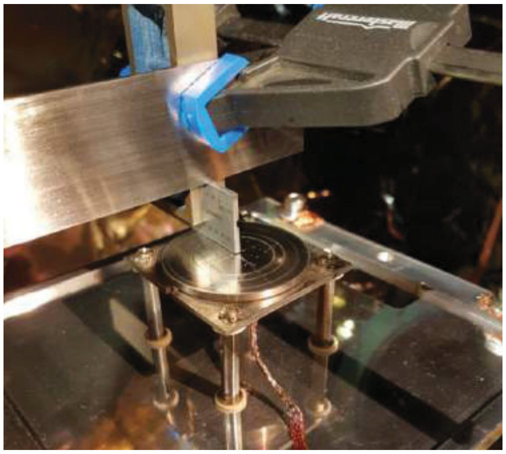

(a)

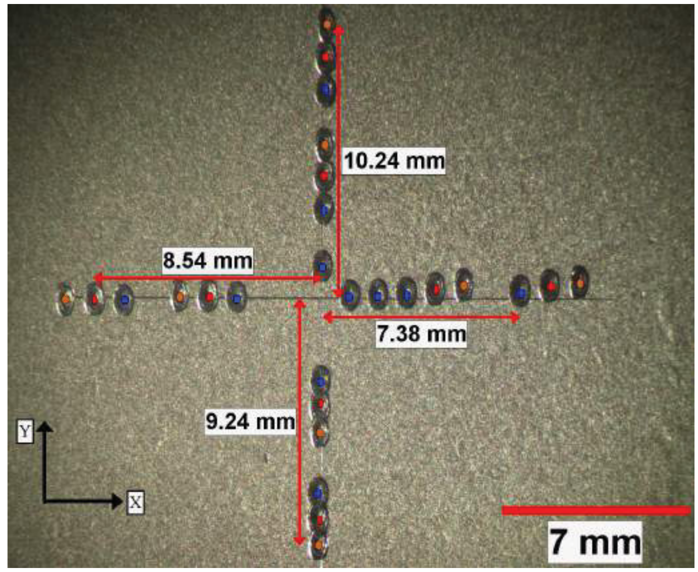

(b)

Figure 3–22: Workpiece alignment with beam axis. Left: Temporary fixturing with machinist squares to align axis of electron beam with the center of the workpiece. Right: Pulse pattern generated using `alignTest` at 60kV and $\theta = 65^o$. The pulses are based on three beam parameter combinations, $[Q_p, I_b, w_b]$; Blue markers $[3.2J, 6mA, 792mA]$; Red markers $[2.6J, 10mA, 815mA]$; Orange markers $[2.3J, 14mA, 828mA]$

After pulsed melting, the chamber is vented to atmosphere, a set of machinist squares are clamped to a fixed section of the fixture. The purpose is align the tip of the square with center of the pulse cross, as shown in Fig. 3–22a. Next, the movable portion of the fixture is adjusted such that tip of the machinist square aligns with the scribed cross. The fixture is then fastened in place, and the process is repeated to qualitatively measure the alignment, as shown in Fig. 3–22b.

It has been observed that the alignment procedure is only valid for a specific cathode/accelerating voltage combination, and realignment is necessary when either setting is changed. Similarly, it was determined that the positional accuracy of the beam relative to the workpiece is ± 0.4 mm, which is attributable to the loose fit associated with the unrestrained workpiece, as well as magnetic coil drift.

As a final note, the pulse pattern in Fig. 3–22b highlights a subtle issue associated with process alignment. Specifically, when examining $+x$ axis pulses, where y axis deflection is zero, we see that the pulses are not aligned along the scribe line, whereas the pulse along the $-x$ are. Moreover, when examining the rightmost pulses, we see that the misalignment is a function of the beam current/focus setting, as highlighted by the color coding of the pulses.

This issue is routinely observed, and it is believed to stem from the coupling between the focus and deflection coil magnetic fields, as well magnetic asymmetry in the deflection coils. In some cases, the distorted coordinate axes were corrected in software with an opposing offset.

Although the alignment procedure is relatively crude, it does illustrate some of the issues associated dimensional tolerance during EB-PBF and EBW, and highlights the importance of continuous machine maintenance.

3.5 gCode Compiler

Arguably the key distinction between Electron Beam Welding (EBW) and Electron Beam Powder Bed Fusion (EB-PBF) is the role of software and digital controls. For instance, melting a single 2D powder layer requires thousands of numerically controlled machine operations, each with a unique combination of beam parameters. Since the number of beam operations scales with the number of layers, a finished 3D part requires millions of process commands, precisely sequenced over the course of many hours. In contrast, EBW is effectively a 1D process, based on a few dozen commands, lasting no more than ten minutes. While both processes require precise beam control, the number of operations involved requires different process control architectures.

The difference in scale between EBW and EB-PBF was encountered in the early stages of this research, as it was determined that manually controlling the machine parameters via the Graphical User Interface (GUI) was both time consuming and prone to human error. To further explore 2D melting, a gCode compiler capable of generating the machine-specific process commands was coded in MATLAB, enabling software-based process definition and execution. The purpose of this compiler was to enable the creation of automated, software based design of experiments, such that process parameter mapping could be accelerated.

A flow diagram outlining the abstraction of this software-based process is shown in Fig. 3–23, and will be briefly summarized. In the first stage of the system, a physics-based

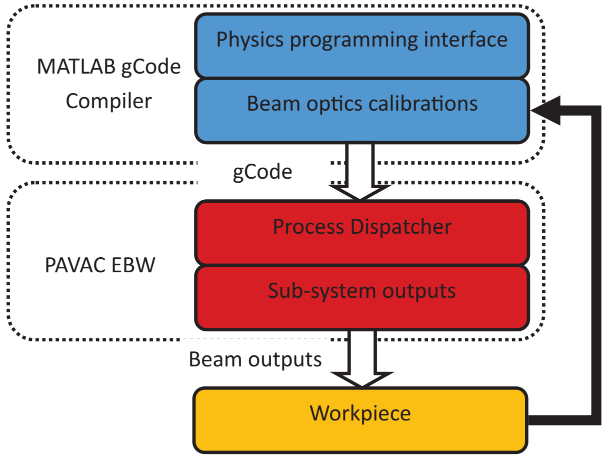

Figure 3–23: Flow diagram outlining the interactions between gCode compiler, EBW equipment and workpiece

programming interface defines the desired process parameters. A simple example of this interface would be defining the melt track according to its length, as opposed to the machine-specific deflection amplitude.

Once the experiment has been coded into a MATLAB script, the compiler references a set of look-up tables that generate gCode commands according to previous beam calibrations. For example, the compiler identifies the accelerating voltage and working distance used, references previous calibrations, and transforms the requested melt track length into a deflection amplitude. These machine-specific commands are written to a .txt file, which is associated with the unique experiment generated from the master MATLAB script.

The .txt file is transferred to the EBW computer via USB, and loaded into the process dispatcher via the system GUI. The process dispatcher then executes the commands according to the sequenced gCode. During execution, it was determined that stepping between commands results in a ≈200mS delay. As an example, to generate two adjacent melt tracks, the process dispatcher executes 4 commands with 3 steps: `beam on`→ `beam off`→ `move deflection pattern`→ `beam on`, resulting in a 3*200mS= 600mS delay between melting operations and impacting the local heat transfer and solidification dynamics. Moreover, it was determined via Faraday Cup (FC) measurements that this delay was not consistent, and varied by approximately ±100mS. Also, some commands prevent the process dispatcher from proceeding to the next command until the requested setting is reached. In this case, the delay between operations will depend on the difference between the current and requested settings.

Another issue identified with the process dispatcher was the lack of synchronization between the beam pulsing and beam deflection. This meant that the end points of the deflection pattern were not in-phase with the beam pulse, implying that the beam could be energized at any point along the requested path.

These timing issues are attributed to the original design of the EBW controls, which were meant to sequence multi-axis motion associated with EBW. After discussions with the PAVAC team, it was determined that significant development resources would be required to redesign the control architecture. Therefore, the issues were managed by designing the experiments and command sequences in order to limit these timing effects. In some cases, special work-arounds were possible, such as driving the deflection coils with synchronized triangle and square waveforms in order to guarantee that 1 of the 2 melt tracks would be continuous.

After gCode execution, the workpiece was removed from the vacuum chamber and inspected. In more than half of the instances, the melting experiment was related to calibration of the beam optics. In this case, the observed results were used to revise the calibration settings for subsequent experiments, as shown by the feedback loop of Fig. 3–23.

The software architecture associated with the gCode compiler of Fig. 3–23 underwent three design iterations over the course of this research. These revisions were based on the need to simplify algorithm development and enhance the parametric mapping capabilities, requiring improved version control, usability and documentation. One of the biggest issues associated with the initial implementations was that algorithms developed in one script were not easily applied to subsequent scripts. Also, it was also determined that the initial architecture was not amenable to generating gCodes using different accelerating voltages.

The final gCode compiler is a class-based, object-oriented software architecture. In this design, every possible beam operation is categorized by one of three possible classes, which are shown in Fig. 3–24, and defined as:

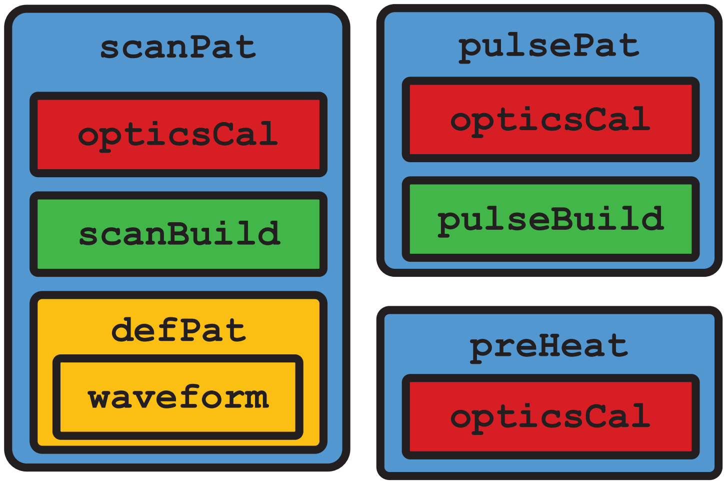

Figure 3–24: gCode compiler class architecture scanning, pulsing and preheat processes

- `scanPat`: one or more melt tracks with identical or variable process parameters
- `pulsePat`: one or more pulse melts with identical or variable process parameters
- `preHeat`: substrate preheat algorithm based on a pre-defined deflection pattern, heating time, power and ramp rate

The biggest advantage of this implementation is that each group of beam operations is instantiated as a unique object, enabling multiple melt patterns to be generated in a single script. In other words, since the code used to create each pattern is nearly identical, it is relatively straightforward to parametrically map out the process parameters, as will be shown at the end of this section. Also, by utilizing class inheritance, beam operations can be designed independent of the specific calibration, allowing beam calibration and algorithm development to be separated. This was done by creating a special `opticsCal` sub-class, which is uniquely associated with a cathode, accelerating voltage and working distance.

Another sub-class associated with Fig. 3–24 is `scanBuild` and `pulseBuild`. These classes contain functions that analyze process requests and generate machine outputs according constrained physical relationships. As an example, consider a script based on a beam current of I_b= 10mA and pulse of energy $Q_p = I_b V_{acc} \tau$= 4J. The accelerating voltage is inherited from the subordinate `opticsCal` object, which in this case is `opticsCal.Vacc`= 60kV. Having defined Q_p, I_b, and V_{acc}, the resulting pulse length is constrained according to τ= 4J/(60kV*10mA)= 6.66mS, which is determined by the `pulseBuild` object.

Although seemingly trivial, the advantage this architecture becomes apparent when conducting parametric studies. For instance, if a new `opticsCal` object is instantiated with `opticsCal.Vacc`= 80kV, `pulseBuild` will automatically re-calculate τ= 4J/(80kV*10mA)= 5mS without any changes to the master script. Alternatively, if the script is modified to operate with I_b = 5mA while maintaining `opticsCal.Vacc`= 60kV, `pulseBuild` automatically calculates the pulse of length to be τ= 4J/(60kV*5mA)= 13.3mS.

The three unique `pulsePat` objects described above can be created with only a few lines of code, while the compiler automatically calculates the required bias, deflection and focus settings and generates the appropriate .txt file. The capabilities enabled by the class-based architecture is best demonstrated with the example melt pattern of Fig. 3–25.

In this example, a 1/8" 304 stainless steel plate was electron beam melted at a normal incidence angle in the translation stage fixturing. All experiments were conducted at V_{acc}= 60kV with a nominal beam current of I_b= 10mA. From this beam current, the `opticsCal` sharp-focus look-up table generated a focus setting of w_b= 807mA.

Along the outer edge of the workpiece, 16*4=64 pulses were generated from four `pulsePat` objects. The topmost pattern, `pulsePat1`, represents 16 nominal pulses of energy Q_p = 3.5J(τ= 5.83mS). The leftmost pulse pattern, `pulsePat2`, is based on incrementing beam current, I_b = [3: 1: 18]mA, moving bottom to top. This pattern is based on the nominal focus and pulse length setting, such that the low current pulses do not supply sufficient Q_p to melt the workpiece, while the high current pulses have distorted melt shape, attributable to the under-focussing of the I_b= 18mA beam.

Along the bottom of the image, `pulsePat3` increments the pulse energy over Q_p= [1.1: 0.3: 5.9]J (τ= [1.83 : 0.5 : 9.83]mS), moving right to left. As expected, the melt area increases with increasing pulse energy. Finally, `pulsePat4` maintains the nominal beam parameters, and varies the focus coil current over the range w_b= [772: 5: 842]mA, moving top to bottom.

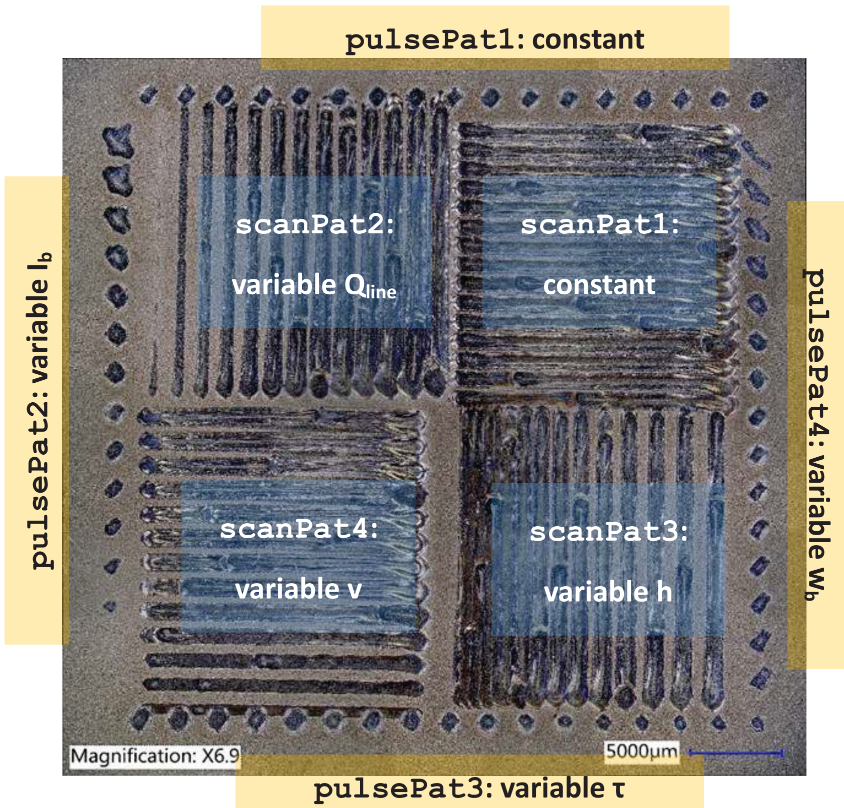

Figure 3–25: Example of gCode compiler architecture: Melting of 304 stainless steel using nominal beam parameters: V_{acc}= 60kV, I_b= 10mA, w_b= 807mA. The pulsed melting operations are varied about Q_p= 3.5J(τ= 5.83mS) while the scanning patterns are varied about Q_l= 4J mm^{-1}(v= 150 mm s^{-1})

The center of the melt pattern contains 13*4= 42 unique melt tracks, generated from four `scanPat` objects. The upper right pattern, `scanPat1`, represents the nominal melt pattern, defined by an incident line energy of Q_l= 4J mm^{-1} and hatch spacing h_s= 1.0mm. Similar to the `pulseBuild` example above, `scanBuild` determines the travel velocity according to the constraint $v = V_{acc}I_b/Q_l$= 150 mm s^{-1}.

In `scanPat2`, the line energy was swept over the range Q_l= [1.0 : 0.5 : 7.0] J mm^{-1} while maintaining v= 150 mm s^{-1}. In order to increase Q_l with the fixed v, a variable I_b must be used. Thus, the compiler references the look-up tables within `opticsCal` to generate commands for a sharp-focused I_b= [2.4: 1.2: 16.8]mA beam. In `scanPat3`, the spacing between lines was incremented over h_s= [0.3: 0.1: 1.5]mm, moving right to left. And finally, in `scanPat4` the travel speed is varied over the range v= [29: 28: 374]mm s^{-1} while maintaining the nominal Q_l= 4 J mm^{-1}. In this case, the beam current is constrained to be I_b= [2: 1.9: 25]mA.

Although the above example appears complex, it is important to re-iterate that the melt patterns were automatically generated from one set of nominal process parameters and varied about those center points. The advantage of the software architecture of Fig. 3–24 is that changes to any of the nominal beam parameters, which are also the center points, can be made with a few keystrokes, assuming `opticsCal` has been properly calibrated. For instance, if the accelerating voltage was changed to V_{acc}= 80kV and beam current reduced to I_b=7.5mA, the nominal beam power of 600W would be maintained. Meanwhile, the build compiler automatically re-calculates all the necessary process parameters and generates the appropriate machine commands. The implication is that each experiment is divided into two steps: creating the master script for a particular experiment, as in the example of Fig. 3–25, and calibrating the beam for the specific operating regime, which will be described next.

For further details regarding each individual class, its properties and the class-specific functions discussed in this section, the reader is directed to the in-code documentation within the MATLAB class definitions.

3.5.1 Beam Calibration via `opticsCal` objects

The previous section outlined a software architecture based on `opticsCal` objects, which represent a series of look-up tables derived from experimental beam calibrations. This approach simplifies process mapping, since beam-specific details are easily adapted to different accelerating voltages, working distance and cathodes. In the following, a brief overview of the tests required to calibrate an `opticsCal` object will be given, with further details found in the MATLAB in-code documentation of script `opticsCal_steps.m`.

The `opticsCal` objects are based on the concept that the requested beam current will govern many of the important beam parameters, such as the laser power applied to the cathode, the bias electrode voltage and focus coil current. For a given V_{acc} and WD, it was determined that each cathode must be calibrated independently, due to variations in W emission surface and installed cathode geometry. It was also determined that each cathode required an initial conditioning period to stabilize the emission characteristics. The conditioning process involved a slow, 10 minute heating schedule to degas any adsorbed contaminants, followed by multiple melting operations that provide the metallic vapor to ion-etch the tungsten surface. The cathode was deemed stable once the $[+bias](I_b)$ relationship stabilized, where $[+bias]$ is the voltage applied to the bias electrode.

Calibrating a `opticsCal` object is based on three sequential steps, which map out the following:

- I_b(laser power) relationship for space-charge operation
- $[+bias](I_b)$ relationship for open-loop beam power operation
- $w_b(I_b)$ relationship for sharp focussed melting

The principle of each step is to measure the relationship over a range of discrete points. Those data points are then stored in a property variable associated with the specific `opticsCal` object, for instance, `opticsCal.wbSharp`. When a calibrated process parameter is requested, a polynomial fit is applied to relevant data such that the compiler can interpolate the optimum setting for any requested beam current value.

Laser Power and Space Charge Operation. As previously discussed in Ch. 2, operating the cathode in space-charge limited regime is a necessary condition for high beam brightness and stable operation, implying that the cathode must operate at high

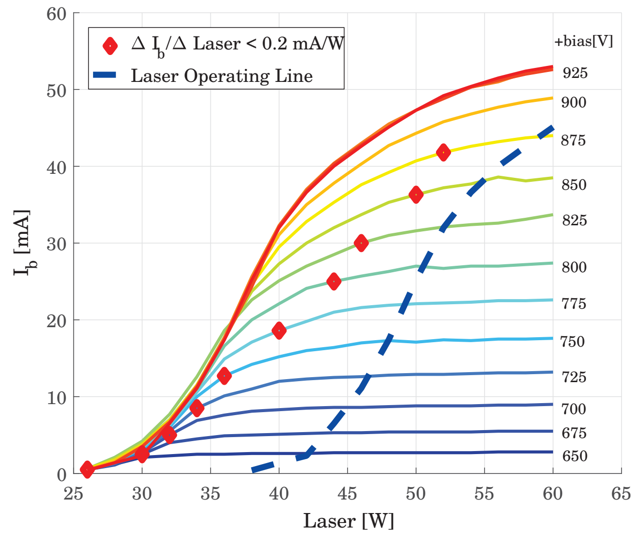

Figure 3–26: Electron beam peaking curve and laser operating line at 60kV

temperatures. If the temperature is too high, the cathode lifetime will be reduced due to evaporation, and the risk of damaging the laser heating optics increases. To balance these requirements, an operating line that determines the laser setting as a function of I_b is used, thus minimizing cathode heating while maintaining space-charge emission.

In the case of the PAVAC system, the cathode is laser heated on the backside of the ribbon filament, thus the laser power governs the cathode temperature. A modification of the method outlined by Geidt for conventional, resistively-heated cathodes was adopted to determine the laser power needed for space-charge limited emission.[158] In this method, the $[+bias]$ voltage is fixed, the laser power is incremented, and the beam current is recorded at each laser step. This process is repeated for a range of $[+bias]$ voltages, with an example measurement shown in Fig. 3–26.

By definition, space charge emission implies that the beam current is independent of the laser power. It was decided that this threshold could be mathematically described as the point where $\Delta I_b/\Delta Laser < 0.2$ mA/W. These threshold points were calculated for each $[+bias]$ value, and displayed by the red markers of Fig. 3–26, with the space-charge domain to the right of these points.

An important feature of Fig. 3–26 is that the space-charge threshold is beam current dependent. It is not clear whether this is true for all electron beam guns, or unique to the PAVAC geometry and cathode heating mechanism. Nevertheless, when the beam is operated for extended periods at low beam currents, as required for powder preheating, the laser power can be programmatically reduced to prevent cathode evaporation and laser optics damage.

To determine the laser(I_b) operating line, a melt-resistant workpiece(Cu or W) is installed within the vacuum chamber. Next, the MATLAB script `opticsCal1_bias980_meas.m` is run, generating a gCode sequence which defocuses the beam and sets a fast, large-area deflection pattern. The script sets [+$bias$]= 900V, which provides a small amount of cathode focussing to minimize anode heating.(*Note: a Cu anode has been melted by repeatedly running this algorithm, thus a delay should be provided to cool the anode*) The code increments the laser power, and the I_b(laser,[+$bias$]=900V) values recorded from the GUI are loaded into the `opticsCal.bias980` property.

Within the compiler, the laser(I_b) operating line is determined by shifting the `opticsCal.bias980` curve 12W to the right, as shown by the blue dashed line of Fig. 3–26. In this case, the operating line is within the space-charge regime, and the compiler inverts the curve to determine laser operating point for space-charge emission. If needed, the 12W shift applied to `opticsCal.bias980` can be modified via the `opticsCal.laserOpShift` property.

Manual Bias setting. During conventional operation of the PAVAC system, I_b is regulated using a digital Proportional Integral Derivative(PID) feedback loop, where the current reading from the high voltage supply is the process variable, the requested current is the set point and the [+$bias$] voltage is the control variable. For a detailed discussion of the PID regulation scheme used in the PAVAC system, see. [65]

This regulation scheme is satisfactory for conventional EBW, as the rise time requirements are not overly stringent compared to the time scale associated with the process. In terms of single-shot, millisecond pulses, it was determined that the PID regulation could not provide consistent pulse energy, and FC measurements demonstrated overshoot and ringing in the beam current reading. The FC measurements also determined that approximately 14mS were required to stabilize the [+$bias$] setting when a I_b= 6mA beam was requested.

After discussions with PAVAC, it was determined that reconfiguring the PID controller required engineering resources outside of the scope of the project. Therefore, the beam was operated in manual bias mode, whereby the $[+bias]$ value is manually set prior to the pulse, thus operating the beam in open-loop power regulation.

In this case, an algorithm similar to setting the laser power was developed. Using the space-charge laser operating line, a gCode is generated by running `opticsCal2_biasIb_meas.m`. This code steps through a series of beam current requests in PID mode, and the $[+bias](I_b)$ relationship is recorded from the GUI. Since the beam is energized for 2 seconds at potentially high beam powers, care must be taken to ensure the workpiece can withstand high heat loads. The recorded $[+bias](I_b)$ values are loaded into to the `opticsCal.biasIb` property and used in subsequent gCode compiles.

Because look-up tables are inherently open-loop, issues surrounding stability of the cathode emission, and thus beam current, needed to be addressed. It was determined that stable emission required a gun vacuum below 1E-5mbar and a stable cathode thermal environment. This latter point is demonstrated by the measurements shown in Fig. 3–27, which represent $[+bias](I_b)$ mappings over the course of 8 minutes, with each data set recorded at 2 minute intervals. The figure also includes a linear fit to each data set, with the results shown in the legend.

From the linear fits, we see that the slope is relatively constant (m= 7.1 V/mA), whereas the intercept decreases by approximately $6V$ over the course of the experiment. This drift is attributed to the stability of thermal environment around the cathode, which includes conductive heating of the cathode holder and radiative heating of the surrounding gun. To stabilize the emission characteristics before each experiment, the cathode was heated for 8 minutes using a custom programmed script.

The data of Fig. 3–27 can also be used to estimate the errors associated with open-loop operation. To begin, $I_b([+bias])$ can be estimated from the inverse slope of Fig. 3–27, which is equal to $1/m \approx 1/7.1 = 0.14$mA/V. Assuming the cathode is not warmed prior to use, a worst case estimate of the$[+bias]$ error is $\approx 6V$. Therefore, it the gCode compiler generates a $[+bias]$ voltage off by 6V, the corresponding current error is 6V$*$0.14mA/V= 0.84mA, suggesting that the proportionality of the error will decrease with increasing

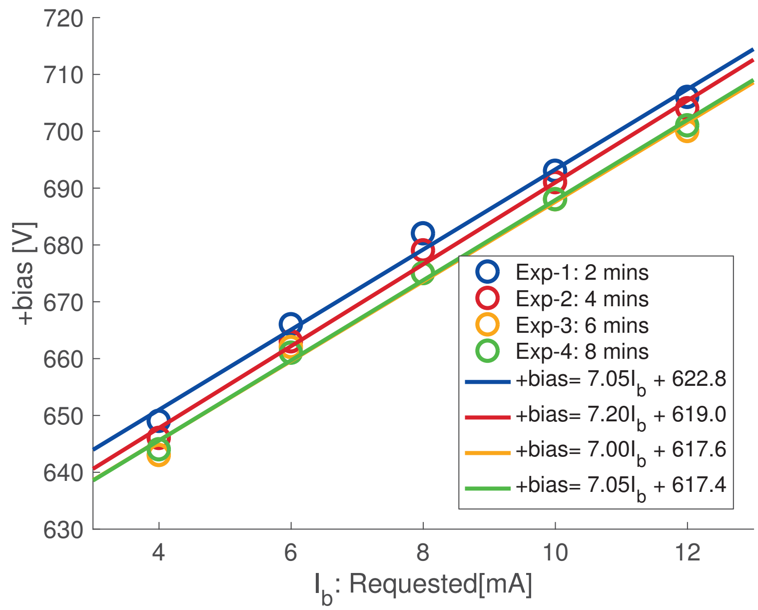

Figure 3–27: Cathode emission drift at 60kV for I_b = [4:2:12]mA recorded at 2 minute intervals. Note that slope of fit is constant, while intercept drifts with time

I_b. In most cases, a reduced $I_b/[+bias]$ mapping was conducted before and after each experiment, with $[+bias]$ drift of no more than 2V, resulting in a 2V*0.14mA/V= 0.3mA beam current error.

As a final note, by periodically recording the $[+bias](I_b)$ relationship over the course of the cathode, it is possible to predict when a cathode has reached its end of life, as mapping will begin to deviate from the previously recorded values.

Focus Setting. Having determined the laser power needed for space charge emission(`opticsCal.bias980`), and the $[+bias]$ voltage needed for stable pulses(`opticsCal.biasIb`), the final step in the calibration process is to determine the beam current/focus current relationship to maintain sharp focus.

As shown by the FC measurements of Fig. 3–10, the focus coil current needed to generate a sharp focussed beam is dependent on both V_{acc} and I_b. Since each `opticsCal` object is uniquely associated with a V_{acc}, this calibration step requires mapping the $w_b(I_b)$ relationship.

Initially, it was believed that the relationship could be mapped once using the FC measurements, but swapping out the various fixtures proved to be time-consuming, especially with respect to alignment. Therefore, a novel calibration technique was developed, based on the previously discussed fluence threshold for melting.

To explain this method, assume a fixed V_{acc}, I_b and Q_p incident on a material with low thermal diffusivity, such as Ti64 (α= 2.9 mm$^2 s^{-1}$). From these fixed values, multiple pulses with incrementing w_b values are generated. By modifying w_b, the beam is generating pulses of variable σ and thus variable fluence q_p[J mm^{-2}], while maintaining a constant Q_p[J]. If Q_p is sufficiently low, we expect that only the beam with the highest q_p will melt, which, by definition, represents the sharp focus condition.

This concept is further illustrated with the array of beam pulses shown in Fig. 3–28, which were automatically generated by using the `opticsCal6_wbEOScan.m` script.

As shown by the axes of the image, each column represents a fixed focus setting, which is scanned over the range w_b= [810: 2: 834]mA. This vector was generated from an initial the sharp focus estimate ($w_{b,i}$= 822mA), defining the number of pulses($2N-1$ =13), assigning a pulse step(Δw_b) such that w_b= $[822-N\Delta w_{b,i},\ 822-(N-1)\Delta w_{b,i}, ..., w_{b,i}, ..., 822+N\Delta w_{b,i}]$. Meanwhile, each row represents a fixed pulse energy, which was scanned over the range Q_p= [0.1: 0.2: 2.5]J, resulting in a total of 169 unique 60kV/10mA pulses.

From the figure, we see that the Q_p=0.1J row did not supply sufficient fluence to melt workpiece, whereas only the middle Q_p= 0.3J pulses melted the Ti. Conversely, for Q_p > 1.3J, all the pulses resulted in melting, albeit with different melt profiles. By inspecting these pulses under the microscope, it is possible to determine that the sharp focus 60kV/10mA is given by w_b= 822mA.

To map out sharp focus for range of I_b values, this concept is extended such that each row is a separate I_b value, with a uniquely assigned Q_p which is on the threshold of melting, similar to the the Q_p=0.3 condition of Fig. 3–28.

Generating the gCode associated with this process has been automated in the `opticsCal3_wbSharp_meas.m` script. An example of a 60kV melting of Ti64 scanned over

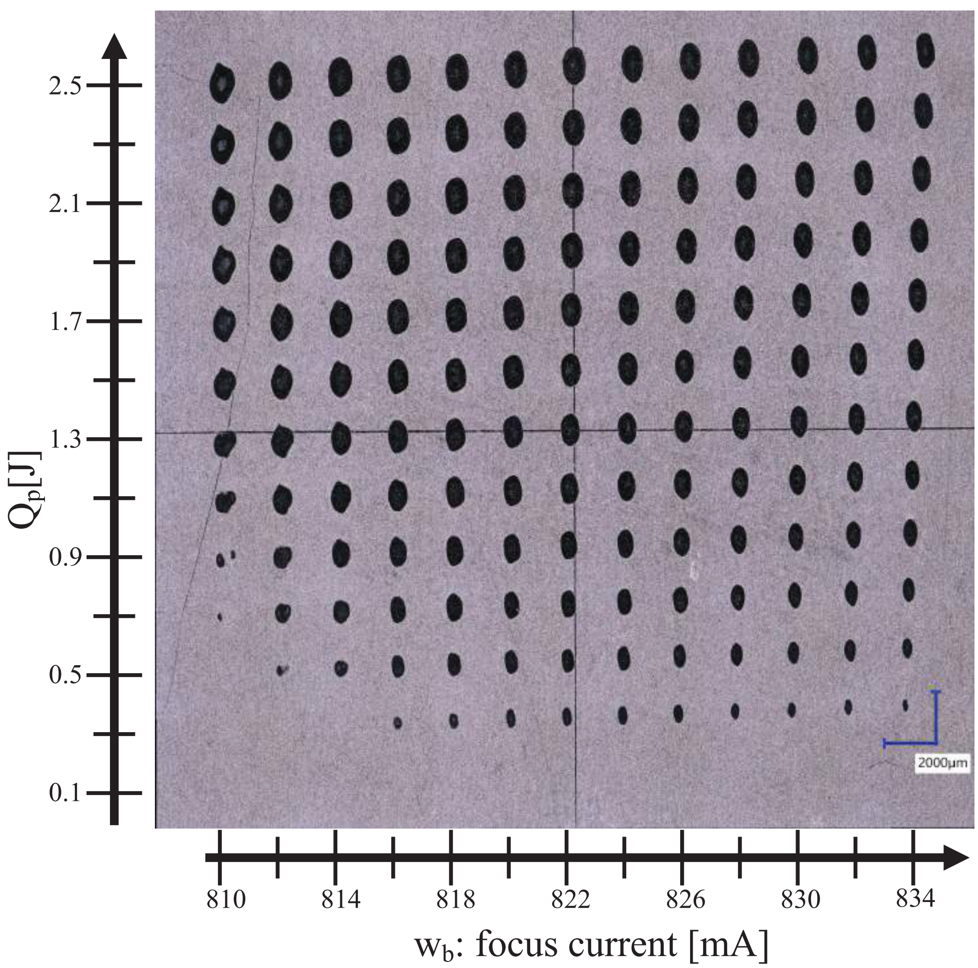

Figure 3–28: Q_p vs w_b at 60kV/10mA on Ti64 at 55^o incidence

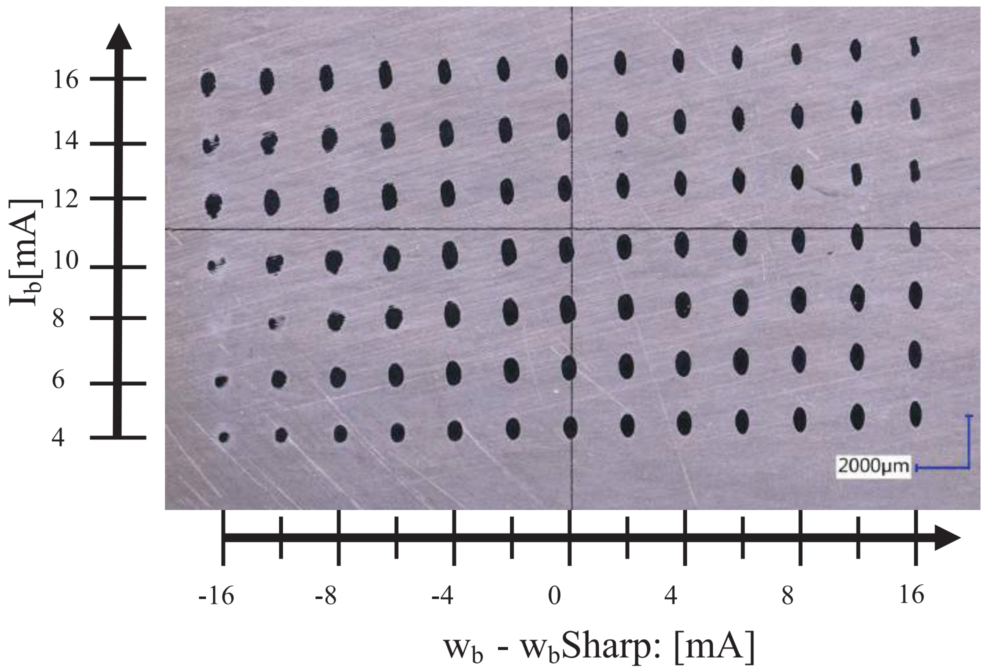

Figure 3–29: Sharp focus calibration routine at 60kV using `opticsCal3_wbSharp_meas.m` on Ti64

I_b= [4: 2: 16]mA using a focus coil step of Δw_b= 4mA is shown in Fig. 3–29, with the beam parameters listed in Table. 3–3

While the Δw_b values of Fig. 3–29 are identical, initial sharp focus estimates for each I_b row are uniquely defined by $w_{b,i}$. For a newly installed and conditioned cathode, a two step procedure to calibrate the sharp focus value is used, using a large Δw_b in the first step, followed by a finer Δw_b in the second step.

Laser Power[W]	I_b[mA]	[$+bias$][V]	τ[uS]	Q_p [J]	$w_b Sharp$ [mA]
35.5	4	647	4167	1	781
36.6	6	664	2222	0.8	797
37.4	8	678	1542	0.74	806
38.2	10	691	1067	0.64	818
39.4	12	702	833	0.6	830
39.9	14	713	690	0.58	836
41.1	16	723	604	0.58	847

Table 3–3: Nominal beam parameters used for `opticsCal3_wbSharp_meas.m` experiment of Fig. 3–29 using a Δw_b= 2mA

The sharp focus $w_b(I_b)$ results are integrated into the compiler via the `opticsCal.wbSharp` property and used in subsequent process calls via polynominal interpolation. The compiler also allows process calls with offset values from these sharp focus settings, enabling a capability similar to the Focus Offset (FO) setting used in the Arcam system. In future work, it would be useful to extend this concept by requesting a physics-based focus offset, either as Peak Power Density (PPD) or distance offset between working and focal plane. Despite a compiler architecture amenable to this abstraction, the extensive integration of the FC measurements with the process compiler were not pursued due to time constraints.

In summary, the I_b dependent process variables of Table 3–3 highlight the importance of the modular process architectures demonstrated in Fig. 3–23 and 3–24. Without a well-devised system to manage various beam interactions, it would not be possible to generate the variable I_b process associated with EB-PBF.

CHAPTER 4
Results: Transient Calorimetry and Monte Carlo Simulations

4.1 Introduction

Electron beam heat transfer models are based on accurate initial data regarding the material properties and absorbed beam energy. While the temperature-dependent material parameters can be determined using ex-situ techniques, the absorbed energy is often process dependent, and scaled according to the incident energy via the prefactor η, commonly referred to as the absorption coefficient or beam efficiency.

In one example, welding process models are calibrated against a variety of experimental results; including transient temperature measurements and metallurgical examination of the weld zone. Since the absorbed energy impacts both quantities, the η parameter is adjusted until sufficient agreement between experiment and model is obtained. [81, 94]

Although thermocouples(TC) are a commonly used temperature sensor, the shrinking process domains and interaction times associated with localized electron beam melting requires careful consideration regarding the sampling frequency, junction size, positioning, joining method and response time.[159] These issues can pose challenges when measuring transient processes such as EBW and EB-PBF.

One solution is a calorimetric approach, whereby the material is heated in a thermally isolated fixture and the absorbed energy is determined by comparing the temperature rise to the net enthalpy increase. The technique was used to determine η during CO_2 laser irradiation, and supported process-microstructure modelling of eutectic Al-Cu 33wt% and single-crystal nickel superalloy.[160, 161, 162] It has also been used to estimate the energy absorption of Inconel 706 during keyhole-mode electron beam welding.[104]

More recently, in-situ TCs have been used to calibrate heat transfer models of EB-PBF of 316L stainless steel and L-PBF of Inconel 718.[146, 163, 164] Thermocouples have also supported Directed Energy Deposition (DED) modelling and calibrated the effective emissivity of solid and powder material at high temperatures.[165, 166, 167, 168]

In some cases, in-situ measurements are supplanted by computational fluid dynamics models with sufficient complexity to directly capture the volumetric heat transfer and the resulting weld zone characteristics. Good model agreement was achieved for explosive backing keyhole-type electron beam drilling of steel using an absorption coefficient of η=0.99 and a beam peak power density (PPD)≈10 kW mm^{-2}.[169] A value of η=0.2 was used to model keyhole-mode electron beam welding of 304 stainless steel over a range of PPDs (8-34 kW mm^{-2}), although the details regarding keyhole reflections are unclear.[85] A model for Nd:YAG laser spot welding of 304 stainless steel using η=0.27 at PPDs of 2-6kW/mm^2 accurately captured many of the process details, including fusion zone shape and alloy evaporation. [82]

This chapter details a novel technique for measuring the conduction-mode absorption coefficient, η, for millisecond electron beam interactions at PPDs less than 2kW mm^{-2}. Using a combination of precisely timed electron beam pulses, a novel process geometry, fast response thermocouples, and non-linear curve fitting, η is uniquely determined over 103 pulsed spot melting experiments. Agreement between experiment and Monte Carlo simulations is shown over a range of beam parameters, including variations in accelerating voltage, beam current, pulse length and incidence angle.[170]

Monte Carlo simulations were conducted using the open-source software CASINO in order to generate the BSE energy spectrum, which is then summed to give the energy reflected out of the sample. Previously, this software was used to examine the heat penetration depth during poly-energetic electron beam ablation, as well as the depth-dose effects during Critical Energy Electron Beam Lithography of insulating substrates.[171, 172, 173] CASINO has recently been used to estimate the beam diameter growth during EB-PBF of 316L stainless steel, although no experimental validation was given.[174] Klassen *et al* calculated the absorbed electron beam energy using semi-empirical equations, but measurements at power densities sufficient for melting were not provided.[175] As far as the author is aware, this work represents the first experimental validation of high power electron beam energy absorption using Monte-Carlo techniques.

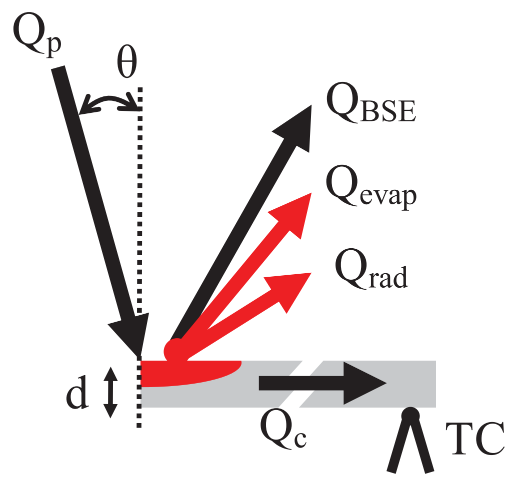

Figure 4–1: Schematic of dominant electron beam energy balance terms, applied to an axis-symmetric geometry

4.1.1 Electron Beam Energy Balance

Each individual absorption measurement is defined by a single electron beam pulse, or spot melt, of incident pulse energy:

$$Q_p = V_{acc} I_b \tau \tag{4.1}$$

During electron beam heating, the incident beam energy is divided among four dominant heat transfer mechanisms:

$$Q_p = Q_{BSE} + Q_{evap} + Q_{rad} + Q_c \tag{4.2}$$

where Q_{BSE}, Q_{evap} and Q_{rad} are the energy loss terms associated with BSE, evaporative cooling and radiative cooling, respectively. The remaining conduction heat, Q_c, is transported through the solid according to Fourier's law. A schematic diagram of these heat transfer mechanisms is shown in Fig. 4–1.

Terms associated with X-ray generation, SE, beam transit losses and convective cooling have been omitted, as they form a negligible fraction of the energy balance during high-vacuum electron beam melting experiments. [36] Also, the heat carried by melt expulsion and vapor shielding will be ignored.

To facilitate process comparisons, Eq. 4.2 is normalized with respect to Q_p, yielding:

$$1 = \Gamma_{BSE} + \Gamma_{evap} + \Gamma_{rad} + \eta \tag{4.3}$$

where Γ_i is the respective fraction of energy transported out of the sample, while the absorption coefficient, η, represents the fraction of incident energy transported through the solid, Q_c/Q_p.

Whereas, the evaporative and radiative terms are only activated at high temperatures, the Γ_{BSE} term in Eq. 4.3 is intrinsic to the electron beam physics, a feature highlighted by the color coding of Fig. 4–1.

To facilitate comparison to simulations, it will prove useful to define η_0 according to:

$$\eta_0 = 1 - \Gamma_{BSE} \tag{4.4}$$

which represents the fraction of available incident beam energy, under the condition that $\eta_0 \leq 1$. Eq. 4.4 enables comparisons to laser-based processes, recognizing that the laser equivalent of Γ_{BSE} is the surface reflectivity, R. Substituting Eq. 4.4 into the normalized energy balance of Eq. 4.3 gives:

$$\eta_0 = \Gamma_{evap} + \Gamma_{rad} + \eta \tag{4.5}$$

It is worth discussing a few characteristic examples that demonstrate the dependencies of Eq. 4.5. In the simplest example, during scanning electron microscopy, the beam power is so low that the local temperature rise at the irradiation point is neglible, implying that $\Gamma_{rad}, \Gamma_{evap} \rightarrow 0$ and $\eta_0 = \eta$. Conversely, to suppress the formation of a heat affected zone, femto-second laser machining requires that $\Gamma_{evap} \rightarrow \eta_0$, resulting in $\eta \rightarrow 0$.[176] During laser surface remelting of Al-Cu33, it was found that η_0 was dependent on the material state(liquid/solid), implying that η_0 and η are coupled via the local enthalpy rise.[160] As a final example, the formation of a vapor capillary during keyhole welding requires $\Gamma_{evap}>0$. Although counter-intuitive, $\Gamma_{evap}>0$ actually increases η_0, since the vapor capillary focuses the reflected energy back into the sample.[36]

These examples highlight the subtle distinctions between the far-field temperature response associated with the η term and the local energy absorption, associated with the

η_0 term. In other words, an η_0 fraction of incident energy can be converted to evaporative or radiative energy, whereas an η fraction of incident energy is conducted far from the spot melt, after these extrinsic heat transfer mechanisms have been removed from the energy balance.

In the following, experiments are presented whereby the electron beam is pulsed onto a thin sheet of 304 stainless steel (SS304), resulting in a localized, conduction-mode spot melt. A thermocouple joined to the backside of the sheet records the temperature response of the pulse, as per the schematic of Fig.4–1. The physio-spatial dimensions of the pulse, sheet and thermocouple(TC) are chosen so that the temperature response can be analytically described by an instantaneous line source of energy $Q_c = \eta Q_p$. Thus, the absorption coefficient associated with far-field heat conduction is directly extracted as a fit parameter from the TC measurements over a wide range of process configurations. Open-source Monte Carlo methods are used to estimate η_0 and these values are compared to experiment.

4.2 Experimental Methods

The specific experimental configuration used during these experiments represents a combination of systems described in Ch. 3. In the following section, the specific details of each system used will be given.

Each measurement campaign is defined by a combination of accelerating voltage, beam current and incidence angle; denoted $[V_o, I_b, \theta]$, where θ is the angle between the surface normal and beam axis. As discussed in Sec 3.5, a unique `opticsCal` object is calibrated for each $[V_o, I_b, \theta]$ combination, which was varied over V_{acc}= [60,80]kV, I_b= [10,15,20]mA, θ= [0, 15, 35, 55, 65]^o. The pulse energy is varied over the range Q_p= [1,...,5.5]J, which yields a peak fluence ranging from q_o =[1.5,...8.5] J mm^{-2} , assuming a σ= 0.32mm. A master MATLAB script generates the two `pulsePat` objects: one with constant Q_p and another with incrementing Q_p. Each `pulsePat` object is composed of 8 pulses, arranged in a circular pattern with a radius of r_0=4mm, with a separation of 25mm between patterns.

304 stainless steel sheets with dimensions 50x75x0.250 mm were placed in the translation stage fixture. The sheet thickness exceeds the electron range, which is less than

t_{SS} [mm]	c_p [J/g K]	$H_l - H_{25C}$[J g^{-1}]	α [mm^2/s]	ρ [g/mm^3]
0.250	0.4853	1129	3.8767	8.015*10^{-3}

Table 4–1: Thermophysical material parameters for 304 stainless steel, as given in *Mills*[26]

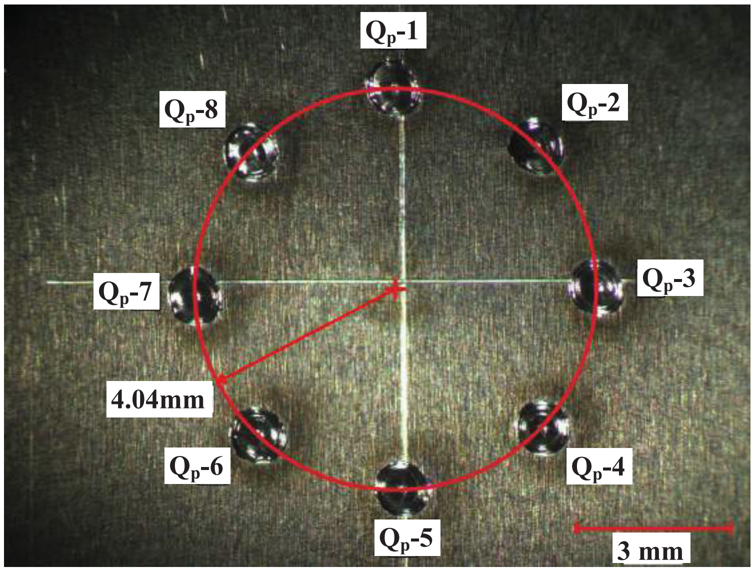

Figure 4–2: Sample surface for x8 pulses of Q_p = [2.5]J. The scribe marks indicating nominal location of thermocouple junction, which is joined to sheet backside

$20\mu m$ for the beam energies and incident angles used.[36, 175] The corresponding surface enthalpy of melting, $\delta h_m = t_{SS} * \rho * (H_l - H_{25C})$= 2.25 J mm^{-2}, using the thermophysical material parameters given in Table 4–1. For comparison, the δ_m associated with most EB-PBF processes is on the order of 0.1-0.4 J mm^{-2}.

Two AWG 30 K-type TCs are welded to the backside of the sheet in the center of each circular pattern. This TC/`pulsePat` configuration, shown in Fig. 4–2, enables 8 separate measurements per TC, while maintaining equal distance between the pulse and TC. Before each pulse, the sheet is allowed to thermally equilibrate over 50s, and it is assumed that the re-solidified material maintains its prior heat transport properties.

With the TC positioned r_0=4mm from each spot melt, the perturbation associated with 0.1mm^2 thermocouple conductance path is low. The signal generated from the furthest TC is used to confirm the inter-pulse cooling period, with a plot of the aggregate, post-processed TC measurements from a `pulsePat` with constant Q_p is shown in Fig.4–3.

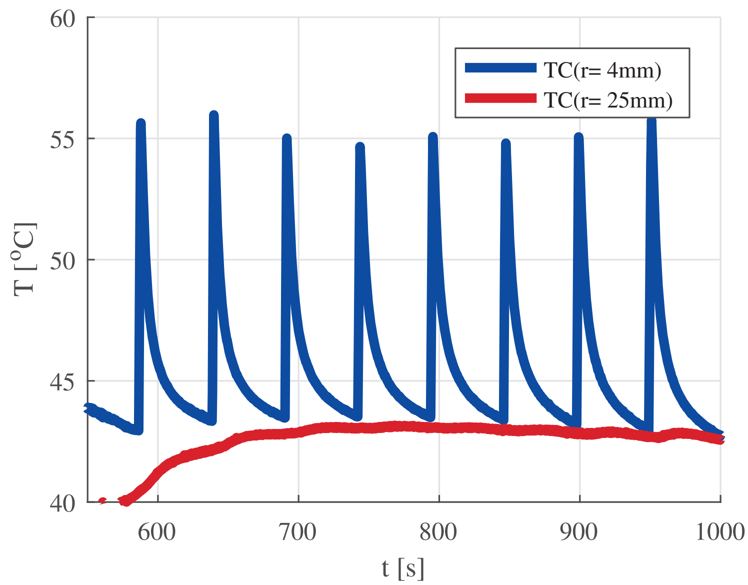

Figure 4–3: Thermocouple signal for eight Q_p= 2.5J spot melts. The TC located at the center of the pulse pattern is shown in blue, while the TC located roughly 25mm away is shown in red. The corresponding pulse pattern is shown in Fig. 4–2.

From these measurements, the maximum ΔT between the two TCs before each pulse can be used to estimate a thermal gradient of order $dT/dr < 0.1$ C mm^{-1}, confirming that the 50 second inter-pulse cooling period is sufficient to homogenize the temperature field within the sheet.

All experiments were conducted at pressures P<2E-5 mbar in both the sample and electron beam chambers.

4.2.1 Temperature Response Model

As previously discussed, the far field absorption coefficient, η, is determined from the transient temperature measurements by modelling the pulse as an stationary, through-thickness line source within a thin, infinite sheet of initial temperature T_0 along with temperature-independent material parameters. If the heat source is instantaneously liberated at $t = t_0$ with an assumed strength $Q_c = \eta Q_p$, the axis-symmetric transient temperature response at position r_0 is defined according to:

$$T_p(t) = \frac{\eta Q_p}{t_{SS}} \frac{exp[-r_0^2/(4\alpha(t-t_0))]}{4\pi\rho c_p \alpha(t-t_0)} - T_0 \tag{4.6}$$

where t_{SS} is the sheet thickness, r_0 is the radial distance from the heat source to the measurement point, α is the thermal diffusivity, ρ is the density, c_p is the heat capacity, and t is time.[77]

The idealizations underpinning Eq. 4.6 will determine the curve fitting accuracy, and will be briefly examined. Firstly, the fit is performed over a 5 second domain, which has an equivalent thermal diffusion length of $L_{th} = 2\sqrt{\alpha t} = 9$mm. This value is less than the distance between any spot melt and the outer copper fixture($\approx$ 20mm), confirming the infinite plane assumption. It was previously shown that the 50s delay between pulses homogenizes the background temperature to T_0<0.1^{o}C/mm, showing that T_0 is nearly constant. Similarly, the range of TC measurements is $40 - 80^oC$, over which the material parameters can be considered constant.

The most challenging idealization is that of the line-source, which implies no through-thickness temperature variation. Experiments at different r_0 values were undertaken to balance the conflicting requirements of large ΔT(small r_0) against accurate model conformance(large r_0). It was found that for $r_0 > 3mm$, the adjusted R-square value, which is a measure of agreement between model and measurement, was in the range of 0.999 or greater. Although the through-thickness temperature gradient is very high at the end of each pulse, by increasing the heat propagation distance such that $r_0 >> d$, the necessary $dT/dz \rightarrow 0$ condition is achieved.

For each individual pulse, the slowly varying background temperature T_0 is removed by performing a linear fit over the 10 seconds prior to the pulse. Shown as a dashed line in Fig. 4–4a, this background signal is then extrapolated forward in time, and subtracted from measurement to yield $T_p(t)$, with the t_0 of each pulse shifted such that T_p >=1^{o}C at t=0s.

Using the MATLAB curve fitting toolbox, the non-linear least-squares method is used to fit the $[t, T_p(t)]$ signal to Eq. 4.6, with fit outputs: [η, r_0,t_0.]. The thermophysical material parameters used in Eq. 4.6 for SS304 are defined in Table 4–1.

Good convergence was obtained when the fit domain was restricted to $0.2 < t < 5$s, ostensibly to reduce the impact of the $1/t$ asymptote of Eq. 4.6. A representative fit for $T_p(t)$ is shown in Fig. 4–4b, with excellent agreement over the entire domain.

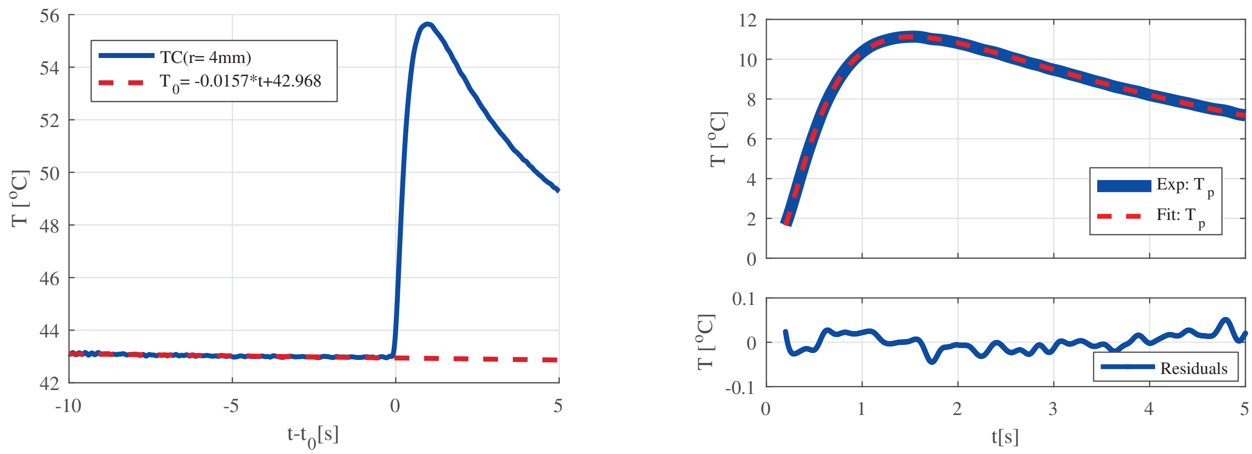

(a) (b)

Figure 4–4: Curve fitting procedure for Q_p=3J (a) Background temperature curve fit with aggregate TC measurements (solid-blue), and extrapolated background temperature(dashed-red) (b) Measured response(blue-upper) and curve fit (red-dashed) to Eq.4.6 with fit residuals shown in lower panel. Fitting Results: η= 0.830, r_0= 4.35mm and adjusted R-square = 0.9999

An important attribute of this methodology is the robustness against errors in thermocouple/beam alignment and finite TC junction dimensions. By monitoring the adjusted R-square value and applying small time-shifts, experiments showed statistically constant η values over a range of r_0 values. This can be explained by considering that the amplitude and shape of the temperature response in Eq. 4.6 is defined by the terms: $1/t * exp[-r_0^2/(4\alpha t)]$. Meanwhile, the fit parameter η can only affect the temperature amplitude, which has good signal-to-noise of roughly 10 ^{o}C over 0.25^{o}C. In other words, by choosing a time domain that includes the temperature peak along with a few $r_0^2/4\alpha$ decay constants, the non-linear fit can accurately discriminate between η and r_0 contributions.

4.2.2 Monte-Carlo Simulations: Γ_{BSE}

Upon entering a solid, electrons undergo a series of elastic and inelastic scattering events, and the interplay between the electron energy and scattering cross-section defines the profile and fraction of energy absorption. To the first order, the material interactions are largely determined by the composite atomic number of the sample, the atomic weight, density and beam energy.[175, 36, 37]

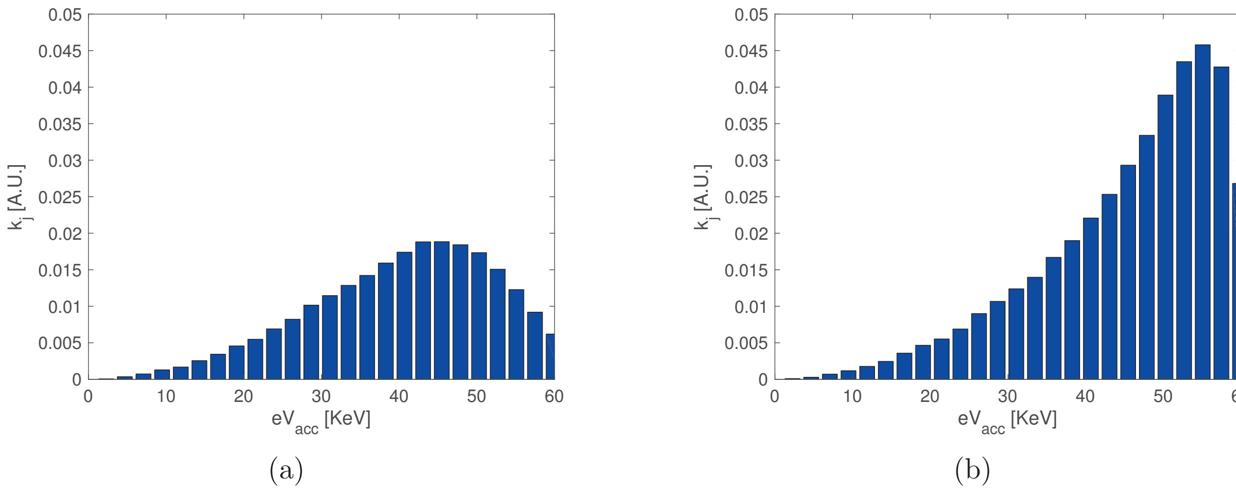

Figure 4–5: Back-scatter electron energy distribution simulated in CASINO using a 60keV beam. Left: Normal incident angle. Right: Incidence angle of θ=55^o

We are specifically interested in the incident electrons that enter the solid, undergo a series of scattering events, and leave the solid, while also depositing some fraction of their incident energy. The characteristics of these electrons, termed Back-Scattered Electrons (BSE), are well suited for Monte-Carlo simulation techniques.

The open-source software CASINO was used to simulate the exit energy spectrum associated with the BSEs over a range of incidence angles and accelerating voltages. The simulations were conducted using nominal material composition of 19wt% Cr - 9.3wt%Ni - 1.0%Mn - Bal.Fe. The addition of trace alloy components were omitted, as the simulation results were insensitive to their addition. For good convergence, 300,000 discrete electron trajectories were simulated for each process combination.[65]

Fig. 4–5 demonstrates the BSE energy spectrum for two incidence angles, θ=0^o and θ=55^o, where the y axis is defined by the fraction of electrons, k_j, exiting the sample with energy V_j.[170]

At higher incidence angels, Fig 4–5 demonstrates that the BSE spectrum is weighted towards higher energies, which can understood by the fact that at grazing incidence, electrons require statistically fewer scattering events before being deflected out of the sample.[175]

From these results, it is possible to calculate the fraction of BSE which are scattered out of the sample, Γ_{BSE-e}.

$$\Gamma_{BSE-e} = \sum_j k_j \tag{4.7}$$

For the results of Fig. 4–5, Γ_{BSE-e^-}= 0.233 and 0.416 for θ= 0,55^o, respectively. This number represents the BSE *charge* carried out of the sample, as high eV electrons are given equivalent weight as low eV ones. Accordingly, the fraction of incident *energy* carried out of the sample due to BSEs, Γ_{BSE}, is given by:

$$\Gamma_{BSE} = \frac{\sum_j k_j V_j}{V_{acc}} \tag{4.8}$$

Eq. 4.8 can be understood considering that each incident electron has a probability k_j of leaving the sample with energy V_j, such that the energy-weighted sum gives the net energy reflected out of the sample. For the results of Fig. 4–5, Γ_{BSE}= 0.152 and 0.309 for θ= 0,55^o, respectively.

The differences in Γ_{BSE} and Γ_{BSE-e^-} are the first indication that charge and energy transfer are not equivalent. Although this topic will be discussed in the following chapter, net charge transfer also depends on the surface state of the workpiece, via the surface-sensitive Secondary Electrons (SE), as well as the ionized evaporative flux of the workpiece.[37, 172, 177, 178]

CASINO simulations were conducted for a variety of incidence angles. The calculated Γ_{BSE} were transformed to $\eta_0(\theta)$ using Eq. 4.4, with the results shown in Fig. 4–6. This figure also includes an empirical fit, which will be used in the subsequent section for experimental comparison.

4.3 Results

4.3.1 Absorption Coefficient at Normal Incidence

Normal incidence spot melts from each `opticsCal` object with a Q_p= 2J are shown in Fig. 4–7. These spot melts represent a matrix of process parameters, with V_{acc}=[60,80]kV and I_b= [10,20]mA. It should be noted that the circular shape of the spot melt is indicative of a sharp-focussed electron beam.[150] The corresponding η fit results from the TC thermocouple signals are shown in Fig. 4–8.

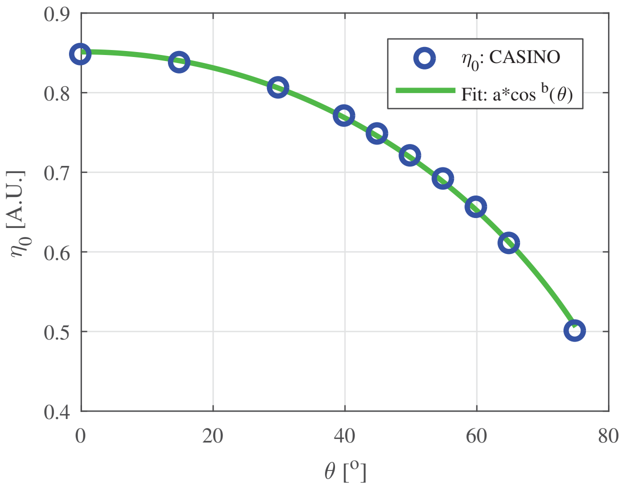

Figure 4–6: CASINO results for $\eta_0(\theta)$, as transformed by Eq. 4.4. Included is an empirical curve fit, $\eta_0 = a * cos^b(\theta)$ with a=0.8513 and b=0.3851 and an adjusted R-square value of 0.9989

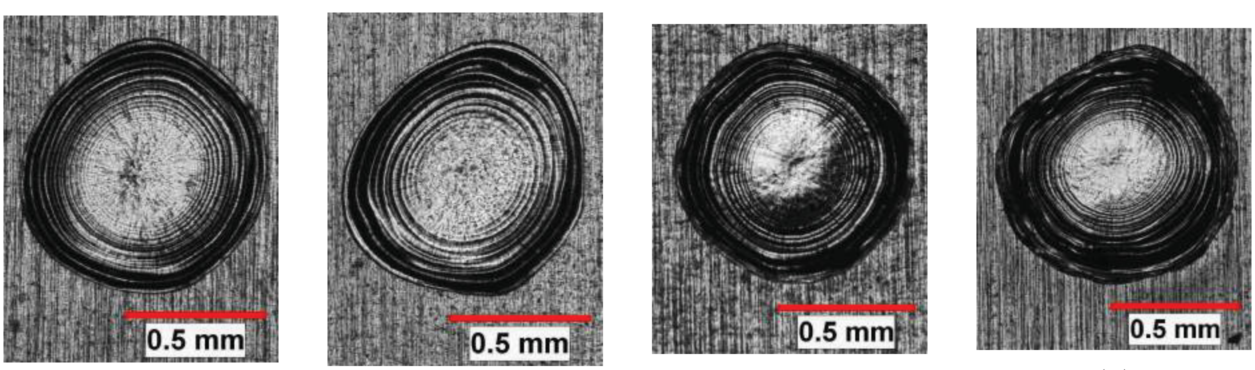

(a) (b) (c) (d)

Figure 4–7: Normal incident angle spot melts with Q_p= 2J. (a) [60kV,10mA] (b) [60kV,20mA] (c) [80kV,10mA] (d) [80kV,20mA]

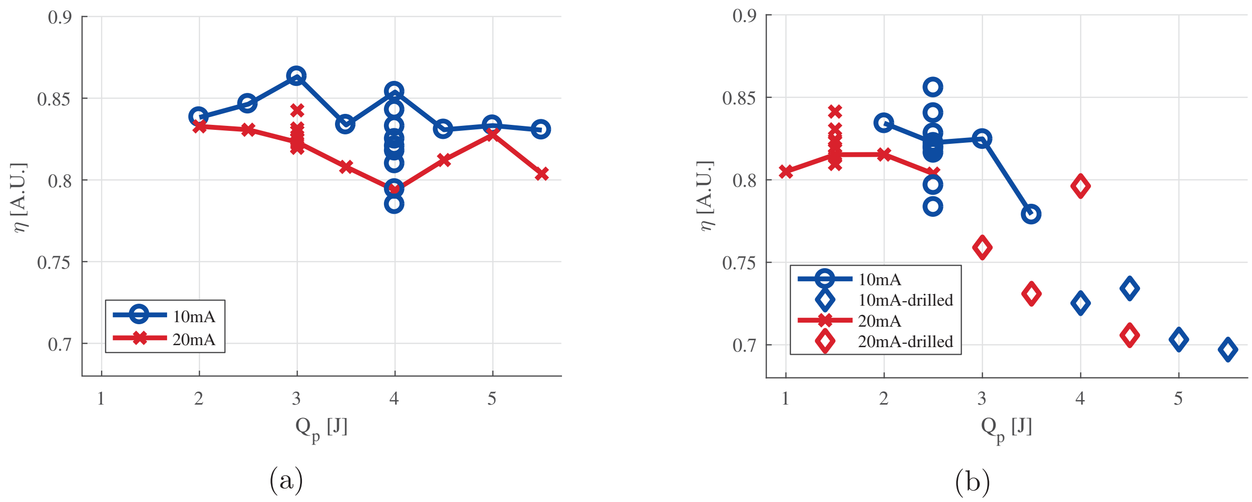

Figure 4–8: Fit results for Q_p vs η, with 10mA pulses (blue circles) 20mA(red x) with drilled holes shown with diamond. (a) V_o= 60kV: η=0.828±0.015 with a mean adjusted R-square statistics = 0.9997 ± 0.0002 (b) V_o= 80kV: η=0.819 ± 0.017 with a mean adjusted R-square statistics= 0.9998 ± 0.0001, excluding perforated spot melts

From the 60kV measurements of Fig 4–8a, it can be observed that the η results are statistically insensitive to beam current and pulse energy for the range of parameters investigated, with a mean value of η=0.828±0.015 over the 32 measurements. Assuming η is a fixed value for conduction-mode melting, the small standard deviation over multiple campaigns demonstrates good process stability and validates the calibration of the `opticsCal` objects.

Fig. 4–8b presents the η fit results measured at 80kV, where it can be observed that η decreases with increasing pulse energy at both I_b= [10,20]mA. This is easily explained, as it was observed that the electron beam had perforated the thin stainless steel sheets at higher Q_p. Therefore, the 80kV samples were inspected, and the perforated spot melts marked with a diamond in Fig. 4–8b. Excluding these perforations, statistics from the remaining 24 measurements yields η=0.819 ± 0.017.

At normal incidence, Γ_{BSE} was calculated in CASINO at 60 and 80kV to be 0.153 and 0.146, respectively. Considering the 5% difference, the average of these values, Γ_{BSE} =0.149 is used to estimated η_0=0.851, according to Eq.4.4. A histogram of the experimentally determined η values for all non-perforated spot melts is compared to the η_0 simulation result in Fig 4–9.

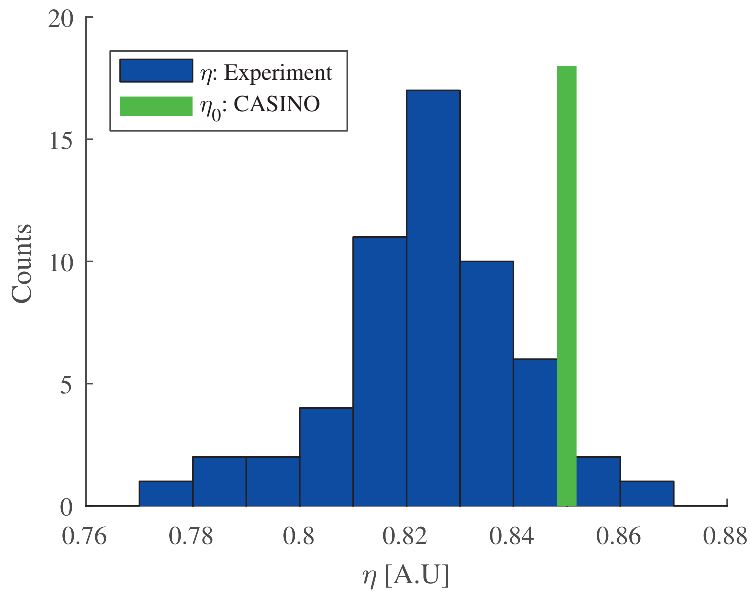

Figure 4–9: Experimental statistics of η at normal incidence with V_o=[60,80]kV and I_b=[10,20]mA with a η=0.82± 0.02. The CASINO simulated η_0 value is 0.851

4.3.2 Absorption Coefficient at Inclined Incidence

Inclined incidence spot melts for V_{acc}= 60kV, I_b= 15mA are shown in Fig. 4–10. In this case, we see that the shape of the spot melt becomes more elliptical with increasing angle. This response is expected, as the power density of the beam is projected onto the inclined workplane.

Statistics similar to Fig. 4–8 were measured using a [60kV,15mA] beam at discrete inclination angles of θ=[15, 35, 55, 65]^o, with no perforations was observed. These $\eta(\theta)$ measurements, along with the $\eta(\theta=0^o)$ results of Fig. 4–9, are shown in Fig. 4–11. In order to compare to the CASINO simulations, the figure includes the empirically derived $\eta_0(\theta)$ result of Fig. 4–6.

4.4 Discussion and Analysis

From Fig. 4–9, it was seen that the agreement between the mean experimental η value of 0.82 and the simulated η_0 value of 0.85 is within 5%. Statistically, the measured and expected values are within one and a half standard deviations. Considering that the experimentally determined η does not account for the extrinsic radiative and evaporative losses, $\eta_0 > \eta$ is to be expected. The contribution of these extrinsic heat loss mechanisms, as well as other error sources, are discussed below.

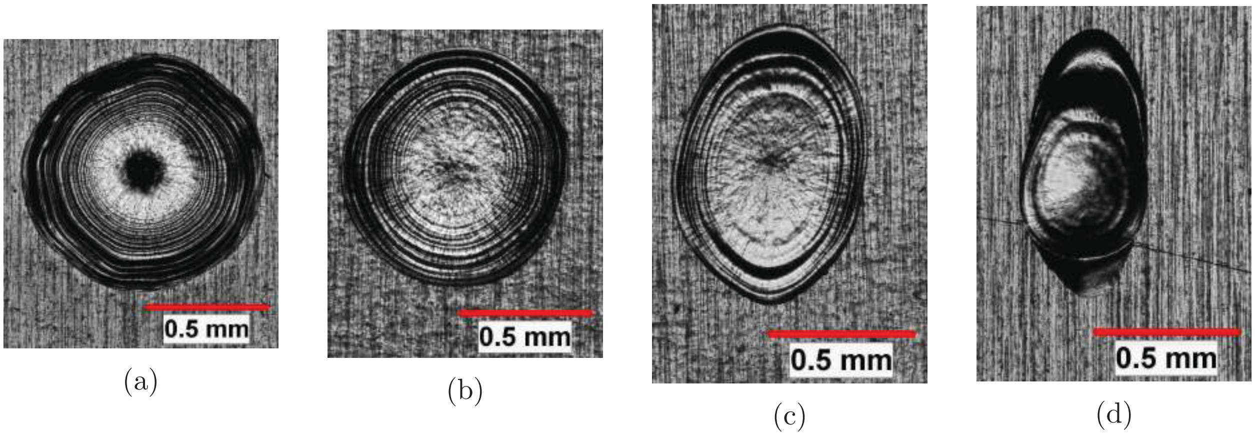

Figure 4–10: Variable incidence angle spot melts with Q_p= 2J, V_{acc}= 60kV, I_b= 15mA (a) θ=15^o (b) θ=35^o (c) θ=55^o (d) θ=65^o

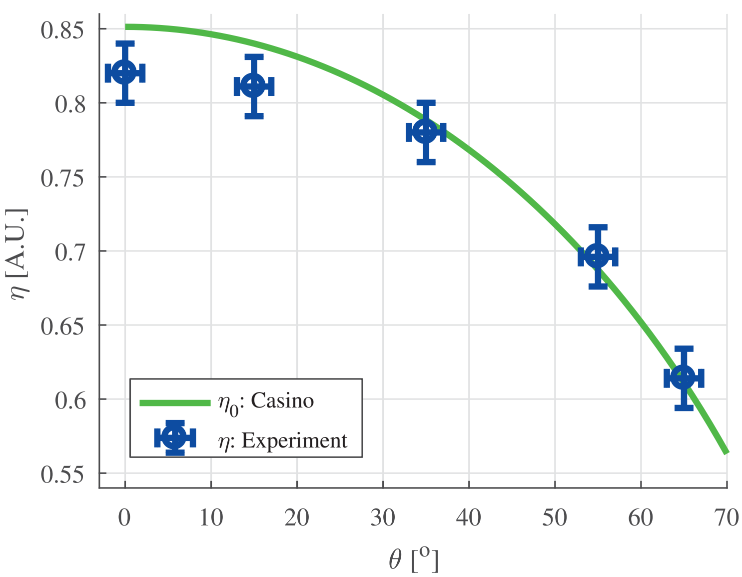

Figure 4–11: Results for $\eta(\theta)$ experiments at [60kV,15mA] with θ=[15,35, 55, 65]^o. Results are compared to CASINO-generated $\eta_0(\theta)$ results. Adjusted R-square statistics for each $\eta(\theta)$ measurement: mean= 0.99960±0.00014, min= 0.9860, excluding drilled holes

As discussed in Ch 2, high-vacuum evaporation is a complex phenomenon that depends on the surface temperature, local fluid dynamics, molecular gas dynamics and the partial pressures of the alloy constituents.[82, 87] During evaporation, a vapor recoil pressure is created on the surface, which increases exponentially with temperature. In some cases, the amplitude of this pressure is sufficient to overcome the surface tension, resulting in keyhole-formation, weld splatter, or in this case, sheet perforation.[82, 36, 179] It was shown that during pulsed laser spot melting of SS304, Fe, Cr and Mn vapor is only generated during the latter portion beam pulse.[82] This is consistent with the observation at 80kV that the holes were formed at higher Q_p/pulse length, and implies that the thin-sheet methodology has an intrinsic mechanism to detect appreciable levels of Q_{evap}: perforation.

A less tractable source of error is related to the radiative heat loss, Q_{rad}. Assuming a worst case scenario, where both sides of the molten pool (A= 2mm^2) are radiating into a room-temperature background (T_o=295^{o}K) at the liquidus temperature(T_l=1727^{o}K) for 100 millisecond like a blackbody(ϵ=1), the Stefan-Boltzmann equation can be used to estimate Q_{rad} ≈0.2J, which is an appreciable fraction of the pulse energies investigated. Although an order of magnitude estimate, radiation heat loss is likely the source of the $\eta_0 > \eta$ inequality.

Decreasing Q_{rad} explains the convergence between measurement and simulation at higher inclination angles, shown in Fig. 4–11. Larger inclination angles imply less absorbed energy, lower peak surface temperature and, thus, reduced radiative loss. A similar argument could be applied to the differences between the 60 and 80kV measurements of Fig. 4–8 which had η values of 0.828 and 0.819, respectively.

For normal incidence, the measured value of η=0.82 is less than the value of η_0=0.99 used in the numerical model of Leitz, with the discrepancy attributable to the differences between conduction and keyhole mode heat transfer previously discussed.[169] Although details of the keyhole-mode heat transfer model were unclear, Rai achieved good numerical and experimental agreement using η_0=0.2 for stainless steel. This value may be related to energy absorption of multiple beam reflections along the walls of the vapor capillary, which Fig. 4–11 shows will decrease with increasing inclination angle.

As previously discussed, the η fit parameter is related to the amplitude of the temperature signal and is therefore is susceptible to systematic errors in the thermophysical material parameters of Table 4–1. As determined from the thermal diffusivity, the thermal conductivity is calculated to be 15.0 W/m K. A non-exhaustive literature search suggests that this can leads to errors can be as great as 10%, which directly affect the experimental accuracy of η. Without corroborating laser flash measurements, these errors will be present in all transient heat transfer analyses. The good agreement with the Monte Carlo simulations, as well as the good adjusted R-square values, suggest that these errors are not as significant.

4.5 Conclusions

Using a semi-automated processing methodology, the far-field energy absorption coefficient during conduction-mode electron beam heating was determined over 103 experiments, at different combinations of accelerating voltage, beam current, pulse energy and inclination angle. These measurements were performed using a novel thin-sheet configuration, in conjunction with fast response thermocouples and analytical curve fitting. It was found that the absorption was not a strong function of accelerating voltage, beam current or pulse energy, assuming the sheet was not perforated, with an experimentally determined value of η=0.82 $\pm$ 0.02. The angle between the sample surface and beam was varied and η was determined to be a strong function of incidence angle.

Monte-Carlo electron trajectory simulations were performed in CASINO to determine the back-scattered electron energy spectrum. Using a simple formula, the fraction of energy reflected out of solid, Γ_{BSE}, was calculated, as well as the corresponding amount of locally absorbed energy, η_0 Despite the omission of radiative and evaporative heat loss, the agreement between the measured η and the simulated η_0 was within 5%, demonstrating the applicability of Monte-Carlo techniques towards estimating electron beam energy transfer.

In comparison to metallurgical cross sectioning, the thermocouple/curve fitting methodology outlined omits issues regarding heating transients as well as localized convective heat transfer.

4.5.1 Future Work

Originally, it was believed that the methodology outlined above could be applied to the more challenging heat absorption geometry associated with a single powder layer. Unfortunately, it was determined that small thermal deformations of the thin workpiece during preheat would displace the loose powder. While thicker workpieces eliminated the deformation issues, the temperature signal associated with a single pulse did not have a sufficiently high signal-to-noise ratio for accurate fitting.

Nevertheless, this section demonstrate that CASINO can accurately simulate η for a variety of alloy compositions and geometries. Specifically, the accuracy of CASINO results at different incidence angles is a key consideration for powder-bed heating, as the spherical metal particles contain spectrum of incident angles.

To extend the experimental component of this work to single pulse EB-PBF, new fixturing and preheat algorithms need to be developed which mininize the substrate thermal deformation. Another alternative would be improving the thermal isolation of the workpiece, reducing its net mass, and correlating the absorption coefficient with the net enthalpy rise of the powder layer. This approach has already been demonstrated in the literature for single powder layer laser melting, but would have to be optimized for the equipment used at McGill.[155] In terms of CASINO modelling, further work would be required using CASINO v3.2.0.1, which has full 3D modeling capabilities. Preliminary results regarding the effect of accelerating voltage and volumetric heating of spherical powder are shown in Fig. 4–12, although issues surrounding the electron accounting between the powder and substrate require further work.

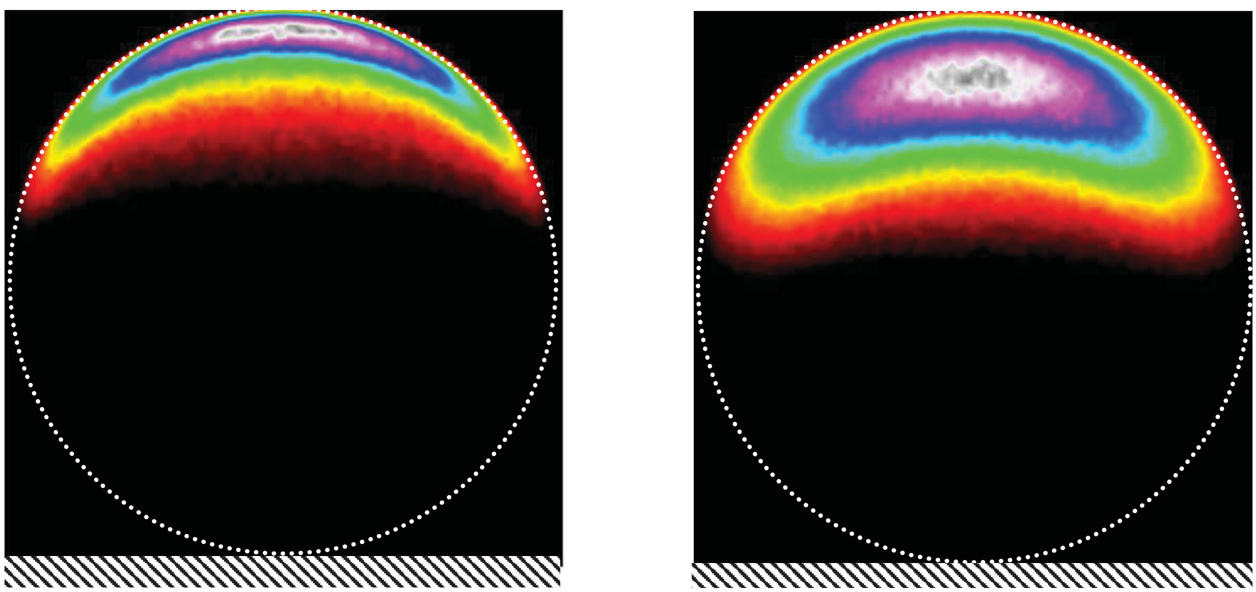

(a) (b)

Figure 4–12: Normalized volumetric heating profile of spherical 80 μm Ti powder simulated in CASINO v3.2.0.1. Left: Heating profile at 40kV. Right: Heating profile at 80kV

CHAPTER 5
Results: Melt Pool Stability during EBW of Nb-Ti

5.1 Introduction

First applied in the 1950s, EBW is considered a mature manufacturing technology, especially in comparison to the relatively new EB-PBF process.[23, 3] At the part-level, EB-PBF can be considered a quasi-2D heat transfer problem, 2D layers stacked into a 3D object, whereas EBW is effectively a 1D problem, as defined by the linear joint dimensions. Yet both cases induce local melt pool convection, which can only be solved with detailed numerical models and accurate material properties. Experimentally understanding how different process parameters impact melt pool stability during EBW is relevant to understanding similar problems in EB-PBF. This is highlighted by a number of detailed single track powder melting experiments, with titles such as *Selective laser melting technology: from the single laser melted track stability to 3D parts of complex shape*.[157, 155, 63, 180, 181, 182] In the following chapter, experiments and analysis of electron beam welding of Nb to Ti will be presented, and represents a summary of a 2015 industrial collaboration with PAVAC Industries. In the course of this analysis, issues which are pertinent to EB-PBF will be highlighted where appropriate.

Dissimilar metal weldments are desirable for both technical and economic reasons, as they enable multiple material properties in a single, finished assembly.[183] In this application, dissimilar electron beam welding is used to join a soft material chosen for its superconducting properties(Nb) to a hard material used to form metal-gasket sealing surface(Ti), with the purpose of fabricating new particle accelerator devices.[7]. Previously, these vacuum flanges were formed from Nb55wt%-Ti, as this solid-solution strengthened material could withstand the 1100^{o}C heat treatment without significant loss of hardness.[7] State-of-the-art Nb processing routines require a 800^{o}C heat treatment, reducing rates of softening due to recrystallization and grain growth.

The engineering challenge of directly joining Nb and Ti is related to the differences in thermal transport and melting enthalpy. This work aims to understand the effects of various process parameters on weld pool stability. These findings were used to develop robust, proprietary welding procedure specifications in consultation with PAVAC Industries.

The 20 EBW experiments were conducted at the PAVAC facility in Richmond, British Columbia, and mapped out how variations in EBW machines, line energy, deflection patterns and joint design affect the resulting linear welds. Because of the differences in atomic number and chemical reactivity, the Weld Zone (WZ) cross sections offered a unique opportunity to visualize and interpret melt pool convection. This is similar to previous analyses, which utilize a plug of high Z material pressed into the joint interface to study melt pool convection.[36, 1] The practical knowledge gained during these experiments is also useful in understanding the composite heat transfer associated with fusing metal powder onto a solid substrate, as both processes are associated with significant differences in thermal diffusivity.[131]

Although the effects of the 800^{o}C high vacuum(P$<$ 2E-6mbar) heat treatment were also studied, detailed results will not be presented. That said, the Nb-Ti interdiffusion distance was determined to be composition-dependent, and measured to be approximately 10μm after 2 hours using Energy-dispersive X-ray spectroscopy. Also, heat treatment relieved the α' martensite formed at the FZ/Ti interface. Finally, the Vickers hardness of the Ti was unchanged after 6 hours of treatment, 190HV,(500gf, 25s hold), which compares well against conventional 316LN stainless steel flange material, which has a corresponding Vickers hardness of 150-170HV.[26]

5.1.1 Thermophysical Material Parameters

For any material or material pair, weldability is a measure of how the Weld Zone (WZ) properties degrade after welding or over the lifetime of its intended service.[184] From the Nb-Ti phase diagram of Fig. 5–1a, we see that no brittle intermetallics are formed in this system. This fact, in addition to the similar thermal expansion coefficients shown in Table 5–1, imply that Nb-Ti joints have excellent weldability.

The challenge lies in selecting process parameters which address the large differences between Nb and Ti melting temperature (ΔT_m= 800^{o}C), volumetric enthalpy ($\Delta h_{vol} \approx$

	cp Ti - grade 2	Nb
Composition	max (0.3 Fe, 0.25 O) wt%	Reactor Grade
T_m [^oC]: Melting Point	1668	2468
T_b [^oC]: Boiling Point	3285	4900
ρ [g cm^{-3}]: Density	4.45	8.55
c_p [J/g^oC]: Specific Heat	0.522	0.26
κ [W/m^oC]: Thermal Conductivity	20.5	52
α [mm^2/s]: Thermal Diffusivity	22.9	8.8
β_T [μm/ m C]: Thermal exp. coefficient	7.1	8.6
h_{vol} [J/mm^3]: Vol. melting enthalpy	5.1	15.3
η[A.U.]: Absorption Coefficient	0.88	0.77

Table 5–1: Thermophysical material parameters for Nb and cpTi.[26, 185] All values are quoted at 25^{o}C, unless other stated. The volumetric enthalpy of melting Nb was estimated from $h_{vol} = \rho(T_m - 25C)c_p + L_{fusion}$, where L_{fusion} is the enthalpy of melting. The absorption coefficients were simulated in CASINO, as per Ch. 4

300%) , and thermal diffusivity ($\Delta\alpha \approx 250\%$). In previous designs, a Nb 55wt%-Ti alloy was joined to Nb without much difficulty, as this intermediary alloy had heat transfer properties which more closely matched Nb.

Significant research has been conducted to understand the Nb-Ti material system, as this ductile alloy is used as superconducting magnet wire.[187, 188, 189, 190] By carefully selecting the drawing and heat treatment schedule, the formation of nanometer scale microstructural features have been found to significantly improve the current capacity of the wires. [191] Assuming a spectrum of compositions in the FZ, the phase diagram of Fig. 5–1a implies a spectrum of M_s start temperatures. The formation of Nb-lean martensite was not found to affect weld cracking, and loss of strength in the FZ after heat treatment was observed using Vickers hardness testing.

Finally, the temperature-dependent vapor pressure of pure Nb and pure Ti are shown in Fig. 5–1b. As previously discussed, vapor pressure is important in the context of keyhole formation, as the recoil pressure formed during intense heating keeps the keyhole open and stable. Roughly, process parameters which are sufficient to raise Nb to its melting temperature will result in a corresponding 10^{2}mbar Ti vapor pressure, which is more than sufficient to sustain a keyhole.[36, 87] As will be shown, this large difference in vapor pressure will make the melt pool very sensitive joint alignment.

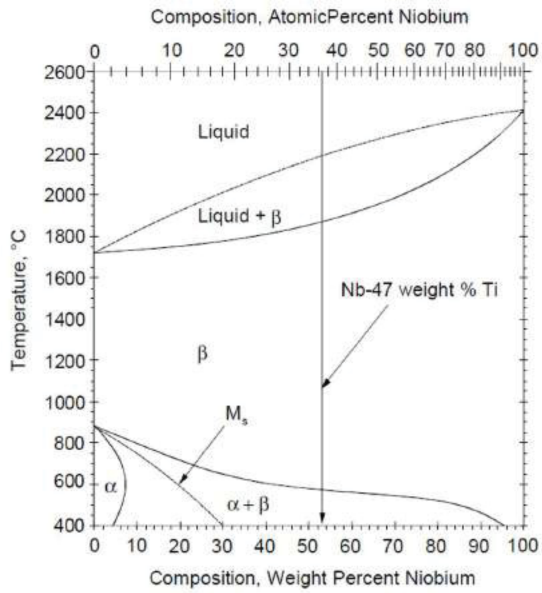

(a)

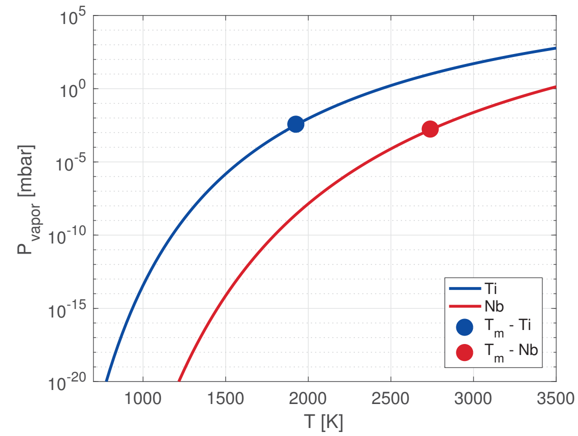

(b)

Figure 5–1: Thermophysical of Nb and Ti. Left: Equilibrium Phase Nb-Ti diagram, including M_s start temperature[186]. Right: Temperature-dependent vapor pressure of Nb and Ti, calculated from *Smithells*[185]

5.1.2 Nb-Ti Test Matrix

In developing the experimental test matrix, past literature concerning EBW of Nb-Ti was analyzed. To compare the effect of different accelerating voltages, beam powers and travel speeds, each process is defined according to the incident line energy:

$$Q_l = \frac{V_{acc} I_b}{v} \tag{5.1}$$

where Q_l[J mm^{-1}] is the line energy, V_{acc}[kV] is the accelerating voltage I_b[mA] is the beam current and v[mm s^{-1}] is the travel speed.

In 1976, Metzger demonstrated 3mm full penetration Nb-Ti EBW butt joints using v= 10 mm s^{-1}, V_{acc}= 130kV and a Q_l = 169 J mm^{-1} by offseting the beam 0.4mm onto Nb.[192]

In 1992, Franchini and Pierantozzi demonstrated partial penetration EBW of the Nb alloy C-103(Nb-l0Hf-lTi) to grade 23 Ti64 for rocket nozzle applications.[193] To meet the weld specification, a 2 pass radial welding procedure was developed to join the 3mm thick material using a travel speed of v= 8.3 mm s^{-1}, V_{acc}= 25kV and a Q_l = 85 J mm^{-1}, along with a 80Hz, 0.3mm circular deflection pattern. Also, a step joint was formed from the fraying surfaces, with a 1.5mm high, 0.3mm deep Nb step beneath the Ti.

In 2014, Torkamany used a 400W pulsed Nd:YAG laser (λ=1.06μm) to join 1mm thick pure Nb to Ti64.[194] In this case, the travel speed was v= 6.6 mm s^{-1} with an equivalent line energy of Q_l= 27 J mm^{-1} and pulse parameters of Q_p= 9J, τ= 6mS with a 20Hz repetition rate.

In 2016, workers at the Centre for Advanced Materials Joining at the University of Waterloo demonstrated sound NiTi/Ti64 pulsed laser joints using a 50μm Nb interlayer. Although the process parameters are not relevant to this study, the discussions surrounding beam offset and composite-material heat transfer were especially illustrative.[195]

Finally, PAVAC engineers had previously experimented with 3mm Nb-Ti butt joints using v = 12.5mm/s, V_{acc}= 80kV and a Q_l= 179J/mm, while offsetting the deflection pattern 0.5mm onto Nb.

In all cases, poor mixing of Nb within the fusion zone was observed, henceforth referred to as macrosegregation. Franchini claims that improved FZ mixing can be obtained at lower travel speeds, although this claim was difficult to discern from the micrographs presented.

Based on previous literature and conversations with the PAVAC staff, a set of processes parameters were identified for further experimental investigation. First, these experiments would be conducted on 2 separate electron beam welders, each with unique accelerating voltages(80 vs 110kV) and WD (157 vs 767mm). Because of the asymmetry in material properties, a 1.5mm triangular deflection pattern was suggested, as this pattern could be asymmetrically offset onto the more challenging Nb material. Two separate joint designs, referred to as step joint and butt joint, would also be tested, with the joint dimensions shown in the schematic of Fig. 5–2.

From Fig. 5–2, the term *[offset]* is defined as the distance from the longitudinal edge of the triangular pattern to the top surface of the joint.

Twenty unique weld parameter combinations were identified, based on variations in line energy, deflection offset and travel velocity. On the 80kV machine, 5 butt joints and 7 step joints were defined, while the 110kV machine would be used to weld 5 butt joints

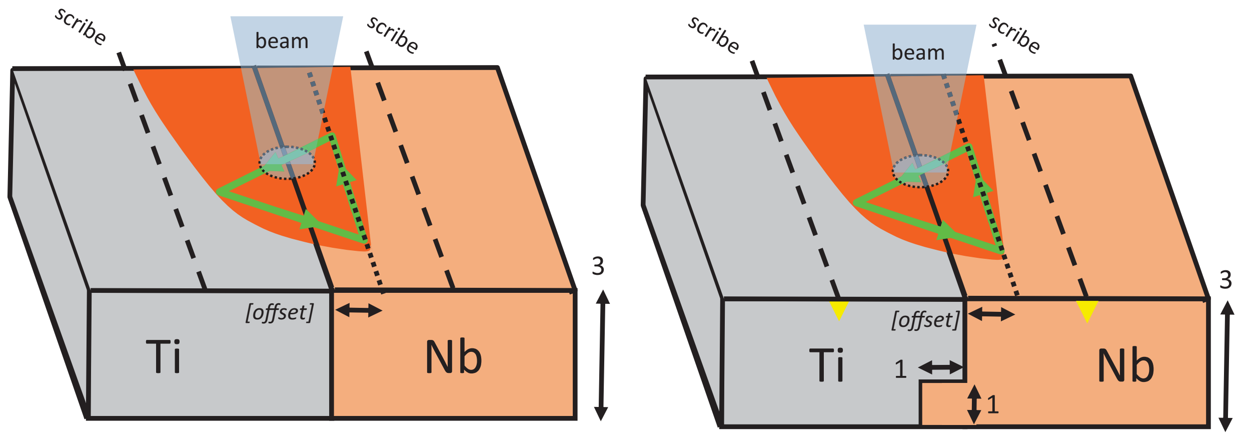

Figure 5–2: Process schematic for EBW of Nb-Ti joints: butt and step joint. All dimensions are in [mm]

and 3 step joints. The resulting process map covers line energies from 96-264 J mm^{-1} and travel speeds between v= 8.3-16.6 mm s^{-1} and *[offset]* between 0-1.5mm, as shown in Fig. 5–3.

5.2 Experimental Procedure

Sheets of 3mm thick Nb and Ti were wire electro-discharge machined into 100x20x3 mm coupons, which were joined along the longest dimension. The step on the Nb and Ti surfaces were machined using a conventional milling operation. Scribe marks were placed 3mm from the upper joint surface on both the Nb and Ti joints, as shown in Fig. 5–2. These scribe marks were useful for joint/beam alignment using the beam boroscope, as the fine marks could be more accurately resolved than the joint interface. The scribe marks were also used to locate the joint interface relative to the FZ dimensions after welding.[196] All welds were conducted with at a pressure of less than 5E-5mbar in both the sample and gun vacuum chamber, with no high voltage arcs observed during welding.

5.2.1 Deflection Pattern

The deflection pattern pitch is defined as the linear distance traveled during one deflection period, v/f_{def}. A small pitch is desirable, as it implies that the melt pool will receive multiple beam passes, promoting melt pool convection. A deflection frequency of f_{def}= 100Hz was chosen as a compromise between a small pitch(high f_{def}) and minimal distortion of the triangular shape(low f_{def}). The resulting deflection pitch is on the order

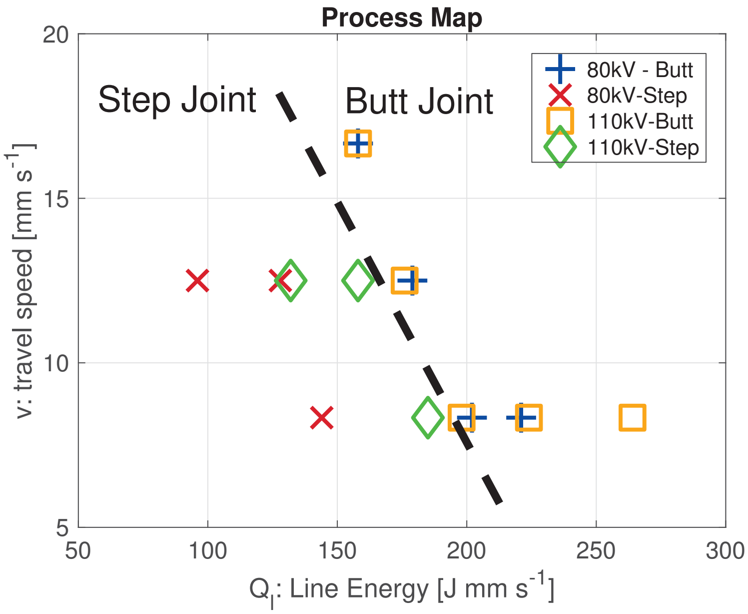

Figure 5–3: Process map for welding butt and step joints on 80 and 110kV machines

of 80-170μm and in comparison to the 1.5mm deflection pattern, implies that the fusion zone will receive multiple deflection passes.

Regarding pattern distortion, the deflection coils used in the PAVAC machines were of similar construction as those at McGill. As will be further discussed, the deflection coils suppress the high frequency components of the drive signal, which implies that the sharp corners of the triangle pattern will become rounded. This effect is shown by the focused, low power triangular deflection patterns melted on Ti and shown in Fig. 5–4.

In comparing the patterns of Fig. 5–4, it is worth noting that the 80kV patterns have sharper definition, despite both beams being at operator sharp focus. This is due to the shorter working distance, which enables a smaller spot size at the workplane. A series of deflection-based patterns were melted onto the Ti coupon using each machine over a range of f_{def}. By measuring the resulting melt length, it was possible to map out the deflection coil frequency response, as discussed in Sec. 3.2.2.

5.2.2 Focus Setting

Following PAVAC standard operating procedure, the algorithm for determining the focus coil setting during welding, $w_b - weld$ was:

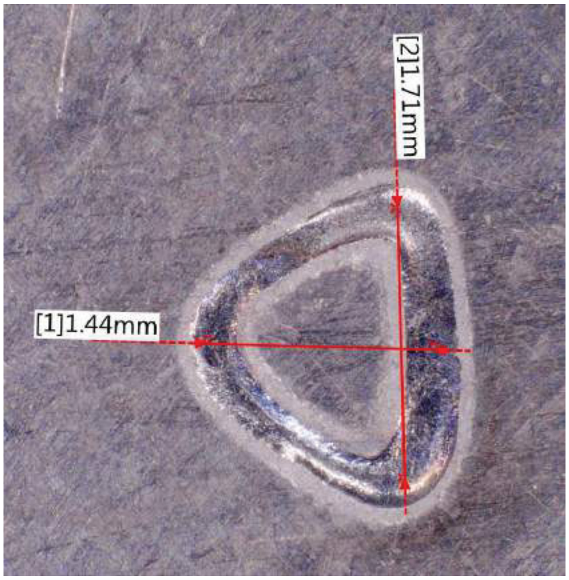

(a)

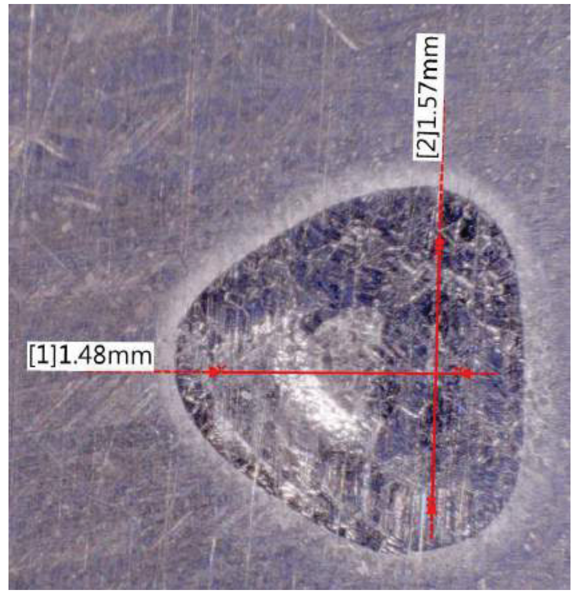

(b)

Figure 5–4: Deflection pattern dimensions melted with I_b= 1.5mA onto Ti using a sharp-focus beam. Left: 80kV/WD= 157mm machine Right: 110kV/WD= 767mm machine

- Determine operator sharp focus at I_b= 1.5mA using a stationary beam incident on Nb, which is referred to as $w_b@1.5mA$
- Set welding focus according to $w_b - weld = w_b@1.5mA + 0.5I_b + 50mA$, where I_b is the beam current used during welding

This algorithm was applied for both the 80 and 110kV machines.

5.2.3 Metallographic Sample preparation

Metallographic sample preparation had to address the large variation in hardness between the soft Nb(HV= 50) and the hard, solution-strengthened fusion zone(HV= 300). Another issue concerned embedding of grit particles into the Nb, therefore various sample preparation techniques were explored before satisfactory samples were created.[197, 198]

Samples were sectioned along the middle 30mm of the 100mm long coupon, ensuring that the weld heat transfer characteristics have had sufficient distance to stabilize. A Buehler IsoMet 5000 automatic cutting saw with a 8” non-ferrous abrasive blade (Buehler 11-4217-00) was used to section the samples. It was determined that a rotation speed of 2500 RPM and a feed rate of 3mm min^{-1} minimized embedding.

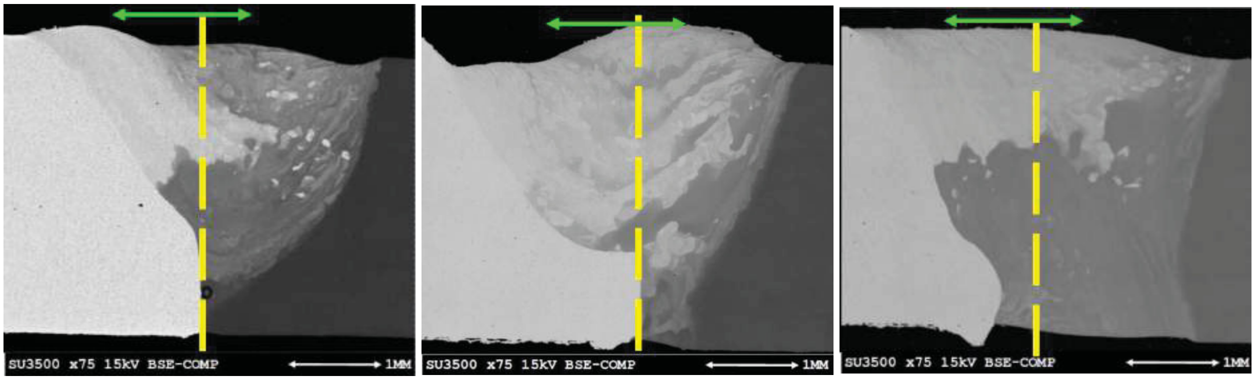

(a) (b) (c)

Figure 5–5: Fusion zone mixing of Nb-Ti butt joint as a function of line energy. Shared process parameters: v= 8.3 mm s^{-1} and V_{acc}= 110kV, WD= 767mm, [*offset*]= 1.0mm. Left: Q_l= 198 J mm^{-1}, Middle: Q_l= 224 J mm^{-1}, Right: Q_l= 264 J mm^{-1}.

Grinding proceeded from 400-600-800-1200 SiC grit grinding paper. It was determined that dry, repeated 600-grit grinding at reduced loads reduced SiC embedding.[198] Polishing was conducted using 3μm-1μm diamond abrasive, and completed after 12hrs of automated VibroMet poilishing using a 0.05μm collodial silica suspension.

For low-resolution macro-analysis, the ground samples were etched in a 1:1:10 HF:HNO3:HCl solution. It was determined that the FZ etched the most rapidly, and the Nb Base Metal (BM) etched most slowly. Therefore, the etch time was dependent on the desired region of observation.

5.3 Results

The interplay between beam parameters, process geometry, melt pool convection and energy transfer is examined via a series of WZ cross sections. In the following images, the niobium portion of the joint is on the left, while the Ti section is on the right. In each image, the top surface joint interface is marked by a yellow dashed line, which was determined using the previously placed scribe marks. To provide dimensional reference to the 1.5mm deflection pattern, a green arrow scaled to the image dimensions has been overlaid in each image, and positioned relative to experimental [*offset*] value.

The first set of results concerns the effect of increasing beam power in the butt joint geometry, which is shown in the cross-sections of Fig. 5–5.

One immediately obvious feature of these BSE images is the high level of contrast between the white Nb and dark Ti, enabling visualization of the convective flow patterns, fusion zone boundary and macrosegregation.

In all cases, these images demonstrate that the Nb is dragged into the melt pool along the upper region of the Nb, as demonstrated by the bright contrast region in the topmost section of each FZ. This region is likely to solidify first, as the T_m will be higher than the Nb-poor regions of the FZ. Figure 5–5a shows individual Nb-rich nodules which transit across the entire FZ, implying that Nb has not had sufficient time dissolve in the liquid. Figure 5–5a also demonstrates weld root porosity, a feature often associated with the partial penetration welds.

As a whole, Fig. 5–5 shows that the FZ area increases with increasing Q_l. Conversely, the level of macrosegegation, which is demonstrated by the variation in contrast of the FZ, decreases with increasing Q_l. With reference to the joint interface, it can also be seen that the FZ preferentially melts the Ti portion of the joint. Meanwhile, a ledge of pure Nb is formed at the bottom left region of the FZ, and is defined by the deflection pattern offset. From the increasing Q_l of Fig. 5–5, the ledge becomes increasingly eroded.

To study the effect of different machines, butt weld cross-sections with identical beam powers and line energies are shown in Fig. 5–6, with the distinguishing parameter being V_{acc}/WD.

In this case, it is observed that Working Distance (WD) has a substantial effect on the fusion zone shape, despite the nominally identical beam parameters. The nearly vertical Ti/FZ boundary associated with the WD= 157mm weld of Fig. 5–6a is indicative of keyhole-mode heat transfer. In comparison, the FZ associated with Fig. 5–6b has a more hemispherical shape, suggesting conduction-mode heat transfer, despite being conducted at a higher V_{acc}.

The concept of keyhole formation is further demonstrated by the images of Fig. 5–7, which concern butt welds with [*offset*]= 0.0 mm, with reduced line energy.

Despite the lower beam power, weld blow-through is observed along the weld length, with an example shown in Fig. 5–7b. In this case, the reduced [*offset*] appears to have had a significant effect, as the beam transfers the majority of its energy the Ti portion of the

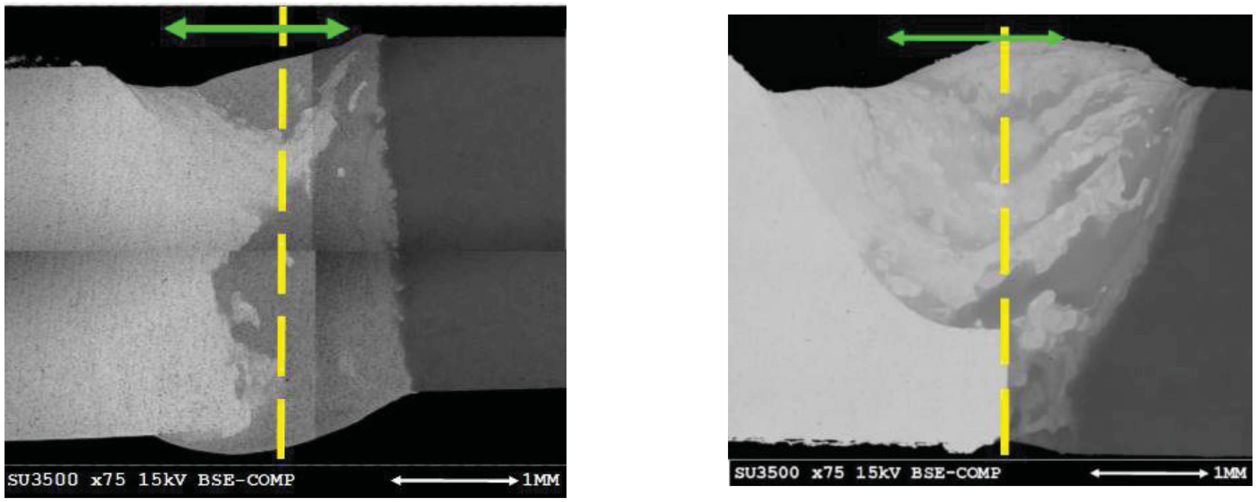

(a) (b)

Figure 5–6: Fusion zone of Nb-Ti butt joints at identical Q_l, P. Shared process parameters: Q_l= 223 J mm^{-1}, v= 8.3 mm s^{-1} and [*offset*]= 1.0mm. Left: V_{acc}= 80kV/WD=157mm. Right: V_{acc}= 110kV/WD=767mm

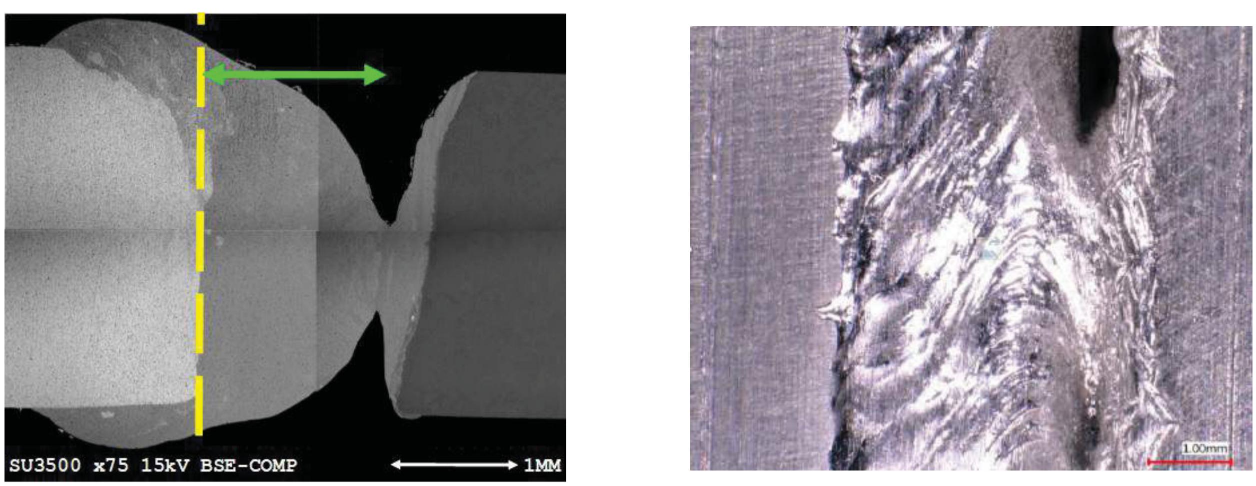

(a) (b)

Figure 5–7: Melt pool instability due to deflection pattern offset. Process parameters: Q_l= 179 J mm^{-1}, v= 12.5 mm s^{-1} and V_{acc}= 80kV, [*offset*]= 0.0 mm. Left: Cross section of FZ zone. Right: Weld crown with blow-through, while Nb on left

(a)

(b)

Figure 5–8: Top Section of Nb-Ti weld Profiles. Upper Image: stable melt weld process. Lower Image: unstable weld process

joint, resulting in melt pool instability. The location of the blow-hole aligns well with the deflection pattern dimensions, suggesting that the keyhole is formed at the Ti-rich section of the deflection pattern. Figure 5–7a also shows a limited amount of Nb melting, as well as Ti-rich liquid that wets the underside of the Nb.

In many cases, it was relatively easy to assess the stability of the melt pool by examining the weld top surface, as shown by the stable and unstable welds of Fig. 5–8.

As a final example, step-joint weld formed on the 80kV and 110kV machines are shown in Fig. 5–9a and Fig. 5–9b, respectively.

These welds further demonstrate issues concerning keyhole stability and beam/joint positioning. The high aspect ratio of the FZ of Fig 5–9a clearly demonstrates the formation of a keyhole, despite being conducted at lower V_{acc} and power compared to Fig 5–9b (1200 vs 1650W). Figure 5–9b also shows two craters formed in the Nb step, which align with the deflection pattern dimensions. Compared to the other examples, the FZ composition is homogeneous, and semi-quantitative EDS shows that the composition is roughly $\approx$ 20wt% Nb- 80wt% Ti. The shape and composition of the FZ implies that the Nb is mixed via a digging action along the top surface of the Nb step. This mechanism is distinct from the top surface mixing associated with the butt joints of Fig. 5–6, and results in a more homogeneous FZ composition.

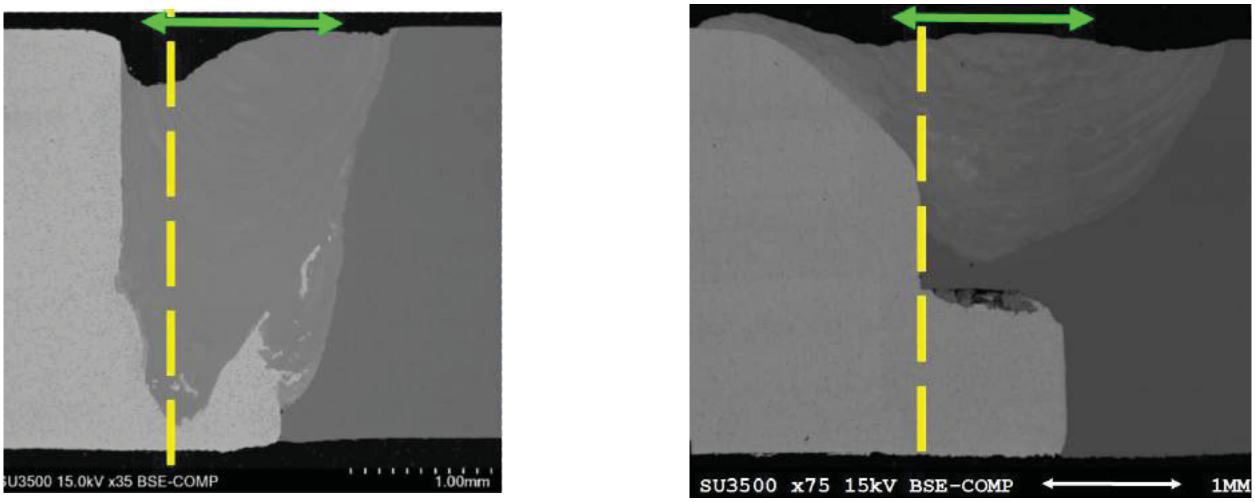

(a) (b)

Figure 5–9: FZ mixing of Nb-Ti step joint. The Nb base metal is shown on the left of the FZ in bright contrast, while the Ti BM is in dark contrast on the left. Shared process parameters: v= 12.5 mm s^{-1}, [*offset*]= 0.25 mm. Left: Q_l= 96 J mm^{-1}, and V_{acc}= 80kV. Right: Q_l= 132 J mm^{-1}, and V_{acc}= 110kV,

Despite a higher Q_l, the weld cross section of the 110kV weld of Fig. 5–9b suggests conduction mode heat transfer, with significantly reduced penetration. Also, porosity is observed at the horizontal Nb/Ti step interface of this weld.

5.3.1 Weld Zone Hardness Mapping

Because of the chemical and microstructural gradients in the with WZ, weldments can be considered to be a type of composite material, thus complicating the interpretation of their properties.[199] To estimate the local mechanical properties of the joint, Vickers hardness mapping was performed on the Q_l= 224 J mm^{-1} weld of Fig. 5–5b, with the color-coded results shown in Fig. 5–10.

As expected, the Nb-rich regions on the left of the FZ have a lower HV compared to the Ti-rich FZ regions on the right. Also, the hardness values of the FZ and Ti base metal are at least twice that of the pure Nb, suggesting that tensile failure will occur in the softer Nb base metal.

5.4 Analysis and Discussion

The presented welds demonstrate the key heat transfer mechanisms associated with these dissimilar metal welds. As a first analysis step, a variation of the dimensionless γ_m

Figure 5–10: Vickers hardness mapping of butt joint formed from Q_l= 224 J mm^{-1}, v= 8.6 mm s^{-1} and V_{acc}= 110kV and [*offset*]= 1.0 mm. The Nb base metal is on the left, the Ti base metal on the right, and the FZ is deliniated by the rose colored outline. Vickers hardness measurements were conducted with a 500gf load and 25s hold.

parameter can be estimated for pure Nb, the Nb/Ti step joint, and pure Ti. As discussed in Sec. 1.2.1, γ_m is a dimensionless term associated with the ratio of absorbed energy per unit area over the enthalpy of melting per unit area. To calculate this parameter, we first assume that the beam FWHM is defined by the deflection pattern dimensions, resulting in an effective σ= 0.63mm. Thus, γ_m can be modified to account for the cited line energies and solid($\Phi = 1$) workpiece properties according to:

$$\begin{aligned} \gamma_m &= \eta \frac{V_{acc} I_b}{\sqrt{2\pi}\sigma v} * \frac{1}{t\Phi\rho(H_l - H_{T_0})} \\ &= \eta \frac{Q_l}{\sqrt{2\pi}\sigma} * \frac{1}{t h_{vol}} \\ &= \eta \frac{Q_l}{\sqrt{2\pi}\sigma} * \frac{1}{\delta h_{surf}} \end{aligned} \tag{5.2}$$

where t is the material thickness and h_{vol} is the composite volumetric enthalpy of melting. The surface enthalpy of melting, δh_{surf} [J mm^{-2}], is calculated by multiplying the h_{vol} by the sheet thickness, which gives 45.9 and 15.3 J mm^{-2} for Nb and Ti, respectively.

γ_m	Pure Nb	Nb/Ti Step Joint	Pure Ti
Q_l= 96J mm^{-1}	1.0	2.0	3.4
Q_l= 175 J mm^{-1}	3.6	4.3	6.3
Q_l= 264 J mm^{-1}	5.5	6.5	9.5

Table 5–2: γ_m matrix for Nb-Ti EBW at different joint compositions and line energies. The material parameters are defined in Table 5–1

The composite δh_{surf} of the step joint is be calculated according to: $t_{Nb}h_{vol-Nb} + t_{Ti}h_{vol-Ti}$ $= 25.5$ J mm^{-2}, where t_{Nb} and t_{Ti} are the thicknesses of Nb and Ti within the step joint, respectively. To estimate the material-dependent absorption coefficient η, the Monte-Carlo method outlined in Ch. 4 was used. The resulting γ_m matrix is shown in Table. 5–2, spanning the full range of line energies tested.

This table shows that γ_m depends heavily on the composition of the material beneath the beam, and that beam parameters which might marginally melt Nb ($\gamma_m = 1$) can superheat Ti. As expected, the composite γ_m has a value between that of pure Nb and Ti, opening the possibility to tailor γ_m either through a combination of joint dimensions or process parameters.

To qualitatively explain some of the transient heat transfer effects associated with this composite system, the Rosenthal thin plate model is applied individually to both Nb and Ti, using identical beam parameters of v= 12.5 mm s^{-1} and Q_l= 175 J mm^{-1}. The 2D temperature contours associated with each material are halved along the $y = 0$ symmetry plane and the results are stacked in Fig. 5–11, with the Nb response in the top portion of the image and the Ti response in the bottom.

The most obvious features of Fig. 5–11 are the differences in both size and shape of each respective fusion zone, which are shown in red. As expected, Nb has a smaller FZ due to the lower γ_m, as well as a more circular shape compared to the elongated titanium FZ. The shape effect can be understood by recalling that the thermal diffusion length equals $L_{th} = 2\sqrt{\alpha\tau}$, which implies that thermal diffusivity is a measure of the speed of heat propagation.[77] In this case, the closely spaced temperature contours of Ti(α= 8.8mm s^{-1}) are to be expected, as energy absorbed by Ti cannot propagate outwards into the cool BM as quickly as in Nb(α= 22.9 mm s^{-1}).

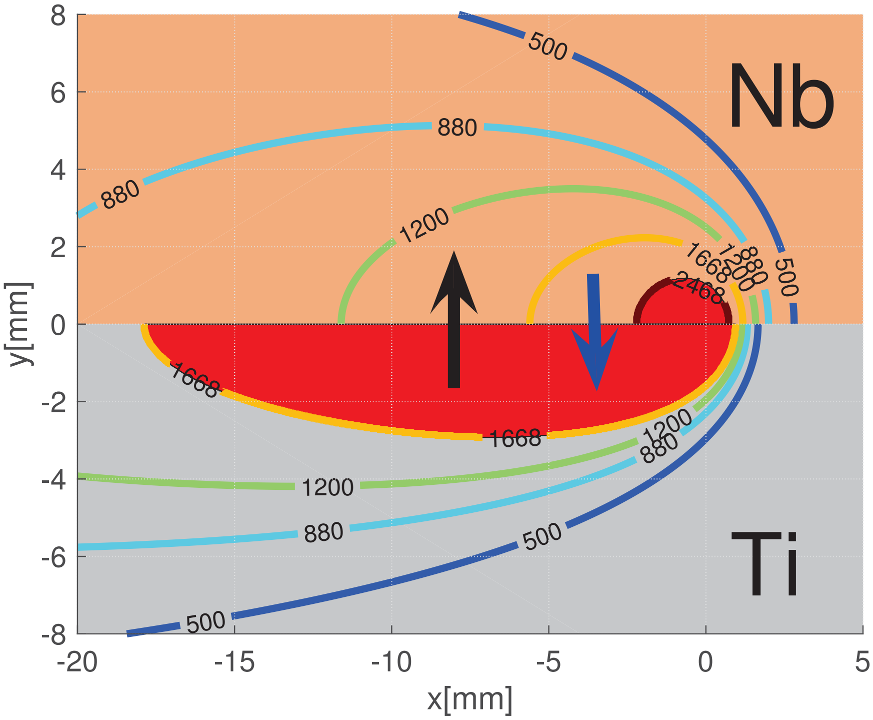

Figure 5–11: Weld zone heat transfer from composite Rosenthal thin plate model: Nb-Ti. t = 3mm, v = 12.5 mm s^{-1}, Q_l = 175 J mm^{-1}. Thermophysical material parameters were taken from Table 5–1. The blue arrow indicates heat flow from the hotter solid Nb to the cooler liquid Ti. The black arrow indicates heat flow from the hotter liquid Ti to the cooler solid Nb

Another feature of Fig. 5–11 is associated with the differences in melting temperature. After solidification at T_m= 2468^{o}C, solid Nb is still hot enough to transfer heat into the molten Ti (T_m= 1668^{o}C), a feature highlighted by the downwards blue arrow of Fig. 5–11. Yet the higher α implies that behind the beam, heat will be transported into the Nb bulk faster than the Ti. This means that at some point behind the heat source, the direction of heat transfer will switch direction, with the higher temperature Ti transferring heat into the faster cooling Nb, which is shown by the upwards black arrow of Fig. 5–11.

Although this simple model ignores the composition-dependent effects of solidification temperature, surface-tension and buoyancy convection as well as asymmetric deflection-based heating, it does demonstrate some of the salient features of this composite heat transfer system. In the butt-weld images of Fig. 5–5, the FZ appears to grow into the Ti portion of the joint with increasing Q_l. Because of the constant interaction period, defined by $\tau = FWHM/v$, the Nb behaves somewhat like a saturated heat sink. In this case, the increased energy in the weld pool is diverted to melting a larger fraction of Ti. Similarly, the melt pool lifetime increases with Q_l, enabling better dissolution of the high T_m Nb nodules.

The idea of a melt pool growing outwards from a heat-saturated substrate has some analogies to EB-PBF. Specifically, if the beam is over-powered, or the underlying solid material is above the steady state holding temperature, the additional beam energy could result in the growth of melt pool dimensions. Often, this implies melting metal particles outside the intended scan pattern, which causes issues regarding part resolution and surface finish. In other cases, this can result in keyhole-induced porosity, as the effective γ_m is outside the ideal operating window.

In terms of FZ shape and WD, the differences observed in Fig. 5–9 can be explained in terms of the PPD associated with each beam. Specifically, the short working distance associated with the 80kV welds generated a beam with sufficient power density to induce keyhole formation in Ti. Despite an identical power and higher intrinsic brightness, the 110kV beam did not obtain the power density needed for keyhole formation, resulting in conduction-mode heat transfer. This loss in power density is due to the additional 500mm of beam transit, which results in increased scattering and space-charge effects, as discussed in Sec. 2.3. The deflection patterns of Fig. 5–4 further demonstrate this idea, as the width of the 110kV melt lines are approximately double the 80kV ones.

While conditions for keyhole and conduction mode heat transfer were discussed in Sec. 2.5, these tests highlight the importance of considering the combined effect of intrinsic beam brightness and WD when discussing power density and spot size. Indirectly, these results demonstrate one of the challenges of building EB-PBF systems with larger build areas. Since the beam can only be deflected within a limited cone, a larger build area requires a longer WD, which in turn results in a loss of power density and an increased spot size.

5.4.1 Deflection Pattern Induced Keyhole

To explain the weld blow-through of Fig. 5–7 as well as the double keyholes formed in Fig. 5–9a, a detailed analysis of the deflection pattern is required. Specifically, the 'sharp' features of the triangular deflection pattern cause extended dwell times at the beam turning points, resulting in higher local fluence [J mm^{-2}], enhanced evaporation and keyhole formation. This is due to the magnetic inertia of the coils, which prevent the magnetic field, and thus the beam, from instantaneously changing direction.

To quantitatively demonstrate this concept, the LR deflection coil circuit model presented in Sec. 3.2.2 was calibrated to the 80kV geometry. This model was then used to simulate the deflection pattern generated from of an idealized deflection coil($f_{3dB} = \infty$), as well as the real deflection coils, which have a low-pass cut-off frequency of f_{3dB}= 80Hz. The method is based on generating the idealized $[x(t), y(t)]$ beam position, then low-pass filtering each axis independently, with the results shown in Fig. 5–12.

The model results of Fig. 5–12 demonstrate the degree to which magnetic inertia distorts the trajectory of each deflection axis. To better visualize this effect, the deflection trajectories are plotted in the $[x, y]$ plane, with the results shown in Fig. 5–13a. In this case, the model generated a deflection pattern with rounded corners, matching the experimental deflection patterns of Fig. 5–4.

The $[x(t), y(t)]$ model results can also be used to calculate the position-dependent beam velocity, $v = \sqrt{\Delta x^2 + \Delta y^2}/\Delta t$, with the results shown in Fig. 5–13b. For reference,

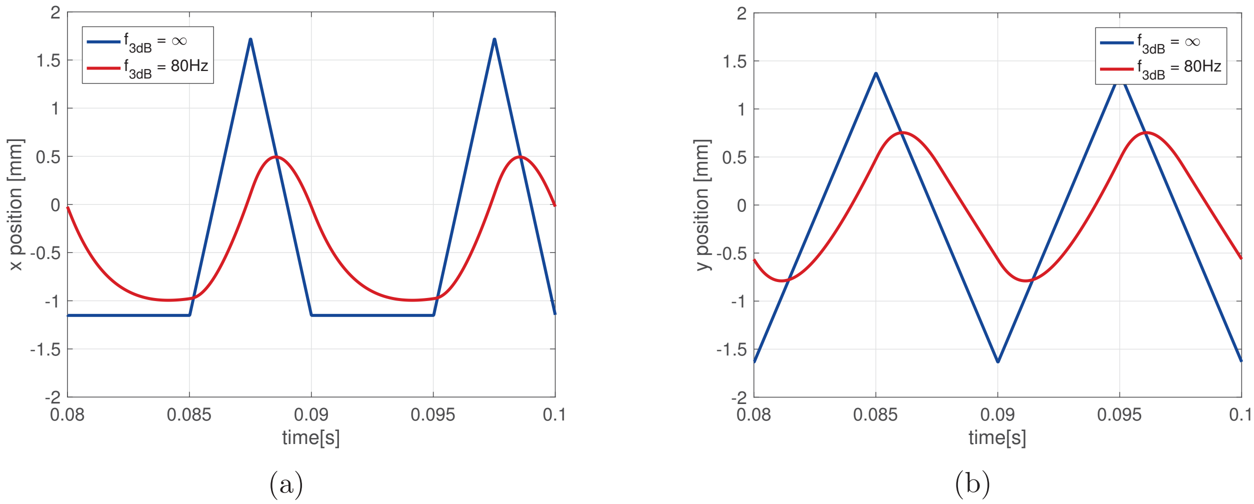

Figure 5–12: Idealized and real $[x(t), y(t)]$ beam positions associated with deflection pattern used during EBW of Nb-Ti joints

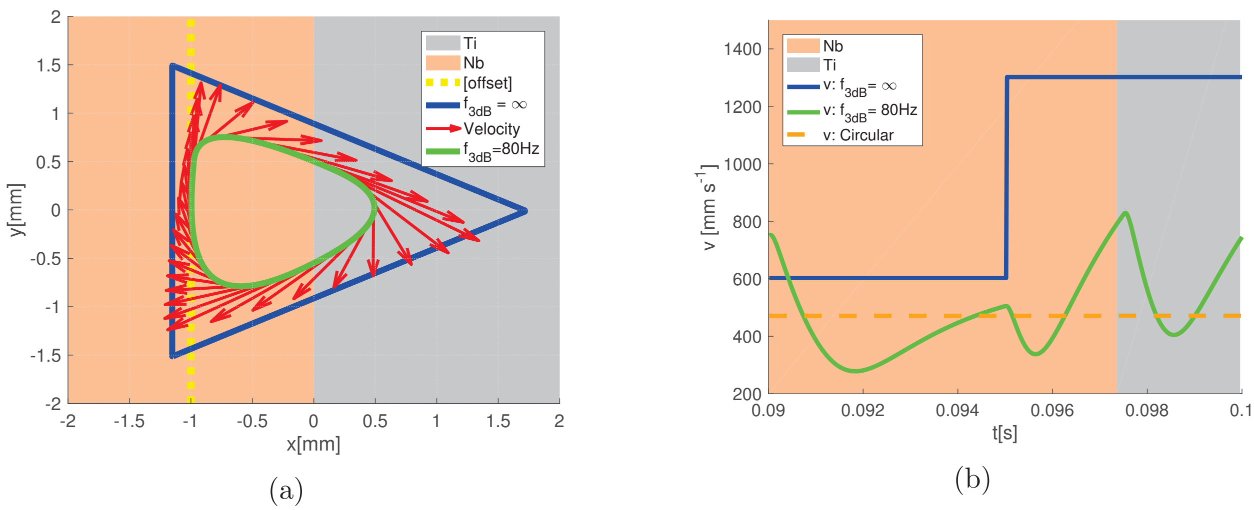

Figure 5–13: Deflection pattern in the x, y plane and position-dependent deflection velocity

the figure includes the equivalent deflection speed of a 100Hz, 1.5mm circular deflection pattern. Finally, the background colors of Fig. 5–13b have been set according to whether the beam is located on Nb, shown in orange, or located on Ti, shown in grey. For $[offset]$=1.0mm, the beam spends 26% of the deflection period on the Ti.

The critical feature of Fig. 5–13b is that the real deflection pattern undergoes velocity minima at each corner of the pattern, as opposed to the circular pattern or idealized triangular pattern. During the Ti-velocity minimum, which occurs on the right side of the pattern, the beam deposits sufficient local energy to cause extensive Ti evaporation and the formation of a keyhole.

This explains why the weld blow-through of Fig. 5–7 aligns with the rightmost portion of the deflection pattern, since the beam locally evaporates and keyholes into the Ti. Also, the composition on this side of the melt pool is low in Nb, implying a greater vapor pressure, as per Fig. 5–1b. This interpretation also explains why keyholing does not occur on the opposite corners, as this region has a better heat conduction path because of the Nb proximity, as well as a reduced vapor pressure, due to the local Nb content.

This interpretation can be extended to the double keyhole example of Fig. 5–9a. In this case, the Nb step prevents the continued evaporation of Ti because of its higher intrinsic γ_m. In simple terms, beam parameters which are sufficient to keyhole Ti (large γ_m) will only cause conduction-mode heating of Nb(small γ_m).

To understand the keyhole formed closest to the Nb interface, it should be recognized that this weld utilized an [*offset*]= 0.25mm, which doubled the Ti duty cycle to 56%. Also, since the deflection pattern corners are aligned, a significantly greater amount of energy is deposited into the Nb interface. In this case, the Nb interface is overloaded with incident heat, resulting in intense evaporation of the Ti-rich melt and the formation of the second keyhole.

Similar deflection-based keyholing effects have been discussed during both L-PBF and EB-PBF, especially when the beam is changing scan direction during hatch melting.[112, 135] In this case, the inertia of the deflection system can induce extended dwell time at the turning point, resulting in intense evaporation and keyhole induced porosity. Similarly, with new developments in *'move-stop-pulse-move'* L-PBF processes, no discussion has been put forward regarding limits of the mechanical inertia of the deflection mirrors.[200]

As a final note, the deflection model presented above was routinely used during gCode algorithm development. Specifically, unconventional deflection patterns could be tested in the model prior to experimentation. The objective was to develop a pattern which generated consistent velocity profiles, and thus consistent fluence and stable melt behavior. Similar realistic models have been developed for some L-PBF systems.[135]

5.5 Conclusion

In this chapter, the material and machine related challenges of dissimilar EBW of Nb-to-Ti were presented. The objective of this work was to identify which process parameters would be most suitable to compensate for the large differences in melting enthalpy, vapor pressure and thermal transport between Nb and Ti.

It was shown deflection $[offset]$ and joint design have a greater effect on weld quality than line energy, due to the ability of Nb to rapidly draw energy away from the beam, as well as the large differences in γ_m between Nb and Ti. Similarly, working distance(WD) was found to have a significant impact on the fusion zone shape, as the beam generated at 80kV/WD=167mm had sufficient power density to achieve keyhole-mode heat transfer in Ti.

These tests also demonstrate that it was possible to control macrosegregation using the step-joint geometry. When combined with keyhole penetration, the fusion zone composition was observed to be more uniform, as Nb was stirred into the FZ from the bottom. In contrast, the butt-joint geometry always demonstrated macrosegregation, which we associate with mixing the Nb into the FZ from the side.

Hardness mapping was performed to confirm that the solid-solution strengthened FZ exceeded the strength of both the Ti or Nb BM, and that tempering of the FZ and Ti BM during heat treatment did not result in significant loss of strength. Due to the low yield strength of pure Nb, it is believed that stress-induced failure will occur within the Nb.

Finally, it was demonstrated that the magnetic inertia associated with the deflection coils could explain the localized keyholing at the pattern turning points. The technique used to demonstrate this effect has been a routine tool in developing gCode process algorithms.

Based on these initial results and the supporting analysis, a fault-tolerant, proprietary welding procedure specification was put into production at PAVAC Industries.

5.5.1 Future Work

Although the industrial objective of this work was achieved, it would be of scientific interest to pursue comprehensive heat transfer modelling of the composite Nb-Ti weld joint. Similarly, it would be beneficial to conduct sub-size tensile tests on the production welds, as well as radiographic examination to confirm the joint performance. Although grade 2 Ti proved to be sufficient for this application, it might be beneficial to form the vacuum flanges from grade 4 commercially pure titanium, as the increased Fe content would limit grain growth at high temperatures, while inducing an acceptable ductility penalty (15% versus 20% elongation).[201] This would make the flanges more robust against possible changes to the heat treatment schedule, but directly mapping the grade 2 results to grade 4 Tu would have to be experimentally validated.

CHAPTER 6
Results: Powder Smoke and Contact Sintering

6.1 Introduction

In this chapter, the absorbed current during pulsed electron beam melting is experimentally measured for commercially pure titanium in both the solid and contact-sintered powder form. These experiments are based on an resistively isolated workpiece, effectively transforming it into a Faraday Cup (FC).

Our experimental data show the initiation of an extrinsic source of charges, whose flow opposes the high energy incident beam, and is only formed under certain process conditions. For a fixed accelerating voltage and beam current, the magnitude of this current depends on the beam Focus Offset (FO), as well as the irradiation time. Compared to the solid Ti melting, the counter current associated with powder melting initiates at a lower fluence threshold and is more chaotic, a feature we attribute to the differences in bulk thermal transport. Taken together, we suggest that these charge transfer effects are related temperature response of the workpiece, suggesting that charge and energy transfer during electron beam melting of Ti are coupled. Based on previous studies, we attribute this current to the recombination of positive ions formed in the metallic vapor above the melt pool surface.

It is also demonstrated that the effective electrical conductivity of the powder bed is determined by the sinter state of the powder, which builds upon the recent temperature-dependent, capacitive contact model put forward by Cordero *et al.*[137] With this finding, we define the term 'contact-sintering', which refers to powder which has achieved electrical contact between the particles but lacks well-developed sinter necks, allowing the powder cake to be processed back into its free-flowing state for subsequent reuse.

Combined, these findings illustrate how charge is locally transported within a powder bed during irradiation and furthers the understanding of electrostatic powder charging.

6.2 Theory

While the physics of generating an electron beam are identical in both EBW and EB-PBF, energy and charge transport within a powder bed are significantly more complex due to the high surface area, dynamic heat transport characteristics and pressureless point-like electrical contacts.[31, 202, 89, 203, 204]. Compared to the relatively simple joint geometries associated with EBW, the stochastic nature of the powder bed surface results in unstable and random convection flow patterns.

For L-PBF, significant understanding has been gained by studying the beam/powder interactions, both numerically and experimentally.[205, 141, 206, 207, 208] In these studies, it has been determined that local variations in the powder structure give rise to sizeable fluctuations in the energy absorption, which depend on material, Particle Size Distribution (PSD), packing density, beam size and Peak Power Density (PPD). These fluctuations in absorption can have major implications regarding powder denudation, keyhole porosity and plasma-based laser dispersion.

In comparison, there have been virtually no detailed experimental studies of electron beam single layer powder melting. Arguably the biggest barrier is the lack of open-architecture EB-PBF systems that provide direct access to beam parameters such as deflection pattern waveforms and accelerating voltage.[209] Another challenge is associated with reliably controlling the electro-optical dependencies of the beam, which were discussed at length in Sec.2.3. Finally, electrostatic powder charging, commonly referred to as powder smoke, requires additional processing steps to suppress powder ejection, including preheating the build platform, using high velocity scanning strategies and admitting inert process gas into the vacuum.[79, 78, 131, 132]

In some studies, bead-on-plate welds were used to understand the focussing characteristics of commercial hardware.[108, 114] By examining the melting behaviour of a solid, these studies inherently focus on energy transfer, neglecting the potential for space-charge related effects.

Although parametric mapping of single layer electron beam weld tracks is rare, numerous powder-level numerical studies have been conducted by the team at the University of Nürnberg-Erlangen using the Lattice-Boltzmann free surface technique.[203] Building off of years of model development, a recent publication detailed the complex relationships between energy input, evaporation and residual porosity associated with melting Ti-48Al-2Cr-2Nb.[89] Numerical comparisons between solid and powder melting showed that the reduced heat transport properties of the powder bed results in a higher evaporative flux and loss of alloying elements. Ostensibly, the higher temperatures are associated with the tortuous, surface-dominated, liquid convection path associated layers 2-3 particles thick.

In both EB-PBF and L-PBF instances, only the role of energy transport is considered, with the incident beam energy divided amongst reflected, conductive, radiative, convective and evaporative loss, which was discussed in Ch. 4. Fundamentally, these relationships are governed by conservation of momentum, mass and energy. Conservation of charge during electron beam processing requires consideration of space-charge effects, opening the possibility for interactions with the surrounding vacuum environment. For example, it is physically possible to scatter more low eV electrons out of the sample than high eV incident electrons. Assuming the workpiece is grounded, the additional electrons are drawn from the electrical circuit formed with the chamber. If the workpiece is isolated, the conduction path is broken and the net outflow of electrons will result in the build up of positive charge until surface-mediated electrical breakdown occurs.

Electrons which are generated directly from interactions between the primary incident beam and the workpiece are commonly defined according to the electron yield:[210]

$$\Gamma_e = \frac{e^- \ leaving \ surface}{incident \ e^-} = \frac{I_{BSE} + I_{SE}}{I_b} = \Gamma_{BSE-e} + \Gamma_{SE-e} \tag{6.1}$$

where I_b is the incident electron beam current, I_{BSE} is the current associated with the high energy backscatter electrons, and I_{SE} are <50eV electrons associated with surface interactions, such as Auger, photo, avalanche electrons.[210, 211, 212, 177] For reference, the electron microscopy community denotes the electron yield with the δ symbol, but the Γ_e symbol is used here to maintain consistency with the reflection coefficient nomenclature defined in Ch. 4. For a given setup, the electron yield is largely dependent on beam conditions, surface state and material composition, which we label as intrinsic charge transfer mechanisms.

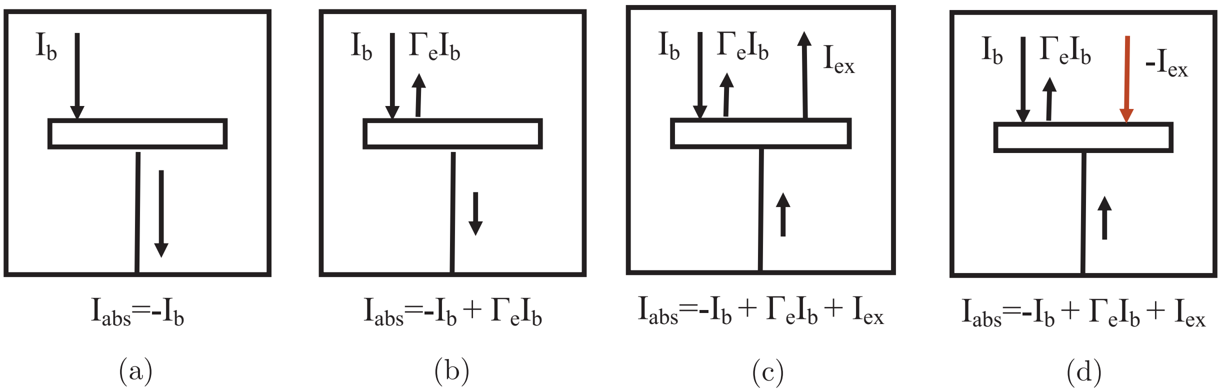

Figure 6–1: Electron and current flow during electron beam charge transfer, the black arrow represents electron flow, and the orange represents positive ion flow. Leftmost: Upward current flow/downward electron flow with no reflected primary electrons, Γ_e=0. Second from left: Upward current flow with some reflected primary electrons, $\Gamma_e > 0$. Second from right: Downward current flow due to extrinsic electrons flowing out of the workpiece. Right: Downward current flow with extrinsic ions recombining at the workpiece.

To define the effective current absorption coefficient, η_e, one must first recognize that conservation of charge requires that the number of charged particles recombining at the interaction zone equals the number of particles leaving it. The conduction path of these particles is not restricted to the electrical contact between the workpiece and chamber and can include free particles interacting with the chamber walls.

Following this, the sign convention for current is defined by the flow direction of positively charged particles. In this case, a current of primary beam electrons into the workpiece must be compensated by an current of electrons moving from the workpiece to the chamber, which is shown in Fig. 6–1a. This implies that the direction of conventional current opposes the incident beam, and is equivalent to a stream of positive ions being absorbed by the workpiece. If some of the primary beam current is scattered out of the workpiece, there is a corresponding reduction of current through the workpiece/chamber contact point, as shown in Fig.6–1b.

This situation becomes more complex when charged particles are generated via indirect beam interactions. For generality, we will define this current as I_{ex}, which represents extrinsic interactions composed of both positive or negative particles.

If the sum of intrinsic and extrinsic electrons leaving the workpiece exceeds the incident beam current, $I_b < \Gamma_e I_b + I_{ex}$, the current will flip directions, as charge conservation requires electrons to enter the workpiece, which is equivalent to positive ions moving in the opposite direction, as shown in Fig. 6–1c. An equivalent situation emerges if a current of positive ions neutralize at the workpiece, which is shown by the flipped direction and charge of Fig. 6–1d.

Having defined some polarity-corrected permutations, the current absorbed by the workpiece is given by:

$$I_{abs} = \Gamma I_b - I_b + I_{ex} \tag{6.2}$$

from which we define the dimensionless absorption coefficient, η_e to be:

$$\eta_e = \frac{I_{abs}}{I_b} = \Gamma_e - 1 + \frac{I_{ex}}{I_b} \tag{6.3}$$

where the sign convention for I_{ex} references negatively charged particles leaving the sample.

Equation 6.3 demonstrates that the direction of current flow into the workpiece can be either positive or negative. In the absence of extrinsic charge transfer effects, it is possible to create a net current leaving the sample via the condition that $\Gamma_e > 1$. Generally, this occurs at primary beam energies between 0.1-3keV and grazing incidence angles, as these conditions enhance electron interactions at the surface.[37] Recently, a novel proposal by JEOL has been put forward to suppress electrostatic powder charging during EB-PBF. This idea is based on using an additional low energy, grazing incidence electron beam flood gun, such that $\Gamma_e \approx 1$, and $\eta_e \approx 0$.[213]

For engineering materials, Γ_e is sensitive to the surface properties of the workpiece. By definition, backscatter electrons are primary electrons which have entered the bulk, then scatter out with an appreciable amount of the incident energy. These electrons form the bulk of the reflected primary beam energy, as discussed in the calorimetric measurements of Ch. 4. In contrast, secondary electrons are low energy electrons which can only escape if they are excited near the surface. In one instance, glow-discharge surface treatment of 6061 aluminium resulted in a significant reduction in the electron yield compared to the as-received surface.[211] Adsorbed layers of water vapor can increase

Γ_e, therefore bake-out of vacuum components is a well established method to suppress spurious electrons generation along accelerator beamlines.[212]

The physical topology of the surface can also impact Γ_e via the solid angle for electron escape. Surfaces with high-aspect ratio rectangular grooves significantly reduced the net electron yield by trapping the BSE and SE electrons within the rectangular channels.[212]

In terms of extrinsic mechanisms, high temperatures can significantly impact charge transfer during electron beam processing through a combination of vapor ionization and thermionic emission. For instance, the origins of charged species during uranium isotope separation via electron beam evaporation has been extensively studied.[177, 214, 215] Nishio *et al* divided the charged particles into two groups: one which produces only electrons (back-scatter, secondary and thermionic electrons) and another group which produces electron-ion/pairs (thermal/Saha ionization and electron-impact ionization). Using detailed thermal instrumentation and plasma diagnostics, the temperature dependence of each charge particle source was identified, and it was determined that a weakly ionized plasma forms within the metal vapor plume, dominating the net charge transfer at high temperatures.[177] Using a similar setup, Dikshit *et al* reported a five-fold increase in Al ion generation with the addition of a porous Ta plug to water-cooled copper crucible.[216] It was postulated that the porous Ta plug enhanced the electron-impact ionization of the Al vapor by enhancing the secondary electron yield. Combining atomic vapor flux and ion density measurements with assumptions regarding the electron impact ionization rates, a method for estimating the evaporation temperature and area of zirconium, tin and aluminum has recently been demonstrated.[217]

In these cases, a 10kV transverse-type evaporator was used, which implies an enhanced SE path length within the vapor due to magnetic bending field, and a rapid cooling of the plasma temperature.[36, 178] Similarly, measurements were conducted after a long heating period, reducing the possibility of adsorbate-enhanced secondary emission.

In the following, both intrinsic and extrinsic charge transfer mechanisms will be examined during pulsed electron beam melting of solid and powder Ti. To the best of our knowledge, the data presented are the first measurements of their kind comparing

C	O	N	H	Fe	Other	Ti
0.01	0.12	0.01	0.002	0.04	0.3	Bal

Table 6–1: Chemical composition of gr1 Ti powder. All values in wt.%

charge transfer of these two material states. Despite an extensive literature review over the course of this dissertation, the fact that similar measurements have not been conducted in English literature is somewhat surprising. One possible explanation is that the beam current regulation of conventional systems has significant rise times and ringing which would prohibit precise control of the pulsed beam power, features which were discussed in Ch. 3. Also, the pulsing circuitry associated with our system was designed to generate sharp pulse edges, leading to a high level of temporal control. Finally, the gCode compiler detailed in Sec. 3.5 enabled a wide range of experimental permutations to be rapidly explored. Combined, these features offered a high level of control of the incident beam fluence, and thus the transient temperature and current response of the workpiece.

6.3 Methods and Materials

The methods and materials described in this section are based on the systems described in Ch. 3, with specific implementation details given below.

The 50x50x1.5 mm solid substrates were made from laser cut, grade 2 commercially pure Ti (Baoji Magotan Nonferrous Metals, Shaanxi, China). The plates were manually ground using 320 grit SiC abrasive paper to a flatness of $\pm 10\mu$m over middle 25mm of the surface. The substrates were then etched for 2 minutes in a modified Krolls reagent of [HF:HNO_3:H_2O] = [1:2:10] to remove any contaminates and set the surface oxide to a controlled state.[218] After processing, the surface finish was measured to be R_a= 0.4μm.

Grade 1 commercially pure titanium powder was formed by plasma atomization resulting in some satellites, which are shown Fig. 6–2a. This EB-PBF-sized powder was sieved to a PSD of 45-106μm, with the corresponding laser diffraction PSD shown in Fig. 6–2b. The powder Hall flow rate was measured to be 24s, with an apparent density of 2.62 g cm^{-3} ($\Phi = \rho_{app}/\rho_s$= 0.57), where ρ_s is the density of solid titanium. The tap density of the powder was 2.90g cm^{-3} (Φ= 0.64), resulting in a Hausner ratio of 1.10. The powder chemical composition is shown in Table 6–1.

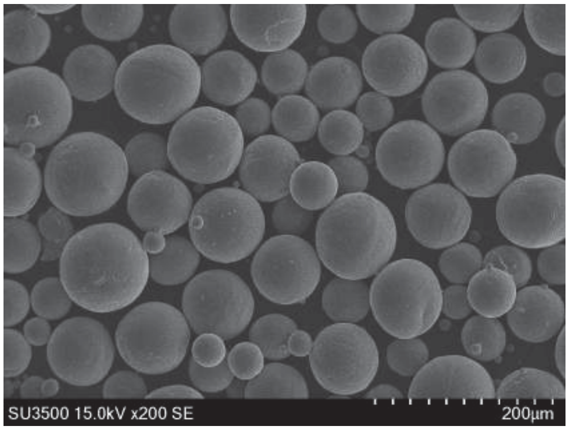

(a)

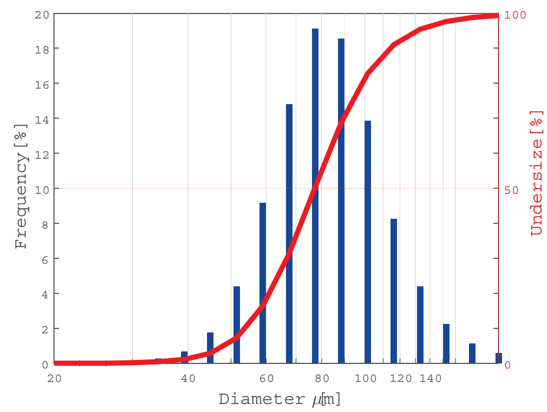

(b)

Figure 6–2: Morphology and PSD of gr.1 Ti powder. Left: SEM micrograph. Right: Particle size distribtuion according to laser diffraction. $D_{10} = 53\mu$m, $D_{50} = 82\mu$m, $D_{90} = 114\mu$m

To minimize adsorbed water vapor, the powders were radiatively heated to approximately 300^{o}C within the high vacuum chamber, and stored under vacuum for subsequent use.[219] Powder was deposited using the powder press described in Sec.3.4.2 with a mass of m_{pow}= 76 mg. The projected area of the resulting circular disk of sintered powder was measured to be A_{pow}= 266 mm^2 using image recognition software. Assuming a uniform layer thickness, the corresponding thickness of solid material is $t_s = m_{pow}/\rho_s A_{pow}$= 62$\mu$m.[26] The corresponding powder surface enthalpy of melting at room temperature is $\delta h_{surf} = t_s \rho_s (H_l - H_{25C})$= 0.41 J mm^{-2}, while the equivalent δh_{surf} at 700^{o}C is 0.30 J mm^{-2}. Using the maximum powder layer height measured from the optical profilometer, $max(t_{pow})$= 160 μm, the powder packing density is $\Phi = \rho_{pow}/\rho_s$= 0.39. If the mean powder height of 98μm is used, the packing density increases to Φ= 0.64, which is identical to the tap density of the bulk powder.

Two variants of the powder fixturing detailed in Sec. 3.4.2 were used, with a beam incident angle of 55^o in both cases, shown in Fig. 6–3a.

In the first variant, the substrate was electrical grounded and two thermocouples were joined to the backside. After powder deposition, the vacuum chamber was pumped down to a pressure of P<2E-5mbar. The substrate temperature was raised by rapidly scanning a defocused beam in a circular deflection pattern centered on the outside of the powder disk.

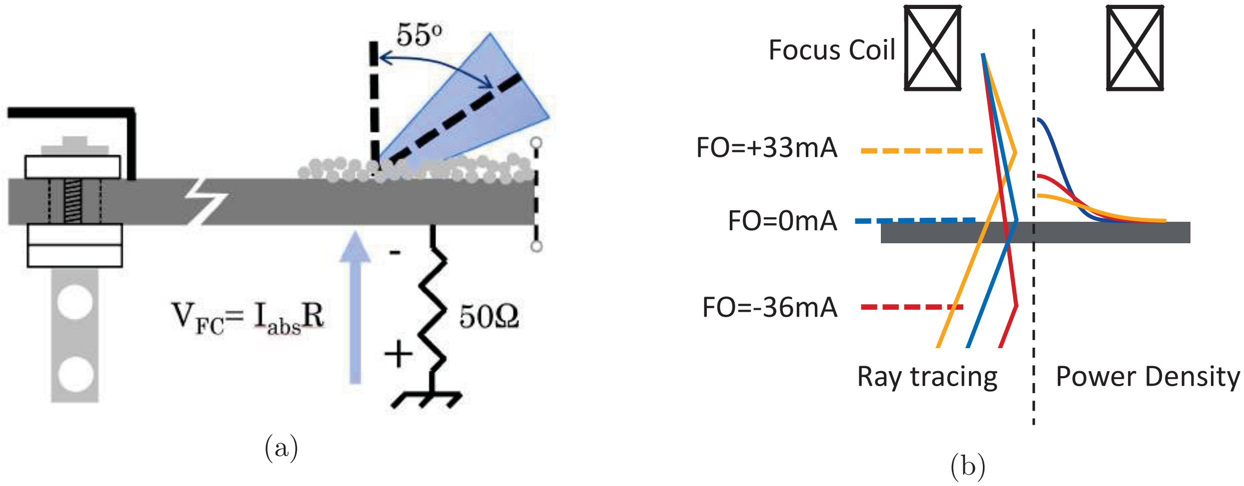

Figure 6–3: Faraday Cup workpiece configuration and FO/power density relationship

In this way, we assume that the thermocouple readings on the backside of the substrate are representative of the powder temperature.

This powder deposition and preheating technique represents an improvement over previously described processes.[220] The ability to measure and retain the powder mass, then directly measure the powder layer height enables precise estimations of powder packing density. Also, the addition of fine gauge thermocouples allows the substrate temperature directly under the powder to be accurately measured.

To preheat the powder, a beam power ramp rate of 36 W min^{-1} was used, while the steady state beam power was varied to control holding temperature. It was determined that the temperature difference between the TCs located at $r = 0$mm and $r = 10.5$mm, i.e. directly beneath the deflection pattern, was less than 50^{o}C.

Once a preheat algorithm was developed that resulted in contact-sintered powder, thermocouples were not applied to the substrate. Maintaining similar time and temperatures was achieved by reusing the same `preHeat` gCode, along with maintaining the torque on the substrate hold-down screws.

After the powder had been contact-sintered to the substrate, the chamber was vented with dry N_2 gas, and the substrate was electrically isolated using alumina washers between the hold-down screws and the substrate. A cover made from Mo foil shielded the insulator from intercepting stray electrons, reducing the risk of electrostatic-induced beam aberrations, as shown in Fig. 6–3a.

To measure the absorbed current, I_{abs}, the workpiece is electrically connected to a known resistor, effectively transforming it into a Faraday Cup. The signal acquisition setup and workflow was described in Sec. 3.2. In this case, the signals were low-pass filtered in MATLAB using a f_{3dB}= 100kHz.

Pulsed beam Faraday Cup measurements were performed for both solid and powder substrates, using a calibrated 80kV/4mA `pulsePat` object with a fixed pulse energy of $Q_p = V_{acc} I_b \tau$= 8J(τ= 25mS).The `pulsePat` object was composed of 24 individual pulses with incrementing Focus Offset (FO) over the range [-36: 3: 33]mA. *Note: FO is defined as the current offset of the focus coil current relative to the unique sharp focus setting.* The geometry of the experiment is configured such that the FO= -36mA pulse is located at the 12 o'clock position and FO increments in the clockwise direction, as will be shown in Sec.6.4.1. Testing pulses of various lengths confirmed that the response was independent of the net pulse length, in other words, the first 10mS of a 25mS pulses was identical to a 10mS pulse.

By varying the FO of each pulse, the position of the beam crossover image plane is varied relative to the fixed workplane, as shown in Fig. 6–3b. The result is a variable beam distribution parameter, $\sigma(FO)$. By varying the FO at a fixed beam and pulse length, we introduce small changes to the beam Peak Power Density (PPD). The resulting variable peak fluence associated with the pulsed beam is:

$$\begin{aligned} q_0 = p_0 \tau &= \frac{V_{acc} I_b}{2\pi \sigma_x \sigma_y} \tau \\ &= \frac{Q_p}{2\pi \sigma_x \sigma_y} \end{aligned} \tag{6.4}$$

At normal incidence and comparable working distances, the minimum distribution parameter of the 80kV/4mA beam at sharp focus was measured to be approximately σ= 0.35mm ($FWHM$= 0.82mm) using the slotted Faraday Cup method outlined in Sec. 3.2. Due to the inclined workpiece, the distribution parameter for these experiments is elongated along the y direction by σ_y= $0.35/cos(55^o)$ = 0.61mm, resulting in a net fluence of $q_0 = 5.9$ J mm^{-2}. Assuming an absorption coefficient of $\eta = 0.72$ for solid Ti calculated in CASINO, the dimensionless melt parameter of the powder layer at room temperature is $\gamma_m = 10.5$.

As a few final notes, it is currently unclear how the packing density of our single powder layers compare to those generated in commercial systems, specifically because of the differences in roughness of the underlying substrate.[133, 221] Nevertheless, great care has been taken to ensure that the powder deposits have repeatable characteristics, and over the course of the 19 experiments conducted with different substrates, the powder mass was maintained within a tolerance of ±3mg (4%), while the resulting powder disk area was maintained within a tolerance of approximately ±19 mm^2(7%). Finally, pulsed and solid powder FC measurements were conducted at 60kV/4mA, 60kV/16mA and 80kV/16mA at both $Q_p = 4$ and 8J. In the following, only the 80kV/4mA measurements will be presented, but the general trends are representative of these all measurements.

6.4 Results

6.4.1 Powder Smoke and Contact Sintering

Charge transfer during EB-PBF is a challenging problem because of the pressureless, point-like contacts between particles, which lead to very high contact resistance.[137, 222] These high contact resistances lead to a well-known problem referred to as powder smoke, which occurs when the beam of negatively charged electrons irradiates the powder. Considering the poor electrical conductivity of the powder, a distribution of charge can develop around the beam target area, resulting in the formation of an electrostatic field. If this charge density exceeds a critical limit, the electrostatic repulsive forces between charged powder particles can exceed the force of gravity, resulting in the violent ejection of the powder from the build platform.[223, 222, 137, 209] Currently, charge absorption and transport within a powder bed is understood to be a function of I_b, V_{acc}, focus offset, beam interaction time, build pressure, bulk electrical conductivity of the powder, powder packing density, scanning strategy, particle size distribution, powder morphology and powder oxide layer.[35, 223, 209]

To simplify this interpretation, we assume that the beam component of powder smoke is related to the amount of incident charge per unit area, which is defined for a pulsed

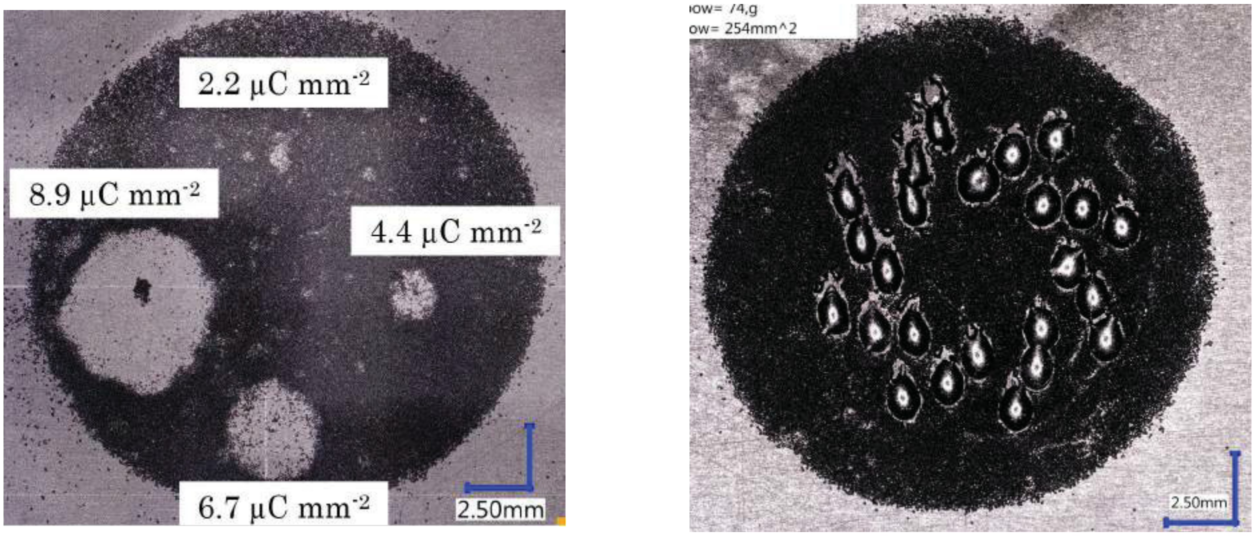

(a) (b)

Figure 6–4: Powder smoke and the effect of powder sinter state. Left: Loose, unsintered powder pulsed with a 80kV/4mA beam. The corresponding j_0 values were calculated according to Eq. 6.5 Right: Contact sintered powder pulsed with a 80kV/4mA beam, with a maximum charge density of 73μC mm^{-2}

beam according to the incident peak charge density, j_0 [μC mm^{-2}]:

$$j_0 = \frac{q_0}{V_{acc}} = \frac{I_b}{2\pi\sigma_x\sigma_y}\tau \tag{6.5}$$

Whether powder or solid, the absorbed charge is defined as $\eta_e j_0$, which has a similar form to absorbed fluence, ηq_0. To demonstrate the relationship between j_0 and powder smoke, a sharp-focus 80kV/4mA beam was pulsed onto room temperature, loose Ti powder at different pulse j_0 values, with the results shown in Fig. 6–4a.

Overlaid on Fig. 6–4a is the j_0 value of each pulse, which clearly shows that increasing charge density results in increased powder ejection. To compare pulsed and travelling beams, the equivalent centerline charge density is:

$$j_0 = \frac{q_0}{V_{acc}} = \frac{I_b}{\sqrt{2\pi}\sigma v} \tag{6.6}$$

Drescher observed Ti64 powder smoke when the travel speed of a 60kV/38mA beam was reduced to v=8600 mm s^{-1}.[78] Assuming the offset between scan lines is equal to the beam FWHM (1.2mm), the beam distribution parameter is estimated at σ= 0.51mm, resulting in a smoke threshold of j_0= 3 μC mm^{-2}, which is in agreement with the results of Fig. 6–4a. Since no details regarding the vacuum pressure were given, the effect of enhanced charge dissipation associated with the Arcam 'Controlled Vacuum' process are unknown.[209]

Equation 6.5 and 6.6 only define the incident charge, and do not account for how charge moves within the powder. Conceptually, this is similar to the discussion of incident, absorbed and conducted heat during the calorimetry measurements of Ch. 4.

To suppress powder smoke, the build-up of negative charge must be kept below the smoke threshold.[137] In this case, charge build-up reaches its maximum immediately following each beam interaction and includes the possibility of residual charge that has not dissipated from previous scans. In this case, the purpose of the Arcam preheat subroutine is to increase the bulk conductivity of the powder such that rate of charge dissipation exceeds the rate of charge absorption during powder melting, which has a high j_0 for the 60kV beam. In the simplest terms, the powder must form a reliable electrical return path before it can melted.

Using powder substrates with thermocouple instrumentation, we observed powder ejection similar to Fig. 6–4a for temperatures up to T=660^{o}C. When the powder was conductively preheated to 720^{o}C for 4 minutes, allowed to cool, then vented to atmosphere, the powder was observed to be loosely adhered to the substrate, allowing it to be transported for subsequent surface profilometry. Similarly, the powder could be inserted back into the vacuum chamber and pulsed without preheating with a $j_0 \approx 70\mu$C mm^{-2} beam without powder ejection, as shown by the 80kV/4mA results of Fig. 6–4b.

While the time/temperature schedules were not rigorously controlled, it is believed that above approximately 650^{o}C, the powder oxide decomposes and surface diffusion forms point-like contacts between individual powder particles.[224, 225] This temperature is well below the 900^{o}C threshold associated with measurable shrinkage during conventional Ti powder metallurgy processing.[226, 227] Therefore, we refer to this powder sinter state as 'contact sintering', as it implies the formation of a network of point-like electrical contacts between the particles and ground. For titanium alloys, the time and temperature required for contact sintering appears to be dependent on Al-content, with informal conversations

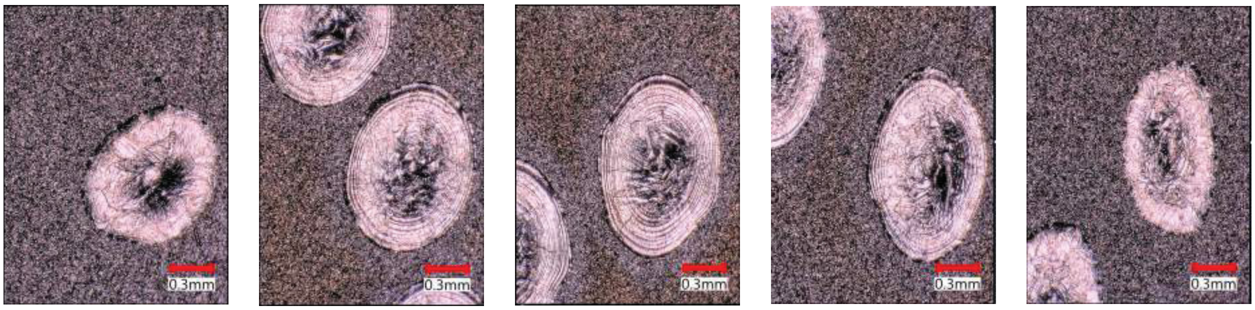

(a) FO = -36mA (b) FO = -15mA (c) FO = 0mA (d) FO = 12mA (e) FO = 33mA

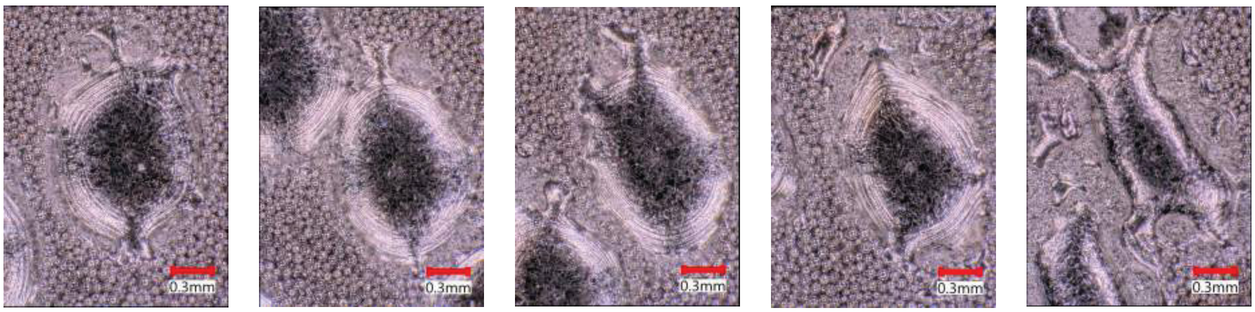

(f) FO = -36mA (g) FO = -15mA (h) FO = 0mA (i) FO = 12mA (j) FO = 33mA

Figure 6–5: Variable focus offset spot melts at 80kV/4mA on powder and solid Ti

suggesting that Ti-6Al-4V and Ti-48Al-2Cr-2Nb require a higher temperatures to contact sinter.

6.4.2 Absorbed Current

The spot melts generated from the *FO*= [-36, -15, 0, 12, 33]mA pulses on solid and powdered Ti are shown in Fig. 6–5. It should be noted that these pulses are zoomed in images of the pattern generated in Fig. 6–4b, therefore there is some overlap in the spot melts, which was needed to maintain identical image scaling.

In all cases, we observed melting of solid and powder for each beam combination used. The *FO*= [-15, 0, 12]mA solid spot melts demonstrate ripples along the resolidified surface, while the defocussed pulses of *FO*=[-36 33]mA do not. The *FO*= 33mA powder melt does not have the same appearance as the other melts, and suggests that surface tension effects prevented the formation of a consolidated deposit.[31]

To compare the melt patterns of Fig. 6–5 to the corresponding current absorption measurements, the t vs V_{FC} data acquired from the oscilloscope is transformed into more appropriate units. Specifically, the x-axis is scaled from seconds to joules according to

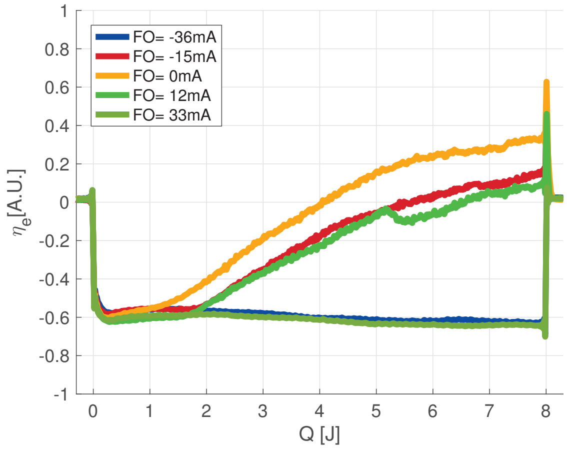

(a)

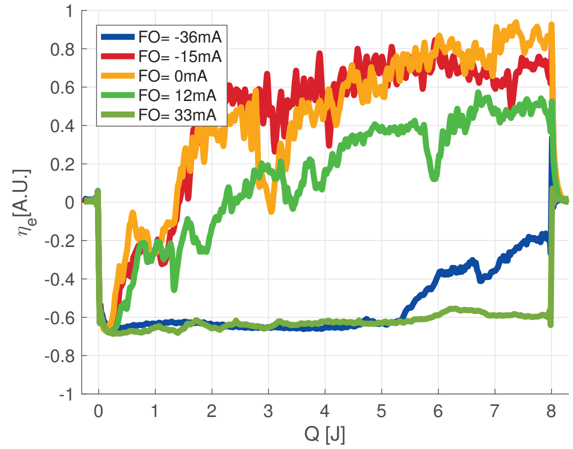

(b)

Figure 6–6: Transformed Faraday Cup current measurements at 80kV/4mA for FO= [-36, -15, 0, 12, 33]mA. Left: Melting of solid Ti. Right: Melting of powder Ti.

$Q_p = 80kV4mA * t$. The y-axis data representing V_{FC} is transformed into the charge absorption coefficient according to: $\eta_e = I_{abs}/I_b = V_{FC}/(50\Omega * 4mA)$. As discussed in the Monte-Carlo simulations of in Ch. 4, it is important to recognize that a value of η_e=-0.5 does not imply that 50% of the incident beam energy is reflected out of the sample, as charge and energy absorption are not equivalent.

The resulting transformed Faraday Cup current measurements for the solid and powder spot melts of Fig. 6–5 are shown in Fig. 6–6a and 6–6b, respectively.

As expected, the FO=[-36, 33]mA pulses demonstrate a flat top, negative polarity pulse. These results also suggest that $I_{abs} \approx 0.6I_b$.

The Faraday Cup response becomes more complex for the FO= [-15, 0, 12]mA pulses. In the case of the FO= [-15, 12]mA pulses, the absorbed current signal begins to decrease at 2J, while for FO= 0mA pulse, this decrease begins with less energy and at a faster rate.

Nominally similar behavior is observed for the FC measurements of powder in Fig. 6–6b, albeit with a more chaotic current response. Compared to the solid melts, absorbed current for FO= [-15, 0, 12]mA pulses begins decreasing at a much lower energy, $Q_p \approx$ 0.5J.

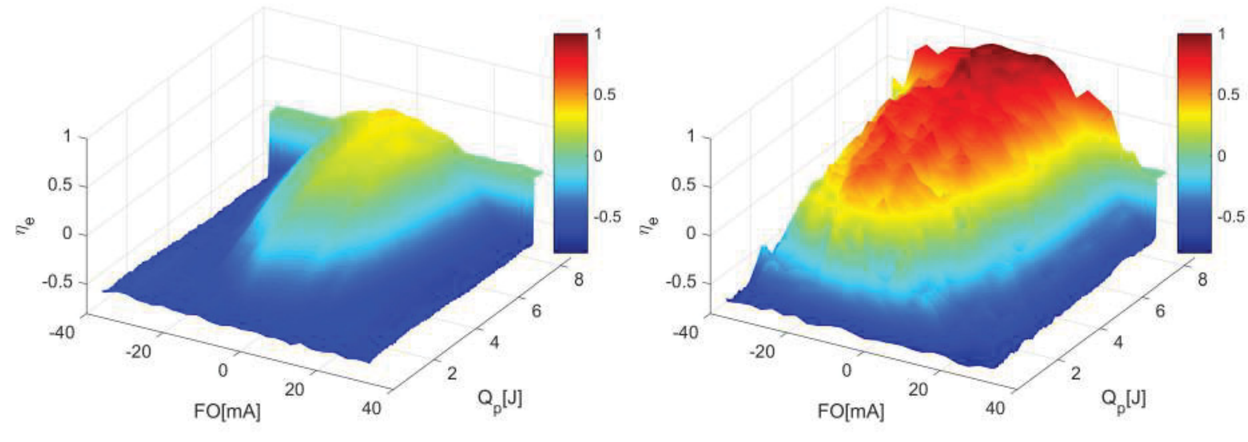

(a) (b)

Figure 6–7: Surface plot of transformed Faraday Cup current measurements at 80kV/4mA for FO= [-36:3:33]mA. Left: Melting of solid Ti. Right: Melting of powder Ti.

To further compare the 24 solid and 24 powder measurements, the FC responses have been plotted in a 3D surface plot, shown in Fig. 6–7, maintaining the same color scales and plot orientations to simplify comparison.

Our first observation is that for solid melting, the pulse energy needed to initiate a reduction in absorbed current is a smooth function of focus offset. These data also indicate that the magnitude of absorbed current for powder is higher than it is for solid. Similarly, the powder response is more chaotic in comparison to melting solid.

Although the solid 80kV/4mA data show a smooth η_e response during pulsed melting, this was not always the case. FC measurements at $FO \approx 0$mA for a 60kV beam at I_b= [8,12,16]mA are shown in Fig. 6–8, demonstrating an oscillatory behaviour at the latter portion of the pulse. In the time domain, the oscillation period is roughly 0.3mS for all beam combinations.

6.5 Analysis

To understand the FC signal response of the preceding section, it is worth noting that the voltage that develops on the substrate during irradiation is $4mA * 50\Omega \approx \pm 0.2$V. While this potential will decelerate the incident beam, the energy loss is inconsequential in comparison to 80,000eV incident energy.[57] Similarly, Q_p vs FO spot melt matrices

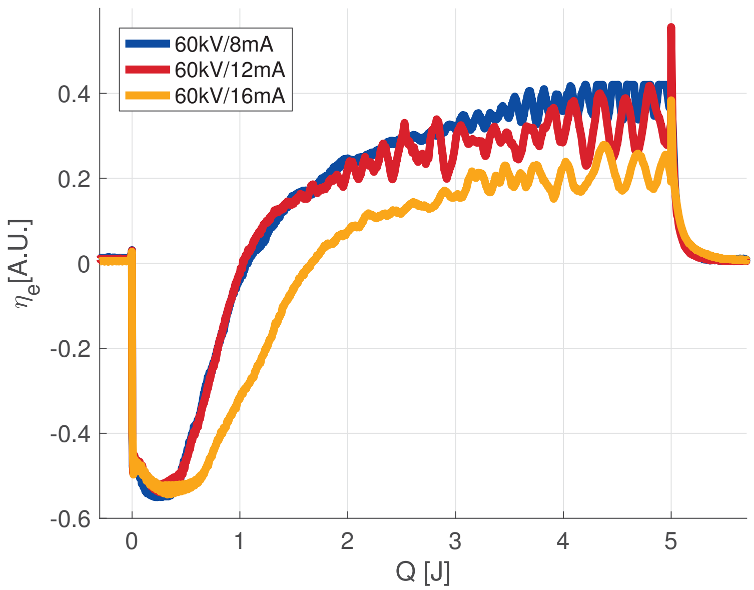

Figure 6–8: Absorbed current oscillations during pulsed melting of solid Ti at 60kV with I_b= [8,12,16]mA

similar to those shown in Sec 3.5 did not result in any distinguishable differences between the top melt area when comparing FC and grounded substrates.

Together, these findings suggest that a resistively isolated workpiece does not induce measurable changes in the absorbed beam energy. Without the calorimetric measurements of Ch. 4 or the Nb-Ti cross section FZ analysis of Ch. 5, this statement cannot be absolutely confirmed, and is largely dependent on our experience microscopically analyzing spot melts.

Additional measurements of a defocussed beam at 60kV and 80kV, similar to the flat top responses of Fig. 6–6a were conducted, where it was determined that η_e= -0.55±0.02 for solid Ti. For comparison, CASINO calculations using the BSE method outlined in Ch. 4 yield a Γ_e=0.42, corresponding to η_e= -0.58. This agreement suggests that the SE current, which is sensitive to oxide layers and adsorbates which is difficult to resolve using Monte-Carlo techniques, is not significant. This is likely due to the chemical etch performed prior to melting, which is quoted to yield an oxide layer thickness of 3-5nm according to angle-resolved x-ray photoemission spectroscopy.[218] Similarly, a value of η_e= -0.73 ± 0.04 was determined for defocussed melting powder, which is consistent with the idea that a surface roughness greater than the electron range enhances trapping of backscatter and secondary electrons.[212]

Assuming the intrinsic electron yield (Γ_e) and absorbed energy are independent of FO setting, the changes in absorbed current imply the formation of an extrinsic current related to power density and beam fluence. Also, due to the polarity of η_e, this extrinsic charge transfer must be either electrons scattered out of the workpiece, or positive ions neutralizing at the workpiece.

One possible source of extrinsic charge is thermionic emission from the molten Ti surface. Referring back to the Richardson-Dusham equation in Sec 2.2, the temperature required to generate a 1mA current of thermionic electrons from the liquid Ti surface can be estimated. Assuming an emission area of $\pi\sigma_x\sigma_y$= 0.6mm^2, a Richardson constant of A = 120 A cm^{-2} K^{-2} and a work function of ϕ=3.96eV, a temperature of T= 1827^{o}C would be required.[228] Although this number is well within the temperature range of electron beam melting, an increase in liquid temperature would result in an exponential increase in thermionic emission, barring any space-charge effects. This contradicts the data in that the extrinsic current appears to reach steady state.

In terms of positive ions recombining at the workpiece, the generation of a vapor medium for ionization must first be considered. Since melting was performed on a clean surface in a high vacuum environment, the only source of appreciable positive ions would be associated with the evaporation and subsequent ionization of the Ti itself. This suggestion is immediately appealing, as evaporative heat loss restricts the maximum vapor flux and thus ion current.

Furthermore, if the extrinsic current is linked to evaporation/ionization, heat transport within the workpiece would be a necessary consideration. The surface temperature at the center of a pulsed Gaussian beam can be estimated according to:[229]

$$T(t) = \eta\frac{V_{acc}I_b}{\sqrt{2}\pi^{1.5}\kappa\sigma}tan^{-1}\left(\frac{\sqrt{2\alpha t}}{\sigma}\right) + T_0 \qquad (6.7)$$

where the thermophysical parameters of solid and powdered Ti are given in Table 6–2. Equation 6.7 was originally derived for pulsed laser irradiation and the beam distribution

State	η [A.U.]	κ[W m^{-1} K^{-1}]	α [mm^2 s^{-1}]
Solid	0.72	22.5	7.7
Powder	0.72	4.5	1.5

Table 6–2: Thermophysical material parameters for cpTi, where the heat transport parameters of contact-sintered Ti were adopted from Smith *et al* [131, 26]. The absorption coefficient for Ti at a 55^o incident angle was calculated using the CASINO method

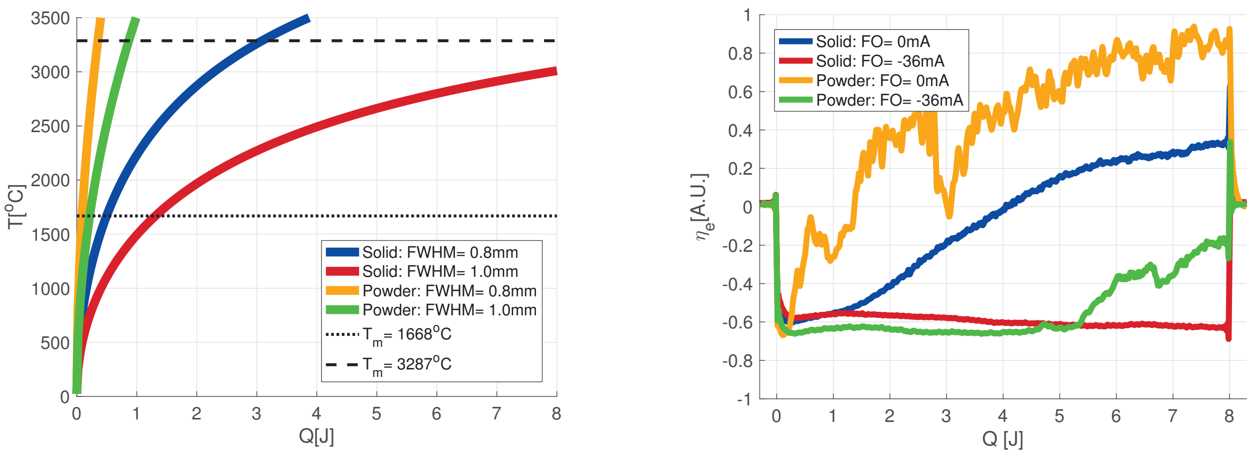

(a)

(b)

Figure 6–9: Temperature and absorbed current response comparison for focussed/defocussed and solid/powder melting

used was transformed to be consistent with this thesis, $exp(-r^2/2\sigma^2)$. Like all analytical heat transfer formulas, the temperature dependence of the material and convective heat transfer are ignored.

Similarly, the effective thermal transport properties of powder have been reduced by a factor of 5 compared to solid, which is consistent with recent laser flash measurements of contact-sintered Ti64 powder.[131] Also, this model assumes that powder heat transport occurs in a continuum, which by definition ignores the discrete nature of the particles. Despite these shortcomings, the model has been used by other researchers to understand the conditions for keyhole formation during L-PBF.[157]

With those qualifications, the temperature response of solid and powder material for a 80kV/4mA beam at a FWHM= [0.8, 1]mm is given in Fig. 6–9a, where the x axis has been scaled according to the incident energy, $Q_p = 80kV4mA * t$.

Focussing on the solid Ti results, we see that the peak temperature of the pulse depends strongly on the beam FWHM. In both focussed and defocussed cases, the temperature at the center of the pulse exceeds the melting temperature of Ti, which is consistent with the spot melt images of Fig. 6–5. The boiling temperature represents a rough estimate for temperature range associated with evaporation. The model shows that only the focussed beam reaches the boiling temperature, which occurs after approximately 3J of incident energy.

Figure 6–9b collates the FC measurements of focussed/defocussed, solid/powder melting for comparison. For solid melting, the data shows that the defocussed beam does not generate an extrinsic current, while it initiates with the focused beam at approximately 1.5J. Assuming the evaporation temperature corresponds to the temperature needed to form an appreciable ion current, these measurements agree with the temperature model of Eq. 6.7.

From these solid melting model results, the appeal of the evaporation/ionization model becomes evident, as it explains the smooth and symmetric absorbed current surface plot of Fig. 6–7a. Specifically, by defocussing the beam in the positive or negative direction, the beam FWHM increases, which in turn increases the energy needed before the onset of evaporation.

In terms of the focussed powder melting, the temperature response shows that the evaporation temperature is reached with much less energy, since the reduced heat transport concentrates the energy to the surface. The temperature model demonstrates that evaporation begins at approximately 0.3J, which agrees with the FC results of Fig. 6–9b.

Conversely, the temperature model suggests that the defocussed beam begins evaporating the powder at 1J, which is not supported by the FC measurements of Fig. 6–9a. This discrepancy could be explained by the molten powder wetting the substrate before evaporation, which efficiently convects heat into substrate. In this case, beam powder density as well as the melt pool characteristics more closely resemble the defocussed solid melting conditions, resulting in a limited evaporation.

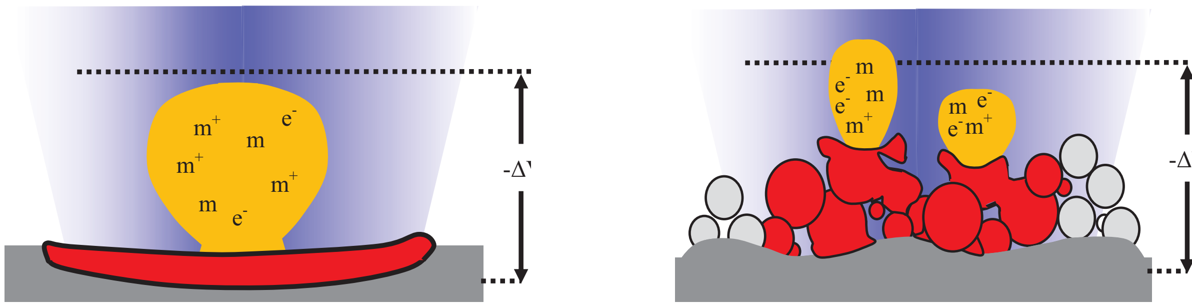

(a) (b)

Figure 6–10: Model for evaporation/ionization of solid and powder Ti

Thermally, this response has characteristics similar to the Nb-Ti EBW welds of Ch. 5. In this case, we saw that the Nb could preferentially draw heat away from Nb-Ti fusion zone, suppressing the formation Ti-vapor generated keyhole.

Returning to the current absorption measurements, after vapor is emitted from the liquid surface, it becomes ionized via a combination of Saha/thermal ionization and electron-impact ionization.[177, 230, 231] Unfortunately, these calculations are outside of the scope of this work, as it requires detailed estimates of the vapor temperature distribution, expansion path, and energy-corrected electron impact ionization rates.[177]

Although the precise model for explaining the sources and magnitude of ionization are complex, we can state that the plasma potential formed above the workpiece is less than -0.2V. This potential is needed to extract the positive ions from the dense plasma plume at a rate on the order of 10^{15} ions per second, which is equivalent to 1mA. In this case, the high translation velocity of the electrons compared to the ions might assist in separating the charged pairs, forming the negative potential within the plume.[232] Similarly, a negative plasma potential would also be consistent with the idea that thermionic electrons are prevented from escaping the Ti surface.

Figure 6–10a demonstrates mechanisms associated with the evaporation/ ionization model for the case of melting solid Ti, with the ionized vapor plume shown in orange. In this case, the evaporative flux is defined by peak surface temperature of the coherent melt pool. Conversely, the evaporative flux associated with the powder bed is more chaotic and localized, as the surface geometry of the powder bed prevents the formation of a stabilized convection flow pattern, as shown in Fig. 6–10b. Again, this interpretation explains why the extrinsic current initiates with less energy in the powder (lower heat transport) and has a chaotic nature (unstable convection).

Furthermore, absorbed current oscillations of associated with the 60kV solid melting measurements of Fig. 6–8 can be explained by melt pool oscillations. Specifically, the vapor plume distribution is strongly affected by the melt pool surface, in which case oscillations in the melt surface would imply oscillations in the ion current.[36, 232] Similar fluctuations have been observed in biased current probes placed above electron beam evaporators and during keyhole electron beam welding.[217, 232]

6.6 Discussion

Admittedly, a detailed understanding of the plasma dynamics above the evaporating surface requires further investigation, both theoretically and experimentally. Nevertheless, the data presented strongly suggests that the extrinsic current is related to the material temperature response. More importantly, the fact that this signal is associated with a temperature above the melting is significant, as it offers a new avenue to probe liquid-phase heat transport.

Although these transient charge absorption measurements for powder melting are novel, there is a precedent for sampling the charge carriers generated during electron beam welding, with examples given in Ch. 2. In these cases, the detectors were placed above the workpiece with the purpose of dynamically regulating FO and deflection pattern during keyhole welding. [233, 232]

These findings support the idea that EB-PBF has many similarities to keyhole EBW, as both instances are characterized by a high power density beam and significant evaporation. In the case of keyhole EBW, very high fluence values are needed maintain the vapor capillary against strong recirculating convection currents. In the case of EB-PBF, the poor heat transport properties of the bed concentrates the incident energy, also resulting in high vapor fluxes.

In this context, anecdotal evidence from experienced EBW operators regarding focus settings during high-aspect keyhole EBW merits re-evaluation for EB-PBF. Specifically, the focus setting that achieves maximum penetration during EBW is generally associated with an underfocussed beam at the workplane.[1, 36] This setting might be compensating for the plasma-induced beam dispersion, which in effect is a plasma-based lens above the evaporating surface.[36] In this case, the beam distribution at the workplane depends on the presence of evaporation, which is a known feature within the laser welding community.[67] This also calls into question the Faraday Cup beam distribution measurements, which inherently omit these plasma effects. Finally, the role of accelerating voltage represents a tuning parameter for these plasma interactions via the energy-dependent electron impact ionization cross sections.

Finally, it should be noted that even without a clear understanding of how these signals are generated, the fact that they appear correlated with the power density of the beam suggests an alternative method to calibrate the beam focus. In other words, instead of calibrating the beam to achieve its minimum beam diameter, the beam could be calibrated against the maximum magnitude or most stable extrinsic current signal. In terms of EB-PBF, the advantage is that this technique could be conducted in-situ throughout the course of a build, with the data fed back to the control settings.

6.7 Conclusion

This chapter presented some of the first measurements of charge transfer during transient electron beam melting of a single layer of Ti powder. It also experimentally demonstrated that electrostatic powder charging during room temperature melting is strictly defined by the powder sinter-state. With this finding, we have defined the state 'contact sintered', which refers to powder which has been sufficiently sintered to form electrical contacts to ground without the formation of extensive necks, which otherwise would prevent the powder from being broken up and re-used.

By analyzing the absorbed charge during pulsed melting of solid Ti, we have demonstrated the formation of a current signal which only forms under certain beam conditions, and is independent of melting. By varying the focus offset of the beam, it was shown that the magnitude of this signal is related to the fluence of the electron beam pulse. A similar signal was observed for pulsed melting of room temperature Ti powder, although the current initiated at a smaller fluence threshold and at over a larger FO domain.

Based on these findings, we suggest that the extrinsic current is associated with the temperature response of material. These findings are qualitatively supported by a simple solid-state heat transport model, which captures the effects of beam FWHM as well as the thermal transport properties of the workpiece.

We associate this signal with the evaporation and subsequent ionization of the workpiece. Based on a simple charge transfer argument, we attribute this extrinsic current to the neutralization of positive ions at the workpiece surface. The presence of a negative plasma potential is a necessary condition to extract the positive ions from the vapor cloud.

Although the precise mechanism, or mechanisms, involved in generating the extrinsic current requires further investigation, these measurements seem to offer an indirect probe of the liquid temperature response, which could be used as a time-resolved method to compare heat transfer simulations and would represent a low-cost alternative to high speed imaging. Similarly, this method could be used as an in-situ method to calibrate beam focus over the course of a EB-PBF build.

6.7.1 Future Work

The conditions for contact sintering merit deeper investigation. In the work presented, the powder was sintered for a comparatively long time, therefore understanding the exact time and temperature threshold needed for contact sintering would be beneficial for both the academic and industrial community. Similarly, a deeper investigation regarding powder ejection and incident charge fluence would beneficial, as the experiments conducted did not include a detailed analysis of how beam defocussing affects powder smoke.

In terms of the absorbed current measurements, significant effort is required to further understand and optimize the work presented. A more detailed analysis of plasma physics and electron impact ionization is needed. Further experimental studies should include a Hall probe or Rogowski coil current sensor, which would allow the current to be measured independent of a resistor-generated substrate voltage. Similarly, the addition of a bipolar electrode above the substrate would allow some degree of charged species discrimination. In this case, the tilted incidence angle of the electron beam would be a significant advantage. Thermal modelling, which accounts for convective heat transfer and evaporative flux, would also be beneficial, as this could assist in determining both the evaporative flux and the degree of plasma ionization.

Melting an array of wires arranged above the substrate could an interesting extension of these measurements for two reasons. For one, this structure is conceptually similar to a powder bed in that a material with low surface melting enthalpy is gently resting above a solid substrate. Yet in the wire case, the conduction path is modified such that heat can be transported along the wire. In a sense, wire/powder comparisons would be comparing heat transport between 0D and 1D objects. A second advantage is that the wires could be electrical isolated, and the current flowing through each element could be measured directly. Considering the cost of the oscilloscope used($400), creating an array of such Faraday Cups would not be prohibitive.

Finally, repeating these measurements for the industrially relevant Ti-6Al-4Al and Ti-48Al-2Cr-2Nb powders would be interesting, from the combined perspectives of contact sintering and preferential Al vaporization/ionization.

CHAPTER 7
Conclusion

The objective of this work was to experimentally investigate the similarities and difference between two closely related topics: Electron Beam Powder Bed Fusion (EB-PBF) and Electron Beam Welding (EBW). This objective was approached by analyzing the energy and charge transfer associated with workpiece melting using thermocouples and current measurements, respectively. While most literature has focused on the energy needed for melting, this dissertation included detailed analysis of how the current density at the cathode transforms into current density at the workpiece. This approach is consistent with the idea that electron beam optics is the science of charge transfer.

To develop the open-architecture, single layer EB-PBF platform used in this work, a dimensionless γ_m parameter was derived which indicated the first order relationship between beam, material and geometry. This equation guided much of the subsequent development with regards to the powder layer thickness and peak power density of the beam. The slotted Faraday Cup measurements indicated that the power density of the beam was beam current dependent, and significantly lower than that found in commercial systems. The low power density of the beam, in conjunction with the 35^o incidence angle, calls into question whether our charge transfer measurements are applicable to commercial processes, and should be investigated on those platforms.

Another development in this thesis was a software framework to control the electron beam. Specifically, the ability to decouple the beam calibration and experiment definition proved extremely valuable when mapping different parameter combinations. Future investigations should improve upon this software/firmware integration, as it will accelerate process mapping. With enough sophistication, the platform should be capable of melting two dimensional planes with zero latency, a key component of commercial EB-PBF. Unfortunately, this objective requires support from seasoned controls and software engineers and thus, a significant budget.

Having demonstrated the accuracy of Monte-Carlo simulations in estimating electron beam absorption, future studies should apply the CASINO software towards electron beam powder bed fusion. Powder-level beam scattering software has proven useful in understanding laser powder bed fusion, and similar, electron-specific simulations could be of significant benefit to the community. The effect of powder packing, accelerating voltage and particle size distribution on local powder absorption would be especially interesting.

The powder-press deposition fixture offered some very interesting insights into the powder spreading dynamics. The ability to directly measure the height distribution of the powder layers using non-contact methods demonstrated that wall effects significantly impact the powder bed packing fraction. Considering the poor understanding concerning powder spreadability, these measurements should be expanded for different powders, and surface morphologies. At the very least, these experiments could be used to calibrate the constitutive properties of discrete element powder models. It is possible that one day, a variation of these low-cost measurements could become a standard for measuring the packing fraction of random, thin powder beds.

In conclusion, this dissertation demonstrates that EB-PBF has many similarities to keyhole EBW, as both instances are characterized by a high power density beam and significant evaporation. In the case of keyhole EBW, very high fluence values are needed maintain the vapor capillary against strong recirculating convection currents. In the case of EB-PBF, lower fluences are used, but the poor heat transport properties of the powder concentrates the incident energy to the surface, also resulting in high vapor fluxes. In both cases, the quality of the beam will have a significant effect on the resulting product, highlighting the need for careful process understanding, calibration and regulation.

Investigating these issues requires a multi-disciplinary approach which considers beam physics, heat transfer, metrology, software integration and finally, physical metallurgy. While a significant amount of academic research has concerned the last item, with the objective of validating commercial platforms, the future growth of additive manufacturing depends on collaborative research and development into these expanded domains.

Appendices

APPENDIX A
Acronyms and Symbols

EBW Electron Beam Welding

AM Additive Manufacturing

PBF Powder Bed Fusion

EB-PBF Electron Beam Powder Bed Fusion

L-PBF Laser Powder Bed Fusion

BSE Back-Scattered Electrons

SE Secondary Electrons

PSD Particle Size Distribution

DED Directed Energy Deposition

GUI Graphical User Interface

FC Faraday Cup

TC Thermocouple

FWHM Full Width Half Maximum

WD Working Distance

HAZ Heat Affected Zone

FZ Fusion Zone

WZ Weld Zone

BM Base Metal

PPD Peak Power Density

FO Focus Offset

SF Speed Function

List of Symbols

ρ $[gcm^{-3}]$ Density

L_f [J g^{-1}] Latent heat of fusion

$[+bias]$ [V] Voltage applied to bias electrode

α $[mm^2s^{-1}]$ Thermal diffusivity

δh_m [J mm^{-2}] Enthalpy of melting per unit area

η [A.U.] Energy absorption coefficient

η_e [A.U.] Charge absorption coefficient

γ $[Nm^{-1}]$ Surface tension

γ_m [A.U.] Dimensionless layer melting parameter

κ $[Wm^{-1}K^{-1}]$ Thermal conductivity

Φ [A.U.] Layer packing density

σ_i [mm] Beam distribution parameter along ith axis

τ [s] Dwell time or pulse length

c_p $[Jg^{-1}]$ Heat capacity

f_{def} [Hz] Deflection frequency

f_s [Hz] Sampling frequency

H [J g^{-1}] Enthalpy

h_s [mm] Hatching spacing

I_b [mA] Beam current

I_{bse} [mA] Back-scatter electron current

j_b [A mm^{-2}]Local current density of beam

L_{th} [mm] Thermal diffusion length $= 2\sqrt{\alpha\tau}$ [m]

p_0 [W mm^{-2}] Peak power density(PPD) of beam

q_0 [J mm^{-2}] Peak fluence

T^* [A.U.] Dimensionless temperature$= (T - T_0)/(T_m - T_0)$

T_0 [^{o}C] Reference temperature

t_l [mm] Layer thickness

T_m [^{o}C] Melting temperature

v [mm s^{-1}] Beam speed

V_{acc} [V] Accelerating voltage

w_b [mA] Focus coil current

z_B [mm] Build table displacement

References

[1] Helmut Schultz. *Electron beam welding*. Elsevier, 1994.

[2] Corey Clark. General Electrics GE9X engine undergoes further testing of 3D printed components. https://3dprintingindustry.com/news/general-electrics-ge9x-engine-undergoes-testing-3d-printed-components-104180/, 2017.

[3] Dietrich Dobeneck. *An international history of electron beam welding*. pro-beam, 2007.

[4] Robert W Messlef. The greatest story never told: EB welding on the F-14. *Welding journal*, 86(5):41–47, 2007.

[5] Patricio F Mendez and Thomas W Eagar. Welding processes for aeronautics. *Advanced materials and processes*, 159(5):39–43, 2001.

[6] American Welding Society. *AWS C71.M: Recommended Practices for electron beam welding and allied processes*. AWS, 2013.

[7] Hasan Padamsee. *RF superconductivity: science, technology and applications*. John Wiley & Sons, 2009.

[8] Timothy W Simpson, Christopher B Williams, and Michael Hripko. Preparing industry for additive manufacturing and its applications: Summary & recommendations from a national science foundation workshop. *Additive Manufacturing*, 13:166–178, 2017.

[9] Fred George. Pilot Report: Flying the 737-8, Boeings New Narrowbody Breadwinner. http://aviationweek.com/commercial-aviation/pilot-report-flying-737-8-boeing-s-new-narrowbody-breadwinner, 2017.

[10] Yari Bovalino and Dmitry Sheynin. A Treat For The AVGeeks: An Inside Look At GEs 3D-Printed Aircraft Engine. http://www.ge.com/reports/treat-avgeeks-inside-look-ges-3d-printed-aircraft-engine/, 2017.

[11] Mathieu Benedict. GE unveils 35% 3D printed ATP engine: 'More additive parts than any engine in aviation history'. http://www.3ders.org/articles/20161101-ge-unveils-3d-printed-atp-engine-more-additive-parts-than-any-engine-in-aviation-history.html, 2016.

[12] Dietrich Alcock. GE's New Turboprop Engine Family Has Deep Roots in Europe. http://www.ainonline.com/aviation-news/business-aviation/2017-05-19/ges-new-turboprop-engine-family-has-deep-roots-europe, 2017.

[13] Dane Halloway. Metal additive manufacturing sector in 'pivotal' year - report. http://optics.org/news/8/4/1, 2017.

[14] Michael Petch. 3D Printing Metal Interview with Arcam CEO Magnus Rene. https://3dprintingindustry.com/news/3d-printing-metal-interview-magnus-rene-arcam-group-ceo-83724/, 2016.

[15] Rachel Park. A Consideration of EBM versus DMLS Industrial Metal 3D Printing Processes, Part 2. http://www.fabbaloo.com/blog/2016/4/17/a-consideration-of-ebm-versus-dmls-industrial-metal-3d-printing-processes-part-2, 2016.

[16] Adam Rivard. The Battle Between Laser and EBM for Production Part. http://www.globalspec.com/events/eventdetails?eventId=1350, 2017.

[17] Alison Warwick. Productivity in metal additive manufacturing: a focus on arcam and electron beam melting. https://www.linkedin.com/pulse/productivity-metal-additive-manufacturing-focus-arcam-alison-m–1/, 2017.

[18] Matthieu Petelet. Whats under the hood of an Arcam EBM System? Arcam.

[19] Rachel Gordon. 3D Printing of Metals: 2015-2025. http://www.idtechex.com/research/reports/3d-printing-of-metals-2015-2025-000441.asp, Date 2015.

[20] Yari Bovalino. The silent revolution. http://www.magazineabout.com/Technology-Digital-Innovation/The-silent-revolution, 2017.

[21] Kira Kellner. GE's Avio Aero orders 10 new Arcam EBM metal 3D printers to produce aerospace parts. http://www.3ders.org/articles/20151222-avio-aero-orders-10-newarcam-ebm-metal-3d-printing-systems-to-produce-aerospace-parts.html, 2015.

[22] S Schiller and S Panzer. Surface modification by electron beams. *Thin solid films*, 118(1):85–92, 1984.

[23] M Weglowski, S Bacha, and A Phillips. Electron beam welding: Techniques and trends: a review. *Vacuum*, 130:72–92, 2016.

[24] Emmanuel Rodriguez, Jorge Mireles, Cesar A Terrazas, David Espalin, Mireya A Perez, and Ryan B Wicker. Approximation of absolute surface temperature measurements of powder bed fusion additive manufacturing technology using in situ infrared thermography. *Additive Manufacturing*, 5:31–39, 2015.

[25] Ulf Ackelid. Nickel superalloy 718 development for electron beam melting, 2014. MS & T 2014.

[26] Kenneth C Mills. *Recommended values of thermophysical properties for selected commercial alloys*. Woodhead Publishing, 2002.

[27] Meurig Thomas, Gavin J Baxter, and Iain Todd. Normalised model-based processing diagrams for additive layer manufacture of engineering alloys. *Acta Materialia*, 108:26–35, 2016.

[28] P Bidare, RRJ Maier, RJ Beck, JD Shephard, and AJ Moore. An open-architecture metal powder bed fusion system for in-situ process measurements. *Additive Manufacturing*, 16:177–185, 2017.

[29] KG Prashanth, S Scudino, T Maity, J Das, and J Eckert. Is the energy density a reliable parameter for materials synthesis by selective laser melting? *Materials Research Letters*, pages 1–5, 2017.

[30] Umberto Scipioni Bertoli, Alexander J Wolfer, Manyalibo J Matthews, Jean-Pierre R Delplanque, and Julie M Schoenung. On the limitations of volumetric energy density as a design parameter for selective laser melting. *Materials & Design*, 113:331–340, 2017.

[31] T DebRoy, HL Wei, JS Zuback, T Mukherjee, JW Elmer, JO Milewski, AM Beese, A Wilson-Heid, A De, and W Zhang. Additive manufacturing of metallic components–process, structure and properties. *Progress in Materials Science*, 2017.

[32] ASTM Committee F42. *Standard Terminology for Additive Manufacturing Technologies.* ASTM International, 2012.

[33] Arcam. Arcam annual report - 2016. http://www.arcamgroup.com/investor-relations/arcam-annual-reviews/, 2016.

[34] Ulf Ackelid. Method and apparatus for increasing the resolution in additively manufactured three-dimensional articles, July 14 2015. US Patent 9,079,248.

[35] Ulf Ackelid. Method and device for producing three-dimensional objects, October 20 2015. US Patent 9,162,393.

[36] Siegfried Schiller, Ullrich Heisig, and Siegfried Panzer. *Electron beam technology.* John Wiley and Sons, 1982.

[37] Joseph Goldstein, Dale E Newbury, Patrick Echlin, David C Joy, Alton D Romig Jr, Charles E Lyman, Charles Fiori, and Eric Lifshin. *Scanning electron microscopy and X-ray microanalysis: a text for biologists, materials scientists, and geologists.* Springer Science & Business Media, 2012.

[38] Miroslave Sedlacek. *Electron Physics of vacuum and gaseous devices.* John Wiley and Sons, 1996.

[39] Rolf Zenker. Electron beam surface technologies. *Encyclopedia of Tribology*, pages 923–940, 2013.

[40] Peng-Fei Fu, Zhi-Yong Mao, Jian Lin, Xin Liu, Cong-Jin Zuo, and Hai-Ying Xu. Temperature field modeling and microstructure analysis of ebw with multi-beam for near titanium alloy. *Vacuum*, 102:54–62, 2014.

[41] Wentao Yan, Wenjun Ge, Jacob Smith, Stephen Lin, Orion L. Kafka, Feng Lin, and Wing Kam Liu. Multi-scale modeling of electron beam melting of functionally graded materials. *Acta Materialia*, 115:403 – 412, 2016.

[42] U Dilthey, A Goumeniouk, S Bhm, and T Welters. Electron beam diagnostics: a new release of the diabeam system. *Vacuum*, 62(2):77 – 85, 2001.

[43] TA Palmer, JW Elmer, KD Nicklas, and T Mustaleski. Transferring electron beam welding parameters using the enhanced modified faraday cup. *Welding Journal*, 86(12):388, 2007.

[44] JW Elmer and AT Teruya. An enhanced faraday cup for rapid determination of power density distribution in electron beams. *Welding Journal*, 80(12):288–s, 2001.

[45] Zachary C Cordero, Ralph B Dinwiddie, David Immel, and Ryan R Dehoff. Nucleation and growth of chimney pores during electron-beam additive manufacturing. *Journal of Materials Science*, 52(6):3429–3435, 2017.

[46] Yoshiaki Arata. *Plasma, electron and laser beam technology: development and use in materials processing*. American Society for metals, 1986.

[47] Glen Lawerence. Triode electron gun for electron beam machines, September 10 1974. US—Patent 3,835,327.

[48] Sofia Del Pozo Rodriguez. *Investigation and optimisation of a plasma cathode electron beam gun for material processing applications*. PhD thesis, Brunel University London, 2016.

[49] Dan M Goebel and Ira Katz. *Fundamentals of electric propulsion: Ion and Hall thrusters*, volume 1. John Wiley & Sons, 2008.

[50] Aman Kaur, Colin Ribton, and W Balachandaran. Electron beam characterisation methods and devices for welding equipment. *Journal of materials processing technology*, 221:225–232, 2015.

[51] Nathan Hobbs. Arcam sales manager. personal communication.

[52] Thorsten Lower. *Electron Beam Welding: the fundamentals of a fascinating technology*. pro-beam, 2011.

[53] T. Satoh. Electron gun, method of controlling same, and electron beam additive manufacturing machine, February 23 2016. US Patent 9,269,520.

[54] Cambridge vacuum engineering: Electron beam welding. http://www.camvaceng.com/electron-beam-welding/150kv/, 2017.

[55] J Worster. The brightness of electron beams. *Journal of Physics D: Applied Physics*, 2(3):457, 1969.

[56] K. Honda. Machine and method for additive manufacturing, October 29 2015. US Patent App. 14/643,002.

[57] Miroslav Sedlacek. *Electron physics of vacuum and gaseous devices*. Wiley, 1996.

[58] M Hosseinzadeh and A Sadighzadeh. Design and numerical simulation of thermionic electron gun. *arXiv preprint arXiv:1509.06363*, 2015.

[59] Stelian-Emilian Oltean and Mircea Dulau. Focusing and deflection system modelling and simulation of the electron beam equipment CTW 5-60. In *Interdisciplinarity in Engineering International Conference Petru Maior University of Trgu Mures, 2009*, pages 138–143, Tirgu Mures, 01 2009.

[60] R Zenker. Modern thermal electron beam processes–research results and industrial application. *la metallurgia italiana*, 49(3), 2009.

[61] H Ohiwa. The design of deflection coils. *Journal of Physics D: Applied Physics*, 10(11):1437, 1977.

[62] C Melde, G Jäsch, and E Mädler. New developments for high power electron beam equipment. Technical report, Bakish Materials Corporation, Englewood, NJ (United States), 1994.

[63] Tien T Roehling, Sheldon SQ Wu, Saad A Khairallah, John D Roehling, S Stefan Soezeri, Michael F Crumb, and Manyalibo J Matthews. Modulating laser intensity profile ellipticity for microstructural control during metal additive manufacturing. *Acta Materialia*, 128:197–206, 2017.

[64] J. Backlund and T. Lock. Method for fusing a workpiece, October 8 2015. US Patent App. 14/636,607.

[65] Paul Carriere. Preliminary Investigations into the Evaporation Process using a High Brightness Electron Beam Gun. Master's thesis, McGill University, Montreal, Canada, 2012.

[66] Peter Petrov, Chavdar Georgiev, and Georgy Petrov. Experimental investigation of weld pool formation in electron beam welding. *Vacuum*, 51(3):339–343, 1998.

[67] KR Kim and DF Farson. Co 2 laser–plume interaction in materials processing. *Journal of Applied Physics*, 89(1):681–688, 2001.

[68] Georgi M Mladenov, Dmitriy N Trushnikov, Elena G Koleva, and Vladimir Ya Belenkiy. Parameters and some applications of plasma generated during keyhole welding using a highly concentrated energy beam–an overview. *International Journal of Engineering Research & Science*, 2(3), 2016.

[69] Dmitriy Trushnikov, Elena Krotova, and Elena Koleva. Use of a secondary current sensor in plasma during electron-beam welding with focus scanning for process control. *Journal of Sensors*, 2016, 2016.

[70] DN Trushnikov. Using the wavelet analysis of secondary current signals for investigating and controlling electron beam welding. *Welding International*, 27(6):460–465, 2013.

[71] Arcam. Arcam EBM System Q-series Pre-Installation Guide, 2017. Document No: 760174.

[72] PS Wei and Chih-Wei Wen. Missed joint induced by thermoelectric magnetic field in electron-beam welding dissimilar metalsexperiment and scale analysis. *Metallurgical and Materials Transactions B*, 33(5):765–773, 2002.

[73] PJ Blakeley and A Sanderson. The origin and effects of magnetic fields in electron beam welding. *Journal of Welding*, 1984.

[74] M Gäumann, C Bezencon, P Canalis, and W Kurz. Single-crystal laser deposition of superalloys: processing microstructure maps. *Acta Materialia*, 49(6):1051–1062, 2001.

[75] YS Lee and DF Farson. Surface tension-powered build dimension control in laser additive manufacturing process. *The International Journal of Advanced Manufacturing Technology*, 85(5-8):1035–1044, 2016.

[76] S Schiller and S Panzer. Thermal surface modification by electron beam high-speed scanning. *Annual Review of Materials Science*, 18(1):121–140, 1988.

[77] HS Carslaw and JC Jaeger. *Heat in solids*, volume 1. Clarendon Press, Oxford, 1959.

[78] Philipp Drescher, Mohamed Sarhan, and Hermann Seitz. An investigation of sintering parameters on titanium powder for electron beam melting processing optimization. *Materials*, 9(12):974, 2016.

[79] Joakim Karlsson Algardh, Timothy Horn, Harvey West, Ronald Aman, Anders Snis, Håkan Engqvist, Jukka Lausmaa, and Ola Harrysson. Thickness dependency of mechanical properties for thin-walled titanium parts manufactured by electron beam melting (ebm). *Additive Manufacturing*, 12:45–50, 2016.

[80] Tl DebRoy and SA David. Physical processes in fusion welding. *Reviews of Modern Physics*, 67(1):85, 1995.

[81] Lars-Erik Lindgren. Finite element modeling and simulation of welding. part 3: efficiency and integration. *Journal of thermal stresses*, 24(4):305–334, 2001.

[82] Phillip William Fuerschbach, Tarasankar DebRoy, Xiuli He, and Jerome T Norris. *Understanding Metal Vaporizaiton from Laser Welding*. United States. Department of Energy, 2003.

[83] A Raghavan, HL Wei, TA Palmer, and T DebRoy. Heat transfer and fluid flow in additive manufacturing. *Journal of Laser Applications*, 25(5):052006, 2013.

[84] R Rai, P Burgardt, JO Milewski, TJ Lienert, and T DebRoy. Heat transfer and fluid flow during electron beam welding of 21cr–6ni–9mn steel and ti–6al–4v alloy. *Journal of Physics D: Applied Physics*, 42(2):025503, 2008.

[85] R Rai, TA Palmer, JW Elmer, and T Debroy. Heat transfer and fluid flow during electron beam welding of 304l stainless steel alloy. *Weld. J*, 88(3):54s–61s, 2009.

[86] T Mukherjee, V Manvatkar, A De, and T DebRoy. Dimensionless numbers in additive manufacturing. *Journal of Applied Physics*, 121(6):064904, 2017.

[87] Alexander Klassen, Thorsten Scharowsky, and Carolin Körner. Evaporation model for beam based additive manufacturing using free surface lattice boltzmann methods. *Journal of Physics D: Applied Physics*, 47(27):275303, 2014.

[88] A Powell. *Transport Phenomenon in Electron Beam melting and evaporation.* PhD thesis, Massachusetts Institute of Technology, 1997.

[89] Alexander Klassen, Vera E. Forster, Vera Juechter, and Carolin Krner. Numerical simulation of multi-component evaporation during selective electron beam melting of tial. *Journal of Materials Processing Technology*, 247:280 – 288, 2017.

[90] TW Eagar and NS Tsai. Temperature fields produced by traveling distributed heat sources. *Welding journal*, 62(12):346–355, 1983.

[91] Daniel Rosenthal. Mathematical theory of heat distribution during welding and cutting. *Welding journal*, 20(5):220s–234s, 1941.

[92] N Christensen, V de L Davies, K Gjermundsen, et al. Distribution of temperatures in arc welding. *British Welding Journal*, 12(2):54–75, 1965.

[93] HE Cline and TRf Anthony. Heat treating and melting material with a scanning laser or electron beam. *Journal of Applied Physics*, 48(9):3895–3900, 1977.

[94] Oystein Grong. Metallurgical modelling of welding. *Institute of Materials, 1 Carlton House Terrace, London, SW 1 Y 5 DB, UK, 1997. 605*, 1997.

[95] JW Elmer, WH Giedt, and TW Eagar. The transition from shallow to deep penetration during electron beam welding. *Welding journal*, 69(5):167s–175s, 1990.

[96] John Goldak, Aditya Chakravarti, and Malcolm Bibby. A new finite element model for welding heat sources. *Metallurgical and Materials Transactions B*, 15(2):299–305, 1984.

[97] YS Lee and W Zhang. Modeling of heat transfer, fluid flow and solidification microstructure of nickel-base superalloy fabricated by laser powder bed fusion. *Additive Manufacturing*, 12:178–188, 2016.

[98] WH Giedt and LN Tallerico. Prediction of electron beam depth of penetration. *Welding journal*, 67(12):299–305, 1988.

[99] JW Elmer, WH Giedt, and TW Eagar. The transition from shallow to deep penetration during electron beam welding. *Welding Journal*, 69(5):167s–175s, 1990.

[100] Lore Thijs, Frederik Verhaeghe, Tom Craeghs, Jan Van Humbeeck, and Jean-Pierre Kruth. A study of the microstructural evolution during selective laser melting of ti–6al–4v. *Acta Materialia*, 58(9):3303–3312, 2010.

[101] C.Y. Ho. Fusion zone during focused electron-beam welding. *Journal of Materials Processing Technology*, 167(2):265 – 272, 2005. 2005 International Forum on the Advances in Materials Processing Technology.

[102] Rémy Fabbro. Melt pool and keyhole behaviour analysis for deep penetration laser welding. *Journal of Physics D: Applied Physics*, 43(44):445501, 2010.

[103] H Tong and WH Giedt. Dynamic interpretation of electron-beam welding. *WELD J*, 49(6):259, 1970.

[104] Paolo Ferro, Andrea Zambon, and Franco Bonollo. Investigation of electron-beam welding in wrought inconel 706 experimental and numerical analysis. *Materials Science and Engineering: A*, 392(1):94–105, 2005.

[105] John W Elmer, G Fred Ellsworth, Jeffrey N Florando, Ilya V Golosker, and Rupalee P Mulay. Microstructure and mechanical properties of 21-6-9 stainless steel electron beam welds. *Metallurgical and Materials Transactions A*, 48(4):1771–1787, 2017.

[106] J Elmer. Characterization of defocused electron beams and welds in stainless steel and refractory metals using the enhanced modified faraday cup diagnostic. Technical report, Lawrence Livermore National Laboratory (LLNL), Livermore, CA, 2009.

[107] Haijun Gong, Khalid Rafi, Hengfeng Gu, Thomas Starr, and Brent Stucker. Analysis of defect generation in ti–6al–4v parts made using powder bed fusion additive manufacturing processes. *Additive Manufacturing*, 1:87–98, 2014.

[108] Sinan Saadi Al-Bermani. *An investigation into microstructure and microstructural control of additive layer manufactured Ti-6Al-4V by electron beam melting*. PhD thesis, University of Sheffield, 2011.

[109] A Antonysamy. *Microstructure, texture and mechanical property evolution during additive manufacturing of Ti6Al4V alloy for aerospace applications*. PhD thesis, The University of Manchester, Manchester, UK, 2012.

[110] Nicolas Béraud, Frédéric Vignat, François Villeneuve, and Rémy Dendievel. Improving dimensional accuracy in ebm using beam characterization and trajectory optimization. *Additive Manufacturing*, 14:1–6, 2017.

[111] TA Palmer and JW Elmer. Improving process control in electron beam welding using the enhanced modified faraday cup. *Journal of manufacturing science and engineering*, 130(4):041008, 2008.

[112] S Tammas-Williams, H Zhao, F Léonard, F Derguti, I Todd, and PB Prangnell. Xct analysis of the influence of melt strategies on defect population in ti–6al–4v components manufactured by selective electron beam melting. *Materials Characterization*, 102:47–61, 2015.

[113] Adnan Safdar, HZ He, Liu-Ying Wei, A Snis, and Luis E Chavez de Paz. Effect of process parameters settings and thickness on surface roughness of ebm produced ti-6al-4v. *Rapid Prototyping Journal*, 18(5):401–408, 2012.

[114] Sneha P. Narra, Ross Cunningham, Jack Beuth, and Anthony D. Rollett. Location specific solidification microstructure control in electron beam melting of ti-6al-4v. *Additive Manufacturing*, 2017.

[115] Anders Snis. Energy beam position verification, May 17 2016. US Patent 9,341,467.

[116] G Schubert. Electron beam welding- process application and equipment. Technical report, PTR-Precision Technologies, 2000. https://www.ptreb.com/electron-beam-welding-information/technical-papers/electron-beam-welding-process-applications-and-equipment.

[117] CH Radhakrishna and K Prasad Rao. The formation and control of laves phase in superalloy 718 welds. *Journal of Materials Science*, 32(8):1977–1984, 1997.

[118] Jyotirmaya Kar, Sanat Kumar Roy, and Gour Gopal Roy. Influence of beam oscillation in electron beam welding of ti-6al-4v. *The International Journal of Advanced Manufacturing Technology*, pages 1–11, 2017.

[119] S Schiller, S Panzer, and R Klabes. High speed scanning electron beam annealing of ion-implanted silicon layers. *Thin Solid Films*, 73(1):221–226, 1980.

[120] Hai-yan Zhao, Xin Wang, Xi-chang Wang, and Yong-ping Lei. Reduction of residual stress and deformation in electron beam welding by using multiple beam technique. *Frontiers of Materials Science in China*, 2(1):66–71, Mar 2008.

[121] Rolf Zenker, Anja Buchwalder, Norbert Frenkler, and Sven Thiemer. Modern electron beam technologies for surface and surface treatment. *Vacuum in Research and Practice*, 17(2):66–72, 2005.

[122] Tatiana V Olshanskaya, Ekaterina S Salomatova, Vladimir Ya Belenkiy, Dmitry N Trushnikov, and Gleb L Permyakov. Electron beam welding of aluminum alloy almg6 with a dynamically positioned electron beam. *The International Journal of Advanced Manufacturing Technology*, 89(9-12):3439–3450, 2017.

[123] The Welding Institute. Surfi-sculpt precision controlled surface shaping. $http://www.camvaceng.com/assets/uploads/documents/Surfi-Sculpt_UK_05.pdf$, 2017.

[124] Caroline Earl, Paul Hilton, and Bill ONeill. Parameter influence on surfi-sculpt processing efficiency. *Physics Procedia*, 39(Supplement C):327 – 335, 2012. Laser Assisted Net shape Engineering 7 (LANE 2012).

[125] Wei Xiong, Bamber Blackman, John P Dear, and Xichang Wang. The effect of composite orientation on the mechanical properties of hybrid joints strengthened by surfi-sculpt. *Composite Structures*, 134:587–592, 2015.

[126] D Dimitrov, M Aprakova, S Valkanov, and P Petrov. Electron beam hardening of ion nitrided layers. *Vacuum*, 49(3):239 – 246, 1998. 2nd Swedish Vacuum Meeting.

[127] Maria Ormanova, Petr Petrov, and Daniela Kovacheva. Electron beam surface treatment of tool steels. *Vacuum*, 135(Supplement C):7 – 12, 2017.

[128] Junji Morimoto, Nobuyuki Abe, Fumiaki Kuriyama, and Michio Tomie. Formation of a cr3c2/nicr alloy layer by an electron beam cladding method and evaluation of the layer properties. *Vacuum*, 62(2):203 – 210, 2001.

[129] I.A. Bataev, D.O. Mul, A.A. Bataev, O.G. Lenivtseva, M.G. Golkovski, Ya.S. Lizunkova, and R.A. Dostovalov. Structure and tribological properties of steel after non-vacuum electron beam cladding of ti, mo and graphite powders. *Materials Characterization*, 112(Supplement C):60 – 67, 2016.

[130] Nobuyuki Abe, Junji Morimoto, Michio Tomie, and Chihiro Doi. Formation of wc-co layers by an electron beam cladding method and evaluation of the layer properties. *Vacuum*, 59(1):373–380, 2000.

[131] CJ Smith, S Tammas-Williams, E Hernandez-Nava, and I Todd. Tailoring the thermal conductivity of the powder bed in Electron Beam Melting (EBM) Additive Manufacturing. *Scientific Reports*, 7(1):10514, 2017.

[132] Tushar Ramkrishna Mahale. *Electron beam melting of advanced materials and structures*. PhD thesis, North Carolina State University, 2009.

[133] HW Mindt, M Megahed, NP Lavery, MA Holmes, and SGR Brown. Powder bed layer characteristics: the overseen first-order process input. *Metallurgical and Materials Transactions A*, 47(8):3811–3822, 2016.

[134] William J. Sames. *Additive Manufacturing of Inconel 718 using Electron Beam Melting: Processing, Post-Processing, & Mechanical Properties*. PhD thesis, Texas A&M University, 2015.

[135] Alexander J Dunbar, Abdalla R Nassar, Edward W Reutzel, and Jared J Blecher. A real-time communication architecture for metal powder bed fusion additive manufacturing. In *Proc. of the 27th Annual Solid Freeform Fabrication Symposium (Austin, TX, 8–10 August 2016)*, pages 67–80, 2016.

[136] A. Plotkowski, M.M. Kirka, and S.S. Babu. Verification and validation of a rapid heat transfer calculation methodology for transient melt pool solidification conditions in powder bed metal additive manufacturing. *Additive Manufacturing*, 18(Supplement C):256 – 268, 2017.

[137] Zachary C. Cordero, Harry M. Meyer Iii, Peeyush Nandwana, and Ryan R. Dehoff. Powder bed charging during electron-beam additive manufacturing. *Acta Materialia*, 124:437–445, 2017.

[138] Timothy Horn. Material development for electron beam melting. https://camal.ncsu.edu/wp-content/uploads/2013/10/Tim-Horn-2013CAMAL.pdf/, 2013.

[139] W.A. Grell, E. Solis-Ramos, E. Clark, E. Lucon, E.J. Garboczi, P.K. Predecki, Z. Loftus, and M. Kumosa. Effect of powder oxidation on the impact toughness of electron beam melting ti-6al-4v. *Additive Manufacturing*, 17(Supplement C):123 – 134, 2017.

[140] Steven Price, Bo Cheng, James Lydon, Kenneth Cooper, and Kevin Chou. On process temperature in powder-bed electron beam additive manufacturing: process parameter effects. *Journal of Manufacturing Science and Engineering*, 136(6):061019, 2014.

[141] BK Foster, EW Reutzel, AR Nassar, BT Hall, SW Brown, and CJ Dickman. Optical, layerwise monitoring of powder bed fusion. In *26th International Solid Freeform Fabrication Symposium; Austin, TX*, 2015.

[142] RR Dehoff, MM Kirka, WJ Sames, H Bilheux, AS Tremsin, LE Lowe, and SS Babu. Site specific control of crystallographic grain orientation through electron beam additive manufacturing. *Materials Science and Technology*, 31(8):931–938, 2015.

[143] Pan Wang, Wai Jack Sin, Mui Ling Sharon Nai, and Jun Wei. Effects of processing parameters on surface roughness of additive manufactured ti-6al-4v via electron beam melting. *Materials*, 10(10):1121, 2017.

[144] A. Snis. Method for production of a three-dimensional body, July 7 2015. US Patent 9,073,265.

[145] Michael F Zaeh and Markus Kahnert. The effect of scanning strategies on electron beam sintering. *Production Engineering*, 3(3):217–224, 2009.

[146] Michael F Zäh and S Lutzmann. Modelling and simulation of electron beam melting. *Production Engineering*, 4(1):15–23, 2010.

[147] M Andreev, S Kovalsky, S Kornilov, M Motorin, and N Rempe. A device for measuring electron beam characteristics. *AIP Advances*, 7(1):015033, 2017.

[148] Anders Snis. Energy beam deflection speed verification, April 12 2016. US Patent 9,310,188.

[149] Anders Snis. Energy beam size speed, April 12 2016. US Patent 9,347,770.

[150] JW Elmer, AT Teruya, and DW O'Brien. Tomographic imaging of noncircular and irregular electron beam current density distributions. *Welding Journal (Miami);(United States)*, 72(11), 1993.

[151] National Instruments. User guide and specifications: Ni usb-9213. http://www.ni.com/en-ca/support/model.ni-9213.html, 2016.

[152] Lampert Instruments. Puk04 operating manual. https://www.lampert.info/en/home, 2015.

[153] A Shinbine, T Garcin, and C Sinclair. In-situ laser ultrasonic measurement of the hcp to bcc transformation in commercially pure titanium. *Materials Characterization*, 117:57–64, 2016.

[154] Leon I Maissel and Reinhard Glang. Handbook of thin film technology. *New York: McGraw-Hill, 1970, edited by Maissel, Leon I.; Glang, Reinhard*, 1970.

[155] Johannes Trapp, Alexander M Rubenchik, Gabe Guss, and Manyalibo J Matthews. In situ absorptivity measurements of metallic powders during laser powder-bed fusion additive manufacturing. *Applied Materials Today*, 9:341–349, 2017.

[156] S Wu, I Golosker, M LeBlanc, S Mitchell, A Rubenchik, J Stanley, and G Gallegos. Direct absorptivity measurements of metallic powders under 1-micron wavelength laser light. Technical report, Lawrence Livermore National Laboratory (LLNL), Livermore, CA, 2014.

[157] Wayne E King, Holly D Barth, Victor M Castillo, Gilbert F Gallegos, John W Gibbs, Douglas E Hahn, Chandrika Kamath, and Alexander M Rubenchik. Observation of keyhole-mode laser melting in laser powder-bed fusion additive manufacturing. *Journal of Materials Processing Technology*, 214(12):2915–2925, 2014.

[158] Warren H Giedt and Richard Campiotti. Method of automatic measurement and focus of an electron beam and apparatus therefor, 1996. US Patent 5,483,036.

[159] ASTM Committee E20 on Temperature Measurement. *Manual on the use of thermocouples in temperature measurement*, volume 12. ASTM International, 1993.

[160] A Frenk, AFA Hoadley, and J-D Wagnière. In-situ technique for measuring the absorption during laser surface remelting. *Metallurgical Transactions B*, 22(1):139–141, 1991.

[161] A. F. A. Hoadley, M. Rappaz, and M. Zimmermann. Heat-flow simulation of laser remelting with experimenting validation. *Metallurgical Transactions B*, 22(1):101–109, 1991.

[162] M. Gumann, C. Bezenon, P. Canalis, and W. Kurz. Single-crystal laser deposition of superalloys: processingmicrostructure maps. *Acta Materialia*, 49(6):1051 – 1062, 2001.

[163] Erik R Denlinger, Vijay Jagdale, GV Srinivasan, Tahany El-Wardany, and Pan Michaleris. Thermal modeling of inconel 718 processed with powder bed fusion and experimental validation using in situ measurements. *Additive Manufacturing*, 11:7–15, 2016.

[164] A. J. Dunbar, E. R. Denlinger, J. Heigel, P. Michaleris, P. Guerrier, R. Martukanitz, and T. W. Simpson. Development of experimental method for in situ distortion and temperature measurements during the laser powder bed fusion additive manufacturing process. *Additive Manufacturing*, 12, Part A:25–30, 2016.

[165] J. C. Heigel, P. Michaleris, and E. W. Reutzel. Thermo-mechanical model development and validation of directed energy deposition additive manufacturing of ti6al4v. *Additive Manufacturing*, 5:9–19, 2015.

[166] Erik R. Denlinger, Jarred C. Heigel, and Panagiotis Michaleris. Residual stress and distortion modeling of electron beam direct manufacturing ti-6al-4v. *Proceedings of the Institution of Mechanical Engineers, Part B: Journal of Engineering Manufacture*, 229(10):1803–1813, 2014.

[167] J Raplee, A Plotkowski, MM Kirka, R Dinwiddie, A Okello, RR Dehoff, and SS Babu. Thermographic microstructure monitoring in electron beam additive manufacturing. *Scientific Reports*, 7:43554, 2017.

[168] Ralph Barton Dinwiddie, MM Kirka, PD Lloyd, RR Dehoff, LE Lowe, and GS Marlow. Calibrating ir cameras for in-situ temperature measurement during the electron beam melt process using inconel 718 and ti-al6-v4. In *SPIE Commercial+ Scientific Sensing and Imaging*, pages 986107–986107. International Society for Optics and Photonics, 2016.

[169] Karl-Heinz Leitz, Holger Koch, Andreas Otto, Alexander Maaz, Thorsten Löwer, and Michael Schmidt. Numerical simulation of drilling with pulsed beams. *Physics Procedia*, 39:881–892, 2012.

[170] Dominique Drouin, Alexandre Réal Couture, Dany Joly, Xavier Tastet, Vincent Aimez, and Raynald Gauvin. Casino v2. 42a fast and easy-to-use modeling tool for scanning electron microscopy and microanalysis users. *Scanning*, 29(3):92–101, 2007.

[171] Sylvain Tricot, Nadjib Semmar, Lyes Lebbah, and Chantal Boulmer-Leborgne. Zno sublimation using a polyenergetic pulsed electron beam source: numerical simulation and validation. *Journal of Physics D: Applied Physics*, 43(6):065301, 2010.

[172] Jaebum Joo, Brian Y Chow, and Joseph M Jacobson. Nanoscale patterning on insulating substrates by critical energy electron beam lithography. *Nano letters*, 6(9):2021–2025, 2006.

[173] K Mohamed, MM Alkaisi, and RJ Blaikie. Fabrication of three dimensional structures for an uv curable nanoimprint lithography mold using variable dose control with critical-energy electron beam exposure. *Journal of Vacuum Science & Technology B: Microelectronics and Nanometer Structures Processing, Measurement, and Phenomena*, 25(6):2357–2360, 2007.

[174] Manuela Galati, Luca Iuliano, Alessandro Salmi, and Eleonora Atzeni. Modelling energy source and powder properties for the development of a thermal FE model of the EBM additive manufacturing process. *Additive Manufacturing*, 14:49 – 59, 2017.

[175] Alexander Klassen and K Carolin. Modelling of electron beam absorption in complex geometries. *Journal of Physics D: Applied Physics*, 47(6):065307, 2014.

[176] Stefan Nolte, Cl Momma, H Jacobs, A Tünnermann, Boris N Chichkov, Bernd Wellegehausen, and Herbert Welling. Ablation of metals by ultrashort laser pulses. *JOSA B*, 14(10):2716–2722, 1997.

[177] R Nishio, K Tuchida, M Tooma, and K Suzuki. Origins of charged particles in vapor generated by electron-beam evaporation. *Journal of applied physics*, 72(10):4548–4555, 1992.

[178] B Dikshit, GR Zende, MS Bhatia, and BM Suri. Evolution of a two-temperature plasma expanding with metal vapor generated by electron-beam heating. *IEEE Transactions on Plasma Science*, 37(7):1196–1202, 2009.

[179] S. A. Khairallah, A. Anderson, A. M. Rubenchik, J. Florando, S. Wu, and H. Lowdermilk. Simulation of the main physical processes in remote laser penetration with large laser spot size. *AIP Advances*, 5(4):047120, 2015.

[180] I. Yadroitsev, A. Gusarov, I. Yadroitsava, and I. Smurov. Single track formation in selective laser melting of metal powders. *Journal of Materials Processing Technology*, 210(12):1624–1631, 2010.

[181] D Faidel, D Jonas, G Natour, and W Behr. Investigation of the selective laser melting process with molybdenum powder. *Additive Manufacturing*, 8:88–94, 2015.

[182] I. Yadroitsev and I. Smurov. Selective laser melting technology: From the single laser melted track stability to 3D parts of complex shape. *Physics Procedia*, 5, Part B:551–560, 2010.

[183] Z Sun and R Karppi. The application of electron beam welding for the joining of dissimilar metals: an overview. *Journal of Materials Processing Technology*, 59(3):257–267, 1996.

[184] SA David, JA Siefert, JN DuPont, and JP Shingledecker. Weldability and weld performance of candidate nickel base superalloys for advanced ultrasupercritical fossil power plants part I: fundamentals. *Science and Technology of Welding and Joining*, 20(7):532–552, 2015.

[185] William F Gale and Terry C Totemeier. *Smithells metals reference book*. Butterworth-Heinemann, 2003.

[186] Peter J Lee. Abridged metallurgy of ductile alloy superconductors. *Wiley Encyclopedia of Electrical and Electronics Engineering*, 21:75–87, 1999.

[187] DL Moffat and UR Kattner. The stable and metastable Ti-Nb phase diagrams. *Metallurgical and Materials Transactions A*, 19(10):2389–2397, 1988.

[188] PJ Lee and D Co Larbalestier. Development of nanometer scale structures in composites of Nb-Ti and their effect on the superconducting critical current density. *Acta Metallurgica*, 35(10):2523–2536, 1987.

[189] DL Moffat and DC Larbalestier. The competition between martensite and omega in quenched Ti-Nb alloys. *Metallurgical Transactions A*, 19(7):1677–1686, 1988.

[190] DL Moffat and DC Larbalestier. The competition between the alpha and omega phases in aged Ti-Nb alloys. *Metallurgical and Materials Transactions A*, 19(7):1687–1694, 1988.

[191] Robert W Heussner, Peter J Lee, and David C Larbalestier. Nonuniform deformation of niobium diffusion barriers in niobium-titanium wire. *IEEE transactions on applied superconductivity*, 3(1):757–760, 1993.

[192] G Metzger and R Lison. Electron beam welding of dissimilar metals. *Welding journal*, 55(8), 1976.

[193] F Franchini and P Pierantozzi. Electron beam welding of dissimilar materials: Niobium-base alloy c-103 with titanium-base alloy Ti-6AI-4V ELI. *Welding international*, 6(10):792–797, 1992.

[194] MJ Torkamany, F Malek Ghaini, and R Poursalehi. Dissimilar pulsed nd: Yag laser welding of pure niobium to ti–6al–4v. *Materials & design*, 53:915–920, 2014.

[195] JP Oliveira, B Panton, Z Zeng, CM Andrei, Y Zhou, RM Miranda, and FM Braz Fernandes. Laser joining of NiTi to Ti6Al4V using a Niobium interlayer. *Acta Materialia*, 105:9–15, 2016.

[196] TWI. EB technique tells tales on weak welds. http://www.twi-global.com/news-events/case-studies/eb-technique-tells-tales-on-weak-welds-059/.

[197] Z-H Sung, PJ Lee, and DC Larbalestier. Observation of the microstructure of grain boundary oxides in superconducting rf-quality niobium with high-resolution transmission electron microscope. *IEEE Transactions on Applied Superconductivity*, 24(1):68–73, 2014.

[198] James L McCall. A review of metallographic preparation procedures for niobium and niobium alloys. In *Niobium-Proceedings of the international symposium*, 1984.

[199] JM Vitek and SS Babu. Multiscale characterisation of weldments. *Science and Technology of Welding and Joining*, 16(1):3–11, 2011.

[200] Abdullah Yahia Alfaify, James Hughes, and Keith Ridgway. Critical evaluation of the pulsed selective laser melting process when fabricating Ti64 parts using a range of particle size distributions. *Additive Manufacturing*, 2017.

[201] Gerd Lütjering and James C Williams. *Titanium*. Springer, 2007.

[202] A Bauereiß, T Scharowsky, and C Körner. Defect generation and propagation mechanism during additive manufacturing by selective beam melting. *Journal of Materials Processing Technology*, 214(11):2522–2528, 2014.

[203] Carolin Korner, Elham Attar, and Peter Heinl. Mesoscopic simulation of selective beam melting processes. *Journal of Materials Processing Technology*, 211(6):978–987, 2011.

[204] JM Montes, FG Cuevas, J Cintas, and JM Gallardo. Electrical conductivity of metal powder aggregates and sintered compacts. *Journal of materials science*, 51(2):822–835, 2016.

[205] WE King, AT Anderson, RM Ferencz, NE Hodge, C Kamath, SA Khairallah, and AM Rubenchik. Laser powder bed fusion additive manufacturing of metals; physics, computational, and materials challenges. *Applied Physics Reviews*, 2(4):041304, 2015.

[206] CD Boley, SA Khairallah, and AM Rubenchik. Calculation of laser absorption by metal powders in additive manufacturing. *Applied optics*, 54(9):2477–2482, 2015.

[207] Manyalibo J Matthews, Gabe Guss, Saad A Khairallah, Alexander M Rubenchik, Philip J Depond, and Wayne E King. Denudation of metal powder layers in laser powder bed fusion processes. *Acta Materialia*, 114:33–42, 2016.

[208] Saad A Khairallah and Andy Anderson. Mesoscopic simulation model of selective laser melting of stainless steel powder. *Journal of Materials Processing Technology*, 214(11):2627–2636, 2014.

[209] C Körner. Additive manufacturing of metallic components by selective electron beam meltinga review. *International Materials Reviews*, 61(5):361–377, 2016.

[210] Kawatkatsu Kanaya and H Kawakatsu. Secondary electron emission due to primary and backscattered electrons. *Journal of Physics D: Applied Physics*, 5(9):1727, 1972.

[211] V Baglin, J Bojko, C Scheuerlein, Oswald Grbner, M Taborelli, Bernard Henrist, and Nol Hilleret. The secondary electron yield of technical materials and its variation with surface treatments. Technical report, SLAC, 2000.

[212] M Pivi, FK King, RE Kirby, TO Raubenheimer, G Stupakov, and F Le Pimpec. Sharp reduction of the secondary electron emission yield from grooved surfaces. *Journal of Applied Physics*, 104(10):104904, 2008.

[213] K. Honda. Machine and method for additive manufacturing, September 29 2016. US 9,452,489.

[214] E Besuelle and J-P Nicolai. Study of the expansion of a plasma generated by electron-beam evaporation. *Journal of applied physics*, 84(8):4114–4121, 1998.

[215] P Ramakoteswara Rao. Laser isotope separation of uranium. *Current science*, 85(5):615–633, 2003.

[216] B Dikshit, GR Zende, MS Bhatia, and BM Suri. Electron beam evaporation of aluminium with a porous tantalum rod in melt pool. *Journal of Physics D: Applied Physics*, 38(14):2484, 2005.

[217] Jaya Mukherjee, V Dileep Kumar, SP Yadav, Tripti A Barnwal, and Biswaranjan Dikshit. Plasma diagnosis as a tool for the determination of the parameters of electron beam evaporation and sources of ionization. *Measurement Science and Technology*, 27(7):075007, 2016.

[218] Y Mizuno, A Tanaka, K Takahiro, T Takano, Y Yamauchi, T Okada, S Yamaguchi, and T Homma. Hydrogen outgasing from titanium-modified layers with various surface treatments. *Journal of Vacuum Science & Technology A: Vacuum, Surfaces, and Films*, 19(5):2571–2577, 2001.

[219] B Engel and DL Bourell. Titanium alloy powder preparation for selective laser sintering. *Rapid Prototyping Journal*, 6(2):97–106, 2000.

[220] M Sigl, S Lutzmann, and MF Zäh. Transient physical effects in electron beam sintering. In *Solid Freeform Fabrication Symposium Proceedings. Austin, TX*, pages 397–405, 2006.

[221] H-W Mindt, O Desmaison, M Megahed, A Peralta, and J Neumann. Modeling of powder bed manufacturing defects. *Journal of Materials Engineering and Performance*, pages 1–12, 2017.

[222] C Eschey, S Lutzmann, and MF Zaeh. Examination of the powder spreading effect in electron beam melting (ebm). *Solid Freeform Fabrication, Austin, TX, August*, pages 3–5, 2009.

[223] M. Larsson and A. Snis. Method and device for producing three-dimensional objects, May 29 2012. US Patent 8,187,521.

[224] Gerhard Welsch, Rodney Boyer, and EW Collings. *Materials properties handbook: titanium alloys*. ASM international, 1993.

[225] Randall M German. *Powder metallurgy and particulate materials processing: the processes, materials, products, properties, and applications*. Metal powder industries federation Princeton, NJ, USA, 2005.

[226] Ma Qian and Francis H Froes. *Titanium Powder Metallurgy: Science, Technology and Applications*. Butterworth-Heinemann, 2015.

[227] Ziya Esen, Elif Tarhan Bor, and ALİ ŞAKİR BOR. Characterization of loose powder sintered porous titanium and ti6al4v alloy. *Turkish Journal of Engineering and Environmental Sciences*, 33(3):207–219, 2010.

[228] Timothy J Drummond. Work functions of the transition metals and metal silicides. Technical report, Sandia National Labs., Albuquerque, NM (US); Sandia National Labs., Livermore, CA (US), 1999.

[229] Mario Bertolotti. *Physical processes in laser-materials interactions*, volume 84. Springer Science & Business Media, 2013.

[230] S Trajmar. Electron impact spectroscopy of high temperature species. In *Modern High Temperature Science*, pages 65–84. Springer, 1984.

[231] S. Trajmar. *Electron Impact Spectroscopy of High Temperature Species*, pages 65–84. Humana Press, Totowa, NJ, 1984.

[232] Elena G Koleva, Georgi M Mladenov, Dmitriy N Trushnikov, and Vladimir Ya Belenkiy. Signal emitted from plasma during electron-beam welding with deflection oscillations of the beam. *Journal of Materials Processing Technology*, 214(9):1812–1819, 2014.

[233] DN Trushnikov, VM Yazovskikh, LN Krotov, and V Ya Belen'kii. Formation of a secondary-emission signal in electron beam welding with continuous penetration. *Welding International*, 21(5):384–386, 2007.